DEVELOPMENTS IN TENSIOGRAPHIC MULTIVARIATE ANALYSIS LEADING TO A NEW APPROACH WITH PREVALENT APPLICABILITY FOR SAMPLE FINGERPRINTING AND DATA REPRESENTATION

SVEN MANFRED RIEDEL

A thesis submitted in partial fulfilment of the
requirements of Kingston University
for the degree of Doctor of Philosophy

This research programme was carried out in collaboration
with Kelman Ltd. and Carl Stuart Ltd.

October 2007

BLANK PAGE IN ORIGINAL

Dedicated
to
Carmen, Jörg and Matti

CONTENTS

ACKNOWLEDGEMENTS

This thesis emerged with the support from two commercial companies Carl Stuart Ltd. and Kelman Ltd. and indeed with the help from many people around Europe. I am very grateful to all of you for putting in the time and effort to make this thesis a substantive body of work that hopefully goes beyond the usual postgraduate study of a prototype that approached a commercial instrument, which was produced and tested by myself and co-workers. I have had to work in so many diverse fields including electronics, software, physics, chemical applications and others that it would be impossible without your help for me to have delivered on this project. There are many others who are due thanks here but of necessity I am limited in space, so to all my friends and who have been involved, a collective thank you.

As with all these things there are special people who deserve to be singled out. Dr. Norman McMillan introduced me to the drop analysis project in 1997 and his supervision during the time of the practical research work and the write-up of this thesis was exemplary and of quality. The time he contributed was vital and stretched well beyond official working hours. McMillan's vision of developing an important liquid analysis tool for the future of both research and commercial industries is slowly becoming a reality. I hope to see my work contributing to new techniques for diagnosing and treating diseases and in other tangible ways being developed for the betterment of mankind. Dr. Andy Augousti took meticulous care of the write-up of my thesis and took the lead here in helping me improve my theoretical and writing skills. In addition, he also devoted a lot of time to necessary administrative work, and again like my other supervisor, his contribution went well beyond normal working hours. Through his constant encouragement Andy ensured that I finished this thesis.

Dr. Martina O'Neill spent many late hours conducting very important measurements with the drop analyser and contributed greatly to the experimental testing in joint work with myself that is seen in the body of this thesis. Des Carbery helped with insights about vibration and anti-vibration techniques. Dr. Dennis Morrin, Dr. Brian O'Rourke and Anne Bertho provided me with foundations in chemical measurement and applications. Mike Baker, Dennis Boller, Mathias, Adrian O'Neill, Julian Mason and Vincent Lawlor were always available to discuss electronic or software issues. Dr. M. Kokuer, Prof. F. Murtagh and Dr. E. O'Mongain contributed by detailed discussions to the statistics and wavelet sections in this thesis. Gavin Dunne was very much involved in the experimental work into the data smoothing studies that are included in a chapter of this thesis. K. Beverley made her expertise available to questions arising about evaporation. Donal Skelly spent a lot of time on drophead improvement and experimental work. Dr. Duncan McMillan, Dr. Douglas McMillan and Logan McMillan assisted with my measurements with the drop analyser and provided me with insights to different applications for this instrument. In a simple but vital way Kevin Arthur's maintenance of the liquid delivery system of the instrument was important. Alan McGragor contributed to the mechanical design issues and the manufacturing process. Jon and Odgar from Norway were heavily involved in the design and testing of the thermally controlled system of the drop analyser. Meds et al from Denmark were able to

take measurements with the extremely sensitive constant-head setup. I also would like to say thank you to all my friends and work colleagues Flemming, Sten, Jorgen, Jasper, Arne, Morton and Alan from Denmark for their support and kindness. Many thanks to the financial and technical support from Carl Stuart Ltd., especially Stuart Smith and Gillian Smith and also to many in Kelman Ltd., but especially John Cunningham, Michael Cunningham, Peter Cunningham and Ken Ritchie. Without the involvement of these two companies this work would not have been undertaken or this written. Last but not least I say thank you for the friendship and encouragement of a less technical kind to Trixie McMillan, Julie Tynan, Mrs. Irene McMillan and indeed all my friends around the world for all their support over the last decade.

ABSTRACT

This thesis describes a comprehensive engineering development of a new commercially important liquid analysis technology that has found applications across a spectrum of industries. These applications include measurements in the water, food, chemical and pharmaceutical industries, but extend to applications for control in the heavy industries of electrical power and manufacture. The tensiograph instrument described in this study evolved from an existing prototype that had an information content of the signal less than 4 bits. This Mark 1 version had been used in various application studies and demonstrated good potential. The project describes how this very limited instrumental system was reengineered to deliver a Mark 2 instrument with very substantial improvement. With this upgraded instrument, it has been possible to provide ultra-sensitive measurements, for example, on priority pollutants (PP) in real water that were detected at ppb levels. The engineering that transformed the instrument was undertaken in a prioritised system engineering development based on using a new information-based approach devised by the author and McMillan. This new approach is described in Chapter 6 and its successful application to the analysis and subsequent engineering of the tensiograph system is described. The approach employs the universal yardstick of information, which is different to the traditional dB methods used in systems engineering. The fundamental issue is that these traditional methods do not provide a unified systems analysis simply because the reference 0dB levels for different energy forms are not the same. The Mark 2 was engineered rationally top-down, so that the instrumental problems were solved in a logically ordered way. In the following chapters the actual rigorous engineering (optical, electronic, mechanical, thermal and software) is detailed. The chapter structure is broken down to present all the phases of this work. Chapter 3 details the electronic engineering development and discusses the electronic circuit design for a light source driver, silicon detector and a temperature controller. This electronic engineering development was done in a professional environment working in Kelman Ltd. who led the 5th Framework EU Aqua-STEW (Surveillance Techniques for Early Warning) project that supported this work, and the highest commercial electronics engineering standards were used throughout. Chapter 4 details the design of acquisition, analysis, control and automation software. The software development was undertaken using the best practice Object Oriented approach and the work described is notable for providing an integrated user environment. Chapter 5 describes drophead developments, which were a serious attempt to optimise the engineering of the key element of the tensiograph; this work in fact contributed in a number of ways to the optimised design. Chapter 6 describes the new system engineering approach discussed above. In addition, this chapter details the engineering advances made in the design of the anti-vibration system and thermal control module. The latter achieves the absolutely vital accuracy of 0.1°C and reproducibility ±0.01°C. The next section describes the development of the improved liquid delivery systems. The software that controls the various pump operations for sample delivery, cleaning and control of the drop formation (stopping at appropriate positions, for example, within the drop cycle) is described. The entire code for all the software runs to over 300 pages and is bound in a separate volume. Chapter 7 is on fingerprinting and data archiving. This work describes the development of a new data mining approach that was introduced by McMillan and the author in 1998 and shows signs at this point of becoming an established technique with several other PhD and Masters studies being developed around this. The theory of data-scatter has been presented based on the original pioneering work done by the author and the utility of this method has been demonstrated in some important tensiographic applications. The chapter concludes with a brief discussion of the use of the technique to reduce data storage in archiving of digital signals.

CHAPTER 1

INTRODUCTION

Liquid analysis is an important subject in many areas of modern science such as product development, quality control (QC), ecological monitoring and medicine. The production processes in the brewing, distilling and soft drink industry, cleanliness monitoring of river water and examination of body fluids are examples of the importance of advanced liquid analysis methods. A liquid study is almost always based on the determination of the chemical and physical characteristics of the liquid under test (LUT) that allow an analyst to discriminate between liquids. Typical characteristics of a liquid are its surface tension, density, colour, refractive index and viscosity that can be measured quantitatively using appropriate 'traditional' measuring devices such as surface tension balances, density meters, ultra-violet-visible (UV-vis) spectrophotometers, refractometers, and viscometers respectively. It is obvious that multiple measurements are necessary to conduct a rigorous liquid analysis, and in many cases of the examples mentioned above the analyst is in fact more interested in relative chemical and physical characteristic changes of the LUT rather than their absolute values. Monitoring the quality of river water over an extended period of time is one example of the study of relative changes in chemical and physical characteristics of the LUT. Furthermore, various 'traditional' measuring devices are required to obtain the measurands that are necessary for the analysis of the LUT.

In the 19th century T. Tait [1-1] devised a surface analysis method based on liquid drops, which was then further developed by Rayleigh et al [1-2] using photography and vibration techniques for the surface analysis of pendant drops. These principles had been adapted in 1987 by McMillan et al [1-3] to provide the basis for a new instrument with the capability of measuring the chemical and physical characteristics of a liquid individually, sequentially or collectively. The new measuring technique of the chemical and physical characteristics of a liquid, which is to date referred to as the optical modality of tensiography, injects light into a pendant drop that is sent, after internal reflection in the drop, to a detector that converts the light signal into an electronic signal, which is then used for further analysis [1-4].

The aim of the thesis will be elucidated in Section 1.1. Section 1.2 describes briefly the optical modality of tensiography and provides the basic terminology used in this thesis, which is helpful for the discussion of the project. An overview of the work carried out over more than a decade on the optical modality by McMillan and co-workers is given in Section 1.3. This chapter continues then with the description of challenges in Section 1.4, which the author of this thesis overcame during the development of an effective tensiographic instrument, and ends with an outline of the content of the remaining chapters in Section 1.5.

1.1 Aim of the Thesis

The thesis is concerned with the engineering of an instrument for liquid analysis in all its related facets. This amplitude modulated fiber optic sensor (AMFOS) based instrument with multiple measurement capabilities will be referred to as the multianalyser or tensiograph. The thesis will give a theoretical description of optical tensiotraces and the engineering issues involved in refining the optical and mechanical engineering of the tensiograph. It will, in particular seek to provide an in-depth analysis of the related electronic and computer issues. These issues will involve the data capture, signal processing, data analysis, data display, and the associated software engineering and definition of algorithms of the multianalyser. The thesis is not therefore about tensiography as such, although it deals with aspects of tensiographic applications, as they are relevant to the study of these instrumental issues. The thesis in its kernel is about the exploration of the inter-relation of optical, electronic and software issues that are specific to the optical modality of tensiography.

1.2 Brief Description of Optical Tensiography

Tensiography, the study of the chemical and physical characteristics of drops, which is a major enhancement to the stalagmometric theory that is mainly employed in conjunction with surface tension related measurements [1-5], provides a method for rapid measurements of multiple chemical and physical properties of the LUT with only one instrument instead of using a variety of 'traditional' measuring devices. J. Tyndall

demonstrated in 1854 the principle of light guidance in a jet of water [1-6]. Inspired by this man, who was also famous for his experiments on drops and rainbows [1-7], McMillan and co-workers began in 1987 to investigate the potential of tensiography by injecting light into the inside of drops to study rainbow type reflections in drops distended by gravitational forces [1-8]. The field of tensiography may now have evolved as a branch of liquid science in its own right with the more recent development of new modalities, especially the capacitive [1-9] and ultrasonic [1-10], [1-11] modalities. The optical modality can supply information related to optical characteristics such as refractive index and colour, whereas the capacitive modality can supply information related to electrical characteristics such as conductivity and dielectric constant. Both techniques supply information on mechanical properties such as density, viscosity and surface tension. In this thesis the author refers to the optical modality when the term tensiography is mentioned.

The optical modality of tensiography is a new branch of science for analysing liquids using what is, in essence, a graphically based method of analysing signals derived from a transducer system monitoring a pendant drop. This technique is based on a fiber drophead and for the simplest case of a two-fiber system as shown in Figure 1-1. The LUT is fed via a poly-ether-ether-ketone (PEEK) or stainless steel liquid delivery tube [*4*] to a concave or flat drophead [*2*] made out of PEEK or stainless steel. The drophead supports the growing drop [*6*] of the LUT until the gravitational forces overcome the surface forces acting on the drop, at which point drop separation occurs. Throughout this process, light from a light emitting diode (LED) [*7*] is injected into the drop through a polymethylmethacrylate (PMMA) or silicon dioxide SiO_2 (silica) source-fiber [*5*] and the signal reflected from the inner surface of the drop is then picked up by a collector-fiber [*3*] and consequently transmitted to a photodiode [*1*]. A knife-edge [*8*] is fitted to the end-face of a flat drophead in order to adjust the height h between the end-face of the fibers and the drop-supporting edge. This height adjustment has an effect on the measurement results, which will be fully explained in Chapter 5.

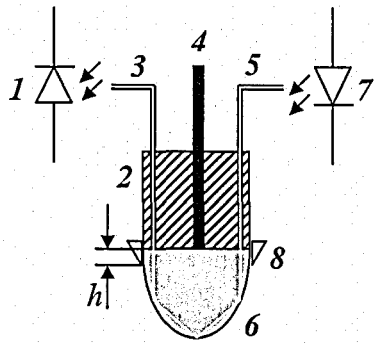

[*1*] **Photodiode** (spectral response range: 320 to 1100 *nm*)
[*2*] **Drophead** (concave or flat, PEEK or stainless steel, ∅ 9.0 *mm*)
[*3*] **Collector-fiber** (PMMA or silica, core: ∅ 1.0 *mm*)
[*4*] **Liquid delivery** (PEEK or stainless steel, inner: ∅ 1.0 *mm*)
[*5*] **Source-fiber** (PMMA or silica, core: ∅ 1.0 *mm*)
[*6*] **Drop** (hanging from the drophead under gravity)
[*7*] **LED** (selectable: 470 *nm*, 530 *nm*, 660 *nm*, 950 *nm*)
[*8*] **Knife-edge** (for fiber-height *h* adjustment)

Figure 1-1. Cross-section of a cylindrical drophead of an optical two-fiber system.

The conversion and amplification of a low photocurrent, generated in the photodiode [*1*], into an adequate voltage signal is necessary before the signal is passed to an acquisition board incorporated in a personal computer (PC). The scheme of the conversion and amplification arrangement is shown in Figure 1-2 and a detailed description is given in Chapter 3. The embedded analogue to digital converter (ADC) of the acquisition board then converts the analogue voltage into a digital signal, which is subsequently transferred to the memory of the PC where it is stored in digital form for later analysis.

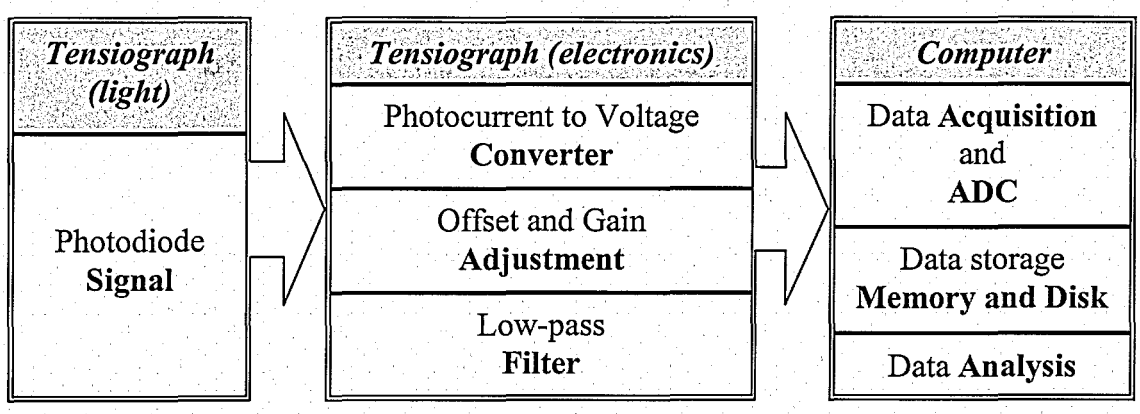

Figure 1-2. The principle of the signal flow.

The key concept of a tensiograph is the fact that all the various physical and chemical processes that modulate the coupled light in the drop produce a signal, which is unique for every specific combination of properties of the LUT. A data set recorded over the time of the life cycle of a drop is called a tensiotrace and Figure 1-3 shows the characteristic features of this signal. The life cycle of a drop starts with a remnant drop, which then grows to full size and eventually separates from the drophead. A tensiotrace is an AMFOS signal derived from the instrument as the result of processes that produce the profile of the tensiotrace, which include partial and total internal reflection (TIR) of the light beam inside the pendant drop, absorption of the light from chromophores in the liquid, scattering of the light from turbid particulate matter, changes in the emission

angle from the source-fiber, and indeed perhaps other processes. The specific shape of the drop of a liquid will however in all cases be the controlling factor in the overall form of the resulting tensiotrace. The unique profile of a tensiotrace is obviously dependent on the physical and chemical properties of the LUT, and shows particular sensitivity to the surface tension/density ratio, absorbance and refractive index. The positioning of the fibers in a drophead has been engineered, as far as possible from empirical adjustments, to optimise the measurement of the physical and chemical properties and these complex engineering issues will be explored in Chapter 5.

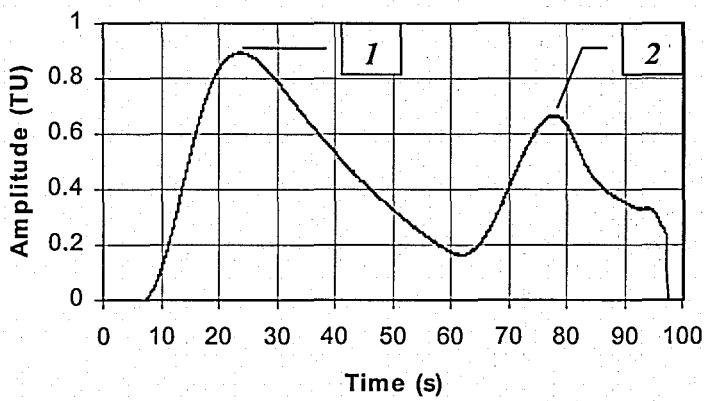

Features of this trace
[*1*] Rainbow Peak
Peak Period: 23.813s
Peak Height: 0.894
[*2*] Tensiograph Peak(s)
(up to two for existing head)
Peak Period: 77.781s
Peak Height: 0.669
Drop Period: 97.156s

Figure 1-3. Typical tensiotrace showing the characteristic features.

A tensiotrace, including the amplitudes of a rainbow peak [*1*] and a tensiograph peak [*2*], is normalised to 4095 (maximum resolution of a 12-bit ADC) and displayed over the time in seconds. The normalised unit of tensiographic amplitudes has been termed tensiograph unit (TU). The rainbow peak height (RPH) and the rainbow peak period (RPP) are very sensitive to the refractive index of a liquid. The name rainbow peak is derived from the fact that in rainbows a measurement of the angle of the bow provides a measurement of the refractive index of the liquid [1-12]. Changing the wavelength of the LED [*7*] (Figure 1-1) in consecutive measurement cycles has an effect on the tensiograph peak height (TPH) and the tensiograph peak period (TPP) due to the absorbance of the LUT, which can be used for colour verification purposes. The drop period (DP) is the time taken for a drop to form and detach from the drophead and can be used to provide information about the surface tension/density ratio of a liquid. These and other physical and chemical properties have been shown to influence the profile of a tensiotrace [1-13], but despite the obvious usefulness of an instrument that provides so many measurands, the principal use of the tensiograph however is its first commercial type as a fingerprinting technique. The software engineering that the present thesis describes is predicated on this fact. It has been demonstrated over a period

of several years now that the complex physical and chemical properties of a drop that ultimately define the profile of a tensiotrace provide a very sensitive fingerprint technique of liquids or solid samples dissolved in a solvent [1-14].

1.3 History of Tensiography

This section gives a brief overview of the various development stages of the tensiograph and its applications commencing in 1987 when McMillan and co-workers began to investigate the potential usefulness of such an instrument. The description of historical objectives in tensiography ends in 1997 when the author of this thesis got involved in this project. The development period of the tensiograph from 1997 to 2001 will then be the subject of this thesis, which discusses the different routes that have been followed to achieve the improvement compared to a preliminary tensiographic instruments.

1.3.1 Preliminary Investigations into Tensiography

Investigations into the analytical potential of measuring a property of a liquid began in 1987 using an instrument that was termed a fiber drop analyser (FDA). This FDA-setup, Figure 1-4, marked the beginning of the development of the optical modality in tensiography [1-3].

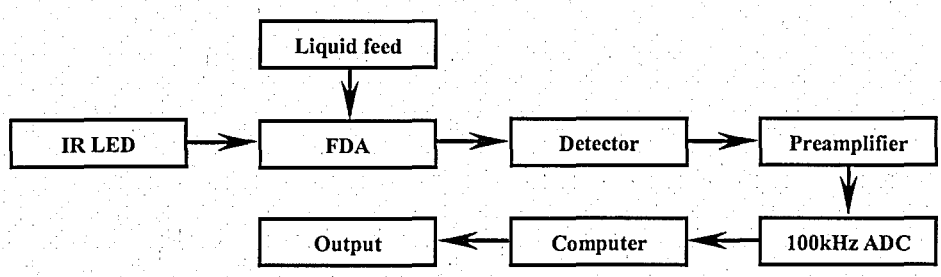

Figure 1-4. Schematic diagram of the FDA apparatus.

In the following phase of the liquid drop investigations the instrument was used to measure individually surface tension, viscosity, refractive index and the chemical composition of the LUT [1-4]. The capability of simultaneously measuring all the above measurands in one measurement cycle was demonstrated on the basis of one set of results obtained from the sugar processing industry [1-15]. The prototype FDA had been operated essentially with one infrared (IR) LED source with a 940*nm* spectral peak matched to a phototransistor, which was used as the light signal detector of the

instrument. The two approaches to the electronic processing of the signal had been via a Tektronics 2201 storage oscilloscope, primarily for troubleshooting and the investigation of small details in the fiber drop trace (FDT), and secondly via a Wild Vision ADC 1208 incorporated in an Acorn Archimedes 440 microcomputer with purpose written software for the data analysis. The software was written in BBC BASIC and presented the captured data in a screen format triggered on the point of drop separation, which is shown in Figure 1-5.

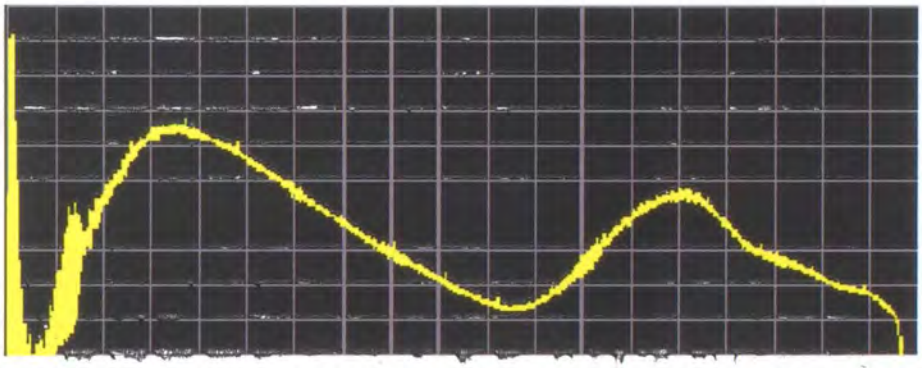

Figure 1-5. FDT captured with a preliminary FDA showing a poor signal-to-noise quality.

For a constant liquid delivery to the drophead of the FDA the apparatus employed a Hamilton Microlab pump fitted with a $500\mu l$ syringe. The capillary used for the liquid delivery was a standard $0.75mm$ inner diameter PEEK high-pressure liquid chromatography (HPLC) tubing. A rather poor signal-to-noise ratio (SNR) of less than $20decibel$ (dB) had been recorded in this early development phase of the instrument. The SNR of the captured tensiographic data presented throughout this thesis was calculated using Eq. (1-1)

$$SNR = 20dB \lg\left(\frac{U_a}{U_n}\right) \tag{1-1}$$

where U_a is the maximum amplitude of the acquired tensiotrace and U_n is the maximum noise amplitude in the trace, which is derived as follows (Consider Figure 1-6 and also Section 2-5 of Chapter 2 for more detailed information).

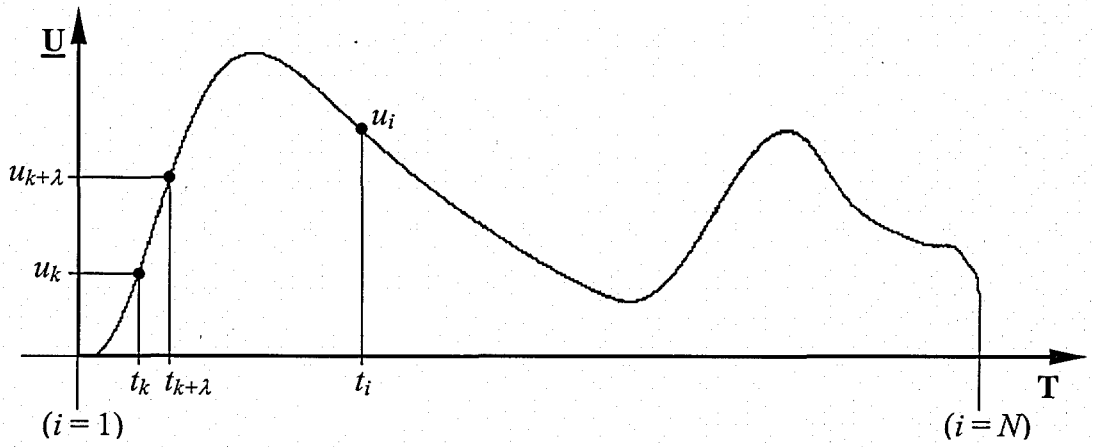

Figure 1-6. A tensiotrace showing an example of the best linear section in the trace.

First, finding the best linear section in a tensiotrace is essential for the calculation of U_n. Note that only one tensiographic data set is available to carry out statistical computations, which usually require numerous independently measured data sets. The linear correlation coefficient r is applied to find a linear section in a tensiotrace.

$$r = \frac{\sum_{i=k}^{k+\lambda}\left[\left(t_i - \frac{\sum_{i=k}^{k+\lambda} t_i}{\lambda}\right)\left(u_i - \frac{\sum_{i=k}^{k+\lambda} u_i}{\lambda}\right)\right]}{\sqrt{\sum_{i=k}^{k+\lambda}\left(t_i - \frac{\sum_{i=k}^{k+\lambda} t_i}{\lambda}\right)^2 \sum_{i=k}^{k+\lambda}\left(u_i - \frac{\sum_{i=k}^{k+\lambda} u_i}{\lambda}\right)^2}} \quad (1 \le k \le N-\lambda) \tag{1-2}$$

where λ is set to 32 data points, and r close to ± 1 is an indication that the data points are in linear correlation. Using the best linear section in a tensiotrace, the standard deviation σ is determined

$$\sigma = \sqrt{\frac{\sum_{i=k}^{k+\lambda}\left(u_i - \left[\frac{(u_{k+\lambda} - u_k)(t_i - t_k)}{t_{k+\lambda} - t_k} + u_k\right]\right)^2}{\lambda - 1}} \tag{1-3}$$

and subsequently multiplied by 3 to fall into the 99.87% confidence range of a normally distributed standard deviation (see Table A4-1).

$$U_n \le 3\sigma \tag{1-4}$$

is then the maximum noise amplitude in this linear section. Note that the factor λ was empirically determined by varying it in size for tensiotraces of different liquids.

1.3.2 Conversion to a Multi-Wavelength Instrument

The introduction of a charge coupled device (CCD) and a tungsten light source in 1992 converted the existing instrument into a multi-wavelength FDA. The FDA had been used as a comprehensive spectrophotometer using a portable multi-channel spectrometer (PMS). It was a landmark that in this configuration the drop absorbance measurements could be made to a high standard of sensitivity, and this experimental fact had some practical consequences for FDT measurements of a multi-wavelength FDA with special reference to applications in medical diagnostics [1-16]. Figure 1-7(a) shows the experimental setup of the PMS-FDA system.

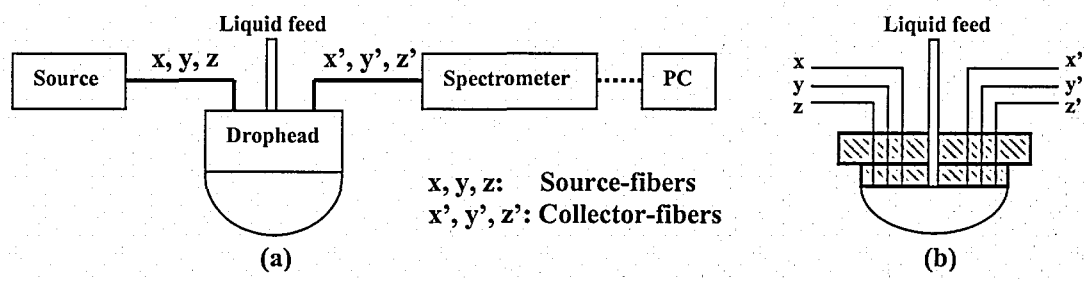

Figure 1-7. (a) FDA experimental setup showing the basic PMS detector system. (b) Cross-section of PMS-FDA cylindrical multi-fiber flat drophead showing positions of three sets of fiber pairs.

For the multi-wavelength PMS-FDA system, white light was injected into the source fiber from a tungsten source, operated from a controlled stabilised direct current (DC) power supply, with the coupling improved by a simple lens focusing arrangement. The single-wavelength system used a standard IR photodiode as the detector. For the PMS system, the spectral content of the returned signal was recorded every 40*ms*, which was a sampling rate determined by the frame rate of the CCD camera of the PMS. This system was capable of analysing the signal from 12 fiber inputs simultaneously and the fibers used were standard 200μm silica fibers that had been polished before mounting in the drophead.

1.3.3 Study of Vibrating Pendant Drops

Qualitative investigations into the visco-elastic surface properties for a series of pure liquids had been conducted using the FDA and Fast Fourier Transform (FFT) analysis, by means of measurement of the damped vibrations in mechanically excited pendant drops. This study revealed a range of processes in the damped vibrations of pendant drops and opened up a new approach to the measurement of physical properties for the micro-volume analysis of liquids [1-17]. The various fiber positions in the drophead, **xx'**, **yy'** and **zz'** as shown in Figure 1-7(b), were used to manipulate the profile of these specific FDTs, and this will be discussed comprehensively in Chapter 5.

1.3.4 Drophead Investigations

Drophead studies had been carried out with special reference to fingerprinting liquids [1-18]. The ideal drophead for the FDA was of a flat cylindrical design, as shown in Figure 1-7(b). Such a drophead enabled surface tension measurements to be made based on the established stalagmometric methods [1-19]. The PMMA fibers used for the single-wavelength measurements were 1*mm* in diameter, and an investigation was made into the profile of FDTs obtained for dropheads of various diameters and positioning of the PMMA fibers. It was understood from the earliest work that most of the FDTs produced with a flat drophead did not contain a rainbow peak. However, a rainbow peak was obtained with a flat drophead (6*mm* and 7*mm* diameter) for aqueous solutions of ethanol. Conversely it was discovered during the studies with a concave drophead, as shown in Figure 1-8, that for all investigated liquids, a rainbow peak was present in the FDT.

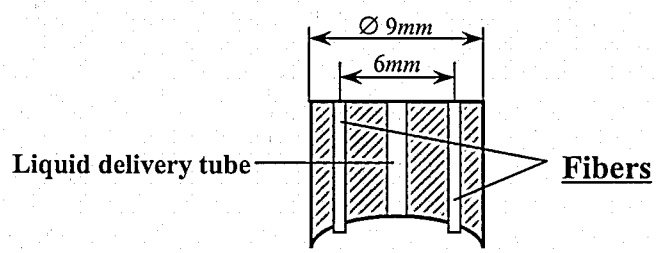

Figure 1-8. Cross-section of a cylindrical concave drophead of an optical two-fiber system.

For this reason, a concave drophead (*9mm* diameter and *6mm* fiber separation) had been selected as being the drophead for general use in the FDA. The multi-wavelength setup during this research period was the same as that shown in Figure 1-7(a), with the exception that the source and detector were replaced by components from Ocean Optics. The light that was injected into the drop came from an Ocean Optics LS-1 tungsten halogen lamp, an Ocean Optics PX-1 xenon flash lamp or from a number of LEDs housed in a specially constructed source and detector box. The light coupled back from the collector-fiber in the drophead was passed either to the Ocean Optics SD1000 CCD fiber spectrometer or to one of the several specially constructed photodiode or phototransistor detectors, which were also located in the source and detector box. In all cases, the amplified signal from the detector was passed to a DASH 16 Junior ADC card, which was incorporated in a PC and digitised the signal for the analysis with a Microsoft Windows 3-11 based software package, which was written in Visual Basic.

1.3.5 Fingerprinting Liquids

In 1994 McMillan and co-workers directed their studies towards manufacturing a commercial instrument that would be used to fingerprint liquids by acquiring a data set generated from multiple changes of physical properties during a life cycle of a drop and subsequently comparison with previously obtained data sets. From that time, in published papers and articles, the name FDA was replaced with tensiograph multianalyser, or either used separately. The term tensiograph was decided as a generic name by the researchers in the Innovation Centre Carlow in Ireland and Kingston University in England working on respectively the optical and ultrasonic/capacitive modalities. The respective data set, previously known as FDT, became referred to thereafter as tensiotrace.

In this research period the emphasis was put on the SNR improvement of the tensiotraces, which is an important issue for fingerprinting liquids. Hence, the pre-production multianalyser was equipped with a specially engineered LED and detector system, working with three plastic-fiber-optic transmitter diodes from Siemens SFH750V, SFH452V and SFH450V at the three wavelengths of 660*nm*, 770*nm* and 950*nm* respectively and the matching detector SFH250V with a photosensitivity spectral range of 400*nm* to 1100*nm*. The existing Windows 3-11 based analysis software package was also upgraded to enable the analyst to fingerprint liquids using a fingerprint method that applies match and difference values, which are termed M-values and D-values respectively (fully explored in Chapter 2), obtained from their tensiotraces to build a database library of products.

A brewing study in cooperation with Brewing Research International (BRI) Ireland had shown that the fingerprint method, using M-values and D-values, was capable of maintaining QC standards from the interpretation of the data in terms of the variation in the various physical and chemical properties of the product, against the standard UV-vis method [1-20]. In addition, a new approach to concentration measurements of pure protein solutions had been devised, to compare once again the measurement capability of the tensiograph with a standard UV-vis instrument [1-21].

This review of the various development stages of a tensiographic instrument and the related applications has demonstrated the potential usefulness of an instrument with multiple measurement capability such as the tensiograph multianalyser. The persistent demand on the improvement of the related optical, mechanical, thermal, electronic and computer aspects has indeed led to the PhD research project of the author, which commenced in 1997 and describes the tensiograph development and related applications until 2001.

1.4 Challenges facing the Effective Tensiographic Instrument Development

During the development of the tensiograph the issues surrounding the choice of drophead, fibers, sources and detector, liquid delivery system, temperature control module and an anti-vibration system have all had to be very carefully considered. In the following discussion the major engineering issues of the tensiographic instrument will

be described briefly and the approaches to minimise the noise contributions from all the components to the total dB overhead will be given.

1.4.1 Drophead

One of the most important issues concerns drophead engineering design for the reproducibility of mechanical drop formation, which is the single most crucial aspect for fingerprinting liquids. A long investigation by the author of this thesis into the production engineering aspects has demonstrated that, even with the best automated production facilities using the most appropriate high-precision tools; it is impossible to produce identical tensiotraces with different dropheads of the same kind. It has to be noted that the reproducibility of drophead performance is limited and can only be carried out to a certain level of accuracy. The tolerances of borehole diameter, angle and the overall dimensions of the drophead vary with the choice of material, head shape and available manufacturing tools. The quality of the boreholes in the drophead is important for the positioning of the fibers. Another second vital characteristic of the drophead is its chemical resistance to damage from aggressive liquids. A PEEK drophead, for example, might not be the best option for conducting experiments with low-concentration acids, whereas a stainless steel drophead is well able to sustain a medium-concentration acid attack, but only glass or preferably quartz should be used for dropheads in long-term experiments involving high-concentration acids. Consequently, both the shape and material of the drophead also influences its ability to be cleaned between measurements of different liquid samples. Obviously smooth surfaces, as they can be found in the flat drophead design, as shown in Figure 1-7(b), are better to clean than concave dropheads, as shown in Figure 1-8, where the placement of fibers can produce crevices that can be easily contaminated and consequently exacerbate the practical problem of decontamination. The suspended liquid on a concave drophead is forced to the edge of the drophead. It has better wetting capabilities as a consequence than a flat drophead, assuming of course that both dropheads are made out of the same material, have the same dimensions and were dry before the liquid delivery started. It has to be noticed that the fibers of both drophead designs, see Figures 1-7(b) and 1-8, are exposed to the LUT causing a problem, which will be discussed in Section 1.4.2. The development of a new flat quartz drophead design originated from the efforts of

McMillan and the author to optimise the engineering of the drophead and to overcome the problem of fiber exposure, see Chapter 5 for more information. This drophead design work was carried out over the entire development phase of the tensiograph since the start of this project and constitutes a major advance in tensiography.

1.4.2 Fibers

PMMA fibers have a number of advantages compared to silica fibers of the same diameter, specifically their flexibility, cheapness and availability. Their outstanding flexibility allows the user to bend PMMA fibers virtually to any position in the tensiograph, which is important for coupling the fibers to the drophead and the opto-electronic components located in the instrument, where the space is limited. The disadvantages of PMMA fibers on the other hand are unfortunately fundamental when the ultraviolet (UV) capabilities of the instrument are given consideration. The two major weaknesses of PMMA fibers are in fact their inability to resist chemical attack and the radical attenuation of the transmitted optical signal in the UV-B and IR-A (Appendix 3, Table A3-2) regions of the spectrum. Covering the tips of the fibers, which are exposed to the LUT, with a specially designed resin, eliminates the possibility of chemical attack of the fibers. The effect the resin has on the transmitted optical signal is negligible, but the positioning of the fibers suffers inconsistency and this affects the drophead reproducibility, which results in the inability to fingerprint liquids. Silica fibers on the other hand withstand chemical attack and transmit the optical signal basically with low attenuation over the whole spectral range from UV-B to IR-A, but their extreme brittleness at $1mm$ diameter makes it difficult to handle these fibers. It is almost impossible to bend silica fibers over an extended time period. This can be avoided after all by connecting the opto-electronic components (LED and photodiode) permanently to one end of the fibers, instead of bending the fibers to a remote location of these opto-electronic components. An additional problem is the difficulty of fixing the fibers in the drophead because the shrinkage of the resin during curing stresses and usually cracks the $1mm$ diameter silica fibers. Eventually McMillan and the author came up with a solution to this problem, a new drophead design that uses silica fibers that are inserted only mechanically in a quartz drophead, being held in position by fixing them to the drophead using a clamping mechanism. Chapter 5 provides an extensive

description of different drophead designs and their related advantages and disadvantages.

1.4.3 Sources & Detector

The optimisation of the opto-electronic components and the fibers is essential in order to maximise the output power to the detector via the processes of coupling optical sources into the source-fiber and on the far side of the drophead the coupling of the emission from the collector-fiber into the detector. The better the optical power coupling is, the less amplification of the signal is necessary and this will result in a marked improvement of the SNR of the tensiotrace. The first fiber and optical device linking mechanism described here is a plastic connector housing, which incorporates a fiber-optic LED transmitter or a fiber-optic photodiode as detector and a micro lens for efficient coupling. The performance of the opto-electronic components contained by these devices is excellent with regard to the tensiograph, but the optical alignment of the fibers is not reproducible and sometimes quite inefficient. These housings are specially designed to mate with $1mm$ diameter PMMA fibers. The fact that both the housings and fibers are made out of plastic, places a limit on the possibility of an optimised connection. Inefficient optical alignment and the restriction to PMMA fibers rule against the plastic devices coupling technique in a tensiograph. A second fiber-optic connectivity option uses the rigid SMA-type housing (Appendix 2, Picture A2-11). The mating connectors for these SMA-type housings are fitted onto the end of the fibers (either PMMA or silica). This coupling method guarantees an optimised optical alignment each time when the opto-electronic devices and the fibers are connected together and therefore reduces any changes from this source on tensiotraces resulting from variations in either the connection to the LED or the detector. The disadvantage of this system is the extremely high cost per connection and the limited availability of commercially high performance opto-electronic components over the range from UV-B to IR-A (Table A3-2). Paradoxically, this has led to both improvements and deteriorations in the performance of the tensiograph. Chapter 6 provides a more detailed examination of different light sources and detectors in tensiography.

1.4.4 Liquid Delivery System

A constant head liquid delivery system is principally the ideal method to form a drop at the end of a drophead. Firstly, it has been noticed from observation in practice, that such a system generates no turbulence in the liquid, as the narrowness of the capillary delivering the liquid ensures a laminar flow. If the system has been properly set up and environmental vibration precautions have been carefully applied, the drop formation shows extremely low noise from mechanical drop disturbances. Secondly, the bubble problem, as described below in this section, is avoided if the LUT has been properly degassed, before it is filled into the constant head delivery system. Unfortunately, liquid delivery via a constant head is extremely difficult to maintain and a constant liquid flow is only realisable for short periods, because of variations in atmospheric pressure, humidity, temperature and perhaps other influential factors. It was therefore decided after a long experimentation period that the only practical solution for the liquid delivery system of the tensiograph was a stepper motor driven pump. The volume flow rate of those particular devices is exceptionally constant and this is a very important aspect to fingerprint liquids. One of the disadvantages of a stepper motor pump is the oscillation it introduces to a drop due to a step-by-step liquid delivery to the drophead, which subsequently generates noise in the recorded tensiotrace. The amplitude of the oscillation of a drop decreases with the increasing number of steps per full stroke of the plunger that pushes the liquid through the delivery tube to the drophead. A more serious problem is the occurrence of bubbles in the liquid delivery tube, which most definitely have an effect on the profile of the tensiotrace during the recording phase. These bubbles occur during the switchover points of the valve, which changes the direction of liquid flow in the syringe of the pump, i.e. a liquid sample can either be taken into the syringe or this sample is ready to be dispensed again. Consequently, the liquid delivery system has to be flushed between measurements to avoid the build up of bubbles and this option is programmed into an acquisition software package of the tensiograph, which will be described in Chapter 4. The liquid delivery systems will be more fully explored in Chapter 6.

1.4.5 Temperature Control Module

The tensiograph incorporates a temperature controlled drophead chamber, which is of fundamental importance for the reproducibility of the drop formation of the same liquid, i.e. the ability to fingerprint liquids. The temperature range of the thermal module ($10°C$ to $40°C$) is suitable for most liquids that can be analysed with the tensiograph, but the relatively high limit on the lowest achievable operating temperature remains a problem for fingerprinting highly volatile liquids. Chapter 6 provides an in depth description of the temperature control module.

1.4.6 Anti-Vibration System

The sensitivity of the technique of analysing and fingerprinting liquids clearly demands efficient vibration isolation. Building, floor and acoustic vibrations are sources of drop disturbances. The ultimate solution to this problem is active vibration damping (vibrations are electronically detected, analysed and eventually compensated by producing counter forces), but such a system is simply too expensive to offer a practical solution for an envisaged commercial multianalyser. Passive anti-vibration systems are relatively inexpensive and can be efficiently used for various applications. Most of those systems are designed to absorb frequencies above $10Hz$ and need to be loaded with a relatively heavy weight, but the tensiograph is very sensitive to frequencies below $10Hz$ and its weight is relatively light. The vibration damping systems, which are appropriate for this kind of application are equipped with soft springs, which can be a problem when the structure that is resting on such an anti-vibration system has to be levelled, as is the case for a tensiographic instrument. The anti-vibration systems utilised will be further discussed in Chapter 6.

1.5 Outline of the Content of the Remaining Chapters

Chapter 2 provides a theoretical review of basics, including optical components, electronic noise, mechanical vibration, information content, principal component analysis of tensiotraces, theoretical concepts of data-scatter and statistical fingerprinting methods adapted specifically for tensiography. Chapter 3 continues then with the electronic engineering development of a tensiograph, comprising the temperature controller driver, Peltier power booster, light emitting diode driver, detector board, acquisition board interfacing, and the system integration of all electronic circuits. Chapter 4 describes software engineering issues, regarding important strategies for the development efficiency of modern software applications, a data acquisition package and the associated interfacing aspects, a software package for the data analysis of tensiotraces, a data-scatter software package, and the integration of these software packages. Chapter 5 concentrates on the drophead engineering development with respect to the concave PEEK drophead design, the flat stainless steel knife-edge design, and the flat quartz drophead design. Chapter 6 discusses the systems engineering development, explaining the vibration damping system, thermal module, pump and constant head liquid delivery systems, disturbing effects such as stray light and evaporation, error budgets in conjunction with information content, and the integration of a tensiographic system. Chapter 7 elucidates fingerprint studies, concerning data-scatter and tensiotrace data smoothing algorithms.

CHAPTER 2

THEORETICAL REVIEW OF BASICS

This chapter will provide a review of some basic theoretical issues that relate to the analytical discussions in subsequent chapters. The issues will not be dealt with in depth here, but these foundations will either be deepened by the subsequent experimental studies that form the major part of the work reported in this thesis, or an understanding of these basic theoretical discussions will be required to appreciate the tensiograph engineering described in the later chapters where these topics arise. It is important here however to point out that the theoretical issues described in this chapter do not constitute new and original contributions, with the exception of Section 2.4 and to a limited extent Section 2.5. Section 2.1 describes basic instrument issues, including optical components, electronic noise and mechanical vibrations. A review of instrument performance in terms of information content is then discussed in Section 2.2. The principal component analysis of tensiotraces is the subject of Section 2.3. Section 2.4 provides a description of the fundamental theoretical concepts of data-scatter, which is a new development that will be more fully explored in Chapters 7. The descriptions of the statistical fingerprinting methods in Section 2.5, while of standard form, are presented here in a way that has been adapted specifically for the tensiograph problem (and here also instrumentation in a more general way), where the issue of the probability of a *false-positive* is really what is required by the user rather than the result of a test statistic.

2.1 Instrument Issues

2.1.1 Preliminary Contemplations

2.1.1.1 Solid Angle

The mathematical description of many quantities used in this study such as spectral reflectance, absorptivity, transmissivity and indeed other physical properties of a substance, e.g. the liquid drop shape and emission cones from silica or PMMA fibers with regard to tensiography, require the definition of the solid angle Ω or its differential $d\Omega$, see Figure 2-1.

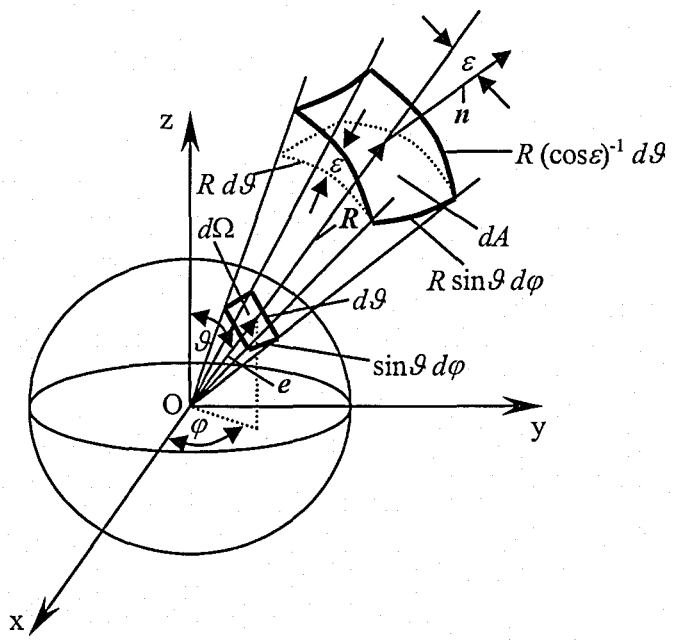

Figure 2-1. For the definition of the solid angle.

The differential of a solid angle $d\Omega$, which is related to an arbitrary infinitesimal small area dA of a medium, e.g. a very small sector on the surface of a drop, can be determined as follows. The projection of dA onto the surface of a normalised sphere, i.e. the absolute value of the radius-vector $\boldsymbol{e}$ of the sphere is one, which has been constructed using O as the origin, determines the associated $d\Omega$.

The definition of $d\Omega$ and dA, using spherical coordinates (ϑ, φ), is then

$$d\Omega = \sin(\vartheta)\, d\vartheta\, d\varphi \tag{2-1}$$

and

$$dA = \frac{R^2}{\cos(\varepsilon)} \sin(\vartheta)\, d\vartheta\, d\varphi \tag{2-2}$$

where R is the distance between the origin O and the sector dA, and ε is the angle between the direction of projection $\boldsymbol{e}$ and the normal $\boldsymbol{n}$ of dA. The solid angle Ω, for an extended area A, can be calculated by integration, after rearranging Eqs. (2-1) and (2-2) and the use of an appropriate coordinate system

$$\Omega = \int_A \frac{\cos(\varepsilon)}{R^2}\, dA \tag{2-3}$$

where ε and R depend on the upper and lower boundaries of the integral over A. The unit of the solid angle Ω is $[m^2 m^{-2}]$ and has been defined as steradian (sr), which is dimensionless.

2.1.1.2 Refractive Index

The speed of light c in a substance, e.g. air, water or glass, is related to the wavelength λ of the electromagnetic signal. The propagation of an electromagnetic signal in vacuum does not depend on the frequency of the signal and is therefore a constant that can be used to determine the absolute refractive index n_x of a substance

$$n_x = \frac{c_o}{c_x} \tag{2-4}$$

where c_o $[ms^{-1}]$ and c_x $[ms^{-1}]$ are the speed of light in vacuum and in the substance respectively. The more practical use of the refractive index in tensiography is in general the retardation of a wavefront, i.e. the surface defined by the locus of adjacent points that have the same phase, passing through a boundary between two dissimilar media. Snell's Law, illustrated in Figure 2-2, defines the angle of refraction

$$n_1 \sin(\theta_1) = n_2 \sin(\theta_2) \tag{2-5}$$

where n_1 is the index of refraction of the medium in which the incident ray (coming from a light source *L1* or *L2*) travels, θ_1 is the angle with respect to the normal at the refractive boundary at which the incident ray strikes the boundary, n_2 is the index of refraction of the medium in which the refracted ray (*1a*, *1b*, *2a* or *2b*) travels, and θ_2 is the angle with respect to the normal at the refractive boundary at which the refracted ray travels. If a ray travels from a medium of lower refractive index into a medium of higher refractive index (Figure 2-2 (a)) and the angle of incidence is greater than zero, it is bent toward the normal (*1b*) and at the same time partially reflected back into the medium from which it originated (*1b'*). The ray is not deviated at the boundary of two dissimilar media, if the incident ray is collinear with the normal of the boundary (*1a* or *2a*). If a ray travels from a medium of higher refractive index into a medium of lower refractive index (Figure 2-2 (b)) and the angle of incidence is greater than zero, it is bent away from the normal (*2b*) and at the same time partially reflected back into the medium from which it originated (*2b'*). TIR occurs when a ray strikes the refracting boundary at an angle of incidence with respect to the normal greater than an angle termed the critical angle θ_c

$$\theta_c = \sin^{-1}\left(\frac{n_l}{n_d}\right) \tag{2-6}$$

where n_l is the refractive index of the optically less dense medium, and n_d is the refractive index of the optically denser medium. The incident ray is in the optically denser medium and if it strikes the refractive boundary precisely at the critical angle θ_c, then the refracted ray is tangent to the boundary at the point of incidence. After the rearrangement of Eqs. (2-4) and (2-5), the refractive index appears in the form

$$n_{21} = \frac{c_1}{c_2} = \frac{n_2}{n_1} = \frac{\sin(\theta_1)}{\sin(\theta_2)} \tag{2-7}$$

where n_{21} is the relative refractive index of two media *1* and *2*, which is the ratio of the absolute refractive indices of both media.

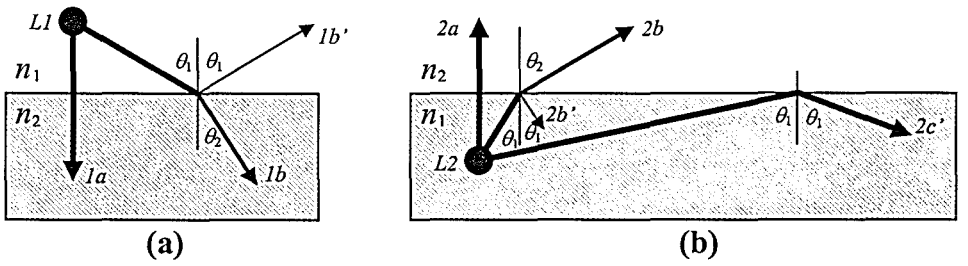

Figure 2-2. Refraction and reflection of light rays travelling from a medium of lower refractive index into a medium of higher refractive index (a) and vice versa (b).

2.1.1.3 Propagation of light in optical fibers according to ray theory

The optical multimode step-index fibers (Figure 2-3) in a tensiograph are composed of two distinct and different types of optically transparent materials. Different modes in Figure 2-3 (a) can be distinguished by the diversity in length of their geometrical and optical light paths, and a constant refractive index from the core-centre of the fiber to the interface between the core and the cladding, as shown in Figure 2-3 (b), characterises multimode step-index fibers.

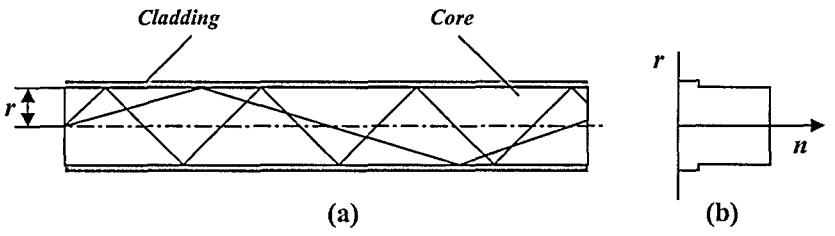

Figure 2-3. (a) Multimode step-index fiber, (b) profile of the refractive index $n(r)$.

The core of the fibers is made out of silica or polymer and has a higher index of refraction n_d than the cladding with a lower index of refraction n_l. The cladding surrounds the core and transmits nearly all the light energy of the fiber. A thin layer of cladding provides an interface at the boundary, which in the ray model of the optics of fiber transmission will produce TIRs of the propagating rays. A polymer jacket protects the core and cladding of the fiber from being mechanically damaged. Figures 2-4 (a) and (b) illustrate the arrangement of an optical fiber and the principle of the light guidance through the fiber respectively.

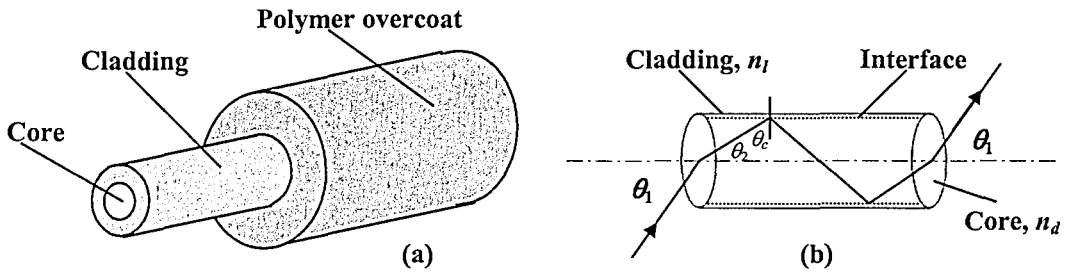

Figure 2-4. (a) Optical fiber, (b) principle of light guidance through the fiber.

With regard to Figure 2-4 (b), the critical angle θ_c, which determines the maximum angle θ_1 (termed the acceptance angle) at the end-face of a straight fiber, within which optical power may be coupled into bound modes, i.e. light rays are totally reflected at the interface between core and cladding of the fiber, is $\theta_c = 0.5\pi - \theta_2$. Using the definition of Snell's Law in Eq. (2-5) with $n_2 = n_d$, and the definition of the critical angle θ_c in Eq. (2-6), the angle θ_1 can be defined as

$$\theta_1 = \sin^{-1}\left(\frac{n_d}{n_1}\sin\left(\frac{\pi}{2} - \sin^{-1}\left(\frac{n_l}{n_d}\right)\right)\right) \tag{2-8}$$

where θ_1 is measured with respect to the fiber axis, and n_1, n_l, n_d are the refractive indices of the medium between light source and fiber, cladding, and core respectively. Rays entering an optical fiber at angles greater than θ_1 are coupled into unbound modes and will be attenuated. The important quantity that defines the light acceptance of a fiber is the numerical aperture (*NA*). For a multimode step-index fiber in air, with a refractive index of n_d and n_l in the core and cladding respectively, the expression in Eq. (2-8) can be manipulated

$$\sin(\theta_1) = \frac{n_d}{n_1}\sin\left(\frac{\pi}{2} - \sin^{-1}\left(\frac{n_l}{n_d}\right)\right)$$

$$\sin(\theta_1) = \frac{n_d}{n_1}\cos\left(\sin^{-1}\left(\frac{n_l}{n_d}\right)\right)$$

$$\sin(\theta_1) = \frac{n_d}{n_1}\sqrt{1 - \sin^2\left(\sin^{-1}\left(\frac{n_l}{n_d}\right)\right)}$$

$$\sin(\theta_1) = \frac{n_d}{n_1}\sqrt{1-\left(\frac{n_l}{n_d}\right)^2}$$

$$\sin(\theta_1) = \frac{1}{n_1}\sqrt{n_d^2 - n_l^2} \qquad (for\ air,\ n_1 = 1)$$

to give a form that provides a measure of the ability of the fiber to accept, in its bound modes, non-normal incident rays

$$NA = \sin(\theta_1) = \sqrt{(n_d^2 - n_l^2)} \tag{2-9}$$

where θ_1 is the acceptance angle defined above. The angle θ_1 is shown at both ends of the fiber, because a short fiber will preserve the angle of incidence during propagation of the light, hence the rays will exit the fiber with an emission cone that is usually equal to the acceptance cone. The *NA* is therefore an important parameter for multimode step-index optical fibers, as this determines both the maximum angle ($2\theta_1$) of the acceptance and emission cone of the fiber. This quantity is particularly important in consideration of the optical alignment between a light source and a fiber, see Figure 2-5, which shows two types of fibers with different maximum angles of their acceptance cones **x**, **z** and an LED with a lens, producing the incident cone **y**. The fiber with the acceptance cone **x** has a smaller *NA* than the fiber with the acceptance cone **z**. The incident cone of the LED is smaller than **z** but bigger than **x**. Therefore, the **z**-cone fiber will accept all of the light from the LED, but the output cone at the other end of the fiber will be the size of **y**. Conversely, the **x**-cone fiber is not capable of accepting all the light from the LED, and will have an output cone of size **x**. Coupling losses also occur if the fiber has been inaccurately positioned with respect to the LED output cone. The maximum optical power cannot be coupled into the fiber, even if the acceptance cone of the fiber is bigger than the incident cone of the LED, as it is illustrated in Figures 2-5 (b) and (c). Only the combination of perfectly optical alignment (sweet-spot position), and the choice of a fiber with the appropriate *NA*, guarantees that the maximum optical output power of the LED is coupled into the fiber, as shown in Figure 2-5 (a).

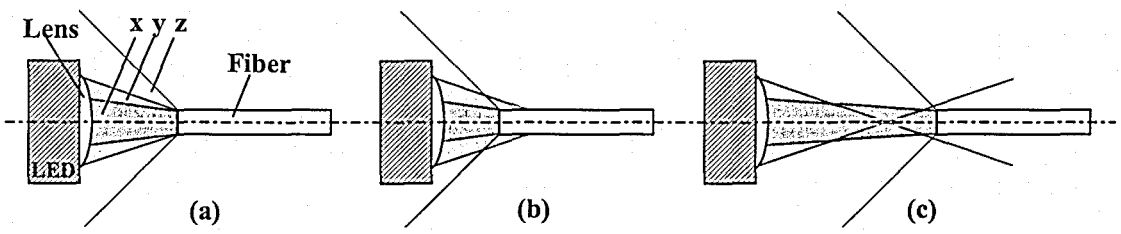

Figure 2-5. Principle of the optical alignment of an LED, with a lens-focused incident cone y, and a fiber with maximum acceptance cone x or z. (a) perfectly aligned, (b) fiber too close to lens, (c) fiber too far away from lens.

Angular misalignment of optical fibers is one of the basic causes of variation in performance in light transmission between supposedly identical optical fiber systems. In addition, if the end-face of a fiber is not cut at a 90° angle with respect to the axis of the fiber, transmitted optical power will be attenuated. The optical output power Φ of an LED in a tensiograph is coupled into the source-fiber of the drophead and subsequently transmitted into the pendant drop of the LUT (Figure 1-1).

2.1.1.4 Spectral Considerations

The relationship of the optical power distribution on the surface of a drop, with respect to the end-face of an optical fiber at the origin O in Figure 2-1, is

$$d\Phi = I\, d\Omega \tag{2-10}$$

where the proportional factor I [Wsr^{-1}] is the optical intensity of the light beam at any point and time on the surface of a growing drop. Replacing $d\Omega$ in Eq. (2-10) with the definition of the solid angle element in Eq. (2-3) yields

$$d\Phi = I\frac{\cos(\varepsilon)}{R^2}dA = E\, dA \tag{2-11}$$

where E [Wm^{-2}] is the irradiance, which is a measure for the optical power per area and it obviously decreases quadratically with increasing distance R from the light source (inverse square law). The light travels from the end-face of the fiber to the surface of the drop and during this progression optical radiation is partially reflected, refracted and absorbed in the liquid, which obviously means that the optical power Φ at the surface of the drop is less than the optical power at the end-face of the fiber. The interaction of the optical radiation with a substance is specific for a LUT and can be expressed by three optical characteristics for liquids that do not contain particulate matter, which implies that they do not scatter radiation:

The spectral reflectance $\rho(\lambda)$ is the ratio of the reflected optical power $\Phi_{\lambda,R}$ and the emitted optical power $\Phi_{\lambda,E}$

$$\rho(\lambda)=\frac{\Phi_{\lambda,R}}{\Phi_{\lambda,E}} \tag{2-12}$$

The spectral transmissivity $\tau(\lambda)$ is the ratio of the transmitted optical power $\Phi_{\lambda,T}$ and the emitted optical power $\Phi_{\lambda,E}$

$$\tau(\lambda)=\frac{\Phi_{\lambda,T}}{\Phi_{\lambda,E}} \tag{2-13}$$

The spectral absorptivity $\alpha(\lambda)$ is the ratio of the absorbed optical power $\Phi_{\lambda,A}$ and the emitted optical power $\Phi_{\lambda,E}$

$$\alpha(\lambda)=\frac{\Phi_{\lambda,A}}{\Phi_{\lambda,E}} \tag{2-14}$$

where $\rho(\lambda)$, $\tau(\lambda)$ and $\alpha(\lambda)$ are dimensionless and the value of each of these properties is within the range 0 to 1. The following definition is limited to non-luminous substances but applies for any wavelength.

$$\rho(\lambda)+\tau(\lambda)+\alpha(\lambda)=1 \tag{2-15}$$

If the optical power of the light is Φ at the end-face of a fiber and propagates in the l-direction, then the optical power will be

$$\Phi-\frac{d\Phi}{dl}dl$$

at the point $l + dl$ (e.g. on the surface of a liquid drop), which means, that

$$-\frac{d\Phi}{dl}$$

is the decrease of the optical power with respect to the length l [cm]. By imposing a form for $d\Phi/dl$ it can also be expressed as

$$\frac{d\Phi}{dl}=-a\,\Phi(l),\quad or\quad \frac{d\Phi}{\Phi}=-a\,dl\quad (a>0)$$

by introducing the proportionality factor a. The integration of this expression yields

$$\ln(\Phi)=\ln(\Phi_0)-a\,l$$

or

$$\Phi = \Phi_0 \, e^{-al} \tag{2-16}$$

where Φ_0 is the optical power at the point $l = 0$, $a(\lambda)$ $[cm^{-1}]$ is the absorption coefficient of a substance. This expression is termed the Lambert Law. A modified Beer-Lambert Law can be used in order to determine the absorbance A in the light path of a tensiograph (Figure 1-1)

$$A = \varepsilon c \int dl = \varepsilon c l_{av} \tag{2-17}$$

where ε $[litre\ mol^{-1}\ cm^{-1}]$ is the molar absorptivity, c $[mol\ litre^{-1}]$ is the concentration of the compound in solution, l $[cm]$ is the path length of rays in a liquid drop that couple from the end-face of the source-fiber to the end-face of the collector-fiber, and l_{av} $[cm]$ is the average path length obtained from integration of all the photon paths that couple across a liquid drop from the source-fiber to the collector-fiber.

2.1.2 Drop Considerations

The shape of the rainbow peak is of some interest. This characteristic shape can be seen in Figure 1-3 with a sharp angular rise and a relatively slow linear descent after the peak maximum. The peak is asymmetric. There are in fact three terms that contribute to this shape.

1. The inverse square decrease in the intensity (Eq. (2-11)) due to the lengthening of the optical path length (OPL) of the triple reflective coupling of the rainbow peak. This is shown schematically in Figure 2-6 (a). From sequential photographic recordings of a drop an estimate of the drop length can be made, see Figure 2-7. It has been assumed that the inverse square law (Eq. (2-11)) applies (this is not true for an emission cone) as only the single-ray triple reflection is considered here. This treatment is of course only an attempt to produce a rough model that aims to uncover the physics behind the profile of the peak.
2. The second term that is of obvious importance here is the variation in the intensity for the coupled rays. Three ray couplings are shown in Figure 2-6 (a) for three different sized pendant drops (strong evidence suggests [2-1] that a triple reflection produces the rainbow peak). The angle α of a given emission ray that couples will have a positive α for ray coupling *1*, an angle close to zero

for ray coupling *2*, and an α of negative sign for ray coupling *3*. The emission cone from a multimode step-index fiber is approximated by a $\cos^2(\alpha)$ term. Note $\cos(2\alpha)=\cos^2(\alpha)-\sin^2(\alpha)$.

3. The third term is illustrated in Figure 2-6 (b). An approximation of this focusing term illustrated here, can perhaps be obtained by ignoring the losses due to Fresnel reflections, i.e. light is reflected back into the fiber at the interface between the end-face of the fiber and the liquid drop. All rays incident on the side of the drop are TIRs, which then are coupled to the collector-fiber by two further TIR processes. The difference between the top of the rainbow peak and the tensiograph peak(s) (Figure 1-3) is that this coupling is close to a focused coupling such as shown in Figure 2-6 (b) for the coupling ray *2* and volume V_2. The situation for the coupling ray *1* in volume V_1 and ray *3* in volume V_3 and tensiograph peak(s) is defocused. For the couplings *1* and *3* the focus is well outside of the focal point of the collector-fiber and the rays are diverging.

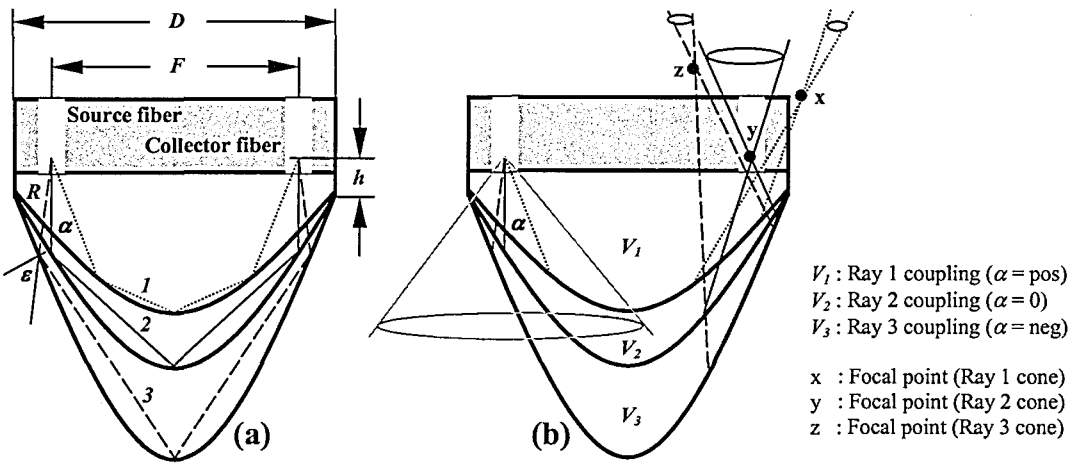

Figure 2-6. The principle of light coupling in a pendant drop for the appearance of the rainbow peak in a tensiotrace.

Figure 2-7 shows the photographs of pendant drops hanging from a drophead under gravity, taken during the life cycles of these drops and Figure 2-8 illustrates the forces acting on a drop to hold it in position and give it its distinct shape.

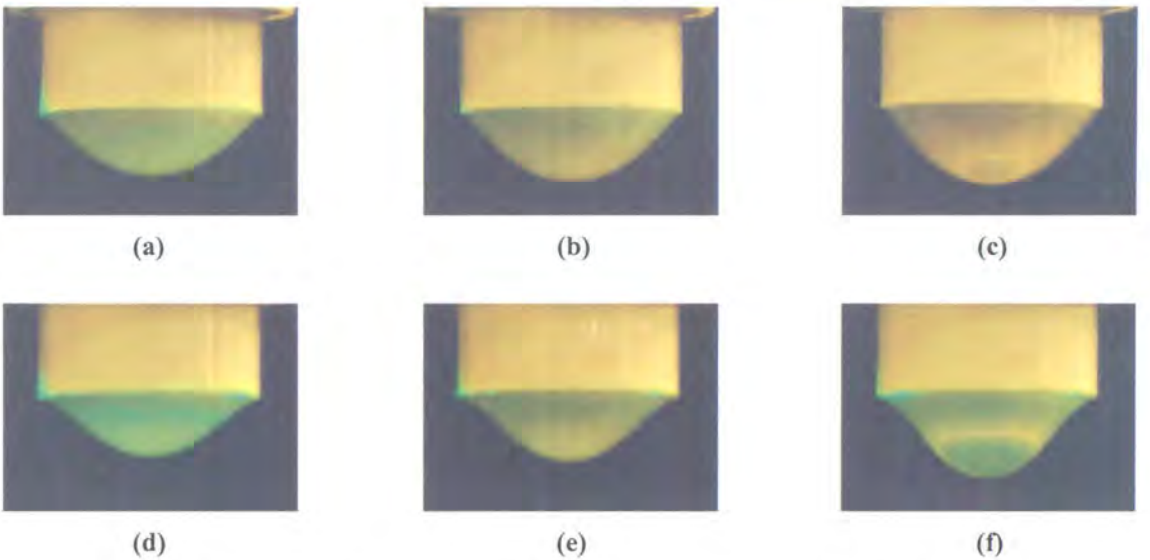

Figure 2-7. Characteristic drop volumes related to the rainbow peak (9mm PEEK concave drophead @ 25°C). (a) Water at the beginning of the rainbow peak. (b) Water at the top of the rainbow peak. (c) Water at the end of the rainbow peak. (d) Ethanol at the beginning of the rainbow peak. (e) Ethanol at the top of the rainbow peak. (f) Ethanol at the end of the rainbow peak.

The forces acting on a drop are twofold, namely those force elements arising from the surface tension of the LUT $\gamma\, dl_1$ and $\gamma\, dl_2$ (microscopic, see Figure 2-8 (a)) and the gravitational force $v\rho g$ (macroscopic, see Figure 2-8 (b)). $\gamma\,[Nm^{-1}]$ is the surface tension of the LUT, dl_1 $[m]$ is the width and dl_2 $[m]$ the length of the surface-element dS $[m^2]$, v $[m^3]$ is the volume of the drop, ρ $[kgm^{-3}]$ is the density of the LUT, and g $[ms^{-2}]$ is the gravitational acceleration. The Laplace pressure p $[Nm^{-2}]$ that arises from the curvature at the surface of a drop is complex because of the variation in radii of the drop surface. For the derivation of the Laplace pressure equation consider the surface-element dS in Figure 2-8 (a) of an arbitrary point M on the surface of a pendant drop illustrated in Figure 2-8 (b). Surface tension forces $\gamma\, dl_1$ and $\gamma\, dl_2$ from adjacent elements on the surface acting on dS, which results in a force that has the direction into the drop of the surface-element normal N.

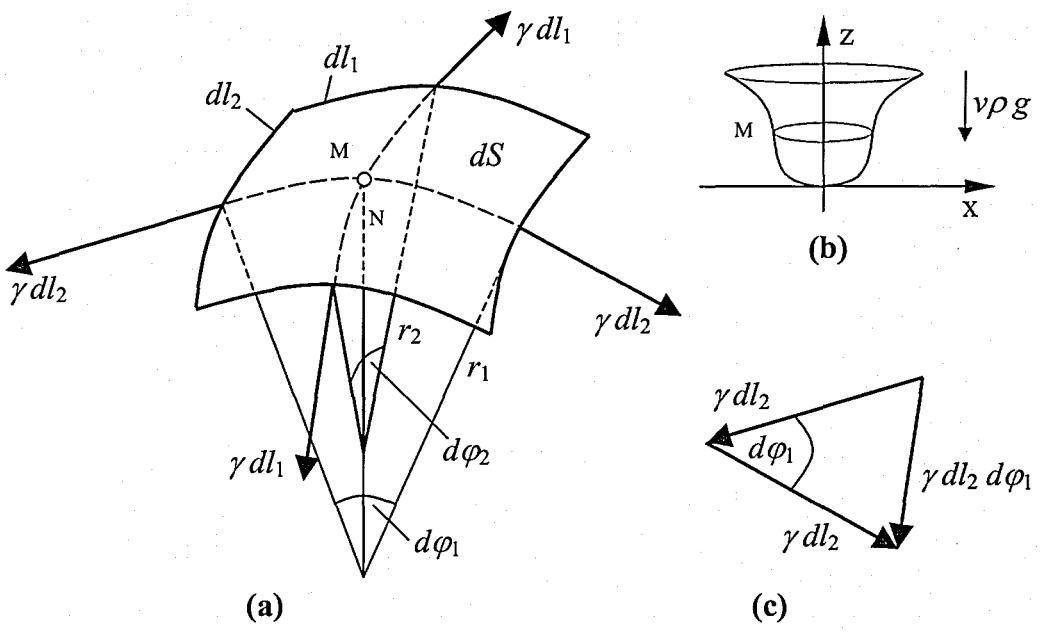

Figure 2-8. For the definition of the Laplace pressure.

The absolute value for the two forces $\gamma\, dl_2$ (Figure 2-8 (c)) is given by

$$\gamma\, dl_2 d\varphi_1 = \frac{\gamma}{r_1} dl_1 dl_2, \qquad \left(d\varphi_1 = \frac{dl_1}{r_1} \right)$$

similarly

$$\gamma\, dl_1 d\varphi_2 = \frac{\gamma}{r_2} dl_1 dl_2, \qquad \left(d\varphi_2 = \frac{dl_2}{r_2} \right)$$

and the summation of the two expressions above yields

$$\gamma \left(\frac{1}{r_1} + \frac{1}{r_2} \right) dl_1 dl_2$$

dividing this term by $dS = dl_1 dl_2$ gives the Laplace pressure

$$p = \gamma \left(\frac{1}{r_1} + \frac{1}{r_2} \right) \tag{2-18}$$

noting this

$$\gamma \left(\frac{1}{r_1} + \frac{1}{r_2} \right) = \rho g z + C$$

where C is a constant. At the point x = 0 and z = 0 (see Figure 2-8 (b)) is $r_1 = r_2$ and can be set to a fixed value b, and C can be defined as

$$\frac{2\gamma}{b}$$

which is the Laplace pressure at the base of a pendant drop, and this pressure is exactly balanced by the head pressure ρgz from the column of liquid standing above this point, which is the controlling factor in all drop dynamics. It is understood that as the drop

grows and z increases that the radius b has a proportional decrease and its magnitude is given by $2\gamma/(\rho g z)$.

2.1.3 Noise Contributions

2.1.3.1 Electronic Noise

Consider n carriers of elementary charge e $[As]$ moving with a velocity v $[m/s]$ through a medium of length l $[m]$. The current i $[A]$ throughout the medium is then

$$i = \frac{nev}{l} \tag{2-19}$$

and the fluctuation of this current is given by the total differential

$$di^2 = \left(\frac{ne}{l}dv\right)^2 + \left(\frac{ev}{l}dn\right)^2 \tag{2-20}$$

where the two terms are quadratic and added together since they are statistically uncorrelated. Eq. (2-20) shows that there are two mechanisms that contribute to the total noise, namely velocity fluctuations and number fluctuations, which are basically expressed as thermal noise and shot noise respectively. Thermal noise and shot noise are both 'white' noise sources, i.e. the power per unit bandwidth (spectral noise power density vs. frequency f $[s^{-1}]$) is constant

$$\frac{dP_{noise}}{df} = const. \tag{2-21}$$

The most common example of noise due to velocity fluctuations is the thermal noise of resistors

$$\frac{dP_{noise}}{df} = 4kT \tag{2-22}$$

where k $[WsK^{-1}]$ is the Boltzmann constant and T $[K]$ the absolute temperature. Since

$$P = \frac{V^2}{R} = I^2 R$$

the spectral noise voltage density $[V^2 s]$ for an ohmic resistor R $[VA^{-1}]$ is

$$\frac{dV^2{}_{noise}}{df} \equiv e_n^2 = 4kTR \tag{2-23}$$

and the spectral noise current density $[A^2s]$ for R is

$$\frac{dI^2{}_{noise}}{df} \equiv i_n^2 = \frac{4kT}{R} \tag{2-24}$$

The total noise depends on the bandwidth of the system. A common example of noise due to number fluctuations is shot noise, which occurs whenever carriers are injected into a sample volume independently of one another (for example, the current flow in a semiconductor diode – emission over a barrier). The spectral noise current density is

$$i_n^2 = 2q_e I \tag{2-25}$$

where q_e $[As]$ is the electronic charge and I $[A]$ is a DC current. Shot noise is negligible in ohmic resistors and conductors, since the number of available charges is effectively very large. However, all electronic circuits of the tensiograph include both semiconductors and resistors that contribute to thermal and shot noise, which result in a combined noise that is superimposed in the signal at the output of each electronic circuit of the instrument. Figure 2-9 shows for example the typical noise characteristics of the low-frequency operational amplifier LTC1051 from Linear Technology. For more information see Schematic A2-6.

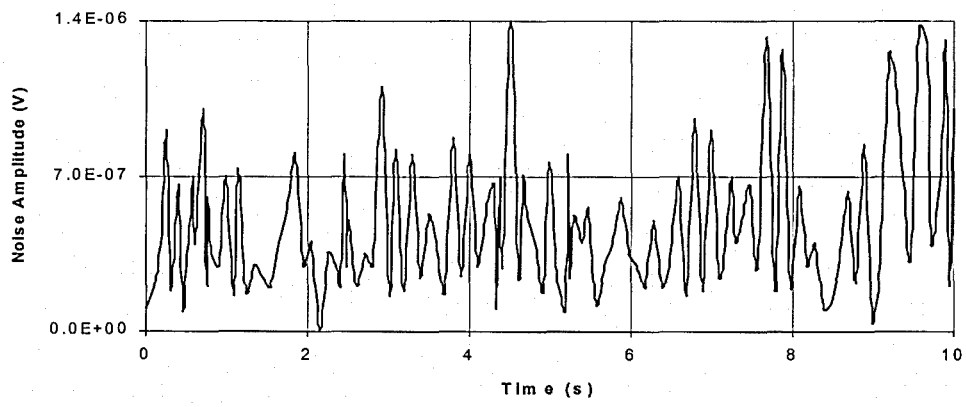

Figure 2-9. DC to 10*Hz* noise performance of the low-frequency amplifier LTC1051.

Both thermal and shot noises are purely random and the amplitude distribution is gaussian.

2.1.3.2 Mechanical Vibration

Figure 2-10 shows a simple model for the explanation of mechanical vibration, which may be thought of as a single mass m supported by an elastic system k that also includes damping c.

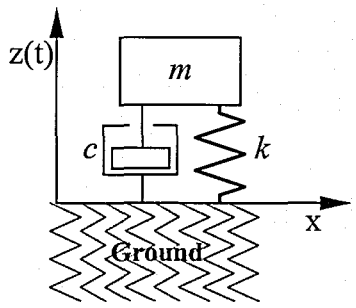

Figure 2-10. A simple model for the explanation of mechanical vibration.

Every type of physical oscillation is essentially an exchange of potential and kinetic energy. In Figure 2-10, potential energy is the energy stored by the elastic deformation of k

$$E_p = \frac{1}{2} k\, z(t)^2 \tag{2-26}$$

and the kinetic energy is the energy of the mass m of the structure in motion

$$E_k = \frac{1}{2} m\, \dot{z}(t)^2 \tag{2-27}$$

In general, all oscillatory motion of sufficiently small amplitude can be described as

$$z(t) = Z \sin(\omega t - \theta_0) \tag{2-28}$$

where Z is the amplitude, ω [*rad/s*] is the frequency of the oscillation, and θ_0 [*rad*] is the initial phase of the oscillation. In unforced, free vibration, each type of energy is at its maximum when the other type is at its minimum. Therefore, whenever the potential energy is at its minimum, i.e. $z(t)$ in Eq. (2-26) is zero, then the kinetic energy in Eq. (2-27) is at its maximum

$$E_k = \frac{m\omega^2 Z^2}{2}$$

and whenever the kinetic energy is at its minimum, i.e. $\dot{z}(t)$ in Eq. (2-27) is zero, then the potential energy in Eq. (2-26) is at its maximum

$$E_p = \frac{kZ^2}{2}$$

Setting the maximum kinetic energy equal to the maximum potential energy in order to describe free oscillation, results in a solution for ω of the form

$$\omega_n = \sqrt{\frac{k}{m}} \tag{2-29}$$

This solution $\omega=\omega_n$ is the natural, or resonant, frequency. When an undamped system with a single degree of freedom, i.e. it consists of one mass only, which moves along one axis only (here the z-axis), is allowed to oscillate freely from some initial displacement or velocity, it will always oscillate at its natural frequency ω_n. Up to this point the discussion of vibration damping considered only undamped oscillation which does not include a mechanism to dissipate mechanical energy from a mass-spring system. Damping (expressed as damping coefficient c in Figure 2-10) dissipates mechanical energy, very often as heat, from the system and attenuates vibration more quickly.

The tensiographic instrument is very susceptible to building vibration and all buildings vibrate from machinery, heating and ventilation systems, or human activity on the inside and often from trucks, trains, and heavy weather on the outside. Though acceptable to people, these vibrations cannot be tolerated by the ultra sensitive multianalyser. Therefore, the instrument has been equipped with a passive air spring anti-vibration system with low natural frequency of ω_n=3.6*Hz*, to attenuate all potentially interfering vibration amplitudes in the 0.5 to 500*Hz* broadband random vibration spectrum. Most building vibrations fall within the range 5 to 30*Hz* (vertical) and 0.5 to 10*Hz* (horizontal), acoustic vibrations are greater than 20*Hz* and motorized equipment and machinery fall within the range 10 to 500*Hz* [2-2]. Note that the resonance frequency (ω_n=3.6*Hz*) of the air spring anti-vibration system lies in the range (0.5 to 10*Hz*) of building vibrations (horizontal), and yet it can be beneficial if the resonance frequency of a liquid drop is high, and in the suppression region of the anti-vibration system. Figure 2-11 [2-2] shows the typical transmissibility of vibrations using an anti-vibration system.

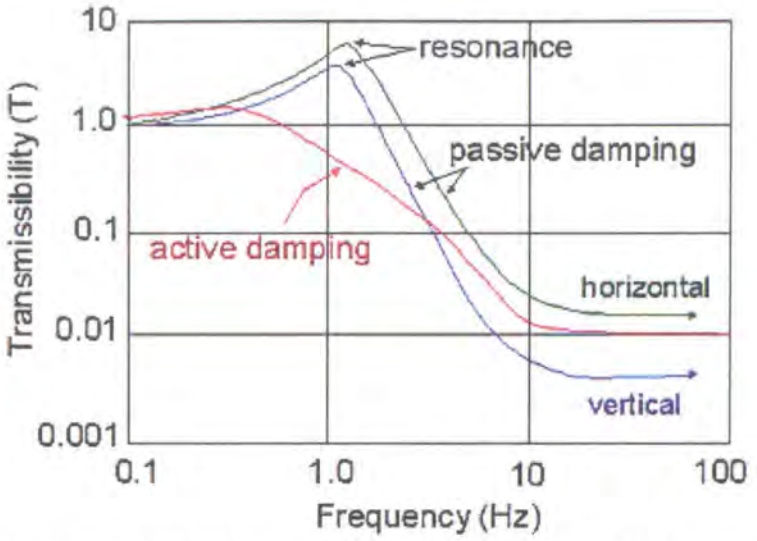

Figure 2-11. Transmissibility of vibration for active and passive anti-vibration systems.

The problem that arises from using passive anti-vibration damping is the existence of the resonance frequency at the lower end of the vibration spectrum. If the ground motion in Figure 2-10 is sinusoidal with a frequency equal to the natural frequency of the anti-vibration system, then the vibration damping system will resonate and the amplitude of its dynamic response can become extremely large. Resonance amplifies vibrations of a building; hence a tensiograph will produce noisy tensiotraces. In contrast, the building vibrations will be damped, but never completely eliminated, if the frequency of these disturbing vibrations is greater than $4Hz$ (see Figure 2-11).

2.1.3.3 Pump Vibrations

The XP3000 micro-stepper pump from CAVRO provides a precision liquid handling device, which has been set up especially for the multianalyser. It was decided to operate this pump with a $250\mu l$ stepper motor driven syringe, a fixed dispense and aspirate resolution of 24,000*steps/stroke* and programmable plunger speeds from 1.2*s/stroke* to 600*s/stroke*. Despite the fact that the XP3000 radiates radio frequency energy, which may cause interference to the tensiograph, the objective of this section is to consider the mechanical vibration and noise that the pump generates in a pendant drop. The velocity v [*steps/s*] of the syringe plunger, which determines the volume flow rate of the liquid delivery system, is an important factor that may have an effect on the quality of the optical signal measurement

$$v = \frac{n}{t} \tag{2-30}$$

where n is the number of steps per stroke, and t [s] is the time that the plunger would need to complete a full stroke. Each step of the stepper motor driven syringe vibrates the pendant drop and for some liquids the noise in the signal, which results from these vibrations, might be unacceptable and makes it necessary to vary the time t in Eq. (2-30) to obtain noise-reduced signals. If the velocity v of the plunger is too high, then the separation of the drop becomes non-reproducible because of the rapid and unpredictable exit of the droplet from the drophead. Conversely, if an experimental setup is used in which v is too low then evaporation of the LUT during the measurement becomes a problem. For most experimental conditions, a time of 200s derives an efficient operating velocity of 120*steps/s* for the LUT, but surveys have indicated that the time t needs to be increased for liquids with high viscosity, e.g. oil, in order to optimise reproducible drop formation. Additionally, air bubbles that might appear in the tubing of the liquid delivery system may act as springs, adversely affecting an accurately dispensed volume and the SNR.

2.2 Review of Instrument Performance in Terms of Information Content

In any electronic or opto-electronic system design the question regarding noise will almost always arise. Noise needs to be tallied to highlight the problem areas that require further design effort or perhaps better quality components. Conversely, a noise analysis may reveal where more inexpensive components may suffice. The traditional method of evaluating electronic system performance is to compute an error or noise budget. A system is essentially broken down into defined components and the root mean squared (*r.m.s.*) noise contribution of each component, and eventually of the overall system, is determined

$$r.m.s. = \sqrt{\frac{\sum_{i=1}^{N} \alpha_i^2}{N}} \tag{2-31}$$

where α is the individual noise contribution, and N is the number of individual noise components. While this method is useful and widely used as the established method in electronics, it cannot indicate how each component of the system affects the quality of

the signal being processed if the noise components are of different generic type (e.g. electrical, optical and mechanical noise components). In addition, it is clear that it is desirable that an indication of signal quality must not be limited to assessments of system noise, but must include the dynamic range of the signal.

The tensiographic information content (TIC) method, described in this thesis, is motivated by data entropy theory. In the 1940s Claude Shannon, working in Bell Laboratories was studying how best to encode signals for transmission down a noisy channel. In 1949 he published a paper [2-3] in which he derived an expression for the amount of information in a signal. Though Shannon was primarily interested in transmitting signals down a telephone line as efficiently as possible, it soon became evident that the expression for information content was essentially the same as that derived in the 19th century in relation to the efficiency of steam engines. Mathematically, the equations for the entropy of heat engines and information content of signals are the same and consequently the expression data entropy was coined [2-4]. Chapter 6 discusses how the TIC may be utilised to evaluate the performance of a tensiograph. A simple working definition of the TIC ($\exists$ [*bits*]) measure of signal quality is taken as

$$\exists = \frac{\sum_{i=1}^{N} \log_2\left(\frac{S_i}{\alpha_i}\right)}{N} = \frac{\sum_{i=1}^{N} \log_2(S_i) - \log_2(\alpha_i)}{N}, \quad (S_i > 0), (\alpha_i > 0) \tag{2-32}$$

where N signifies all signal and noise components in the system, S_i and α_i are respectively the *r.m.s.*-signal level and the *r.m.s.*-noise level of the i-th components in the system. Note that the term *bit* here denotes a unit of information and is not to be confused with *bits* representing signal levels, for example, generated from an ADC. This metric offers a number of advantages over the usual noise budget method. Fundamentally, since TIC is a dimensionless quantity, errors or noise from a wide variety of sources such as electrical, optical, mechanical and environmental may be directly summed.

2.3 Principal Component Analysis of Tensiotraces

A set of M-functions (match) has been defined in order to compare two tensiotraces. The comparison approach identifies a defined set of principal components of two traces, namely the reference and test trace, and quantifies the match between each principal component. A software-implemented search algorithm is employed to extract the following principal components of a tensiotrace:

- Drop period (DP)
- Rainbow peak period and height (RPP, RPH respectively)
- Tensiograph peak period(s) and height(s) (TPP, TPH respectively)
- Data points

Six normalised M-functions, i.e. ($0 \leq M \leq 1$), give information on various aspects of a tensiotrace. More specifically, the comparison of two traces, using the normalisation approach, is an advantage as this always shows how close the two values are on a normalised scale, regardless of which trace is actually the larger. Figure 2-12 gives details of the labelling of the tensiotraces with respect to M-function analysis. Values associated with a maximum of the tensiotrace are shown in upper case. Conversely, relative values are shown in lower case. The period and height of the i-th data point that is associated with the smaller trace value is indicated by an $_S$-index, the larger trace value on the other hand is indicated by an $_L$-index. The $_S$ and $_L$-indices are exchangeable for any data point of the tensiotraces, e.g. the i-th height value of the reference trace can be larger than the test trace value, i.e. $\{\text{Reference}(u_L)_i > \text{Test}(u_S)_i\}$, but the height value of the test trace might be larger than the reference trace value at the $(i + j)$-th position, i.e. $\{\text{Test}(u_L)_{(i+j)} > \text{Reference}(u_S)_{(i+j)}\}$, where $(1 \leq i < N_{\max})$, $(i < j \leq N_{\max})$ and $((i+j) \leq N_{\max})$. The value $N_{\max}$ is the maximum number of data points in the data set of the tensiotrace with the larger DP.

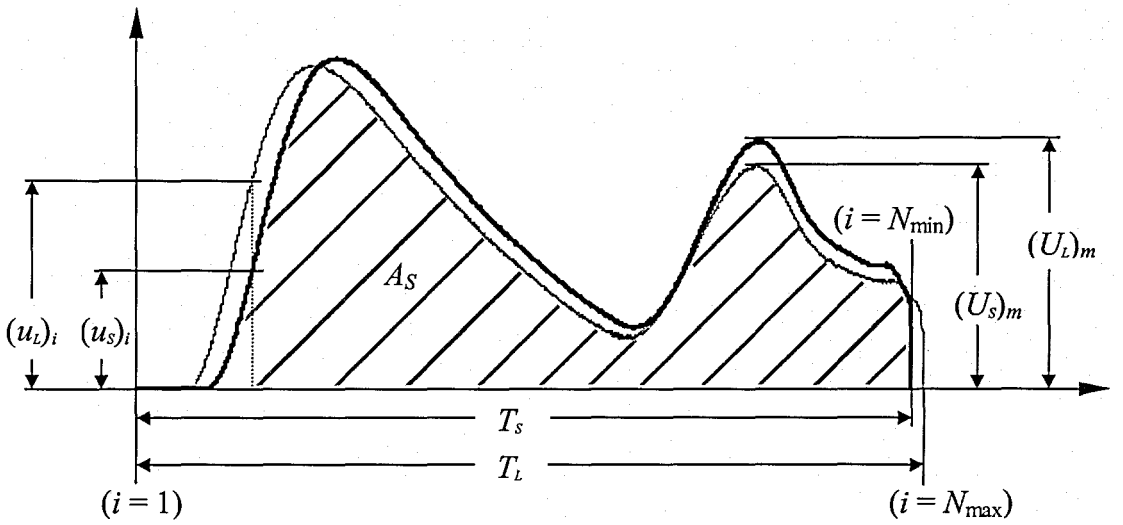

Figure 2-12. Labelling of tensiotraces for the principal component analysis with *M*-functions.

An *M*-function that has been defined for the DP is simply

$$M_T = \frac{T_S}{T_L} \qquad (M_T \equiv 1 \; for \; (T_L = 0)) \tag{2-33}$$

where T_S is the smaller DP value and T_L is the larger DP value of the two tensiotraces. If T_L=0 then T_S=0 and M_T is subsequently set to 1 since the division by zero is mathematically undefined and that also applies to the following equations in this section. Usually there are at most three peaks in a tensiotrace, using a drophead with the specification in Figure 1-8, namely the rainbow peak and up to two tensiograph peaks. An *M*-function that considers RPH and TPH(s) has been defined as

$$M_H = \frac{(U_S)_m}{(U_L)_m} \qquad (M_H \equiv 1 \; for \; (U_L = 0)) \qquad (1 \le m \le 3) \tag{2-34}$$

where m indicates the individual peak of a tensiotrace. A similar definition of the *M*-function for the RPP and TPP(s) is

$$M_T = \frac{(T_S)_m}{(T_L)_m} \qquad (M_T \equiv 1 \; for \; (T_L = 0)) \qquad (1 \le m \le 3) \tag{2-35}$$

where m has the same meaning as in Eq. (2-34). Figure 2-12 shows an overlap of two traces representing the i-th series of data points that have a signal value respectively $(u_S)_i$ and $(u_L)_i$ for the traces with the smaller and larger height value. An *M*-function "Points-Analogue" has been defined that computes the sum of the ratio of these signal sizes over the entire series of data points N_{max} and normalises the result by taking the sum over the maximum number of data points N_{max}.

$$M_{PA} = \frac{\sum_{i=1}^{N_{\max}} \frac{(u_S)_i}{(u_L)_i}}{N_{\max}} \qquad \begin{matrix} \frac{(u_S)_i}{(u_L)_i} \equiv 0 \\ \frac{(u_S)_i}{(u_L)_i} \equiv 1 \end{matrix} \; for \; \begin{matrix} (u_L = 0) \wedge (i > N_{\min}) \\ (u_L = 0) \wedge (i \le N_{\min}) \end{matrix} \tag{2-36}$$

where $N_{\min}$ is the number of data points of the tensiotrace with the smaller drop period T_S. An alternative M-function "Points-Digital" has been defined using a tolerance set {0(no-match), 1(match)} summation thus over the entire series of data points and normalises the result in the same way as in Eq. (2-36)

$$M_{PD} = \frac{\sum_{i=1}^{N_{\max}} x_i}{N_{\max}}; \quad \begin{matrix} x_i = 0 \\ x_i = 1 \end{matrix} \; for \; \begin{matrix} \left(\left(u_L - u_S\right)_i > \mu\sigma_{\max}\right) \vee \left(i > N_{\min}\right) \\ \left(\left(u_L - u_S\right)_i \le \mu\sigma_{\max}\right) \wedge \left(i \le N_{\min}\right) \end{matrix} \quad (\mu > 0) \tag{2-37}$$

The difference between the tensiotraces is compared point-by-point with the maximum standard deviation $\sigma_{\max}$ (Eq. (1-3)) of the two traces, and a match is accepted if the difference is within the range of $\sigma_{\max}$ and discarded otherwise. The factor μ can be varied to weaken or strengthen the match criteria for which a match can be accepted. Finally an M-function has been defined, which is called the "Area-Overlap-Integral", because it estimates the area A_S that both tensiotraces overlap, see Figure 2-12.

$$M_A = \frac{\sum_{i=1}^{N_{\max}} (u_S)_i}{\sum_{i=1}^{N_{\max}} (u_L)_i} = \frac{A_S}{A_L} \qquad (M_A \equiv 1 \; for \; (A_L = 0)) \tag{2-38}$$

where A_S is the smaller area that both tensiotraces overlap and A_L is the larger area.

The graphical representation of differences in two tensiotraces (see Chapter 4) is preferably used for a rapid trace comparison, and in this case it is usually more convenient to apply D-functions (difference) that are simply defined as

$$D = 1 - M$$

where M is one of the M-functions in the Eqs. (2-33) to (2-38).

2.4 Hough Transform Inspired Fingerprinting and Archiving Technique

The new tensiotrace analysis technique, briefly described here and fully explained in Chapter 7, has been developed based on the well-known Generalised Hough Transform (GHT) [2-5]. This new technique offers the potential of reducing the entire data set of a tensiotrace to a single point in a two-dimensional feature space, which then may be used to test for mismatch between both reference and test samples. In addition, an archiving method has been devised as an extension of the technique above that stores the specific information of a liquid as a single data point in a three-dimensional feature space. To achieve the greatest utility in the tensiographic approach it is important initially to establish the objectives for the visual archiving system. This knowledge then allows for the definition of the algorithms and the procedural modifications of the GHT.

1. Each data set of a tensiotrace has to be represented by a 'single point' (T_c,U_c,P) in a three-dimensional feature space (T,U,P). The computation of the feature vector is performed over the entire data set $\{(t_i,u_i,p)|(1 \leq i \leq N_{\max})\}$ that constitutes the tensiotrace and hence each trace point contributes to the final measurement with equal weighting.
2. It is desired that all liquids with similar physical properties will be located in this feature space at a position that visually indicates that they are in the same category, e.g. water is at a position removed from that of ethanol and so forth. Hence, two of the dimensions (T,U) in the feature space have been reserved exclusively for the representation of the shape of a tensiotrace. The third dimension P has been assigned to serve as a refractive index, colour and turbidity indicator of a liquid.
3. The specific location and distance between two points in the feature space should represent the differences between liquids. Two equations, namely the 'difference' Δ (Eq. (7-13)) and 'closeness' ς (Eq. (7-14)), have been defined to express the differences between liquids mathematically.
4. An 'exchange operator' Ξ (Eq. (7-6)) has been defined to facilitate the visual representation of the differences between the two data sets of tensiotraces. This difference measure is visually represented as a scattering of data points after the

exchange operator has been applied. The amount of scatter depends on the differences in the data sets of the tensiotraces being compared.

5. The condition for a forensic feature match of two liquids is that the centroids (see Eqs. (7-2) and (7-3)) for both the 'Test' and 'Reference' traces are deemed close enough in the two-dimensional feature space to be satisfactory and when the exchange operator Ξ has been applied that there is an acceptably small resulting scatter.

Chapter 7 will describe how the GHT has inspired the development of a new approach to data-scatter that is called the *Tensiotrace Transform* (TT). This new data-scatter technique provides the user with a graphically aided rapid fingerprinting and conceptual archiving method for multianalyser tensiotraces, based on the 5 themes discussed above. The experimental results also underpin the theoretical contemplation of the TT.

2.5 Statistics Reference Measurements

In nearly every laboratory in which liquid measurements must be undertaken there arise QC issues, or research issues related to the measurements of samples that require fingerprint analysis. The multianalyser differentiates fundamentally between the tensiographic forensic fingerprint capability, i.e. instrumentally determined identity of two liquids made with high resolution, and fingerprint QC measurements, which will identify liquids in a more flexible and less demanding way. The statistics of a multi-measurand tensiotrace, discussed here, have been developed specifically for QC measurements and they are an approach towards forensic fingerprinting. A tensiotrace gives in effect the signature that defines the product. Deviations from this signature can be instantly analysed with a purposely-designed software package, which is included in Appendix 5. Well-established standard statistical tests have been implemented for the analysis of tensiotraces, including correlation coefficient, normal statistic tests, nonparametric tests (Wilcoxon and Spearman) and others. The statistical fingerprint test of two tensiotraces, namely the reference (*ref*) and test (*tst*) trace, can be described as follows.

2.5.1 Normal Distribution Inference

First of all the basic information of a tensiotrace is obtained, which is in particular the number of data points (N_{ref} and N_{tst}) and the maximum sample number, represented by the number of data points (($N_{\max} = N_{ref}$) if ($N_{ref} > N_{tst}$) else ($N_{\max} = N_{tst}$)). The two traces can be considered as relatively large in sample number size and it makes sense to draw inferences from the point estimation of the mean-difference

$$\overline{U}_D = \frac{\sum_{i=1}^{N_{\max}} |u_d|_i}{N_{\max}} \qquad (N_{\max} > 0) \tag{2-39}$$

where $u_d = u_{ref} - u_{tst}$ is the difference in the signals of the reference and test tensiotraces. It should be noted that the absolute value of u_d is used to overcome the problem of alternating signed values that may occur during the computation, see Figure 2-12. The object of point estimation is to calculate, from the sample data, a single number (here $\overline{U}_D$) that is likely to be close to the unknown value of the parameter. A statistic intended for estimating this parameter is called a point estimator and the standard deviation of this estimator is called its standard error ε_D. The standard deviation σ_D of each sample difference u_d can then be determined using

$$\sigma_D = \sqrt{\frac{\sum_{i=1}^{N_{\max}} \left(|u_d|_i - \overline{U}_D \right)^2}{N_{\max} - 1}} \qquad (N_{\max} > 1) \tag{2-40}$$

and the standard error ε_D of the mean-difference $\overline{U}_D$ is defined as

$$\varepsilon_D = \frac{\sigma_D}{\sqrt{N_{\max}}} \qquad (N_{\max} > 0) \tag{2-41}$$

If two tensiotraces, with randomly added noise, represent a fingerprint of one and the same liquid, then u_d will be nearly normally distributed with mean $\overline{U}_D$ and standard error ε_D, by computing the sample differences over $N_{\max}$ data points. It is understood that this measure is particularly susceptible to differences in the DP (see Figure 2-12) of two tensiotraces, hence its significance can only be judged in conjunction with the nonparametric procedures described below in this section, which deals with tensiotraces

that have a different DP. To understand how closely u_d is expected to estimate $\overline{U}_D$, see Figure 2-13 (a).

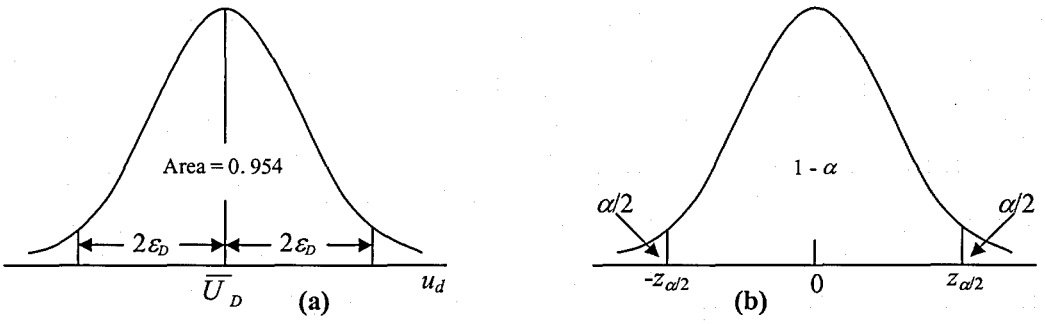

Figure 2-13. (a) Approximate normal distribution of u_d, (b) the notation $z_{\alpha/2}$.

In the normal distribution, the interval running two standard errors ($2\varepsilon_D$) on either side of the mean $\overline{U}_D$ contains probability 0.954. Use of the probability 0.954, which corresponds to the multiplier 2 of the standard error, is by no means universal. The following notation will facilitate the writing of an expression for the 100(1-α)% error margin where 1-α denotes the desired high probability such as 95.4% or 98.2% for instance. The upper $\alpha/2$ point of the standard normal distribution is $z_{\alpha/2}$, that is, the area to the right of $z_{\alpha/2}$ is $\alpha/2$, and the area between $-z_{\alpha/2}$ and $z_{\alpha/2}$ is 1-α, see Figure 2-13 (b). A few values of $z_{\alpha/2}$ obtained from the normal distribution table appear in Table A4-1 for easy reference. An example is given, which determines the 90% error margin, to illustrate the $z_{\alpha/2}$ notation. Setting 1-α = 0.90, which means that $\alpha/2$ = 0.05 gives $z_{0.05}$ = 1.645 (see Table A4-1).

The next question is, does the normal distribution serve as a reasonable model for fingerprinting tensiotraces that produced the data set of the differences u_d? An effective way to check the plausibility of a normal model is to construct a 'normal-scores plot' of the sample data. The term normal-scores refers to an idealised sample from the standard normal distribution, namely the z-values that divide the standard normal distribution into equal probability intervals.

$$m_i = z\left(\frac{i}{N_{\max}+1}\right) \qquad (1 \le i \le N_{\max}) \tag{2-42}$$

Suppose the sample size is $N_{\max}$ = 4. Figure 2-14 (a) shows the standard normal distribution where four points are located on the z-axis so that the distribution is divided into five segments of equal probability 1/5 = 0.2. These four points, denoted by m_1, m_2, m_3 and m_4, are precisely the normal scores for a sample of size $N_{\max}$ = 4. The m-values shown in Figure 2-14 (b) can be found using Table A4-1.

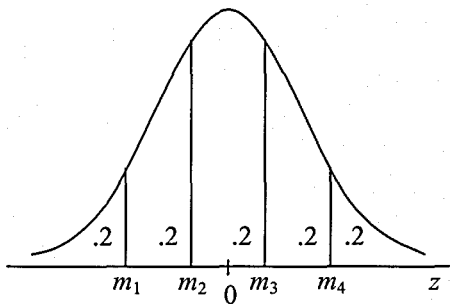

(a)

$m_1 = -.84$
$m_2 = -.25$
$m_3 = .25$
$m_4 = .84$

(b)

Figure 2-14. (a) Normal distribution and (b) normal scores for a sample of size $N_{max} = 4$.

A 'normal-scores plot' assesses how well a sample mimics the idealised normal sample. To construct a 'normal-scores plot':

Order the differences of each data point of two tensiotraces from the smallest to the largest value

$$|u_d|_i \le |u_d|_{i+1} \qquad (1 \le i < N_{max}) \tag{2-43}$$

and check if the i-th largest observed difference $|u_d|_i$ is linear related to the i-th largest normal-score ($\overline{U}_D + \sigma_D m_i$), using the linear correlation coefficient r [2-6]

$$r = \frac{\sum_{i=1}^{N_{max}} \left(|u_d|_i - \overline{U}_D\right)\left(\left(\overline{U}_D + \sigma_D m_i\right) - \overline{U}_D\right)}{\sqrt{\sum_{i=1}^{N_{max}} \left(|u_d|_i - \overline{U}_D\right)^2 \sum_{i=1}^{N_{max}} \left(\left(\overline{U}_D + \sigma_D m_i\right) - \overline{U}_D\right)^2}} \tag{2-44}$$

The number r is an indicator of how well the points ($|u_d|_i$, $\overline{U}_D + \sigma_D m_i$) fit a straight line and if the differences $|u_d|_i$ of two tensiotraces are normally distributed, then r is close to ±1, i.e. the points ($|u_d|_i$, $\overline{U}_D + \sigma_D m_i$) lie close or on a straight line; if r is close to 0, the points are uncorrelated and have little or no tendency to lie on a straight line, i.e. the differences $|u_d|_i$ are not normally distributed. An example should clarify this statistic. Assuming that the four sample values are u_{d1}=.0075, u_{d2}=.0082, u_{d3}=.0068, and u_{d4}=.0044 yields $\overline{U}_D$=.00673 and σ_D=.00165 using Eqs. (2-39) and (2-40) respectively. Table 2-1 shows the ordered observed values and the associated idealised values.

Observed Values	Idealised Values
.0044	$\overline{U}_D + \sigma_D m_1 = .00673 - .00139 = .00534$
.0068	$\overline{U}_D + \sigma_D m_2 = .00673 - .00041 = .00632$
.0075	$\overline{U}_D + \sigma_D m_3 = .00673 + .00041 = .00714$
.0082	$\overline{U}_D + \sigma_D m_4 = .00673 + .00139 = .00812$

Table 2-1. Ordered observed values and the associated idealised values.

Using Eq. (2-44) gives $r = -.145$, indicating a strong evidence that the sample values are not normally distributed, which however was not the point to prove but shows how this statistic can be applied to data sets of tensiotraces.

A more quantitative measure of the fit can be found by using Table A4-2 (it can be assumed that the number of data points N, in a tensiotrace, is always greater than 100). For any given observed value r_o, $\text{Prob}_N(|r| \geq |r_o|)$ is the probability that N measurements of two uncorrelated variables would give a coefficient r as large as r_o. Thus, if a coefficient r_o was obtained for which $\text{Prob}_N(|r| \geq |r_o|)$ is small, it is correspondingly unlikely that the variables are uncorrelated; that is, a correlation is indicated. In particular, if $\text{Prob}_N(|r| \geq |r_o|) \leq 5\%$, the correlation is called significant; if it is less than 1%, the correlation is called highly significant. For example, the probability that 90 measurements ($N = 90$) of two uncorrelated variables would yield $|r| \geq 0.3$ is given in Table A4-2 as 0.4%. Thus, if 90 measurements gave $r = 0.3$, the evidence of a linear correlation between the two variables would be highly significant.

2.5.2 Nonparametric Inference

Nonparametric refers to inference procedures that do not require the data points of the tensiotraces to be normally distributed. The Wilcoxon rank-sum test and Spearman's correlation coefficient, two useful nonparametric procedures named after their proposers Wilcoxon and Spearman, will be described here [2-7]. For a comparative study of two tensiotraces, namely reference (*ref*) and test (*tst*), the data points are recorded in the following way

ref-trace $\quad R_1, R_2, \ldots, R_{nref}$

tst-trace $\quad T_1, T_2, \ldots, T_{ntst}$

It is desired to test the null hypothesis H_0 that there is no difference between each data point (R_i, T_i), i.e. there is no difference between the two tensiotraces (the opposite to H_0 is the alternative hypotheses H_1).

Hypotheses

H_0: The two tensiotraces are identical.

H_1: The two tensiotraces are shifted apart; see Figure 2-15.

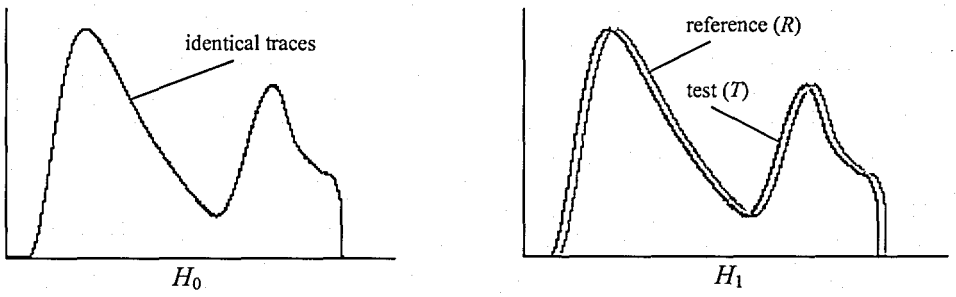

Figure 2-15. For the explanation of the Hypotheses H_0 and H_1.

Note that no assumption is made regarding the shape of the distribution of the tensiotrace data points. The following intuitive line of reasoning can now explain the basic concept underlying the rank-sum test. Suppose that the two sets of tensiotrace data points are plotted on the same diagram, using the markings R and T to identify their sources. Under H_0, the samples come from the same population, so that the two sets of points should be well mixed. However, if the larger observations are more often associated with the first trace, for example, it can be inferred that population R is possibly shifted to the right of population T. These two situations are shown in Figures 2-16 (a) and 2-16 (b), where each combined set of data points is serially numbered from left to the right. These numbers are called the combined sample ranks. In Figure 2-16(a) large as well as small ranks are associated with each sample, whereas in Figure 2-16(b) most of the larger ranks are associated with the first sample (in this example with R). Therefore, considering the sum of the ranks associated with the first sample as a test statistic, a large value of this statistic should reflect that the first trace is located to the right of the second.

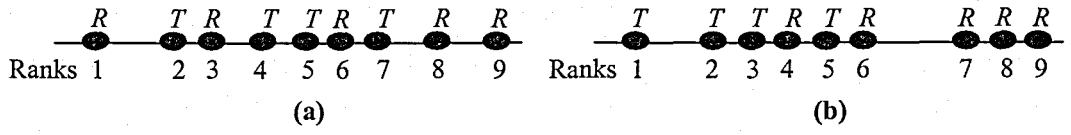

Figure 2-16. Combined plot of the two samples and the combined sample ranks, (a) mixed results, (b) higher ranks are mostly associated with *R*.

To establish a rejection region with a specified level of significance, the distribution of the rank-sum statistic under the null hypothesis H_0 must be considered. The procedure for the rank-sum test, to test H_0 (the two tensiotraces are identical), is as follows:

1. Rank the combined samples of $n = n_{ref} + n_{tst}$ data points in increasing order of magnitude.
2. Find the rank-sum W_{ref}, which is the sum of all ranks labelled with an R.
3. When the sample sizes are large (this can always be assumed for tensiographic traces), the null distribution of the rank-sum statistic is approximately normal (Figure 2-13(b)), and the test can therefore be performed using the Table A4-1. Under H_0, the distribution of W_{ref} has

$$mean = \frac{n_{ref}\left(n_{ref} + n_{tst} + 1\right)}{2}$$

and

$$\text{var}iance = \frac{n_{ref} n_{tst}\left(n_{ref} + n_{tst} + 1\right)}{12}$$

which yields

$$z = \frac{W_{ref} - \dfrac{n_{ref}\left(n_{ref} + n_{tst} + 1\right)}{2}}{\sqrt{\dfrac{n_{ref} n_{tst}\left(n_{ref} + n_{tst} + 1\right)}{12}}} \tag{2-45}$$

the rejection region for the z-statistic can be determined by using Table A4-1.

If there are ties present in the ordered data set, i.e. different data points have the same value, then the average rank of the tied values is assigned to each of these data points.

Ranks may also be employed to determine the degree of association between two tensiotraces. The n pairs (R_1, T_1), (R_2, T_2), ..., (R_n, T_n) are independent and the R_1, ..., R_n are then ranked respectively ρ_1, ..., ρ_n among themselves, and the T_1, ..., T_n are ranked respectively τ_1, ..., τ_n among themselves. Before a measure of association can be presented, note a few simplifying properties. Because each of the ranks 1, 2, ..., n must occur exactly once in the set ρ_1, ..., ρ_n, it can be shown that

$$\bar{\rho} = \frac{1+2+...+n}{n} = \frac{n+1}{2}$$

and

$$\sum_{i=1}^{n}(\rho_i - \bar{\rho})^2 = \frac{n(n^2-1)}{12}$$

for all possible outcomes. Similarly

$$\bar{\tau} = \frac{1+2+...+n}{n} = \frac{n+1}{2}$$

and

$$\sum_{i=1}^{n}(\tau_i - \bar{\tau})^2 = \frac{n(n^2-1)}{12}$$

Spearman defines a measure of correlation that is analogous to the linear correlation coefficient r in Eq. (2-44), except that Spearman replaces the observations with their ranks. Spearman's rank correlation r_{sp} is defined by

$$r_{sp} = \frac{12\sum_{i=1}^{n}\left(\rho_i - \frac{n+1}{2}\right)\left(\tau_i - \frac{n+1}{2}\right)}{n(n^2-1)} \tag{2-46}$$

This rank correlation shares the properties of r that $-1 \le r_{sp} \le 1$ and that values near +1 indicate a tendency for the larger values of the first trace to be paired with the larger values of the second trace, and values near −1 indicate the opposite relationship. However, the rank correlation is more meaningful, because its interpretation does not require the relationship to be linear.

CHAPTER 3

ELECTRONIC ENGINEERING DEVELOPMENT

During the development process that comprised the electronic engineering facet of the work on the tensiograph it was decided to modify the electronic circuitry, which existed in preliminary tensiographic instruments, involving the replacement of electronic components, new printed circuit board (PCB) design and the use of shielded cable, connectors and housings in order to achieve a better SNR of the tensiotraces. Figure 3-1 shows a schematic overview of the electronic and optical system of a tensiograph. The shaded units in this block diagram, which constitute the core developmental electronic engineering work, will be fully described in this chapter, whereas the non-shaded units, commercially available, were added for a more complete system overview and their description in this chapter has been kept brief.

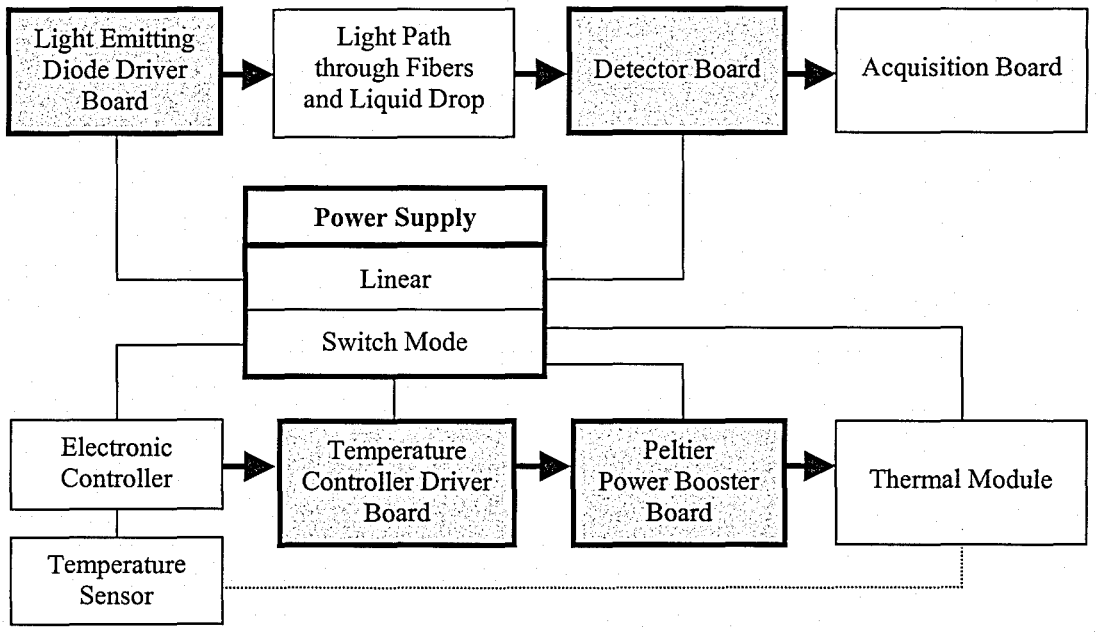

Figure 3-1. Arrangement of electronic and optical devices in the tensiograph.

Given the brief of engineering a near-commercial instrument, in some instances it has been necessary to design new electronic circuits to avoid the purchase of relatively expensive components. The temperature controller, for example, incorporates the low-cost temperature controller driver board, which will be discussed in Section 3.1 and fundamentally enhanced the functionality of the electronic controller device that controls the thermal module of a tensiograph. Section 3.2 deals with the Peltier power

booster board that drives the current for the thermal module. The light emitting diode driver board will be discussed in Section 3.3. It describes the generation of light, which is injected into the source-fiber, and Section 3.4 discusses then the detector board, which converts the light signal, coming out of the collector-fiber, into an electronic signal (see also Figures 1-1 and 1-2). After this conversion, the signal is passed on to an acquisition board and the acquisition board interfacing in Section 3.5 explains how this is done. The system integration in Section 3.6 finalises this chapter. Each section starts with an explanation of the electronic circuits (schematics are given in Appendix 2) and a description of the changes that have been made to improve the performance of a multianalyser with regard to the electronics. This chapter, in many places, provides the basis for the description of the work in later chapters. This chapter therefore must be viewed in the fuller context of the overall thesis in providing an overview of the electronic engineering, but the more substantial details of the engineering content will be dealt with later in the thesis.

3.1 Temperature Controller Driver Board

An extensive market investigation was carried out to select the most suitable electronic controller device (Picture A2-7) for the temperature system of a tensiograph. The Peltier-based thermal module will be fully examined in Chapter 6, but it is of importance here to point out that this particular thermal module operates with a bipolar voltage supply. To allow the electronic controller device to control the thermal module efficiently it must generate an output voltage that ranges from a positive to a negative value. Such devices are available on the market, but the cost is high compared to an electronic controller with only a unipolar output voltage, and therefore a low-cost electronic circuit has been developed to overcome this problem. The additional circuit is connected to a less expensive electronic controller with a unipolar output and mimics the functionality of an electronic controller device with a bipolar voltage output. Figure 3-2 shows the arrangement of the modified electronic controller device. A detailed electronic circuit diagram of the temperature controller driver board is provided in Appendix 2 (Schematic A2-1) and will be used as a reference of the various components discussed below in this section.

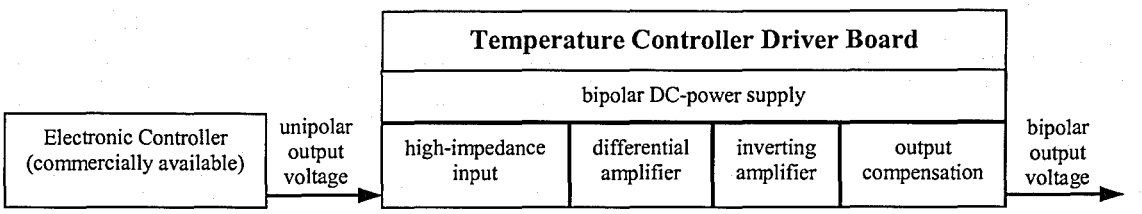

Figure 3-2. Principle of the output-voltage conversion of the electronic controller.

The output voltage of the electronic controller (0 to $10V$) provides the input signal, which has to be altered, to the temperature controller driver board. This board is theoretically divided into five sections and the bipolar DC power supply is the first section that is connected to all subsections on the board. The voltage ($\pm 15V$) is taken from a switch mode power supply (see Picture A2-2) and allows for the output signal of the board to be bipolar. Two capacitors, namely C_2 and C_5, are used on the board to filter unwanted noise that may have been induced in the relatively long leads from the power supply to the board and could affect the performance of the integrated circuit (IC) device LF347N, which forms the basis for the four remaining subsections of the whole electronic circuit. It is recommended in the data sheet of the quad operational amplifier LF347N, which is the IC U_1 on the board, that the two capacitors C_1 and C_3 should be placed as close as possible to the IC to minimise disturbing interferences that may be produced on the path from the input capacitors C_2 and C_5 to the power supply terminals of the amplifier. Coupling the output voltage of the electronic controller device into the high-impedance input terminal of the temperature controller driver board (pin3 of U_{1A}) ensures that virtually no current is drawn from the output of the electronic controller and this on the other hand eliminates driver board interventions with the electronic controller device. The third section on the board, which is the arrangement of U_{1B} as a differential amplifier, generates the actual desired result of this additional electronic circuit by subtracting the on-board produced $+5V$ from the input signal. The output signal of the third section versus the input signal of the board is shown in Figure 3-3(a). It has to be pointed out here that the next section of this electronic circuit reduces the original signal amplitude due to the 0.22 gain setting of the amplifier, and this will be one issue that has to be discussed in Section 3.2. The best method to trim the amplitude of the given signal is to use U_{1C} as an inverting amplifier, which is not necessarily desired at this point, but the gain of a non-inverting amplifier can only be set to 1 or greater. In Section 3.2 it will be shown that this inverting effect does not impinge on the performance of the temperature controller driver board.

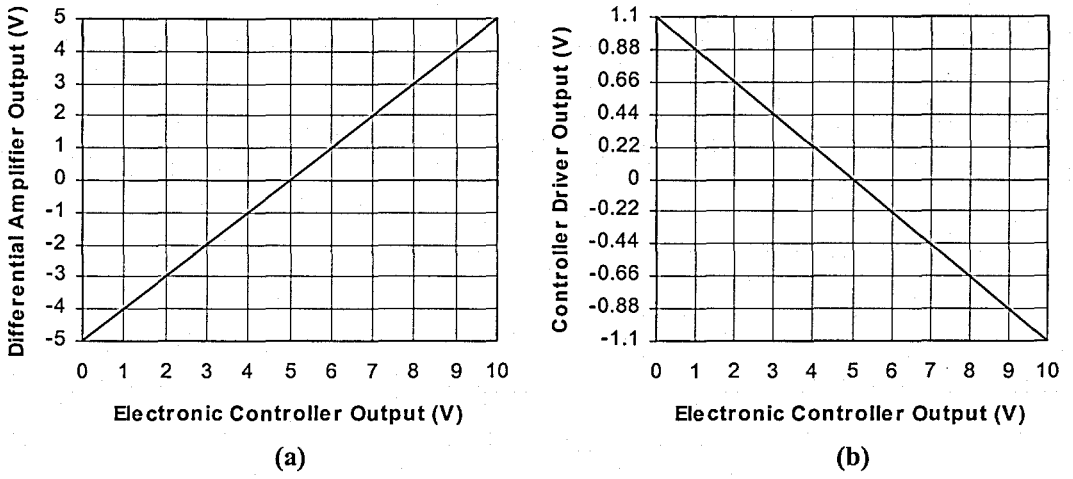

Figure 3-3. (a) The output signal of the third section, and (b) the output signal of the last section of the temperature controller driver board.

The inverted signal is then the input signal of the last section on the board (consisting of the components U_{1D}, R_3, and C_4), which represents the, so-called, lead compensation that is usually used to prevent oscillation at the output caused by a phase shift of the output signal to the input signal of the amplifier. Normally, only high-power amplifiers tend to oscillate when they are connected to a capacitive load, which occurs automatically with long leads connecting the output to an input of a different device. In the case of the temperature controller driver board the output current is very low, but the two extra components R_3 and C_4 (the cost is less than 10 pence) have been added only to facilitate future developments of the electronics. Specifically, these upgrade decisions enable modifications of this circuit, so that it can drive different applications to the one the board is currently designated for. R_3 and C_4 have no detrimental influence on the output signal generated in the presently used application and the fourth amplifier U_{1D} of the IC LF347N was available anyway. The output signal of the temperature controller driver board is illustrated in Figure 3-3(b).

3.2 Peltier Power Booster Board

The objective of the electronic circuit of the Peltier power booster board is to drive a current, which can be as high as $\pm 2A$, through two Peltier devices (see Picture A2-3) connected in series. Peltier devices will be fully explained in conjunction with the thermal module in Chapter 6. Only the basic behaviour of these devices is of concern at this point of the discussion, which is, that a Peltier device and an ohmic resistive load

show similar characteristics to a current-driving source, with the major exception that the Peltier device generates a back electromagnetic field (EMF), caused by a temperature gradient between the two planes of this device. Schematic A2-2 serves as an easy reference with regard to the electronic circuit and its components of the Peltier power booster board. Figure 3-4 shows the block diagram of this electronic circuit.

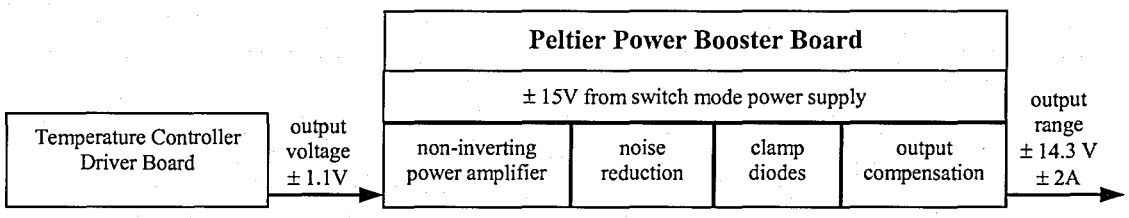

Figure 3-4. Principle of the high-power amplification.

The power supply terminals of the high-power operational amplifier L465A (IC U_1) are bypassed with low series impedance capacitors for good stability (see the noise reduction section in Figure 3-4). This technique, using ceramic (C_1, C_3) and tantalum (C_5, C_6) types in parallel is recommended in the data sheet of the high-power operational amplifier OPA548 from BURR-BROWN (10/97). In addition, it is recommended to put C_2 between the positive and negative power supply terminals and physically as close to the IC U_1 as possible. In practice, these stability precautions have been shown to be vital, considering that the switch mode power supply in Picture A2-2 provides this electronic circuit with $\pm 15V$ (ripple and noise 2% peak-to-peak). The relatively high noise level of about $300mV$ would turn the power operational amplifier L465A into an unwanted oscillator without taking the stability issues, discussed above, into account. Many hours have been spent to reach the goal of a properly working high-power DC amplifier that operates in the specified range ($\pm 15V$, $\pm 2A$) that does not oscillate or overheat. For better stability performance, the data sheet of the L465A from SGS (03/83) recommends operating this amplifier with a gain greater than $20dB$, which has been realised with a resistor network (R_1 and feedback resistor R_2), connected to the non-inverting power amplifier. Now it becomes clear why the amplitude of the temperature controller driver board, described in Section 3.1, has to be reduced before the signal is passed on to the high-impedance input terminal of the L465A (pin1 of IC U_1). In order to achieve high circuit stability the gain of the power amplifier U_1 has been adjusted to $22.3dB$, and therefore the Peltier power booster generates the output voltage in the desired range $\pm 14.3V$, due to the $\pm 1.1V$ input voltage range generated by the temperature controller driver board. The relationship between the input and output signal of the Peltier power booster is shown in Figure 3-5. Note, that the gain setting of

the power amplifier generates only an output voltage in the range $\pm 14.3V$ instead of the expected $\pm 15V$ that is supplied to the amplifier. This has been carefully designed to operate this circuit within its full input signal range from $-1.1V$ to $+1.1V$. If a gain value greater than $22.3dB$ had been used, the output voltage of the amplifier would have saturated at about $-14.3V$ or $+14.3V$ anyway, because of the internal losses in the power amplifier L465A.

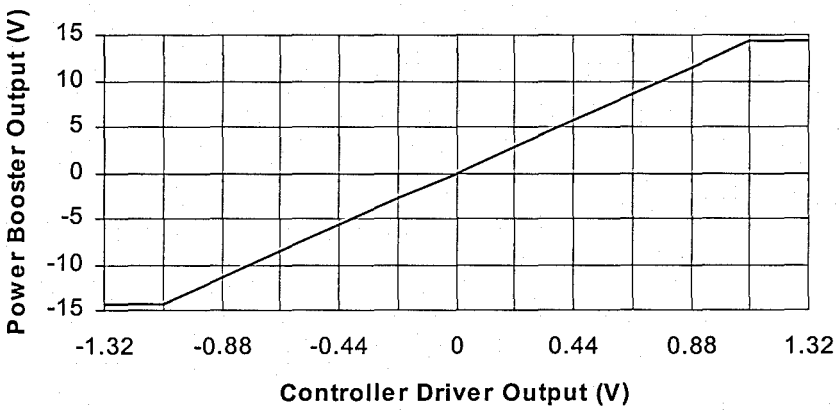

Figure 3-5. Linear relationship between input and output signal of the Peltier power booster.

The Peltier device, representing an EMF-generating load, can return load current to the amplifier U_1, causing the output voltage to exceed the power supply voltage. This damaging condition has been avoided with clamp diodes (D_1, D_2) from the output terminal of U_1 to the power supply rails. The output compensation (R_3, C_4) avoids oscillation due to phase shift as described above in Section 3.1.

During the process of driving current through the Peltier devices, the high-power operational amplifier L465A produces heat, which has to be dissipated. The power dissipation depends on the power supply, signal, and load conditions. For DC signals, power dissipation is equal to the product of the output current times the voltage across the conducting output transistor in the amplifier. For resistive loads, the maximum power dissipation occurs at the DC output voltage of one-half the power supply voltage. The L465A requires a heatsink HS to ensure that the maximum operating junction temperature of $125°C$ ($145°C$ minus $20°C$ safety margin) is not exceeded. In addition, the junction temperature should be kept as low as possible for increased reliability. The thermal resistance R_{thHS} [$°C/W$] of the required heatsink can be determined according to Eq. (3-1):

$$R_{thHS} = \frac{\vartheta_j - \vartheta_A}{P_D} - R_{thjc} \tag{3-1}$$

where ϑ_j [°C] is the maximum junction temperature, ϑ_A [°C] is the maximum ambient temperature, P_D [W] is the power dissipation, and R_{thjc} [°C/W] is the thermal resistance junction/case of the amplifier. With one-half the power supply voltage (7.5V) across the conducting transistor of the L465A and maximum current (2A) – thus P_D = 15W, thermal resistance junction/case (3°C/W), and maximum ambient temperature (45°C), the thermal resistance R_{thHS} has been calculated to 2.33°C/W. A heatsink with thermal resistance R_{thHS} = 2.0°C/W is a part commercially available and has been chosen for the Peltier power booster board. The thermal module of a tensiograph incorporates two Peltier devices (Picture A2-3), which are usually connected in series but the power booster with its heatsink HS has also been designed to drive the two Peltier devices connected in parallel. As explained in Chapter 6, this has the advantage of giving both, an increased temperature range of the thermal module and a quicker response time to temperature changes without replacing any of the electronic circuits or components. The electronic circuit has been tested for both parallel and series connection of the Peltier devices and showed great performance in experimental tests. The disadvantage of drawing a higher current out of the power amplifier is obviously the decreased reliability brought about because the device is operating close to its maximum rating. In addition, a more powerful power supply would be required to drive a higher current through the Peltier devices.

3.3 Light Emitting Diode Driver Board

Different types of a light source may be used to illuminate the inner surface of a drop to generate TIRs during drop formation, as described in previous chapters. It is advantageous, for analytical reasons that will be explained in Chapter 6, to choose from a variety of light sources of different wavelengths for the analysis of various LUTs with dissimilar physical properties. This has been realised in the development of the light emitting diode driver board, which incorporates 4 LEDs (D_1 to D_4) of distinct operational wavelengths. Schematic A2-3 will be used as the reference for the electronic circuit and component description in this section. A preceding version of an LED driver

board employed the simplest electronic circuit that can be used to drive LEDs. This simple circuit is shown in Figure 3-6(a). When the sensitivity and SNR increased during the development process of the multianalyser, exploiting better and more sophisticated technology in this tensiographic instrument, it became evident that the simple circuit in Figure 3-6 (a) could not retain the desired quality standard of the apparatus.

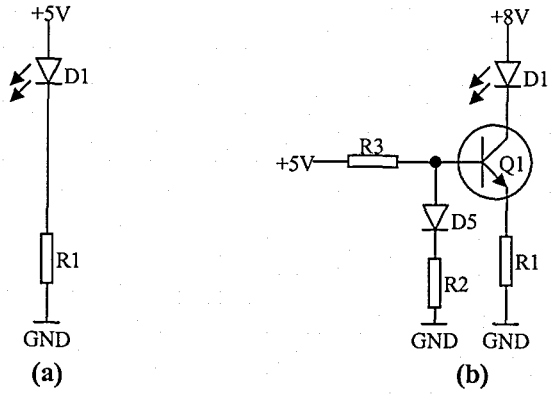

Figure 3-6. (a) simplest LED control, (b) constant-current control of an LED.

It was therefore necessary to develop a more advanced electronic circuit that meets the requirements of a constant current-driven LED system. This circuit is shown in Figure 3-6(b). For a comparative study of the two circuits in Figures 3-6(a) and 3-6(b), it is important to mention the fact that the light intensity of an LED is a function of the forward current I_F of the LED. This relationship is graphically represented in Figure 3-7 (Example: super bright LED IF-E97, 660nm from Industrial Fiber Optics Inc).

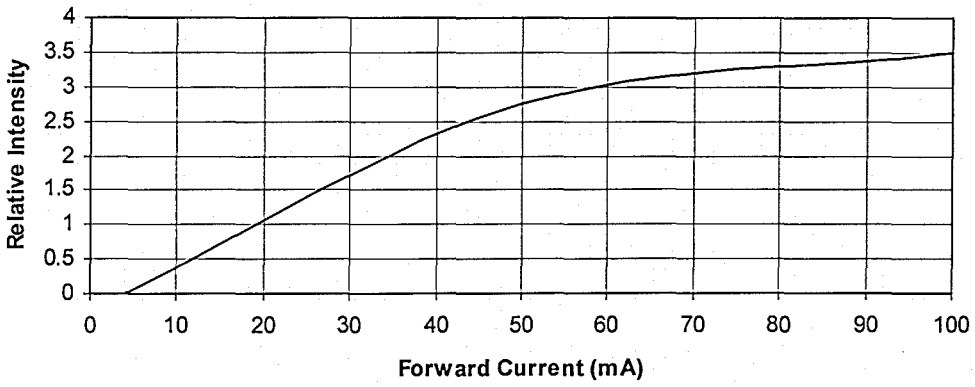

Figure 3-7. Normalised power launched versus forward current I_F of a super bright LED (IF-E97, 660nm), source: Product Catalogue Industrial Fiber Optics, Inc.

The intensity of the light delivering LED must be kept as constant as possible when the emphasis on operational requirement is for the fingerprinting of liquids, because a small drift in the light signal intensity generates a relatively large error during the signal detection process. Both circuits in Figures 3-6(a) and 3-6(b) follow the same basic concept, which is, driving a specific current through the LED to emit a light signal.

Under ideal conditions (for instance, no changes in ambient temperature, a constant voltage drop across the LED), circuit 3-6(a) would be the best system to meet the operational requirements. Conversely, ambient temperature changes occur that alter, for instance, the resistor value of R_1 in both circuits by

$$R(\vartheta) = R_0(1+\alpha\vartheta), \qquad \alpha = \frac{1}{R_0}\frac{dR}{d\vartheta} \tag{3-2}$$

where α $[K^{-1}]$ is the temperature coefficient of the resistor, R_0 $[\Omega]$ is the resistor value at $0°C$, and ϑ $[°C]$ is the temperature of the resistor [3-1]. Furthermore, the current through the LED D_1 in circuit 3-6(a) is determined by the voltage V_1 across R_1 over the resistance R_1 ($I_F = V_1/R_1$), which means that I_F, and therefore the intensity of the LED, varies with a change in resistor value R_1. Similarly, the intensity of D_1 in circuit 3-6(a) will change if the voltage drop across D_1 varies. It must be concluded that circuit 3-6(a) is not suitable to drive the LEDs in a high-sensitivity tensiograph as it exists today. The circuit in Figure 3-6(b), on the other hand, overcomes the problems of the circuit in Figure 3-6(a). The emitter potential of the transistor Q_1 rises about $2mV/°C$ [3-2], which can be compensated (base potential of Q_1 rises equally) by connecting the diode D_5 (thermally close to Q_1) from the base of Q_1 to the resistor R_2, as shown in Figure 3-6(b). It is important that the resistors R_2 and R_3 of the voltage divider in Figure 3-6(b) are located thermally close together and have the same temperature coefficient α, to retain the resistance ratio of the divider, which consequently anchors the base of Q_1 constantly at the same potential. R_1 in Figure 3-6(b) is a special resistor with an impressively low temperature coefficient $\alpha = \pm 3ppm/°C$, thus a change in temperature has virtually no effect on the resistance of R_1. This constant current source therefore drives a remarkably constant current through the LED D_1, allowing for variations in the voltage drop across D_1 (see Eq. (3-3)).

$$I_F = \frac{V_{R2} + V_{D5} - V_{BE}}{R_1} \tag{3-3}$$

where V_{R2} $[V]$ is the voltage drop across the resistor R_2, V_{D5} $[V]$ is the voltage drop across the diode D_5 and V_{BE} $[V]$ is the voltage drop across the base/emitter path of the transistor Q_1. It should be noted here that the base current of Q_1 is not included in the calculation of I_F, because it is negligible due to an extremely high DC current gain h_{FE} (500) of the transistor ZTX690B (Q_1).

In addition, this circuit has the advantage of being able to give on/off control to the constant current through the LED D_1. Thus the multiplexer U_1 has been added to make this possible. This multiplexer is computer controlled via a digital interface that is part of the acquisition board PC30G from Amplicon, which is located in a PC and will be the subject of the discussion in Section 3.5. With different combinations of the digital input signals DO_4, DO_5, and DO_6 of U_1, the voltage ($+5V$, pin3 of U_1) can be switched to one of the outputs Y_0 to Y_7 successively. Only the LED in use needs to be driven, which is selected via a HIGH signal of one of the output channels Y_0 to Y_7. This selectivity in the driver circuit limits the aging and hence operational drift of the non-illuminated LEDs on the light emitting diode driver board. The software issue that will be discussed in Chapter 4 gives details of the monitoring of LEDs used during a measurement by the encoded selection of a particular LED.

The second part of the electronic circuit (Schematic A2-3) has been developed to expand the pulse width of the output signal of a slotted opto-switch, which is used to trigger the computer-controlled data acquisition of the tensiographic instrument and will be explained below in this section with regard to Figures 3-8 and 3-9.

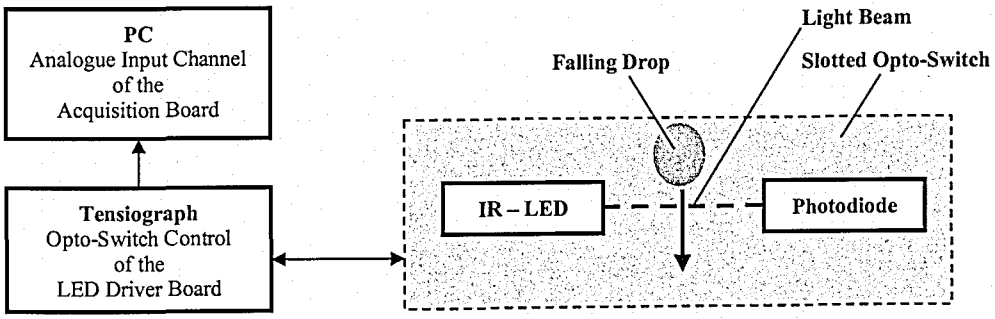

Figure 3-8. The principle of triggering the tensiotrace acquisition process.

The first unit (C_1, U_3, and C_7) of the opto-switch control circuit provides the power for the opto-switch U_4 and the timer IC NE555N (U_2), and it is also used to supply the entire light emitting diode driver board with a constant and noise-reduced voltage ($+8V$). Due to a relatively high current ($25mA$ to $38mA$, drawn by a selected LED of the circuit) through the integrated fixed voltage regulator U_3 and the voltage drop ($7V$) across this device, heat is produced and has to be dissipated by mounting a heatsink HS on the voltage regulator U_3. Eq. (3-1) was used to determine the minimum size of the required heatsink HS for the voltage regulator U_3. However, the opto-switch itself contains an IR-LED that transmits a light signal to a photodiode, which is located opposite to the IR-LED, thus there is a line-of-sight path between these two components (see Figure 3-8). Whenever an object intercepts this light beam, the output voltage of

the opto-switch becomes $0V$, otherwise the output voltage is almost equal to the supply voltage of the device. This functionality has been used in the tensiograph, where a falling drop intercepts the light beam for a fraction of a second and generates therefore a signal on the output of the opto-switch, which is subsequently sent to an analogue input channel of the acquisition board PC30G (see Figure 3-8) and used to trigger or stop the tensiotrace data acquisition. Figure 3-9(a) shows an example of the output signal of the opto-switch when a falling drop intercepts the light beam (see Figure 3-8) for the time $t_{int} \approx 1ms$. The time t_{int} varies with the size of the drop and the distance between the drophead and the opto-switch. The size of the drop depends on the physical properties of the LUT, and the dimensions of the thermal module determine the distance between drophead and opto-switch.

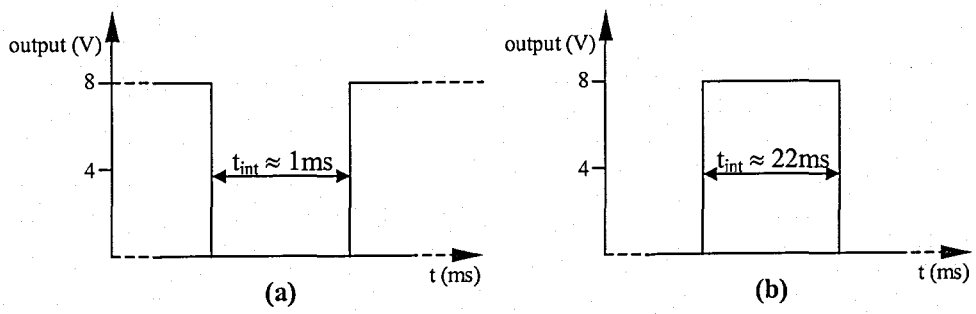

Figure 3-9. Trigger signal of the opto-switch, (a) real signal-time t_{int} of the light beam interception (opto-switch output), (b) extended signal-time t_{int} of the light beam interception (NE555N timer output).

In Chapter 4 it will be discussed why it is necessary to generate an expanded pulse width t_{int} as shown in Figure 3-9(b). Further discussions here concentrate on how this pulse width expansion is implemented. Using the signal t_{int} in Figure 3-9(a) as the input signal for the timer U_2, an expanded interception-time t_{int} will be generated according to the values of the components R_{14} and C_2 of the associated RC-network,

$$t_{int} = 1.1R_{14}C_2 = 22ms \text{ (see data sheet NE555N, Phillips Semiconductors, 08/94).}$$

3.4 Detector Board

In this section the electronic circuit of Schematic A2-4, which has evolved from a preliminary detector circuit of a tensiograph, will be used as a reference to underpin the signal quality improvement that has been achieved during the development process. Further research, concerning the signal quality of the electronic circuit shown in Schematic A2-4, has led to the production of the modified and improved version of the

circuit, which is shown in Schematic A2-5. The principle of the conversion of a light signal into an adequate voltage that is then being used for the tensiotrace data acquisition is illustrated in Figure 3-10.

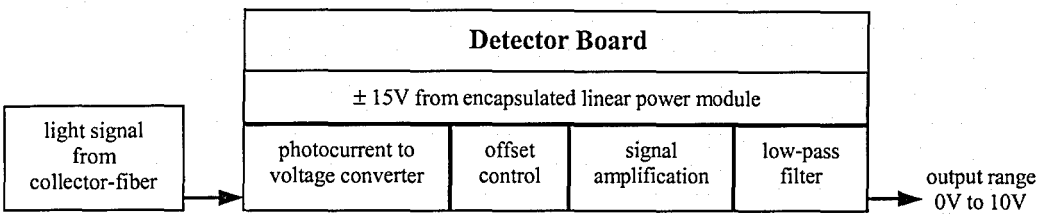

Figure 3-10. Principle of converting a light signal into a voltage.

Firstly, the light signal that has been coupled into the collector-fiber, as discussed in Chapter 1, is sent to the photodiode D_1 and generates a photocurrent that varies in its amplitude with the light intensity of the detected signal. The implementation of the photocurrent to voltage converter in two consecutively constructed tensiographic instruments were different. Figure 3-11(a) shows the obsolete version of this electronic circuit and Figure 3-11(b) illustrates the design of the up-to-date photocurrent to voltage converter. The comparison of the two circuits (see Figures 3-11(a) and 3-11(b)), with identical photodiodes D_1 and D_4, reveals the disadvantage of the circuit in Figure 3-11(a), because a relatively high dark current I_D, continuously flowing through the photodiode D_4, reduces the performance of this component. The dark current I_D is a function of the reverse voltage V_R across a photodiode and Figure 3-12 displays graphically this relationship. It should be remembered that the shot noise increases with the increasing current through a semiconductor, see Eq. (2-25). It is therefore extremely important to keep the input section of the detector board at the lowest possible noise level, since this noise affects the efficiency of the subsequent electronic circuitry. In order to achieve this noise-reduction goal, the dark current through the photodiode must be adjusted to a minimum, which is possible with the electronic circuit shown in Figure 3-11(b). Pin3 of the IC U_{3A} has the potential $0V$ and therefore pin2 of U_{3A} has also the potential $0V$, which means, that the voltage drop across the photodiode D_1 is always kept at $0V$.

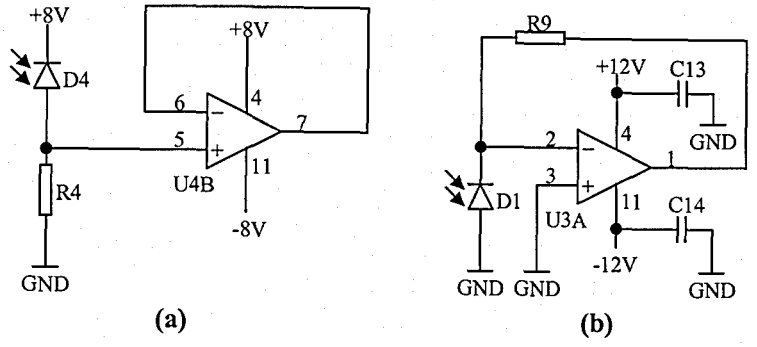

Figure 3-11. **(a) preliminary version of the detection of a light signal, (b) presently employed application of the photocurrent to voltage converter.**

Whenever the photodiode D_1 in Figure 3-11(b) is illuminated, a photocurrent flows and generates a voltage drop across the resistor R_9, which is proportional to the photocurrent of D_1. The modified photocurrent to voltage converter (see Figure 3-11(b)) is more sensitive in the lower detection range than the circuit shown in Figure 3-11(a), which is very important for sensing the extremely attenuated light rays produced by TIR in the LUT. Another limitation of the circuit in Figure 3-11(a) is the $8V$ power supply that generates only a voltage range ($0V$ to $8V$) on the output of the detector board. This is a limitation considering the input voltage range ($0V$ to $10V$) of the acquisition board PC30G.

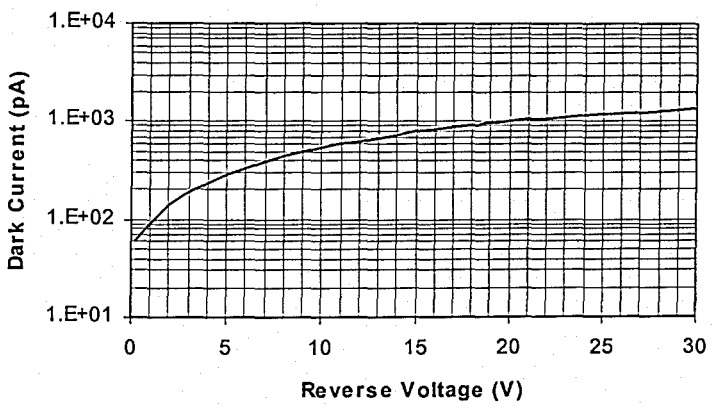

Figure 3-12. Dark current I_D versus reverse voltage V_R of a Si PiN photodiode (FDR 850 IR), source: Data sheet, The Fibre-Data Group, Cornwall TR15 3RH.

The next section on the detector board (see Schematic A2-4(b)) may be used to adjust the amplitude of the output signal to a value within the range $\pm 12V$, which is sometimes necessary to subtract an offset from the wanted signal; or, for example, to preset an offset for vibration experiments, which is briefly described in Chapter 4. The old design of the detector board controls the offset via an ordinary potentiometer, but the fine-tuning reproducibility of these devices is not good enough for a fingerprinting application such as the tensiograph. A better reproducibility of the offset adjustment has

been achieved by using one of the analogue outputs of the acquisition board to control one of the input voltages of the offset-regulating section via a computer controlled digital value, which is then converted into the required analogue voltage.

The second last section on the detector board (see Schematics A2-4 (c_1, and c_2)) represents a switchable gain amplifier, and again, the computer controlled gain setting mechanism has replaced the previously used potentiometer controlled system for better reproducibility and user friendliness. It is possible to change the potential divider ratio of the resistor network in (c_2), connected to the non-inverting amplifier in (c_1), in eight steps by using the functionality of the multiplexer in (c_2), which has been discussed in Section 3.3, setting the gain in a range from 1 to 9 (these gain values have a historical background and will be explained in Section 3.5).

The amplified signal is then passed on to the last section (d) of the electronic circuit on the detector board, which is a 3rd order Bessel low-pass filter, to de-noise the output signal efficiently [3-3]. The amplitude plot of a Bessel low-pass filter is shown in Figure 3-13. In order to retain an unchanged output signal, the cut-off frequency f_c has to be set to a value greater or equal to the highest desired frequency that passes the filter without changing the amplitude of the signal. The cut-off frequency f_c is the frequency above which the power output of a low-pass filter is one-half the power of the passing frequency. Since voltage V^2 is proportional to power P, V is $\sqrt{1/2}$ of the V in the passing frequency. This happens to be close to –3dB and the cut-off frequency is frequently referred to as the –3 dB point. Experimental investigations into drop vibrations [3-4] require a cut-off frequency of about $20Hz$, thus fc $\approx 32Hz$ including a safety margin.

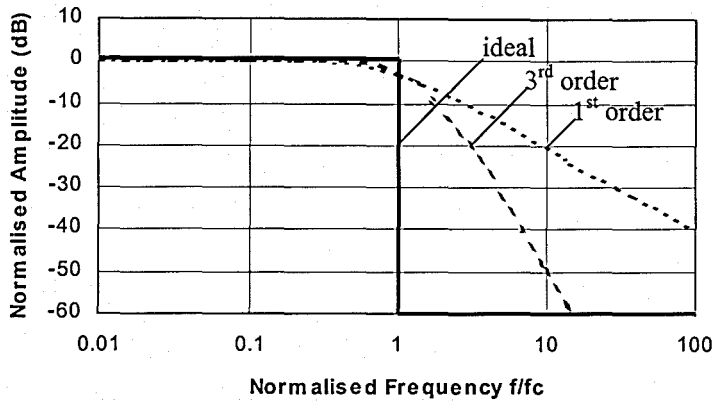

Figure 3-13. Amplitude plot of different order Bessel low-pass filters.

The major disadvantage of the electronic circuit in Schematic A2-4 is its gain setting mechanism. The gain can only be set in relatively large steps, and this is uneconomic for small amplitude adjustments of the output signal. The gain is typically set to a value that does not saturate the output signal, but generates almost the largest possible amplitude in the range $0V$ to $10V$ for the highest peak in a tensiotrace. This ensures that the SNR is at its maximum and the ADC of the acquisition board operates within the full conversion range (see Section 3.5). Furthermore, the 3rd order Bessel low-pass filter is over-engineered, as the comparison with a 1st order low-pass filter has revealed. A simpler low-pass filter design does not reduce the quality of the output signal of the detector board and spares one unit in the quad operational amplifier U_1. With these discoveries in mind, the electronic circuit of the detector board was redesigned, and the circuit in Schematic A2-5 has been produced. For the explanation of this electronic circuit, it is important to note that the two sections offset control and signal amplification have been exchanged. The signal amplification control (b) now employs the much more sophisticated digitally controlled potentiometers AD5220 (R_2, R_4), which allow the user of a tensiograph to change the gain A in the range from 1 to 121 (see Eq. (3-4))

$$A = \frac{(R_2 + R_3)(R_4 + R_5)}{R_3 R_5} \tag{3-4}$$

in 8256 *steps* (see Eq. (3-5)) [3-5], and the much neater design of this circuit stage, compared to the arrangement in Schematics A2-4 (c_1) and (c_2), reduces also the overall noise level.

$$steps = \frac{n(n+1)}{2} \quad (n = 128\, positions\, of\, potentiometer\, wiper) \tag{3-5}$$

The instrumentation amplifier (c) is due to its high common mode rejection ratio (*CMRR*) the ideal system to handle the offset issue and to eliminate most of the noise in the signal. The *CMRR* describes the ability of a differential amplifier to reject interfering signals common to both input terminals, and to amplify only the difference between the inputs. The higher the *CMRR*, the better the amplifier can extract differential signals in the presence of common mode noise. The *CMRR* [*dB*] for the instrumentation amplifier (c) (see Eq. (3-6)) is about 84*dB* [3-6]

$$CMRR = 20dB \lg\left[\left(1 + \frac{R_6 + R_8}{R_7}\right)\frac{2\alpha}{\Delta\alpha}\right] \tag{3-6}$$

where $\alpha = R_9/R_{11} = R_{10}/R_{12} = 1$, $\Delta\alpha = 0.1\%$ is the tolerance of these resistors. The output signal of the instrumentation amplifier (c) is then the input signal of the low-pass filter (d) that has the cut-off frequency $f_c = 1/(2\pi R_{13}C_5) \approx 25Hz$. The electronic circuit in Schematic A2-5 generates a qualitatively improved output signal compared to the output signal of the electronic circuit in Schematic A2-4, and consequently replaced the circuitry (version 01) on the detector board.

3.5 Acquisition Board Interfacing

The data acquisition board PC30G from Amplicon (see Table A2-2) is the interface between the generated analogue signal from the electronic circuitry in a tensiograph and the digitised data display and storage of this signal on a PC. It also provides controlling features such as the gain and offset settings on the detector board and the LED selection on the LED driver board located in a multianalyser. The PC30G technology allows all of its features to be controlled from software, increasing the reproducibility of the various settings and the user friendliness of the instrument, as discussed earlier in this chapter. Software issues raised in this section are brief and will be fully explored in Chapter 4.

The instrumentation amplifiers (analogue inputs CH0 and CH1) of the PC30G have been configured as differential inputs for the signals AI1 (see Schematics A2-4 and A2-5) and AI2 (see Schematic A2-3). Remember, the advantage of operating an

analogue input in differential mode is its remarkable *CMRR*. The analogue signals AI1 and AI2 are converted into digital signals and then transferred directly to the main memory of a PC using the direct memory access (DMA) facility of the PC30G. Recall the power supply issue in section 3.4, that the obsolete electronic circuit of a previous tensiograph provided only an output voltage range $0V$ to $8V$ (0 to 3276 resolution of the 12-bit ADC on the PC30G), which is a loss in signal information content, considering that the analogue input channels of the PC30G are configured to convert voltages in the range $0V$ to $10V$ (0 to 4095 resolution of the 12-bit ADC on the PC30G).

The user of a tensiograph may start the data acquisition by pressing a virtual button in an application software package (see Chapter 4), and a specially assigned function simultaneously triggers the DMA. The throughput of the DMA channel is not of importance with regard to the multianalyser, since the maximum sample rate ($320Hz$) of the instrument is by any means small compared to the maximum sample rate ($100kHz$) capability of the PC30G. The more important motivation for using the DMA mode is the ability of the user to operate the PC without any performance constraints, while transferring the data to the main memory of the PC. The data acquisition sample rate is controlled via an on-board 16-bit counter/timer that is also triggered at the beginning of the data acquisition process. Although it is possible to set the gain (1, 10, 100, 1000) on the PC30G, it is always set to 1. It has been discovered that a gain greater than 1 causes problems due to a noisy environment in the PC. The electronic circuit in Schematic A2-4 provided a gain from 1 to 9 that had been used in conjunction with the variable gain of the PC30G. The signal quality was diminished after being amplified in the noisy environment of the PC, and now it becomes clear why the redesign of the gain-setting section on the detector board was necessary, which led to the electronic circuit design in Schematic A2-5. The signal AO1 (see Schematics A2-4 and A2-5) is connected to one of the digital to analogue converters (DAC) of the PC30G that provides a voltage in the range $-5V$ to $+5V$ to adjust the offset as required. Three of the 24 available digital input/output lines of the PC30G are connected to the signals DO4, DO5, and DO6 (see Schematic A2-3) and select, configured as outputs, one of the LEDs on the LED driver board. Similarly, digital outputs of the PC30G are used to encode the gain on the detector board (see Schematics A2-4 and A2-5).

3.6 System Integration

The electronic system of a multianalyser consists of three independent units that form an interconnected structure, which controls the instrument via a specially designed software application (see Chapter 4). Figure 3-14 shows the two units that control the temperature of the thermal module of a tensiograph.

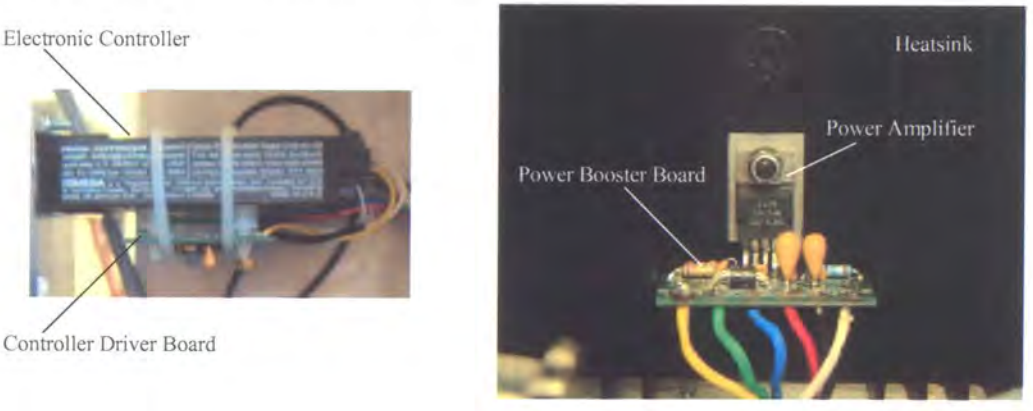

(a) (b)

Figure 3-14. (a) temperature controller unit and (b) Peltier driver unit.

The controller driver board is strapped to the electronic controller and both devices in unit 3-14(a) interchange signals via single core cables. A cable connection between unit 3-14(a) and 3-14(b) provides the communication channel that controls the current through the Peltier devices, which is drawn from the switch mode power supply in the instrument (see Picture A2-2).

The LED driver and detector boards are incorporated in a shielded metal box to protect these sensitive electronic circuits against electromagnetic interference (EMI) and physical damage. This arrangement is displayed in Figure 3-15.

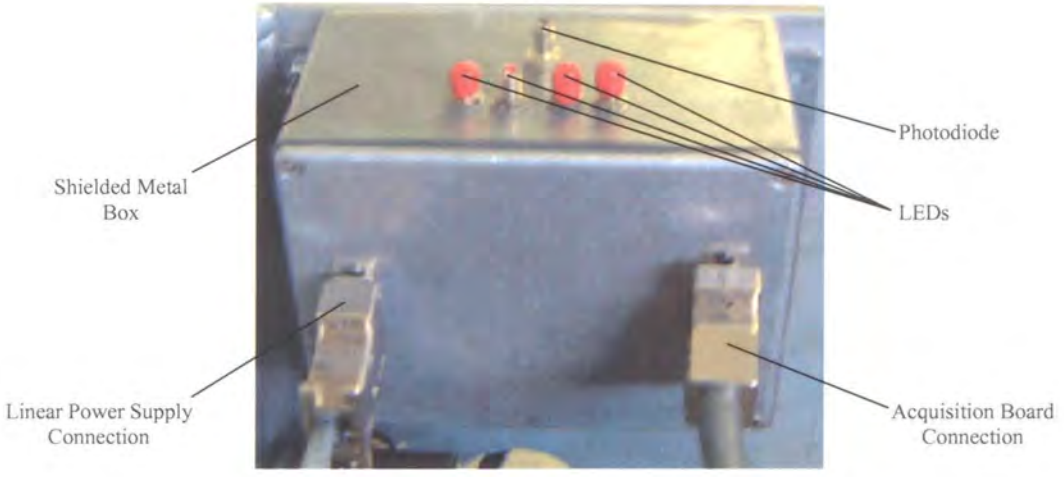

Figure 3-15. Tensiograph source and detector unit.

The encapsulated linear power module (see Picture A2-1) supplies the electronic circuitry inside the box via a shielded cable, and a shielded multi twisted-pair cable transmits the electronic signals between the source and detector unit and the acquisition board in the PC.

CHAPTER 4

SOFTWARE ENGINEERING DEVELOPMENT

Sophisticated diagnostic laboratory instruments, such as the multianalyser in its present state, require in most cases complex software tools that acquire, analyse and administer the vast amount of data that have been generated from measurements. The development of various software packages for the tensiograph was inevitable with respect to data mining, and a considerable amount of time has been invested to produce these software tools to a high-quality standard. The emphasis of the software development was put on the commercial aspect rather than the research perspective of the tensiograph as a laboratory instrument, which means that the software has been designed for flexibility, extensibility, portability, and most importantly for efficiency and reliability. However, researchers in the Carlow laboratory (Ireland) have been using the entire tensiograph software suite (developed by the author and McMillan) for the past few years with great success, which has proven the reliability and effectiveness of these tools for research and the commercial market. Mainly two graphical user interface (GUI) programming toolkits, namely Microsoft Visual Basic and Borland C++ Builder integrated development environments (IDE), have been used throughout the software development cycle to produce the acquisition, analysis and data-scatter software packages for the multianalyser, which will be subject of this chapter. For the discussion of these software packages flow-event-diagrams (FED) are used to explain the fundamental functionality of important modules within a particular software package and, if necessary, pseudocode describes the significantly important program fragments. The complete source code of the entire tensiograph software suite can be found in Appendix 5 for easy reference. Section 4.1 briefly describes important strategies for the development efficiency of modern software applications. A data acquisition package and the associated interfacing aspects will be the subject of Sections 4.2 and 4.3, which explore the signal processing and controlling software issues of the tensiographic instrument. The software package for the data analysis of acquired tensiotraces will be discussed in Section 4.4 leading to a more advanced software tool for data analysis described in Section 4.5. An overview of the system integration is consequently given in Section 4.6.

4.1 Software Design Issues

The most fundamental problem in software development is complexity. There is only one basic way of dealing with complexity, that is, divide and conquer. A problem that can be separated into two sub-problems that can be handled separately is more than half solved by that separation. In particular, the use of a module, or a class, in the design of systems separates the program into two parts – the implementation and its users – connected only by an (ideally) well-defined interface; this is the fundamental approach to handling the inherent complexity of a program [4-1].

One approach that has been made to break down the complexity of the analysis software package of the tensiograph into manageable modules is the use of ActiveX technology. The GUI programming language Visual Basic from Microsoft supports the ActiveX technology programming style and it provides facilities that make it convenient (reasonably easy, safe, and efficient) to use that style. An ActiveX component is a unit of executable code, such as an .exe, .dll, or .ocx file that follows the ActiveX specification for providing objects [4-2]. ActiveX technology allows programmers to assemble these reusable software components into applications and services. In other words, it is possible to create an ActiveX component with the desired functionality that is required in a particular software package, but can also be used in any other software design that needs exactly the same functionality and supports ActiveX technology. An example may clarify this situation. Suppose one creates a GUI software application (a tensiotrace observation tool for example) that provides, besides a variety of other features, the list facility as shown in Figure 4-1, which is used to open, select, remove, and find files of a certain format.

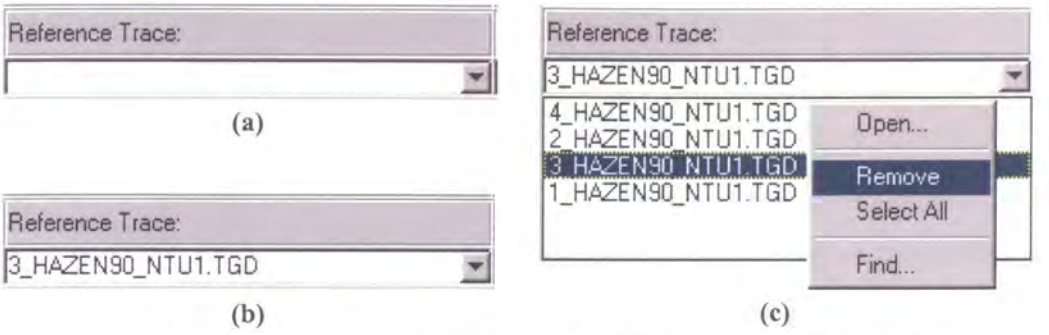

Figure 4-1. (a) List prior file selection, (b) post file selection, and (c) prior file removal.

The list facility was originally designed to provide its service to the application that was developed to solve the problem, here the tensiotrace observation tool, but due to the ActiveX technology it can be linked into an application that displays a text file, for example, when a list entry has been selected. This is illustrated in Figure 4-2. The functionality of the list facility remains the same but the associated application has changed. The list facility could even run without assigning it to any application (this is very useful for module testing purposes) when it has been compiled as an executable (.exe) file. This software development technique supports divide and conquer, and produces reliable and efficient modules by encapsulating data types and functions, that belong together, into a maintainable unit and give access only to a well-defined interface between the user and the ActiveX component. A compilation of ActiveX modules can then be linked together to build a rather complex and relatively large software application, such as the analysis package for the multianalyser (Section 4.4).

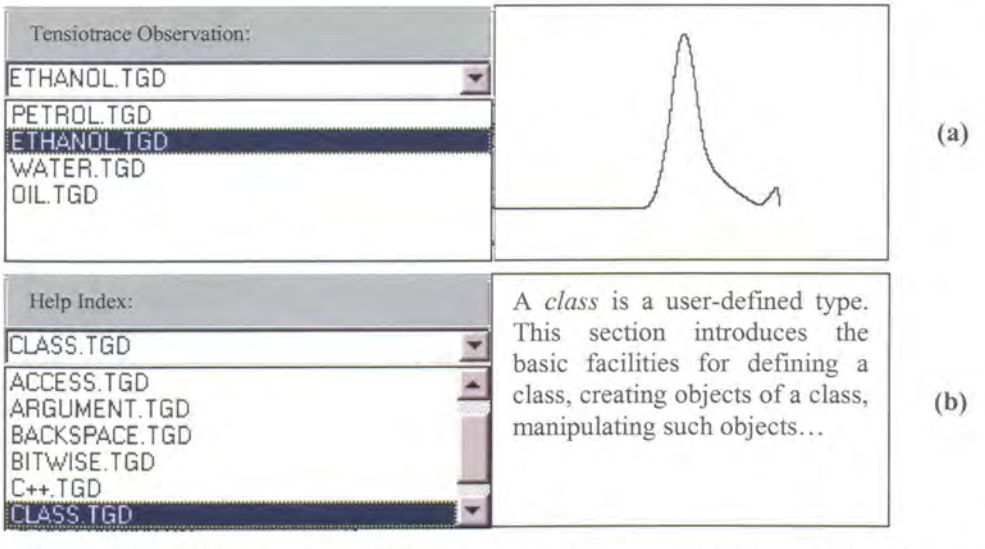

Figure 4-2. Example of two different applications (a) tensiotrace observation, and (b) help file, using exactly the same list-facility.

The programming language in the Visual Basic IDE is BASIC, as the name of the toolkit already implies. This programming language suffers the lack of 'low-level'

features that are standard in languages such as C or assembler, for example. It is possible but extremely inefficient (in the experience of the author) to write software applications in Visual Basic that operate on a 'low-level' basis (for example, the bit shifting operator does not exist), which encouraged the author to choose a more appropriate programming language for the acquisition and data-scatter applications (see Sections 4.2 and 4.5 respectively), where the use of 'low-level' programming is basically unavoidable. The programming language C has been designed to cope perfectly with the 'low-level' aspects and includes all the language constructs that are part of the programming language BASIC. C++ offers the object-oriented programming (OOP) scheme that supports the software engineer to design reliable and efficient modules, which encapsulate the data types and functions (known as methods) that are operating on these data types in a unit that is called a class. The Borland C++ Builder IDE supports also GUI software development and it was therefore decided to use this toolkit instead of the Visual Basic IDE.

The great advantage of OOP is that a user-defined data type (known as the object of a class) can be created, assigned, modified, and destroyed like any other standard data type (for example an INTEGER) used in a program. The following pseudocode example (button on a form) describes these conditions and Figure 4-3 illustrates the pseudocode step-by-step.

```
class button
        private:
                colour, size, caption, ...          //properties of button
        public:
                press, drag, ...                    //functions (methods) for button
end class
program fragment
        button b                                    //create new button (a)
        b → Form1                                   //assign button to a form (b)
        if b.press
                b.size = (x, y)                     //modify button size (c)
        end if
        b.drag(xPosition, yPosition)                //modify button location (d)
        destroy b                                   //button does not exist anymore (e)
end program fragment
```

(a) (b) (c) (d) (e)

Figure 4-3. Illustration of the pseudocode button example, (a) create button, (b) assign button to a form, (c) resize button after it has been pressed, (d) button has been dragged to a different position, (e) button has been destroyed.

OOP is ideal to replace the ActiveX technology programming style, which was formally used in the Visual Basic IDE. It also supports divide and conquer and it is definitely easier and more flexible to use in a program than ActiveX components.

All software packages described in this chapter have been designed to run on the operating system Windows 95/98 from Microsoft. Windows 95/98 distinguishes itself from the historical disk operating system (DOS) in the way that it uses the *event* mechanism, which changes the classical (linear) programming style into event driven programming (EDP). In essence, event driven means that the program does not restrict what the user can do next. For example, in a Windows program, the programmer has no way of knowing the sequence of actions the user will perform next. They may pick a menu item, click a button, or mark some text. So, EDP means that the designer writes code to handle whatever events occur that the user is interested in, rather than writing code that always executes in the same restricted order. The software, which has been produced with the C++ Builder IDE and runs on a Windows operating system, is based on the properties, methods, and events (PME) model. The PME model defines the data members (properties), the functions that operate on the data (methods), and a way to interact with users of the class (events). Properties are characteristics of existing components in the IDE (properties can also be self-designed). It is possible to see and change properties at design time and get immediate feedback as the components react in the IDE. Well-designed properties make the components easier for others to use and easier for the designer to maintain. Methods are functions that are members of a class. Class methods can access all the *public*, *protected* and *private* properties and data members of the class and are commonly referred to as member functions.

Consider Figure 4-4 for the explanation of the nomenclature of the FED used throughout this chapter.

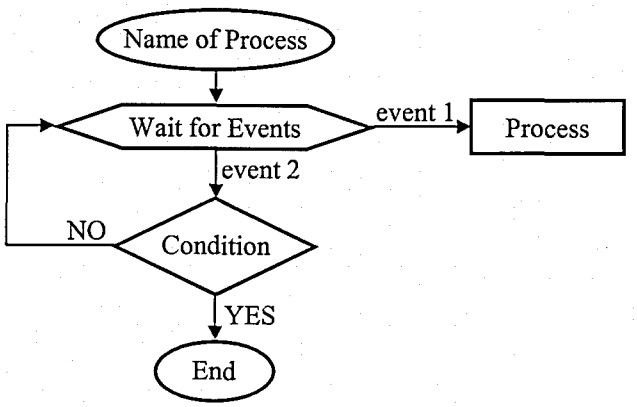

Figure 4-4. Flow-event-diagram.

An elliptical shape introduces the process for which the FED is displayed, or labels the end of this process. The event-queue of the Windows operating system is represented in a hexagonal shape. Every single event (for example timer-event, mouse-move, program-start, keyboard-activity) that a user triggers on the PC is transmitted to the event-queue and ordered by priority of the events (for example timer-event has higher priority than mouse-move). The next event in the queue (if available) is then processed, but only events associated with the tensiograph application software 'fire' and consequently switch to another state in the FED, which is symbolised by an arrow. A process that needs to be expanded into an FED is represented as a rectangle, and the rhomboid shape implies that the user or the program has to make a decision at this point in the program flow. Events are always in lower case (here: event 1, event 2), decisions in upper case (here: YES, NO), and the rest starts with a capital letter (here: Process, Condition, End...).

4.2 Acquisition Package

Figure 4-5 shows the main FED of the acquisition software package that is used to acquire the electronic data of a tensiotrace (light signal converted into a voltage and then digitised).

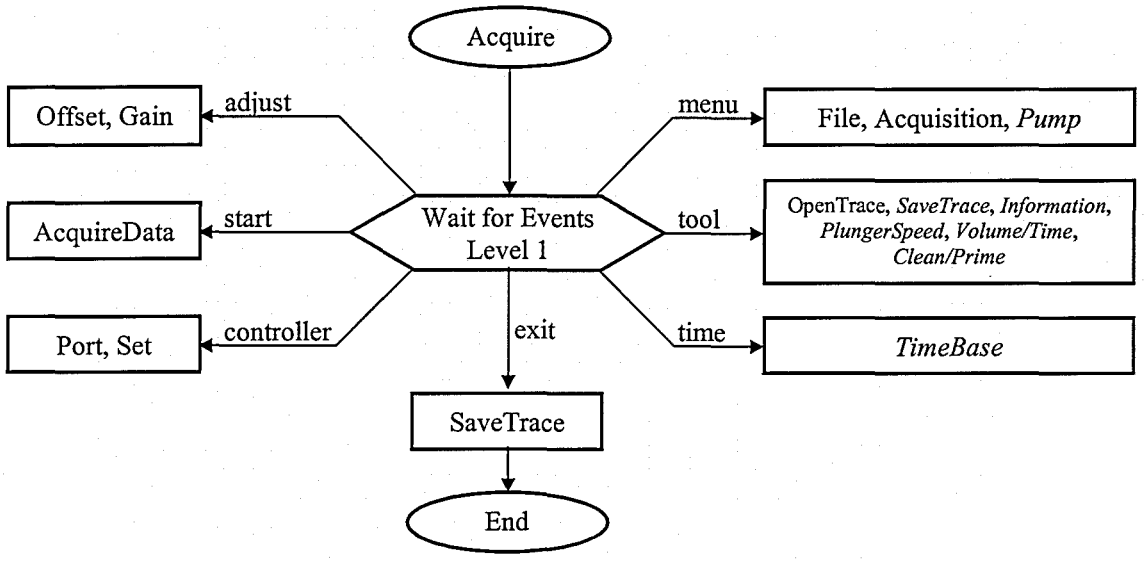

Figure 4-5. Main FED of the data acquisition software package (Acquire).

After the application Acquire has been started, which the Windows operating system classifies as a process, this 'Acquire'-process waits for an event to occur. The user may decide to end the running process immediately by triggering the 'exit'-event, which switches to the 'SaveTrace'-process (see below in this section), and since no data has been acquired yet, the 'End'-process is called and the program is terminated. The 'End'-process is a function of the operating system. It is responsible for clearing up, which means for example that allocated memory is freed again and the event-queue reorganised. However, it is more likely that the user triggers an event that does not exit the program directly after the 'Acquire'-process was started.

The 'menu'-event activates one of the processes 'File', 'Acquisition' or '*Pump*', depending on which menu item has been selected. The FEDs in Figure 4-6 illustrate these conditions. Note the italic font in '*Pump*'-process in Figure 4-5. This is, because this process might not be accessible in some situations due to specific program conditions, e.g., there is no need for pump accessibility when the constant head facility is used. Also '*Save*', '*Information*', '*PlungerSpeed*', '*Volume/Time*', '*Clean/Prime*', and '*TimeBase*' specify a similar behaviour.

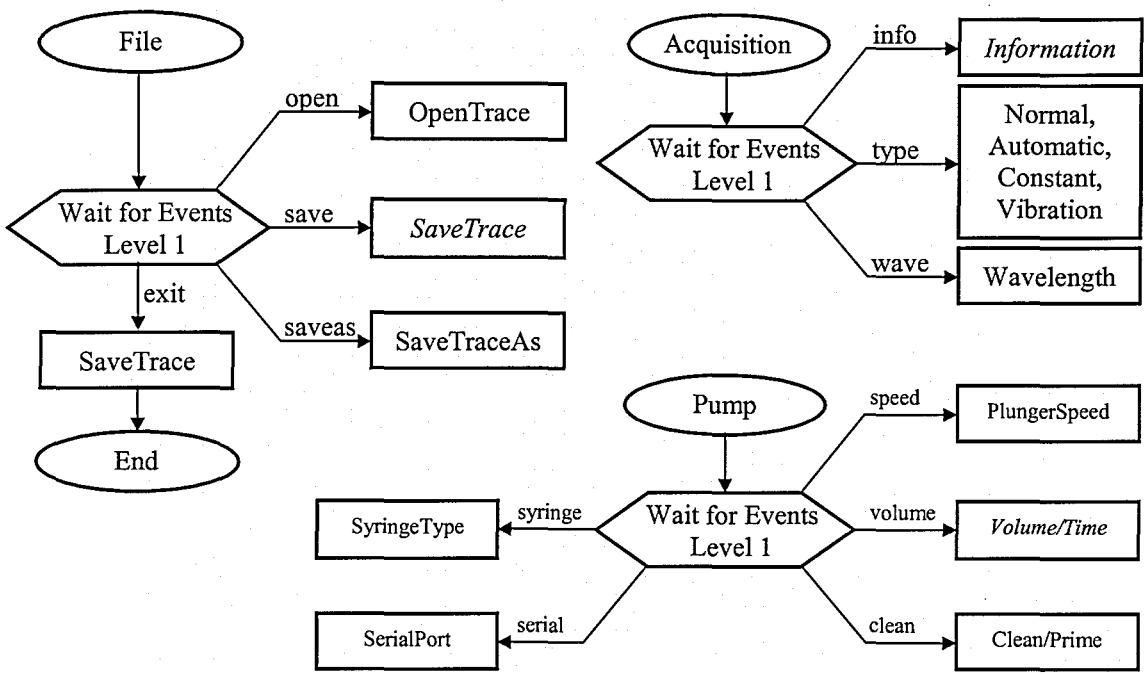

Figure 4-6. FEDs of the 'menu'-event ('File', 'Acquisition', and 'Pump'-process).

All the processes 'File', 'Acquisition', and 'Pump' display separate menus on the screen (a user may choose an item from a menu that has to be processed) and returns to the 'Wait for Events'-state. Note that events occurring at this point refer to Level 1 and it is possible to trigger an event that does not belong to the processes 'File', 'Acquisition', and 'Pump', but share the same event level (in this case Level 1). There are different event levels in the Acquire application, as shown below in this section, and only events specified for the associated event level can be triggered at this particular point of the program flow.

After triggering the 'open'-event (user chose Open on the menu) the 'OpenTrace'-process is started, see Figure 4-7.

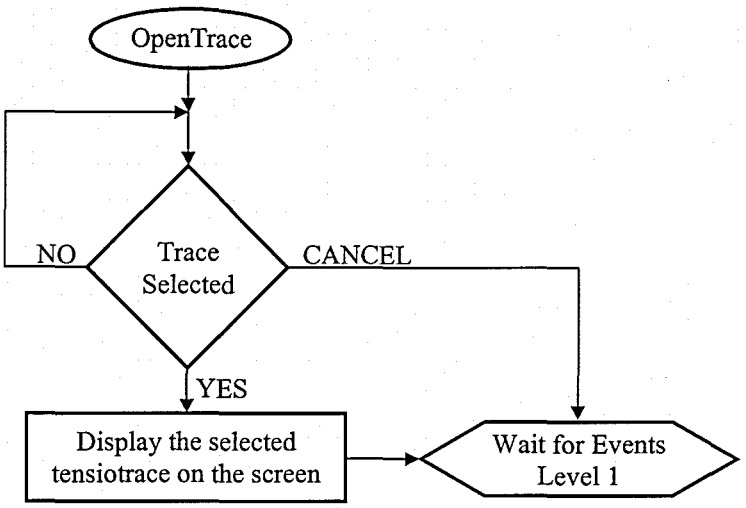

Figure 4-7. FED of the 'OpenTrace'-process.

The 'OpenTrace'-process opens a new window in modal mode on the screen (when a window runs modally, the user must explicitly close it before working in another running window), which means that no events can be triggered until this window has been closed again, i.e. YES or CANCEL decision in Figure 4-7. The trace that has been selected in the window of the 'OpenTrace'-process is then displayed on the canvas in the main window of the Acquire application. This enables the user to review tensiotraces that have been acquired and saved in previous experiments.

Figure 4-8 illustrates the procedure of the 'save'- or 'saveas'-event.

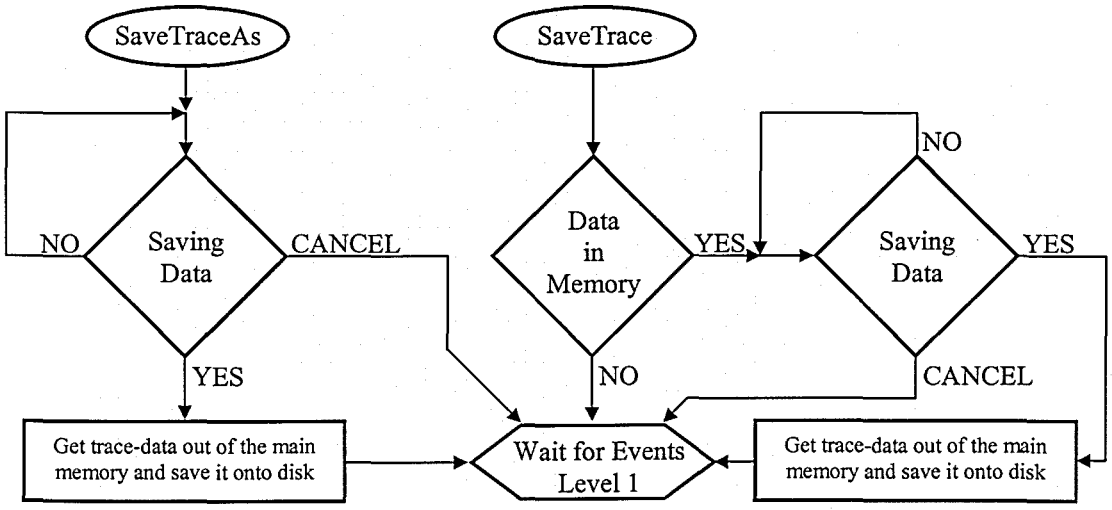

Figure 4-8. FEDs of the 'SaveTraceAs'- and 'SaveTrace'-processes.

Two different data-saving methods assure that the user can save the acquired tensiotrace data at any time and under alternative names for the same trace (SaveTraceAs), and also reminds the user of data that has not been saved yet (SaveTrace), which is important to prevent data loss before the termination of the application (see Figures 4-5 and 4-6).

The information on tensiotraces, including DP, RPP, and various other useful values can be viewed in a separate window that appears in modal mode when the 'info'-event is triggered, see Figure 4-9.

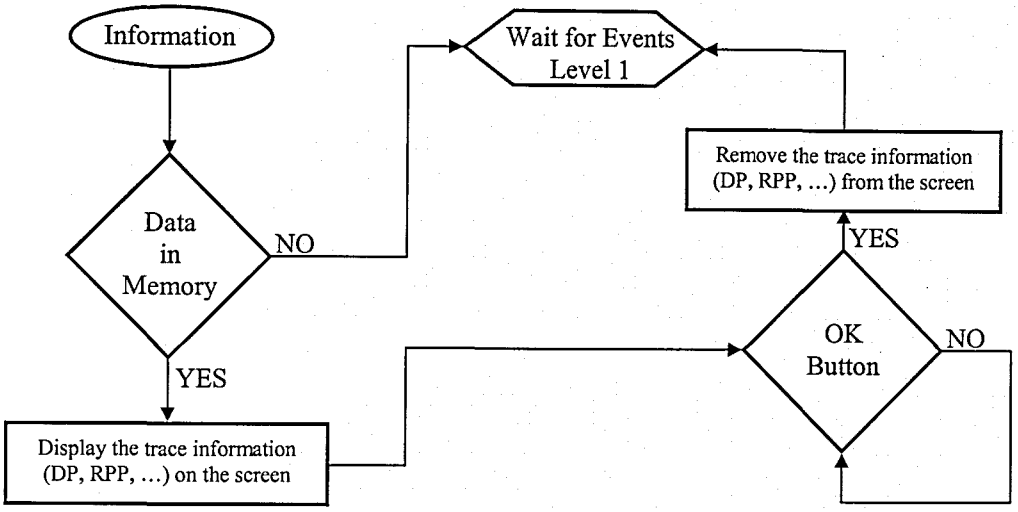

Figure 4-9. FED of the 'Information'-process.

If the 'info'-event is triggered without any information available then this event is ignored and the application returns to the waiting-state. Conversely, information is represented if tensiotrace data has been acquired. The tensiotrace information is usually used for a quick reference and analysis of the data, whereas the Analyse software package (see Section 4.4) is used for a detailed analysis of the tensiotrace data.

Acquiring the data of a tensiotrace can be done in four different modes (Normal, Automatic, Constant, Vibration) and with a variety of LEDs (wavelengths 470, 530, 660, 950*nm*). Figure 4-10 shows the arrangement of these selection-type FEDs.

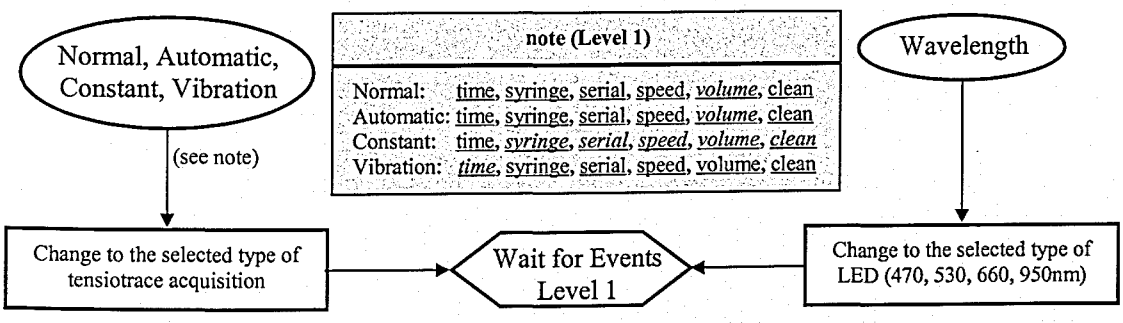

Figure 4-10. FEDs of the acquisition-type and 'Wavelength'-processes.

In Normal mode the instrument uses a pump as the liquid delivery system and the data of a single tensiotrace is acquired after starting the data acquisition. The user has to manually save or discard the acquired data and start another acquisition process after the instrument has finished the previous measurement. This procedure is extremely tedious and time consuming when many samples of the same liquid have to be acquired (the user is required to periodically restart the acquisition process). Driving the tensiograph

in Automatic mode, on the other hand, requires the attention of the operator only at the beginning of a series of measurements, i.e. selecting the desired number of tensiotraces and starting the data acquisition. The acquisition software of the tensiograph automatically acquires, saves, and restarts measurements until the preset number of tensiotraces has been reached and subsequently stops the data acquisition process. In Constant mode a constant head liquid delivery is required, as all pump activities have been cancelled, which is sometimes convenient to avoid pump vibrations. The Vibration mode offers features that support drop vibration measurements (higher sample rate and drop volume variation facility). It has to be noted here that varying the acquisition mode toggles assorted event responses of the program. This is indicated by the underlined events (note in Figure 4-10), and events displayed in italic font cannot be triggered until another program condition activates these events again (normal font).

The plunger speed of the pump and the volume or time settings of the liquid delivery to the pendant drop can be varied as illustrated in Figure 4-11.

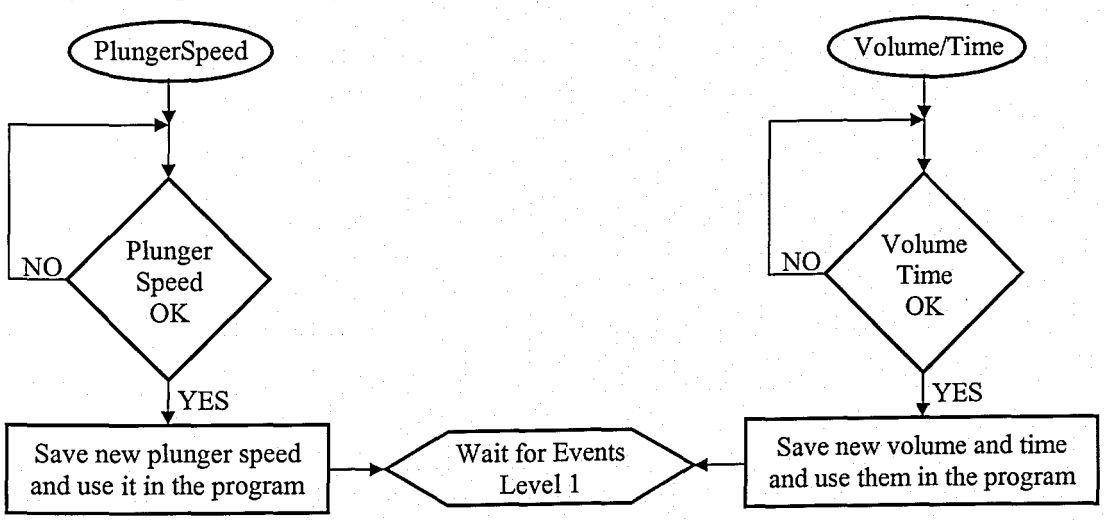

Figure 4-11. FEDs of the 'PlungerSpeed'- and 'Volume/Time'-processes.

Some experimental measurements with the multianalyser require the pump to stop the liquid delivery to the pendant drop after a defined volume has been pumped to the drophead, or a specific liquid delivery time has elapsed. Vibrating a pendant drop of a certain volume for surface tension and viscosity studies is one example for the usefulness of the volume/time adjustment feature. The investigation of drop evaporation (fully explored in Chapter 6) could not have been carried out without this facility.

It is important to provide the functionality to control the cleaning and priming of the drophead and tubing of the liquid delivery system respectively. Such functionality is employed in the acquisition software and Figure 4-12 shows this concept.

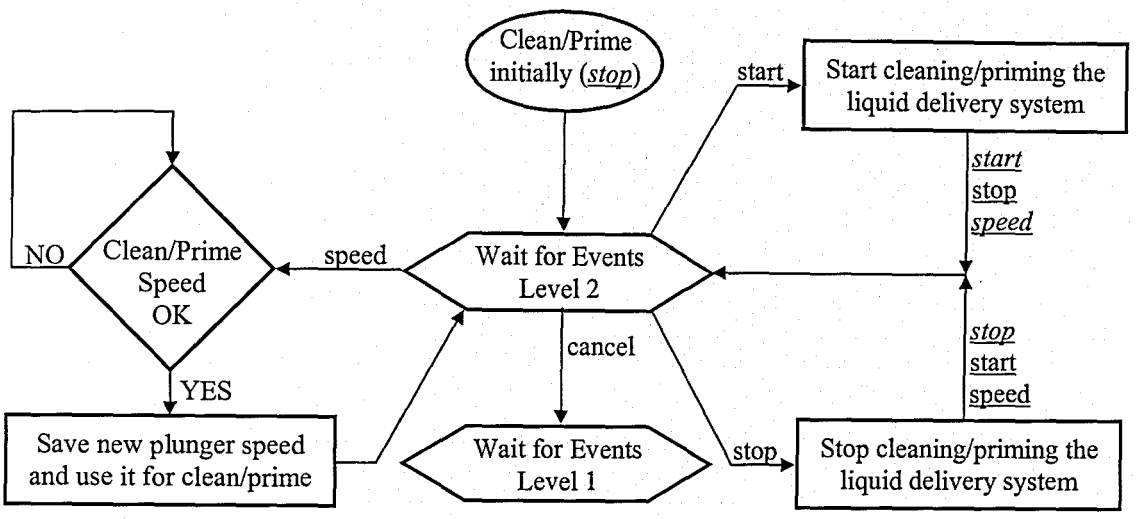

Figure 4-12. FED of the 'Clean/Prime'-process.

The main waiting task (Wait for Events) of the Clean/Prime window (opened in modal mode) is now on Level 2, which implies that the events of Level 1 cannot be triggered at this point of the program execution. Conversely, events of the special Level 0 (all events that are not associated with the application Acquire) can always be triggered. This means, the user of the tensiograph software package may start and work with as many different applications as desired on the same PC, without affecting the running application Acquire. Whenever the 'Clean/Prime'-process is started, the 'stop'-event is initially deactivated and only the 'start'- and 'speed'-events are active.

The syringe size has to be changed in the software when a different sized syringe has been fitted to the pump, in order to maintain consistency during the measurements related to volume or time variations, e.g. vibration and evaporation experiments. The 'SyringeType'-process gives the user the opportunity to adjust the syringe size (software) after a different sized syringe has been fitted (hardware). A standard PC generally incorporates two serial RS-232 ports (COM1 and COM2) [4-3]. The tensiograph occupies both of these serial ports, used for the pump and temperature controller, and sometimes it is necessary to provide a third RS-232 port to connect more devices that need this facility, e.g. a mouse designed for RS-232 connection. In this case the existing RS-232 ports have to be accompanied by an RS-232 expansion board that provides two more serial connections (COM3, COM4). It is not recommended to operate a PC with more than four RS-232 ports, as this usually causes conflicts between these RS232 devices. The tensiograph software is designed to control four RS-232 ports independently. Figure 4-13 shows the mechanisms to change the syringe size, RS-232 connections, and the time base of the sampled data.

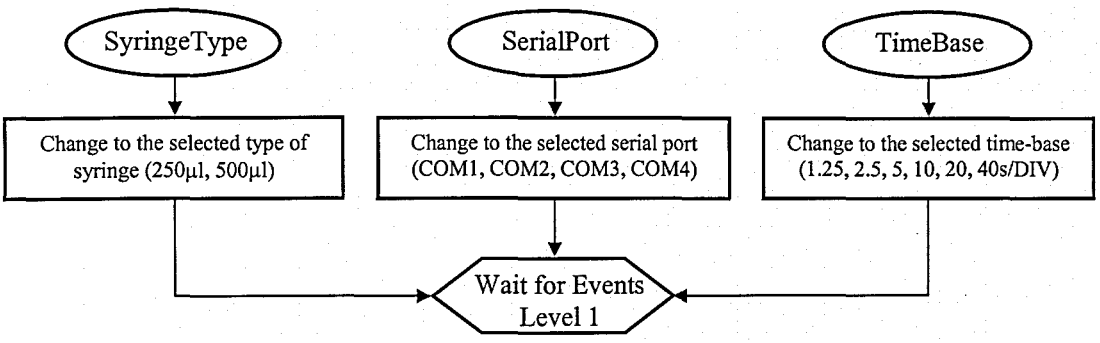

Figure 4-13. FEDs of the 'SyringeType'-, 'SerialPort'- and 'TimeBase'-processes.

The pump can be controlled from any of the four possible existing RS-232 ports and the user of the tensiograph selects the appropriate serial connection (COM1 to COM4) in the Acquire software package. The speed with which the plunger of the pump pushes the liquid to the drophead may be altered via software control, as mentioned above. Following a plunger speed change, the time base of the acquired data has to be adjusted in order to sample the detected signal efficiently and to display the tensiotrace correctly and in an unclipped manner on the screen of the PC (see Section 4.6 for more information).

The most important issue of the Acquire software package is its 'AcquireData'-process that provides the main functionality of this software package, which is illustrated in the FED of Figure 4-14. Note the event level (Level 3) of this process that allows only the specified events (adjust, stop, controller, and dma) to trigger the associated sub-processes.

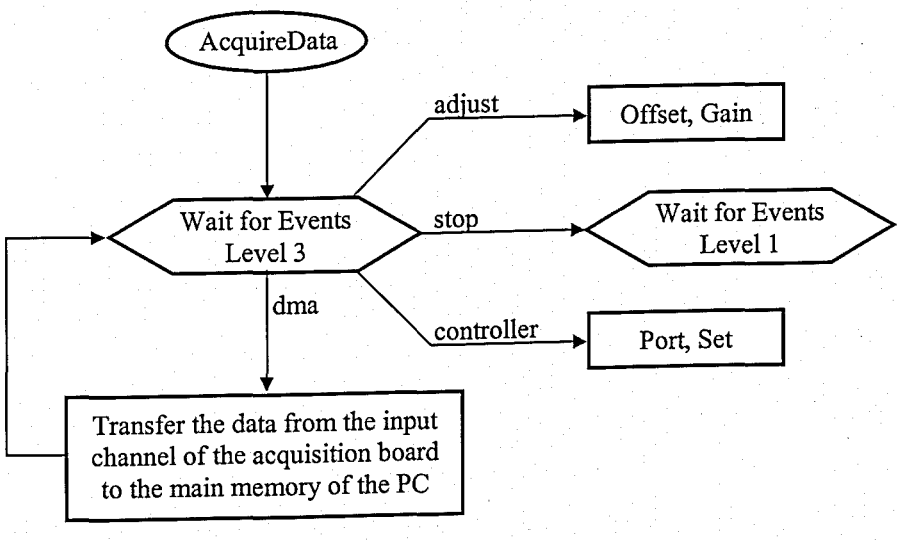

Figure 4-14. FED of the 'AcquireData'-process.

The following pseudocode of the program fragment explains the 'AcquireData'-process in more detail (excluding the 'adjust'- and 'controller'-event).

The software development kit (SDK) functions ADInBinBackground, CTWrite, BackgroundADInStatus, and StopBackgroundADIn of the application programming interface (API) of the PC30G will be discussed in Section 4.3.

```
class TStorage          //provides functionality for saving acquired data
 private:
   p[array-size] ...    //allocate main memory for data storage
 public:
   Add, Erase ...       //member functions to organise the allocated memory p[]
end TStorage

class TBoard            //provides functionality for the acquisition board PC30G
 private:
   Initialise Board ... //initialises the PC30G board upon creation of an object
 public:                //API-functions of the SDK for the PC30G
   ADInBinBackground, CTWrite, StopBackgroundADIn,
   BackgroundADInStatus ...
end TBoard

AcquireData
 b TBoard, s TStorage              //create the objects b and s
 s.Erase                           //clear the main memory allocated by p[]
 b.CTWrite(sample-rate)            //initialise counter/timer on the board
 b.ADInBinBackground               //start sampling the data in DMA-mode
 repeat
   check for events                //Level 0 and Level 3
   if BackgroundADInStatus(d)      //ensures that new data is available
     s.Add(d)                      //store data in buffer p[]
     canvas(d)                     //display data on canvas of main window
   end if
 until 'stop'-event occurs         //stop button, drop separated, p[] full
 b.StopBackgroundADIn              //stop the DMA data sampling
end AcquireData
```

The API provides the interface between the hardware of the acquisition board PC30G and the application software package Acquire. The 'AcquireData'-process passes the

control over to SDK functions and these functions handle the data acquisition process in the background, which means that currently running processes are not interrupted or new processes can be started without noticeable performance loss, e.g., the user can start a data acquisition process Acquire and analyse the acquired data with the analysis software tool Analyse (see Section 4.4) at the same time. This is only possible due to the capability of the SDK function ADInBinBackground to acquire the data in the background. Without the background feature, the 'AcquireData'-process would 'freeze' the user interface of the PC until the 'AcquireData'-process has completed its task, which could take up to several minutes. At this point it is time to answer the question raised in Section 3.3, why it is necessary to generate an expanded pulse width t_{int} as shown in Figure 3-9(b). Remember that this signal is generated from a falling drop intercepting the light beam of a slotted opto-switch, see Figure 3-8. For further explanations consider the pseudocode that is shown above. The code segment between the *repeat* and *until* statements is responsible for acquiring and displaying data during a tensiographic measurement of the multianalyser. The time that the SDK function BackgroundADInStatus requires to return from its task depends on the time that the PC30G needs to update internal register settings, i.e. the registers associated with the input channels CH0 and CH1 of the PC30G, and sometimes it has been the case that this time exceeded the pulse width $t_{int} \approx 1ms$. Whenever a falling drop intercepts the light beam of the slotted opto-switch just after updating the internal registers of the PC30G, but the time to return from the SDK function BackgroundADInStatus exceeds $t_{int} \approx 1ms$, then the interception signal would be lost and the occurrence of drop separation would consequently be missed, using the pulse width t_{int} as shown in Figure 3-9(a). Conversely, using the pulse width $t_{int} \approx 22ms$, as shown in Figure 3-9(b), ensures that the drop interception signal is still present when the program flow returns to the SDK function BackgroundADInStatus, which then reads the values of the updated registers, associated with the input channels CH0 and CH1 of the PC30G and therefore senses that drop separation has occurred.

Changing the offset and the gain uses also SDK functions to communicate with the analogue and digital output channels of the PC30G, but it is unnecessary to do this in the background, because these processes take only microseconds to complete their tasks. Figure 4-15 shows the 'Offset'- and 'Gain'-processes.

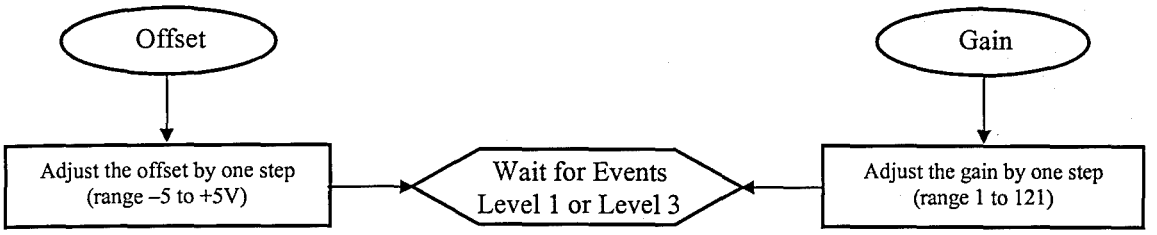

Figure 4-15. FEDs of the 'Offset'- and 'Gain'-processes (Level is the origin of 'adjust'-event).

Note that one step of the offset adjustment is determined by $10V/4096 \approx 2.44mV$ (see Section 3.5) and one step of the gain adjustment is determined by $A/steps \approx 1.47E\text{-}2$ (see Eqs. (3-4) and (3-5)). The SDK function DAOutVoltage has been used in conjunction with the 'Offset'-process to control one of the analogue output channels of the PC30G. Similarly, the 'gain'-process employs DIOPortOutput to adjust the gain of the detector circuit according to the software settings.

The temperature controller is also controlled via software, using one of the RS-232 ports as a communication channel between the user interface of the software and the electronic controller CNi3252-C24-DC from Omega. A communication protocol has been defined by Omega, in order to send/read data to/from the controller. The software interface (see Appendix 5) for this electronic controller converts then the encoded data into values that can be used for the display and control of the temperature in the thermal module of the multianalyser. Figure 4-16 illustrates the arrangement of the temperature controller software interface.

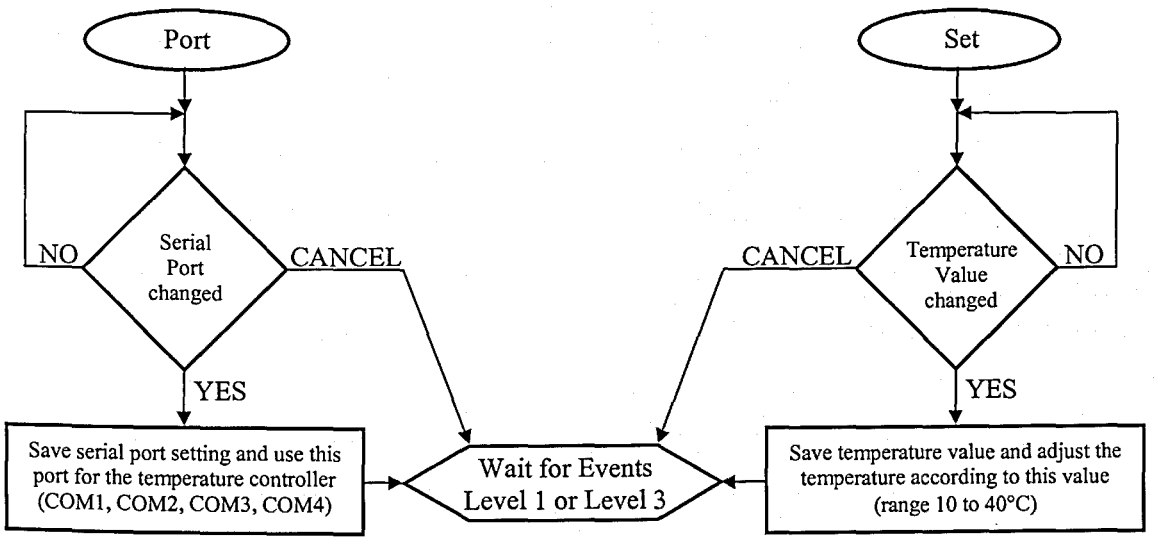

Figure 4-16. FEDs of the 'Port'- and 'Set'-processes (Level is the origin of 'controller'-event).

The 'Port'-process offers a similar functionality as the 'SerialPort'-process with the exception that the 'Port'-process opens a window in modal mode so that no other events can be triggered until the window has been closed, i.e. YES, CANCEL decisions, and supports also Level 3 events. The temperature of the thermal module has to be adjusted

in an additional modal window that opens when the 'Set'-process is started due to the 'controller'-event. The temperature controller will be more fully explored in Chapter 6.

4.3 Acquisition Board Interfacing

The API functions of the SDK of the acquisition board PC30G insulate the software designer from the actual hardware details of the PC30G. This makes it easier to write applications and to change acquisition boards as new models are released. The SDK is supplied with the PC30G and is also available for download on the web site from Eagle Technology (http://www.eagle.co.za). Extensive analogue to digital (A/D), digital to analogue (D/A), digital input/output (DIO), DMA, and configuration functions are provided, but only a subset has been employed in the acquisition software package Acquire.

All SDK functions require a board handle as their first parameter. Board handles are integers obtained by calling AllocBoardHandle. Once allocated the board handle must be initialised to the PC30G before it can be accessed. This is done by calling InitBoardType, which links the board handle to the PC30G and fills in configuration information for it. The board handle can now be used to access the PC30G using the SDK functions. It is important to release the board handle using FreeBoardHandle before the program terminates. Any board handles not released when the program terminates will cause a conflict the next time AllocBoardHandle is called (start of the Acquire software) and it will be necessary to reboot the PC.

The two input channels CH0 and CH1 of the PC30G are assigned respectively to the output terminals AI1 and AI2 of the tensiograph. Channel CH0 is monitoring the generated signal of the detector circuit and channel CH1 is connected to the optical switch in order to sense a drop separation. The SDK function ADInBinBackground initially starts the background data acquisition and acquires blocks of A/D data from the two channels in use (CH0, CH1). This SDK function uses the current sampling frequency, allocated memory, and transfer mode. The sampling frequency is determined by the on-board counter/timer of the PC30G and can be set using the SDK function CTWrite, which writes the specified value to the counter/timer. The required memory is represented by an array of the standard data type INTEGER and allocated before ADInBinBackground is called. The transfer mode has been set to DMA, which is an

extremely efficient way to sample data. It requires very little work on the part of the central processing unit (CPU) of the PC. The DMA controller of the PC is programmed to transfer the data blocks from the PC30G to the allocated memory without going through the CPU of the PC. During the process of transferring data blocks, the SDK function BackgroundADInStatus needs to be called periodically to check if the transfer of a data block has finished. As soon as a new data block is available it needs to be separated into the signals from the channels CH0 and CH1. The interpretation of the signal from channel CH1 (sensing drop separation) then decides whether to proceed with the data acquisition or to stop this process (drop separation occurred). The data acquired through channel CH0 is displayed on the screen and stored in memory for later analysis. When the data acquisition process has completed or if it has to be stopped early the SDK function StopBackgroundADIn must be called.

The SDK function DAOutVoltage sets the voltage on the D/A channel DAC0 of the PC30G using a microvolt value. DAC0 is connected to the input terminal AO1 of the detector circuit in the tensiograph and consequently determines the offset of the detected signal. Similarly, the SDK function DIOPortOutput is used to write bytes of data to the DIO ports A, B, and C of the PC30G adjusting the gain and selecting an LED. The least-significant-bit (LSB) of port A determines the direction (up/down) of the digitally controlled potentiometer AD5220, whereas the LSB of port C is used to clock the wiper of the AD5220 up or down (see Schematic A2-5). DO4, DO5, and DO6 of the LED source circuit (see Schematic A2-3) are connected to three lines of the DIO port B and an encoded byte signal on this port selects the LED that has been chosen on the menu in the Acquire software.

4.4 Analysis Package

The data analysis of the tensiotraces, which have been acquired with the Acquire software package, requires a comprehensive software tool that generates rapidly the results of the analysing process. An enormous amount of information related to the tensiotraces has to be presented in an adequate format, so that a user of the analysis software does not get confused. It is also important that the operator of the analysis software tool can choose the appropriate method to examine the results on the screen of a PC, and to focus on properties in a tensiotrace that are of relevance to a particular

application. To clarify this statement envisage the QC process in the brewing industry, where the operator of the analysis software tool is concerned about the comparison of two beers of the same kind from different batches, for example. Considering the first part of the statement above, a graphically displayed result of the comparison of two tensiotraces (representing the two beers) is the most suitable technique for rapid fingerprinting hiding the rather confusing numerical representation of the data analysis. Conversely, the study of the quantitative measurands is inevitable for a rigorous inspection of the differences between the two beers. The second part of the statement suggests that various match criteria of the tensiotrace comparison can be relaxed or strengthened, which means that a user is allowed to adjust M-Values (weighting or disabling match criteria) in order to concentrate on the tensiotrace properties that are of more importance to a particular measurement. For example, a user may only want to compare the two peaks RPH and TPH of the two tensiotraces, which can be done by switching off all remaining match criteria in the analysis software (see Section 4.6 for more information). Such a software tool has been developed as one part of the research programme to provide the functionality discussed above. This analysis software package is the subject of this section and it will be referred to as Analyse.

The description of Analyse is similar to that of Acquire following the same concept, which means that the entire software package is divided into FEDs representing processes that are triggered by the use of events. The main FED of the tensiotrace analysis software is shown in Figure 4-17.

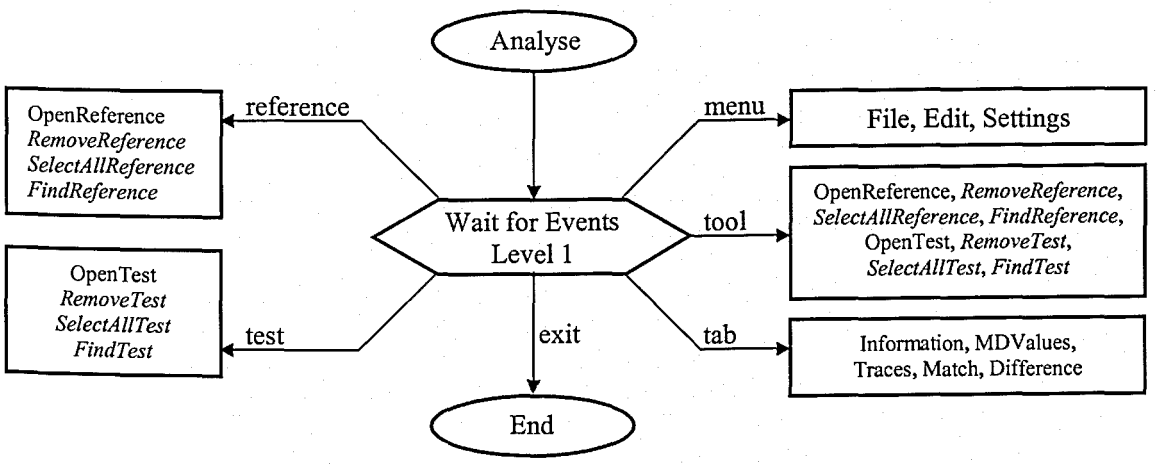

Figure 4-17. Main FED of the tensiotrace analysis software package (Analyse).

Analyse has been developed under control of the Visual Basic IDE and although the programming language and conceptual use of modules (ActiveX instead of classes) differ from those of the C++ Builder IDE, it is essential to understand that the Windows-based PME model remains exactly the same.

Figure 4-18 illustrates the 'menu'-event as an FED that simply corresponds to the display of one of the menus File, Settings, or Edit on the screen of the PC.

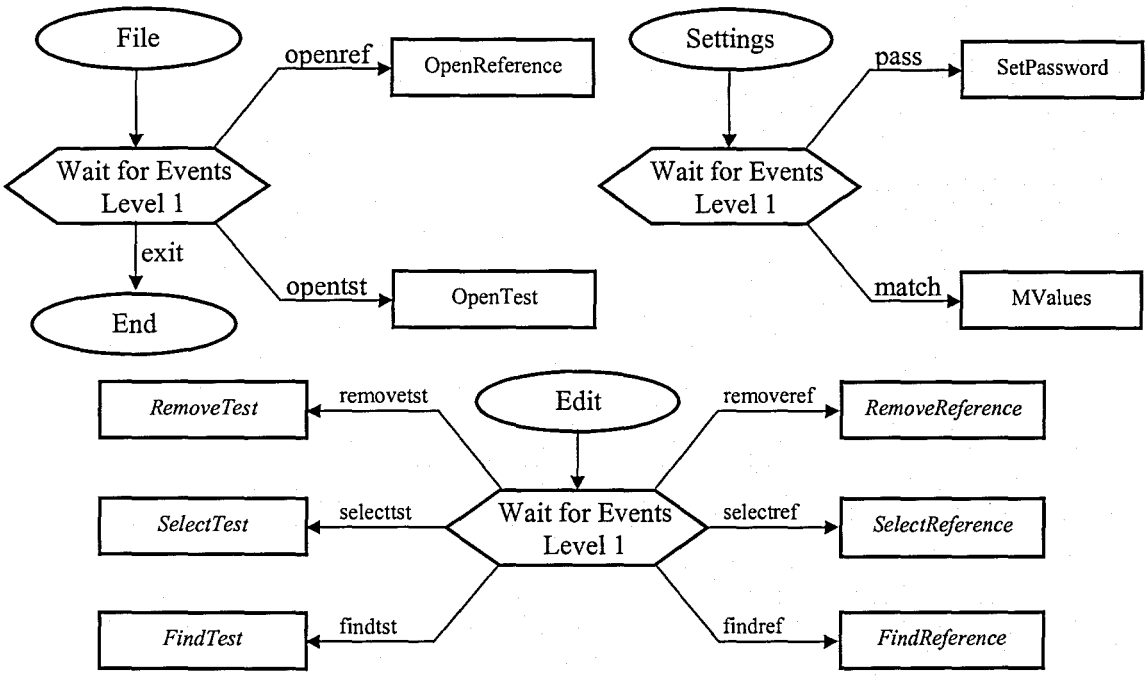

Figure 4-18. FEDs of the 'menu'-event ('File', 'Settings', and 'Edit'-process).

Note the similarity between the 'openref'-event and 'opentst'-event (both events trigger a process that opens a tensiotrace file (.TGD) in Analyse), which implies that one of the events in the 'File'-process might be redundant. This implication can be rejected and the reason for using two separate processes ('OpenReference' and 'OpenTest') is the fact that reference and test tensiotraces are strictly held in two independent lists for easy access and maintainability. To make this abundantly clear in the software design the representation of the FED in Figure 4-18 has been chosen. The same applies for the 'Edit'-process, where again the reference and test traces are processed individually.

The FEDs in Figure 4-19 underpin the separation of the 'OpenReference'- and 'OpenTest'-processes.

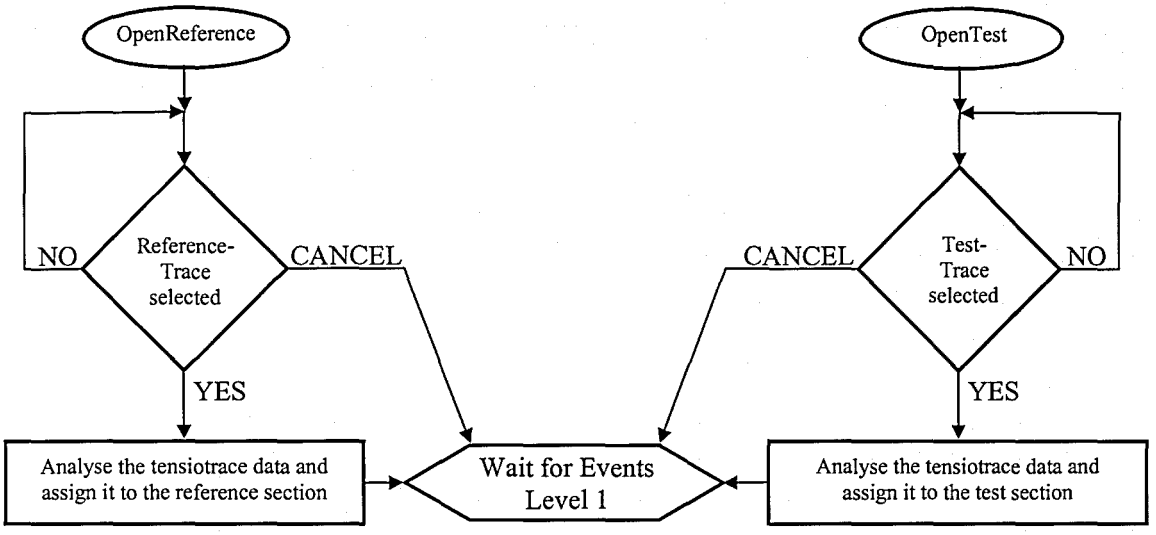

Figure 4-19. FEDs of the 'OpenReference'- and 'OpenTest'-processes.

At this point of the program execution, the data of the tensiotraces are assigned to table modules, which are always referenced to the calling process (OpenReference or OpenTest). Section 4.6 will clarify this situation. The data in the table modules can then be accessed through a well-defined interface using an index mechanism that makes it simple to carry out computations with any combination of the data in these table modules. Applying the ActiveX technology, by keeping the data and their associated functions in one module, ensures that the process of assigning the analysed data to the right section (reference or test) is done efficiently and without inconsistencies. This is not an easy task in any way using the classical procedural programming approach, where data and functions that belong together are usually torn apart and basically distributed over several modules.

The FED in Figure 4-20 illustrates the M-Values scheme, which will be more fully explored in Section 4.6. However, at this point of the discussion it is important to notice that the M-Values setting mechanism is password protected.

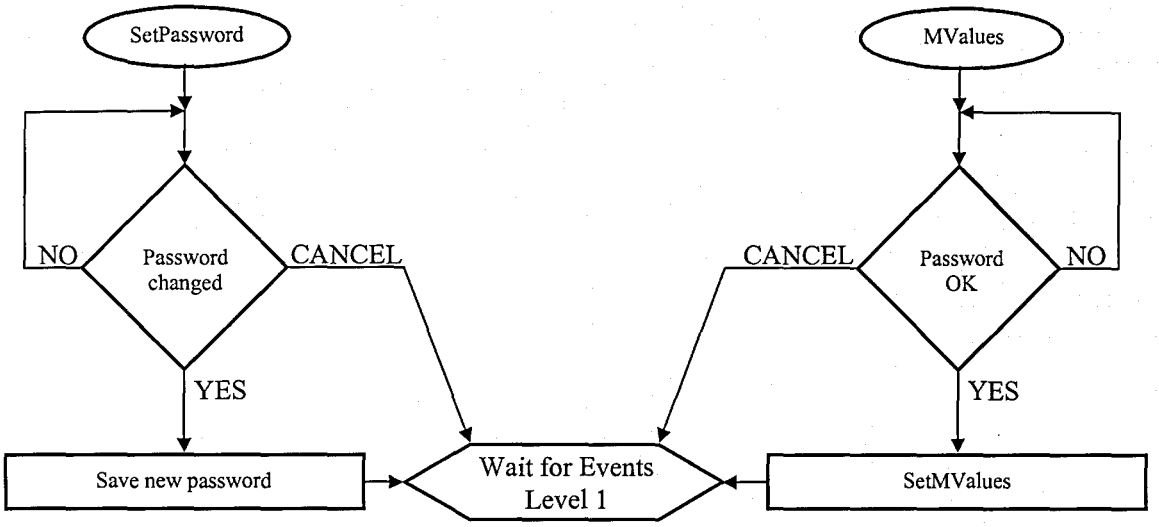

Figure 4-20. FEDs of the 'SetPassword'- and 'MValues'-processes.

When the 'match'-event triggers the 'MValues'-process, the user is about to modify the match criteria of the comparison of two tensiotraces as described earlier in this section. This has almost always a vital impact on the outcome of the tensiotrace analysis and only authorised personnel should have permission to change the M-Values. The 'SetPassword'-process enables the user of the Analyse package to change the password, which should be done on a regular basis to protect the M-Value settings from misuse.

It has been mentioned above that the quickest way of comparing tensiotraces, in a QC laboratory, for instance, is the graphical representation of the data analysis. The software package Analyse provides two graphical displays that present the results of the analysis, which is suitable for rapid QC. These two processes (Match and Difference) and the additional 'Information'-process are illustrated in Figure 4-21.

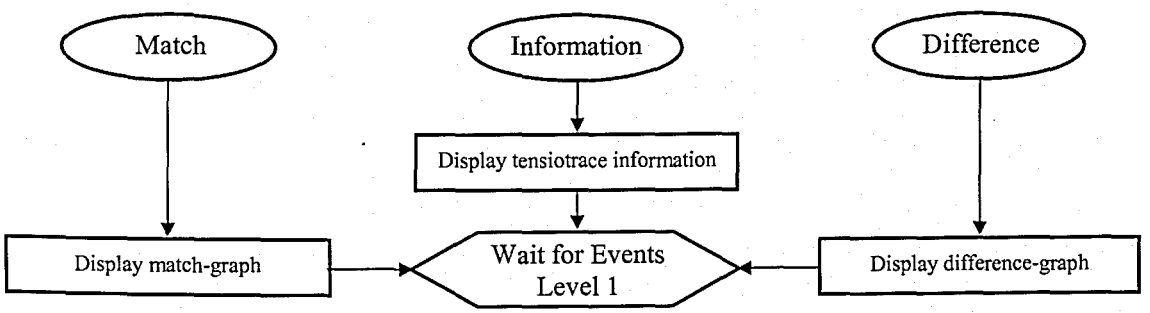

Figure 4-21. FEDs of the 'Match'- 'Information'- and 'Difference'-processes.

The display of the match and difference graphs represents eleven characteristics of the tensiotrace comparison in a bar chart. For a close match of two tensiotraces the bars of the match-graph are almost totally extended and close to the 100% mark, and the bars of the difference-graph on the other hand are close to the 0% mark. This is exactly the other way round when the two traces are completely different. The 'Information'-process obtains characteristic values of a single tensiotrace (stored as header

information in the tensiotrace files (.TGD) that have been acquired with the software package Acquire) and displays this information in the assigned table modules, as demonstrated in Section 4.6.

The numerical values of the match and difference graphs are displayed on a separate form that provides the user with the data for a rigorous tensiotrace analysis. For the visualisation of the tensiotraces under test the 'Trace'-process can be triggered, which displays the profile of these traces on the screen. This is important when a user is interested in the exact location of major differences between the two tensiotraces. Figure 4-22 illustrates the two FEDs of the 'MDValue'-process and the 'Traces'-process.

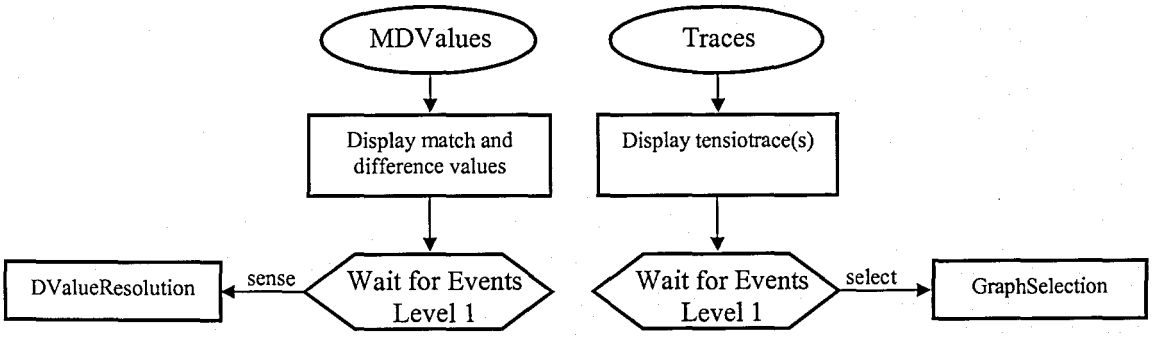

Figure 4-22. FEDs of the 'MDValues'- and 'Traces'-processes.

Note that the two events 'sense' and 'select' can only be triggered when either the 'MDValue'-process ('sense'-event active) or the 'Traces'-process ('select'-event active) has been called. These two processes use different windows to display their data and the 'DValueResolution'-module resides in the 'MDValues'-window, whereas the 'GraphSelection'-module is located in the 'Traces'-window.

Increasing the resolution of the graphically displayed differences between two tensiotraces ensures that even the smallest differences are visualised. This is shown in an example in Section 4.6. The profiles of tensiotraces can be displayed on the screen either separately (reference trace on its own, or test trace on its own) or as an overplot of both traces to locate possible differences between the two traces easily. Figure 4-23 shows the FEDs of this arrangement.

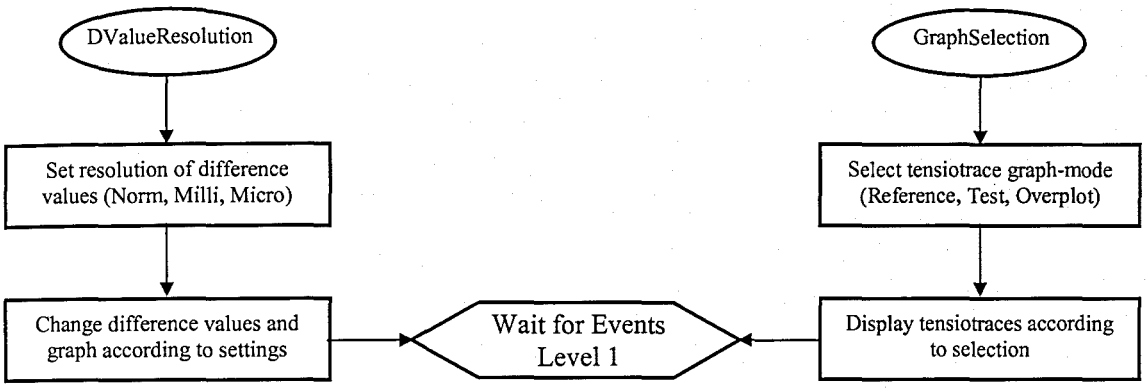

Figure 4-23. FEDs of the 'DValueResolution'- and 'GraphSelection'-processes.

It should be noted here that the resolution adjustment 'Micro' in Figure 4-23 is beyond the capability of the present acquisition board (12-bit ADC) to distinguish between two acquired data points. Future developments will solve this problem employing a new 16-bit ADC.

The processes in Figure 4-24 are used for the administration of the tensiotraces in their associated list modules.

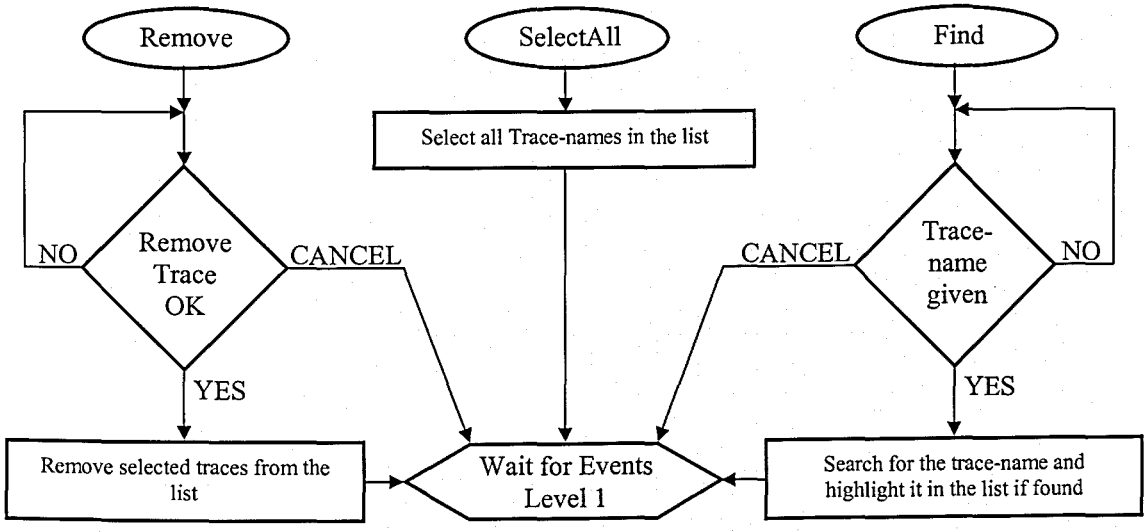

Figure 4-24. FEDs of the 'Remove'-, 'SelectAll'-, and 'Find'-processes.

The principle of these processes is the same for the reference and test list, thus the generalised presentation (Remove, SelectAll, and Find) of these FEDs is adequate at this point of the discussion.

4.5 Data-Scatter Package

The data-scatter software is an essential contribution to the graphical aided comparison of tensiotraces. Unlike the software package Analyse it visualises the analysed data of the tensiotrace comparison in a very detailed manner, using the entire dataset of both

traces. This extremely powerful software tool (here referred to as Data-Scatter) and its underling algorithms are fully described in Chapter 7. The software interface of Data-Scatter and its conceptual functionality is the subject of this section.

The software interface of Data-scatter is illustrated using FEDs in the same way as for the software packages Acquire and Analyse in previous sections. Five events trigger the various processes of the data-scatter software. Figure 4-25 shows the main process Data-Scatter.

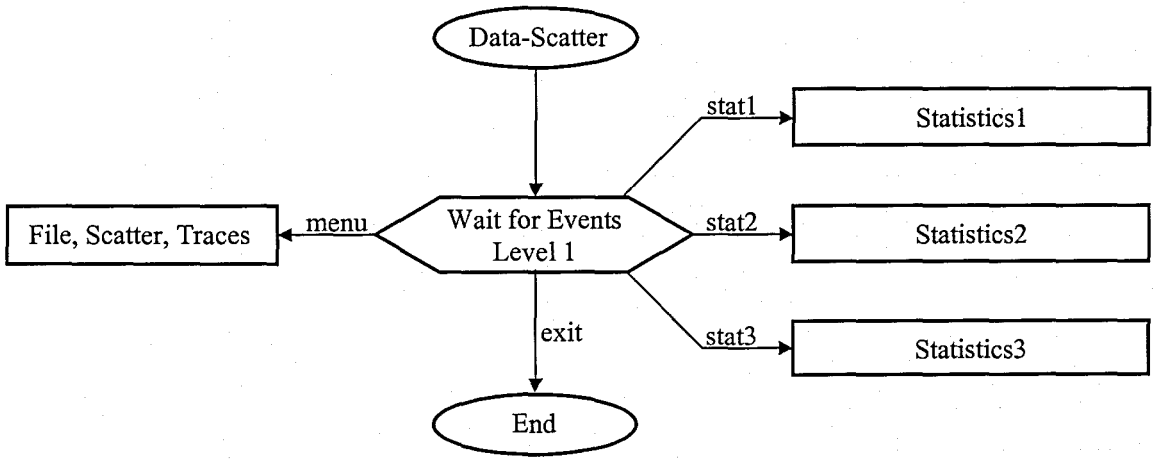

Figure 4-25. Main FED of the data-scatter software package.

The processes File and Traces illustrated in Figure 4-26 respectively terminate the Data-Scatter program and transfer the data of the reference and test tensiotraces from the mass storage medium (compact, hard or floppy disk) to the main memory of the PC, which is represented in more detail in the FED of Figure 4-27.

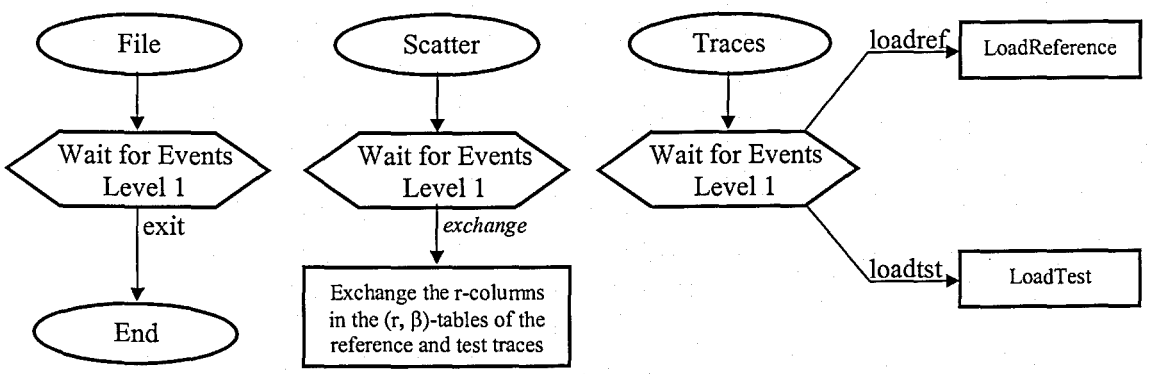

Figure 4-26. FEDs of the 'menu'-event ('File', 'Scatter', and 'Traces'-process).

These data points are then displayed in two independent scatter diagrams on the screen of the PC as shown in Section 4.6.

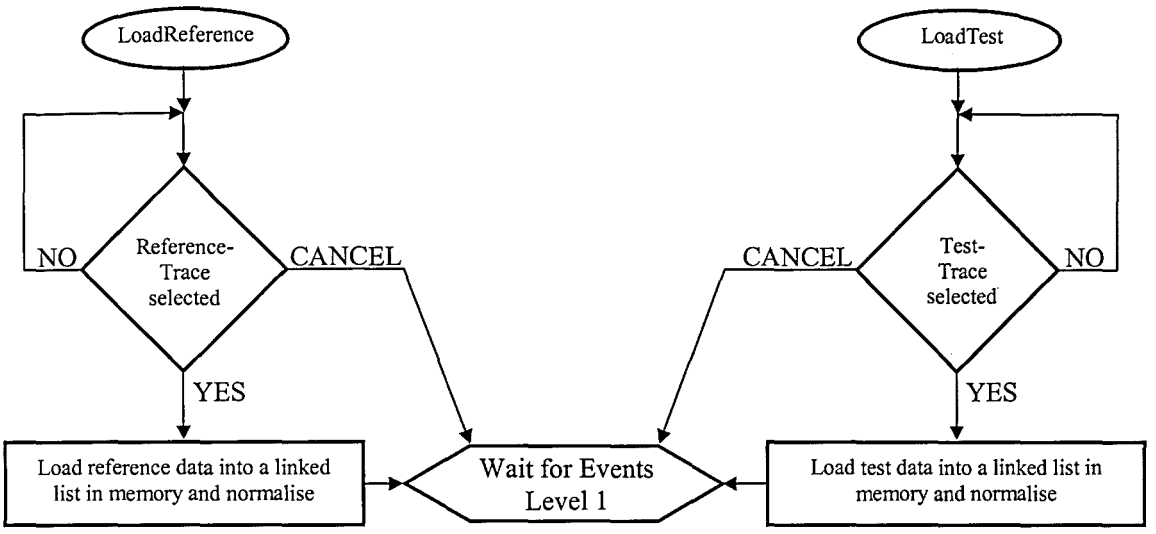

Figure 4-27. FEDs of the 'LoadReference'- and 'LoadTest'-processes.

Numerical values support the graphically displayed data analysis with specially designed statistics as illustrated in the FEDs of Figure 4-28.

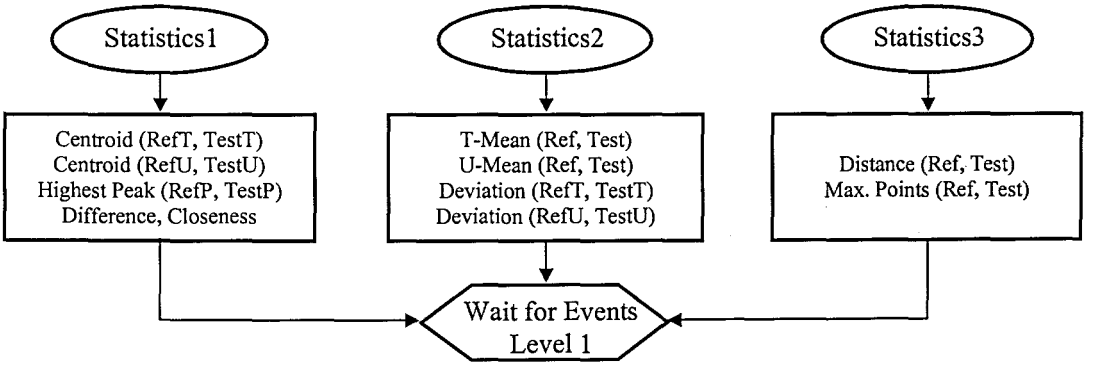

Figure 4-28. FEDs of the 'Statistics1'-, 'Statistics2'- and 'Statistics3'-processes.

The following pseudocode describes the conceptual functionality of the data analysis software package Data-Scatter. Also see Chapter 7 for more information.

- Load the data of the reference and test tensiotraces into memory
  - Create independent dynamic linked lists for the reference and the test trace with the elements $(t_i, u_i)_{ref}$ and $(t_i, u_i)_{tst}$ respectively
  - Normalise the values in both lists
- Compute the centroids of both tensiotraces $(T_c, U_c)_{ref}$ and $(T_c, U_c)_{tst}$
  - Estimate the area between the trace boundary and the T-axis, Eq. (7-1)
  - Determine half of the area in U-direction
  - Determine half of the area in T-direction
  - The interception of the two half areas represents the centroid (T_c, U_c), Eqs. (7-2) and (7-3)
- Compute the (r, β)-table (Table 7-1) for the reference and the test trace
  - For all data points (t_i, u_i) do

    - Calculate r_i, Eq. (7-4)
    - Calculate β_i, Eq. (7-5)
    - Store values in (r, β)-table
- Compute the P-coordinate
    - Search for the highest peak in tensiotrace and assign it to P
- Calculate the 'Closeness' ς, Eq. (7-14)
- Perform the data-scatter analysis and generate the statistical values
    - Apply the 'exchange-operator' Ξ, Eq. (7-6)
    - Display the data-scatter derived from Eq. (7-7) on the screen of a PC
    - Calculate mean values $\overline{T}$ Eq. (7-8) and $\overline{U}$ Eq. (7-9)
    - Calculate standard deviations σ_T Eq. (7-10) and σ_U Eq. (7-11)
    - Calculate the 'Distance' δ, Eq. (7-12)
    - Calculate the 'Difference' Δ, Eq. (7-13)

4.6 System Integration

In this section assorted screen shots of the three software tools Acquire, Analyse and Data-Scatter provide useful information on various aspects related to the software description of the previous sections.

4.6.1 Acquisition Package

Two important factors of software design guided the author throughout the development of the user interface for the data acquisition package Acquire. First, the acquired data has to be displayed and represented rapidly and in a meaningful way on the screen of a PC. Second, user-friendly mechanisms are provided to control the data flow and also allow necessary adjustments to be made during the use of Acquire. The result of these efforts is shown in Picture 4-1. Also see Figures 4-5, 4-14, and 4-15. Just pressing virtual buttons of the software user interface easily triggers events, and the data is displayed and represented graphically in real-time during the measurement of the LUT.

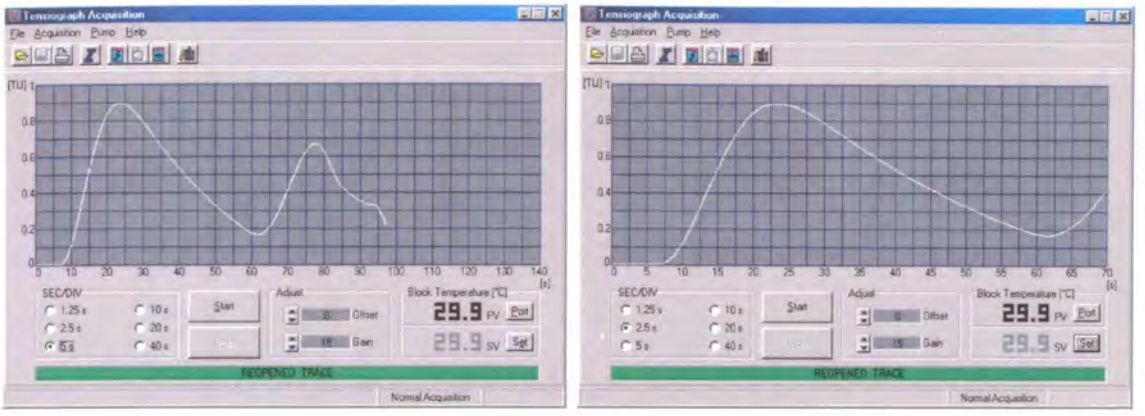

(a) (b)

Picture 4-1. Software user-interface of the data acquisition package Acquire.

Note that Picture 4-1(a) shows a recorded tensiotrace using a different time base than the tensiotrace shown in Picture 4-1(b), thus the tensiotrace is displayed in an unclipped manner and in a clipped manner respectively. In order to acquire the data properly, i.e. in an unclipped manner during a full life cycle of a liquid drop, the time base must be set appropriately according to the speed of the pump and the properties of the liquid.

The use of menus is a convenient way to select an item from a set of functions in a software package. Picture 4-2 shows the menus of Acquire that a user can choose from. Also see Figure 4-6.

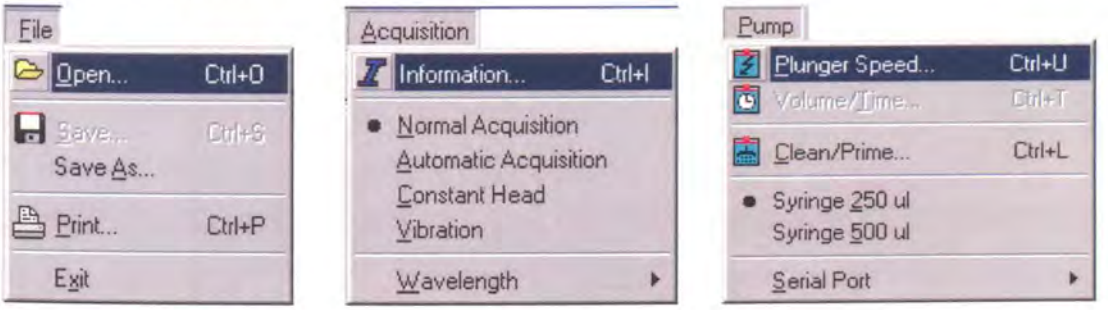

Picture 4-2. Pull-down menus of the data acquisition package Acquire.

All of the items on these menus can be selected using the mouse of the PC on which the application Acquire is running. More frequently used items on a menu can also be selected using accelerator keys (for example Ctrl+O). By pressing the Ctrl-key and the O-key on the keyboard of the PC at the same time, the 'Open'-dialog will be activated even if the pull-down menu is invisible at the time of this action. All menu items with the accelerator key facility, i.e. Ctrl+'key', work in the same way as described above. Menu items that also display a solid black dot in the first column specify a permanent selection, which is valid until another menu item of the same kind will be selected. The solid black triangle in the last column of a menu item indicates the display of a submenu as soon as this particular menu item is selected.

After the selection of 'Open…' from the 'File'-menu, the open dialog as shown in Picture 4-3 will be displayed on the screen of the PC. Also see Figure 4-7.

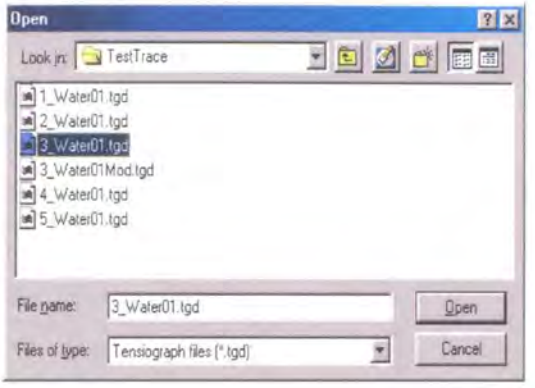

Picture 4-3. Open-dialog of the data acquisition package Acquire.

To display the data of a tensiotrace on the canvas of the Acquire application, the user has to highlight one of the files with a tgd-extension (tgd stands for tensiographic data) and subsequently press the open button of the open dialog. The open dialog also provides a browser option, filename filter, folder creation option and more, but these facilities are of minor importance, thus they will not be discussed.

The save dialog will be displayed on the screen of the PC following the selection of the 'SaveAs'-item or 'Save'-item of the 'File'-menu. Combined with this action the detail input window pops up to allow a user to classify the data of the tensiotrace that will be saved in non-volatile memory, i.e. on a hard disk, CD, or a similar storage medium. Picture 4-4 shows the two screenshots of the save dialog and the detail input window. Also see Figure 4-8 for more information.

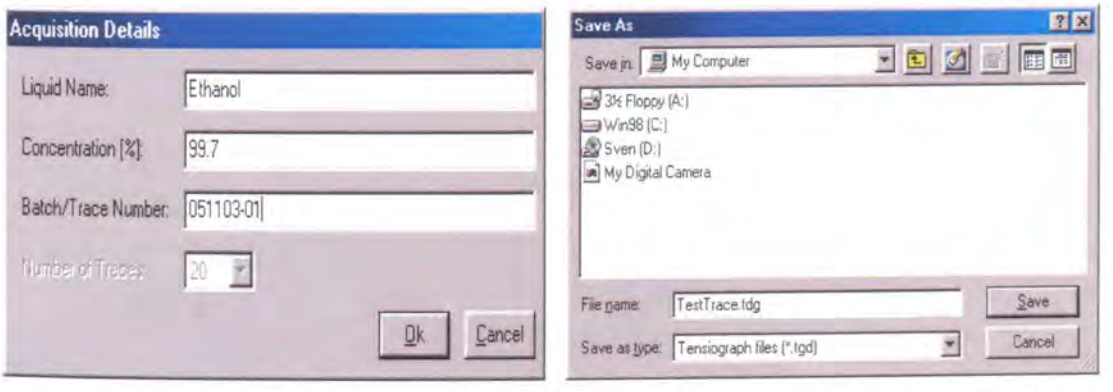

Picture 4-4. Acquisition-details and Save-dialog of the data acquisition package Acquire.

To save the data of a tensiotrace, the user of a tensiograph has to type in a filename and press the save button of the save dialog. Subsequently the acquisition details will be added to the header of the tensiograph data file, and this header information is then used to distinguish between various files that were saved previously. In 'Automatic' mode, the field 'Number of Traces' of the acquisition details dialog determines how many

tensiotraces should be acquired without user interference. Tensiotraces of the type 'Automatic' are saved with a leading number in their filenames as shown in Picture 4-3.

Numerical principal component values of the graphical representation of a tensiotrace can be displayed by opening the information window as shown in Picture 4-5. Figure 4-9 shows the interactive FED of the information window.

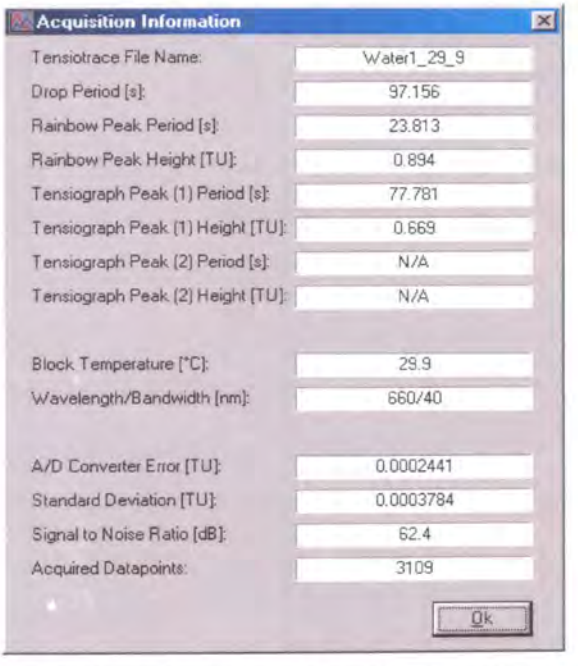

Picture 4-5. Acquisition-information of the data acquisition package Acquire.

The most important principal components of a tensiotrace are summarised in the acquisition information window. The displayed information is divided into three parts, namely the liquid-specific values (DP, RPP, etc.), the machine-specific values (block-temperature and wavelength), and the statistical values A/D conversion error (see Table A2-2), *SNR* (see Eq. (1-1)), standard deviation σ (see Eq. (1-3)), and acquired data points *N*.

The acquisition mode and the wavelength of the LED, which illuminates the LUT (see Figure 1-1), can be selected from the menu as shown in Picture 4-6.

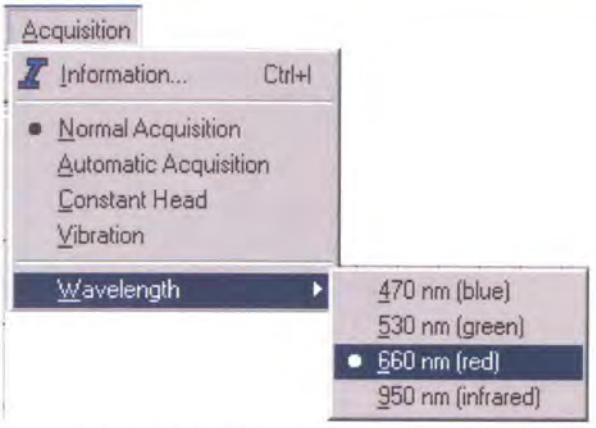

Picture 4-6. Pull-down menu of the data acquisition package Acquire.

Both the acquisition mode and wavelength items on the menus will be permanently selected, even after a restart of the PC and Acquire application, so that the user does not need to select these items every time Acquire was started, unless the user wants to choose a different item on these menus. Figure 4-10 shows the associated FED.

Chapters 1 and 2 briefly discussed the need for a feature that is incorporated in Acquire, which provides an option to change dispense and aspirate time of the liquid delivery system, and also facilitates a user of the tensiograph to dispense a defined amount of liquid to the drophead.

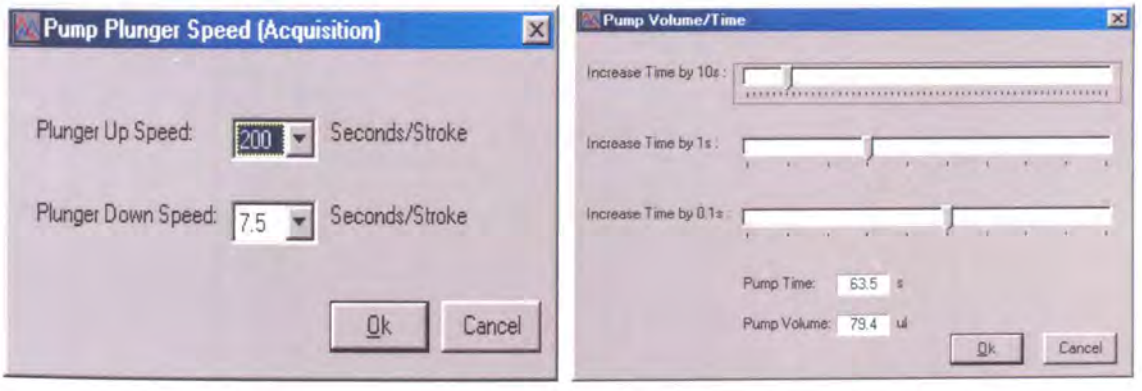

Picture 4-7. Pump-setting dialogs of the data acquisition package Acquire.

The 'Pump Plunger Speed'-dialog in Picture 4-7 (also see Figure 4-11) presents the user with the possibility to change the plunger speed of upward and downward directions in several steps, whereas the 'Pump Volume/Time'-dialog can be used to stop the pump of the tensiograph, after a predefined dispense time has elapsed, which results in a defined volume of the LUT hanging from the drophead. This feature was used to carry out vibration and evaporation studies that will be discussed in Chapter 6.

Drophead cleaning procedures and the prime process of the liquid delivery system, i.e. pump, tubing, and drophead, are vital tasks during a measurement of LUTs. Picture 4-8 shows a screenshot how the 'Pump Clean/Prime'-dialog is presented to the user of Acquire. Figure 4-12 represents this dialog in a more detailed manner.

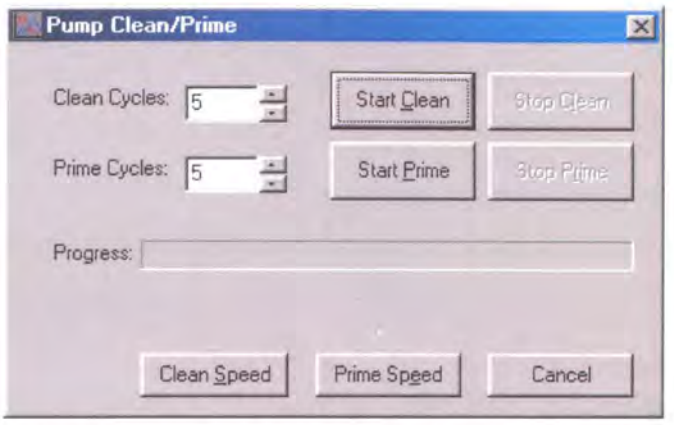

Picture 4-8. Clean and Prime dialog for the pump of the data acquisition package Acquire.

Priming requires usually a higher plunger speed of the pump than cleaning, which can easily be adjusted by opening the 'Pump Plunger Speed'-dialog (Picture 4-7) from the 'Pump Clean/Prime'-dialog to choose the appropriate speeds for cleaning and priming. A preset number of pump cycles will be used to pump the LUT or a cleaning solution from a sample container via the pump and tubing to the drophead. Chapter 6 describes these issues in more detail.

The changing of the syringe type and serial port connection has been described in conjunction with Figure 4-13. Picture 4-9 shows now how this is implemented in the user interface of the data acquisition package Acquire.

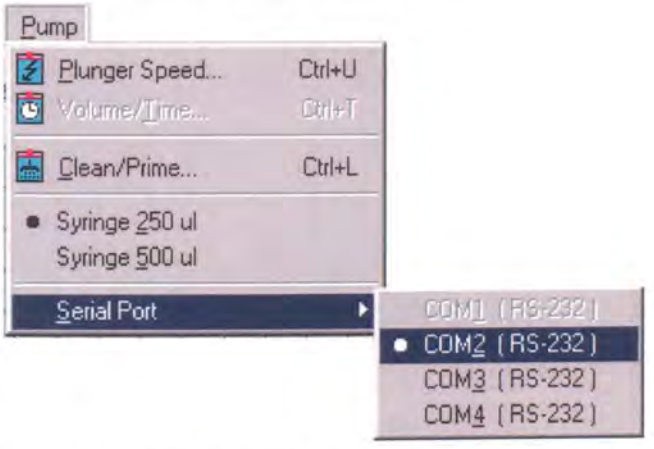

Picture 4-9. Pull-down menu of the data acquisition package Acquire.

A 250μl syringe is usually used with the micro-stepper pump of the tensiograph and will only be changed to 500μl for research purposes; hence the syringe options on the 'Pump'-menu are not assigned to an acceleration key. However, the appropriate syringe type has to be selected on the 'Pump'-menu, following an amendment of the syringe size, in order to maintain the expected performance of the tensiograph. Communication between the pump and the acquisition software of the tensiograph is computer controlled via an RS-232 connection. One of a number of possible COM ports of the PC has to be assigned to the pump, which can also be done from the 'Pump'-menu.

A second COM port of the PC is reserved for the communication between the temperature controller and the acquisition software of the tensiograph and can be selected in the 'Digital Display Communication Port'-dialog as shown in Picture 4-10. The mutual exclusion of choosing an active COM port, i.e. a COM port of the PC that is already assigned to an external device, is indicated by a faded option on the menu in Pictures 4-9 and 4-10. That means two devices can never be assigned to one and the same COM port.

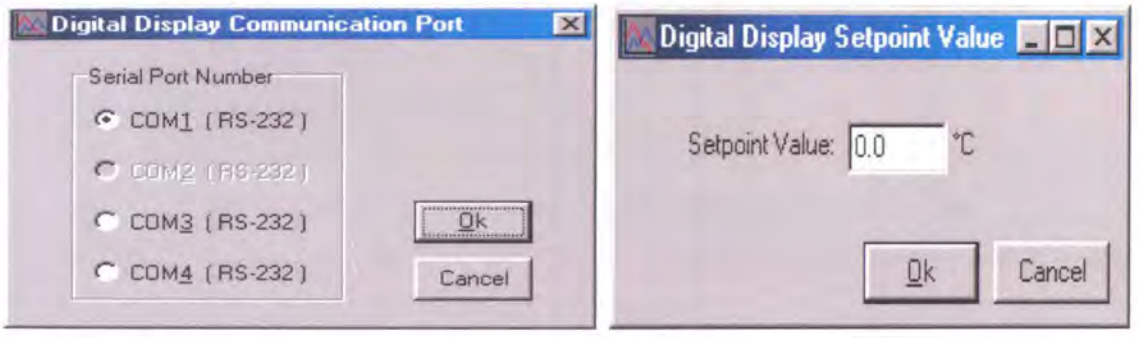

Picture 4-10. Temperature-controller settings of the data acquisition package Acquire.

Picture 4-10 also shows that the temperature of the thermal system, incorporated in a tensiograph, can be adjusted in a dialog of the software user interface. Also see Figure 4-16. The thermal system will be discussed in Chapter 6.

4.6.2 Analysis Package

The objective of the analysis software package Analyse is to elucidate the data of tensiotraces more comprehensively than is possible with the acquisition software Acquire. The presentation of a relatively large amount of information while maintaining a user-friendly software interface challenged the author during the development phase of this software package. Picture 4-11 shows the user interface of the data analysis package Analyse. Figures 4-17, 4-21, and 4-22 show the associated FEDs of this particular screenshot.

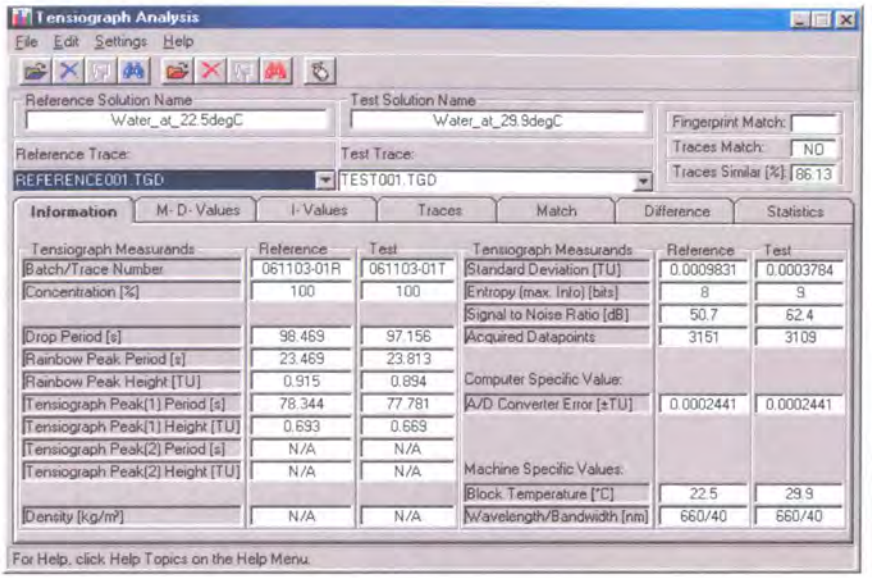

Picture 4-11. Software interface of the data analysis package Analyse.

Note that the principal components displayed in Picture 4-11 are the same as in Picture 4-5 (Information screen of Acquire), with the exception that the data of two tensiotraces are shown. This is the inherent characteristic of Analyse and facilitates the comparison of two tensiotraces at the same time and many traces in subsequent order. Further information on multiple tensiotrace comparisons is provided below in this section.

The menus of Analyse, shown in Picture 4-12 and more fully explored in Figure 4-18, operate in the same way as the menus of the data acquisition package Acquire, which has been discussed above in the previous section.

Picture 4-12. Pull-down menus of the data analysis package Analyse.

'Open Reference' and 'Open Test' on the 'File'-menu display the same dialog as shown in Picture 4-3 enabling the user of Analyse to select various tensiotraces from a mass storage device and load them into the main memory that is allocated by Analyse. Also see Figure 4-19.

Analyse includes a password protection mechanism to prevent the maltreatment of values in the 'M-Values Setting'-dialog. Picture 4-13 shows the screenshot of the user interface that was described in conjunction with Figure 4-20 in Section 4.4.

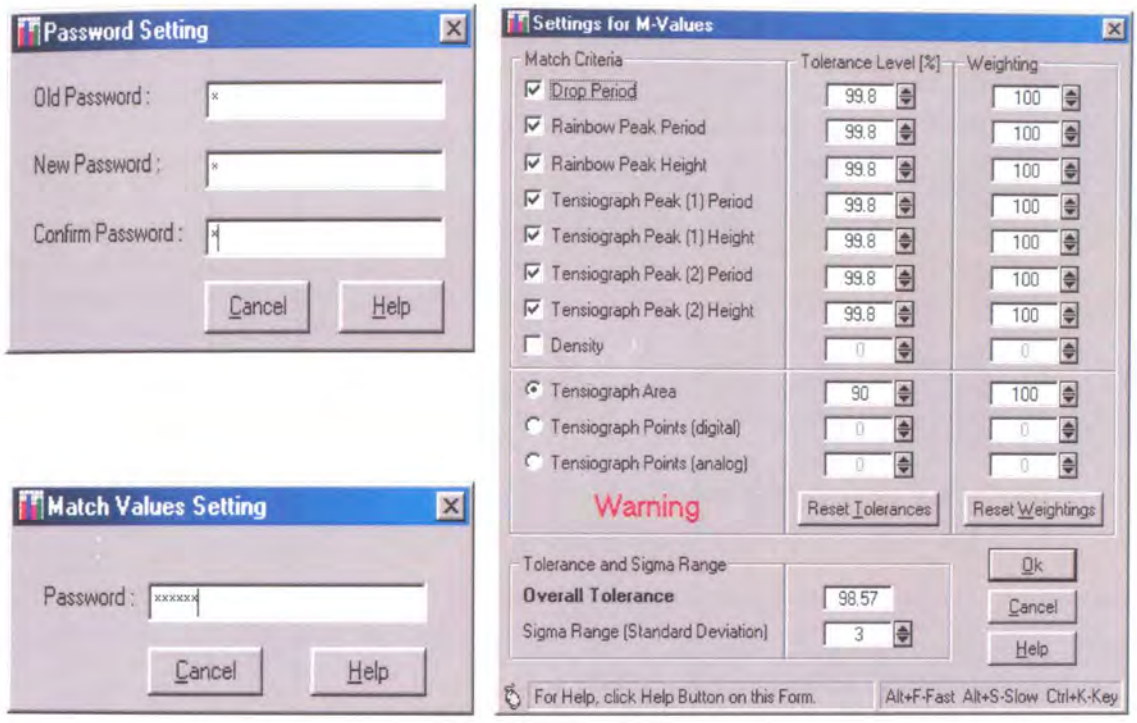

Picture 4-13. Password and M-Values dialogs of the data analysis package Analyse.

It should be noted here that the match criterion of any principal component in a tensiotrace can either be switched off, strengthened or weakened by respectively altering the check boxes (squared-shaped) on the left hand side of the principal component name, or by using the up/down buttons on their right hand side. Slightly different behavior of the option buttons (circular-shaped) guarantees that at least one of the less flexible match criteria, namely 'points-analogue' (Eq. (2-36)), 'points-digital' (Eq. (2-37)), and 'tensiograph area' (Eq. (2-38)), is active for the comparison of two tensiotraces.

Pictures 4-14 and 4-15 conceptually show three different visualisation schemes comprising the comparison of two tensiotraces, namely the reference and the test trace. The comparison of two tensiotraces, using bar graphs as shown in Picture 4-14 (also see Figure 4-21), is the quickest method, whereas a rapid interpretation of the numerical representation in Picture 4-15 is more difficult.

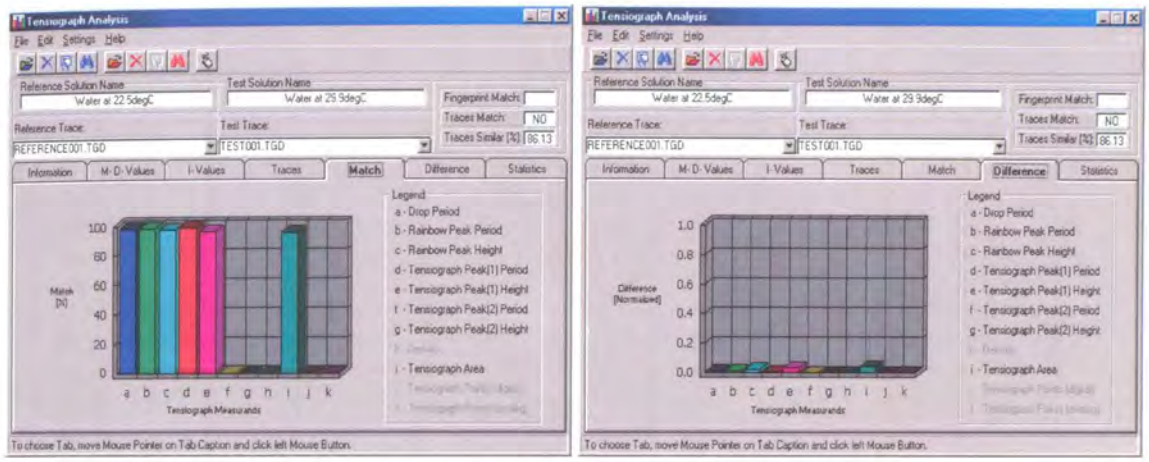

Picture 4-14. Match and difference views of the data analysis package Analyse.

The tensiotrace profile representation, shown in Picture 4-15 (also see Figure 4-22) proves to be very useful, when it is important to locate the exact location of differences in the two tensiotraces, which can be done by dragging a cross hair across the display and resting it at the position of interest.

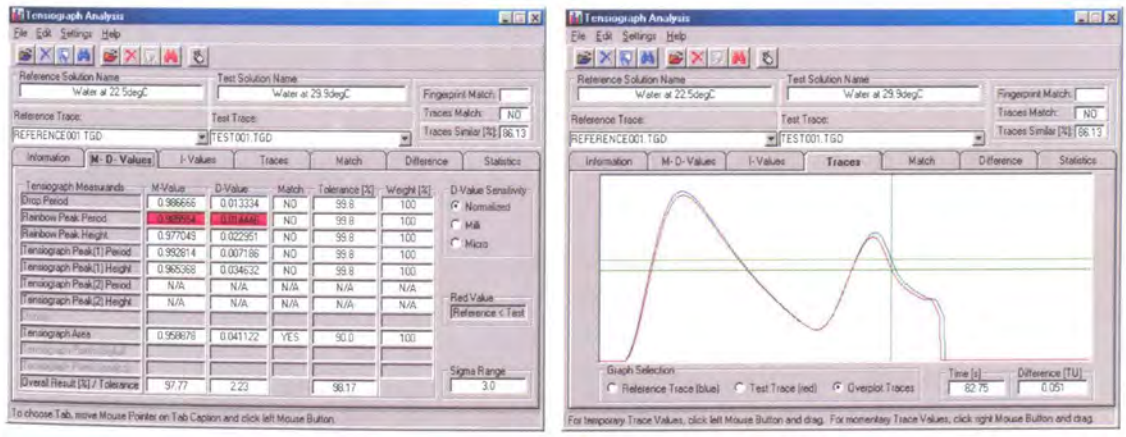

Picture 4-15. MD-Values and traces views of the data analysis package Analyse.

It has to be noted that this tensiotrace analysis tool is usually used to fingerprint two liquids, which means, that the differences in the two tensiotraces will not be as obvious as illustrated in these pictures.

The D-Value sensitivity setting, as shown in Picture 4-16 (also see Figure 4-23), has been implemented to increase the visibility of differences in two tensiotraces (compare the two bar graphs in Pictures 4-14 and 4-16 where the D-Value sensitivity is set to normalised and milli differences respectively).

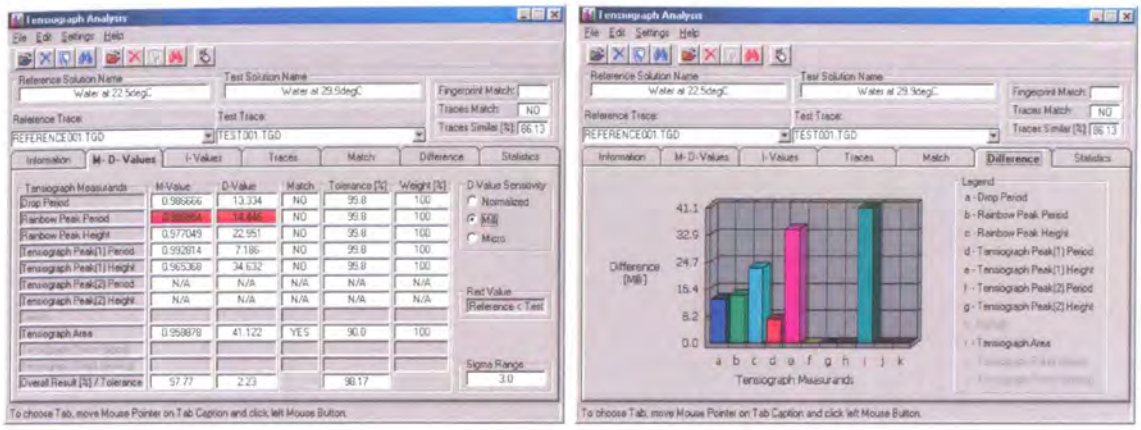

Picture 4-16. D-Value sensitivity-control of the data analysis package Analyse.

The D-Value sensitivity feature facilitates the user of Analyse, with regard to the bar graph analysis, to discriminate two tensiotraces of the same liquid (noise will always be present), unless the reference and test traces are identical, which is only possible when one data set of a tensiotrace is used as the reference and the test trace.

To display the profile of the tensiotraces in an unclipped manner the time base and amplitude range of the displayed traces can be adjusted appropriately. Picture 4-17 illustrates this facility.

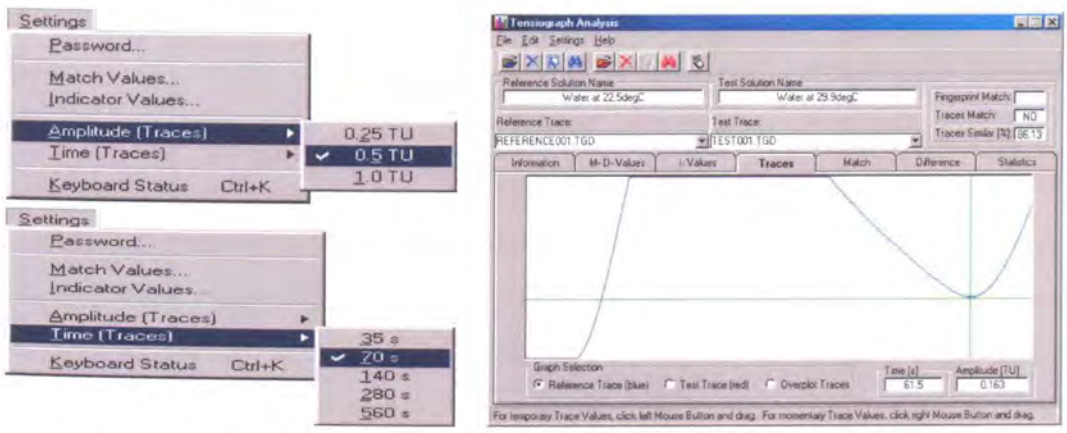

Picture 4-17. Amplitude and time-control of the data analysis package Analyse.

The analysis package Analyse incorporates two independently controlled list modules in order to conduct a rapid analysis of multiple tensiotraces. In Picture 4-18 it is illustrated that a variety of tensiographic data sets can easily be added to the list, removed from the list, or found in the list.

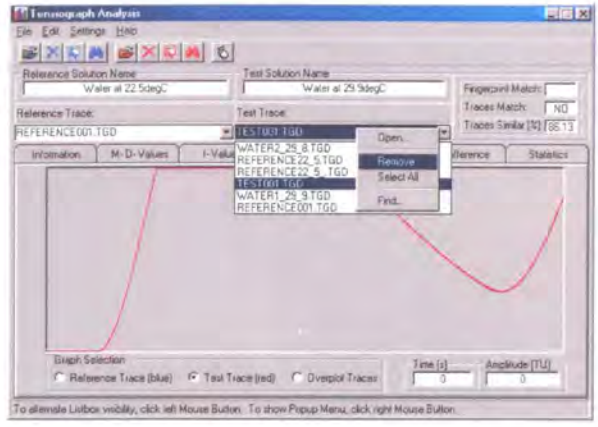

Picture 4-18. Sample-list control of the data analysis package Analyse.

The comparison of multiple tensiotraces is initiated by a step-by-step selection of items in the test list, following the selection of an item in the reference list, which means that all data sets in both lists can be compared against each other. For more information see also Figure 4-24.

4.6.3 Data-scatter Package

The data-scatter software package Scatter, briefly described here and fully discussed in Chapter 7, has been developed in addition to the software tool Analyse. The visualisation of differences in tensiotraces, compared to the method in Analyse, is much more effective because every single data point in both tensiotraces, namely the reference and test trace, contributes to the visualisation process as described below. Picture 4-19 shows the user interface of the software package Scatter. Also see Figure 4-25.

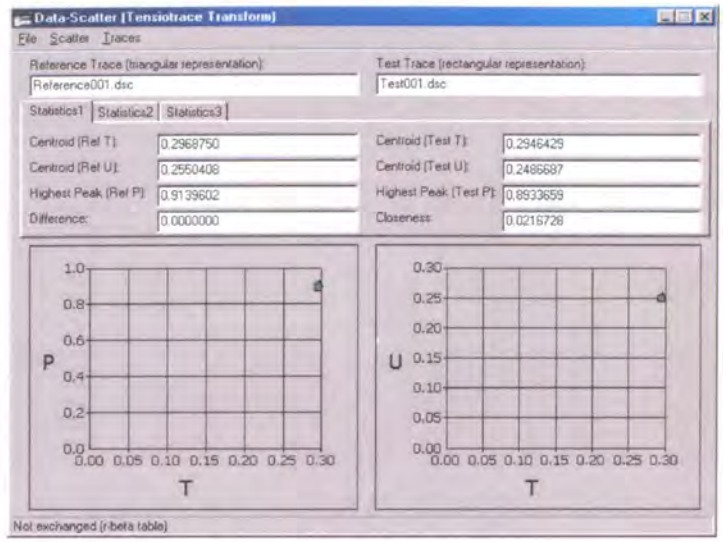

Picture 4-19. Software interface of the data-scatter package Scatter.

Loading two tensiographic data sets, which have been acquired with the software tool Acquire, position the two centroids (each consisting of overlapped data points of the entire tensiographic data set) and two additional points (representing the maximum peak height of a tensiotrace) onto the (T,U)-plane and (T,P)-plane respectively. The pull-down menu 'Traces', shown in Picture 4-20, can be used for loading tensiographic data sets in the same way as described in previous sections of this chapter.

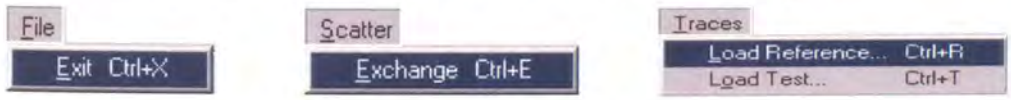

Picture 4-20. Pull-down menus of the data-scatter package Scatter.

Figures 4-26 and 4-27 provide more information of the underlying functionality of the menus shown in Picture 4-20.

The two currently compared tensiotraces might be similar or even identical if the centroids of both traces are placed at the same position of the (T,U)-plane and only the use of the exchange operator (Eq. (7-6), triggered by clicking on Exchange in the 'Scatter'-menu or using the accelerator key Ctrl-E) divulges the differences between the two tensiotraces.

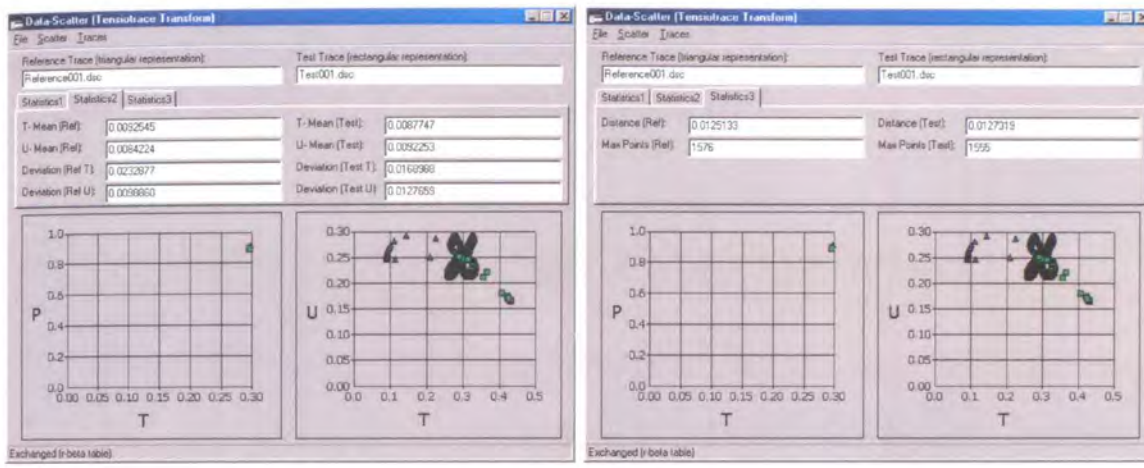

Picture 4-21. (r, β)-table in the data-scatter package Scatter is exchanged.

Picture 4-21 shows the screenshot of the user interface subsequent to the utilisation of the exchange operator. Sets of statistical values, which describe the differences between the two tensiotraces in a numerical manner, are also displayed and can be used for further analysis. Also see Figure 4-28.

CHAPTER 5

DROPHEAD ENGINEERING DEVELOPMENT

Since the beginning of the tensiographic project in 1987, drophead design has always been of major concern to scientists and engineers involved in this project. The author of this thesis was for quite some time implicated with drophead design issues and therefore allocates a full chapter to the engineering development of the drophead. Although a drophead comprises four essential components, namely the liquid drop supporting part, optical fibers, liquid delivery tube, and the outer sleeve, which acts as the supporting structure for all remaining parts and also as a thermal conductor, only the liquid drop supporting part is of interest at this point of the description of the project. Chapter 6 examines the functioning of a drophead as a multiple component device and provides a detailed explanation of the four main parts that constitute such a drophead. The term drophead throughout this chapter is used for the liquid drop supporting part, unless the author refers to the whole assembly of the drophead parts that form a multiple component device, which will then be explicitly conveyed to the reader. Section 5.1 discusses the concave PEEK drophead design and its related advantages and disadvantages. Some of the problems with a concave PEEK drophead design have been reduced after the introduction of a flat stainless steel knife-edge drophead design, explained in Section 5.2. With the flat stainless steel knife-edge design new problems were introduced, thus further drophead studies, which are discussed in Section 5.3, had to be conducted to eliminate any weaknesses of the two previous drophead designs. Following these studies, McMillan and the author devised a new drophead design, which is examined in Section 5.4. A new drophead made according to this design will be employed in future tensiographic instruments.

5.1 Cylindrical Concave PEEK Drophead

A cylindrical concave drophead made out of PEEK, with the dimensions as shown in Figure 5-1, was used for most of the liquid drop measurements carried out with a tensiograph over the past years of the tensiographic instrument development. The features of this drophead design can be summarised as:

- Easy to manufacture.
- Low cost.
- Use of PMMA and silica fibers without major constraints.

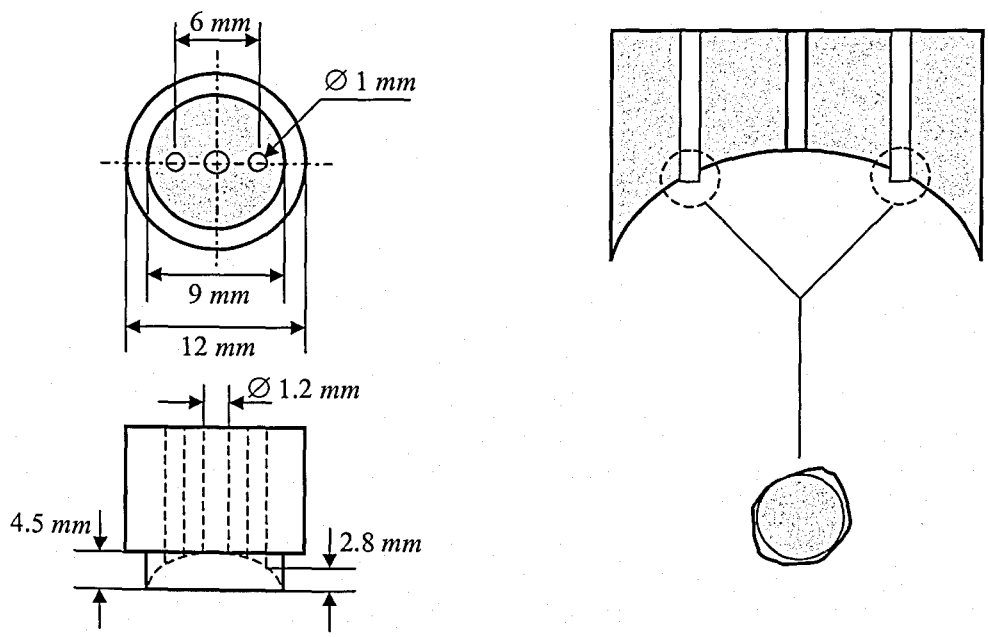

Figure 5-1. Dimensions of a cylindrical concave drophead and the magnification of the boreholes for the optical fibers.

- Relatively good wetting capability.

Machining this drophead in one piece from a rod of PEEK is a major advantage compared to the drophead designs described in the following sections of this chapter. For an envisaged commercial tensiographic instrument it is important to keep manufacturing tasks as simple as possible, which on the other hand keeps the costs relatively low. Another vital drophead design issue is the reproducibility of such an important part of the tensiograph that in essence represents the ability to fingerprint liquids. PEEK is a relatively soft material, hence the size of the boreholes for the fibers can be chosen in such a way that the fibers are inserted into a push fit without putting

too much strain on the fibers and also to form a sealed interface between the fiber and the borehole avoiding gaps in which contamination usually occurs. By applying the push fit method, both PMMA and silica fibers can be fitted into the drophead efficiently without using any glue or clamping mechanisms. Additionally, the slope of the concave shaped drophead guarantees that the liquid fed into the liquid delivery tube is pushed immediately to the edge of the drophead and therefore supports a good wetting capability. Remember that the fibers need to have a certain distance from the drop supporting edge (here 2.8*mm*, see Figure 5-1) in order to generate tensiotraces with a rainbow peak and tensiograph peak(s) during the life cycle of a drop hanging from the drophead. The concave shaped drophead produces the required distance with regard to the end-face of the fibers and the drop supporting edge. However, this also introduces some drawbacks to this design that can be summarised as:

- Problematic fiber positioning.
- Usage of araldite to protect PMMA fibers.
- Difficult to clean due to cavities.

To improve the performance of the light transmission from the LED to the Photodiode (see Figure 1-1), the end-faces of the fibers need to be polished before they are inserted into the boreholes of the drophead. The positioning of the fibers, while inserting them into the boreholes of the drophead, is quite a difficult task because of the relatively complex shape of the drophead and its inherent tolerances. Only a very small displacement of the fibers results in different profiles of tensiotraces for the same liquid and hence diminishes the reproducibility of the drophead. The use of PMMA fibers usually requires a coating of the end-faces with araldite in order to protect the fibers against aggressive liquids that would otherwise destroy the polished end-faces, which in turn deteriorates the performance of the tensiographic instrument. This coating generates arbitrarily shaped rough surfaces that are difficult to clean and also increase the probability of light signal degradation due to scatter effects, refraction, and reflection at these uneven surfaces. Conversely, silica fibers do not require a coating with araldite, since they can withstand a chemical attack of aggressive liquids, but it is possible that micro gaps between fiber and borehole, as shown schematically in the magnified part of Figure 5-1, diminish the overall quality of a cylindrical concave drophead. In any case, there will always be the inevitably existence of inconsistencies on the liquid supporting surface of the drophead, which typically cause a problem during drophead cleaning procedures. In the case of a heavily contaminated drophead, a

cleaning solution especially devised for a tensiograph has to be used to clean the drophead [5-1]. A less contaminated drophead can always be cleaned with pure water between measurements as discussed below in this section. Consider Figure 5-2 for the first steps involved in the overall measuring procedure for a particular liquid.

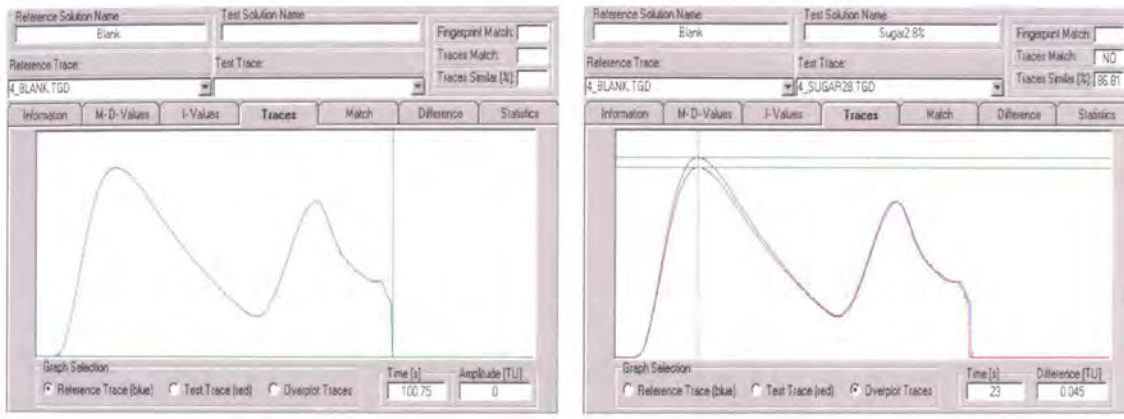

(a) **(b)**

Figure 5-2. (a) Reference tensiotrace of water measured with a clean drophead and (b) overlapped tensiotraces of water and a sugar solution measured with the same drophead.

The most important issue is to start a new measurement with a clean drophead. To ensure that this is the case, one can prime the tensiographic system with water until the profile of a measured tensiotrace indicates acceptably small differences to a previous recorded tensiotrace out of the same batch. The data of this trace are then stored in memory and serve as the first reference trace (Figure 5-2 (a)) of the overall measuring procedure. Similarly, the LUT (in this case a sugar solution) is fed to the drophead until the variation between the water reference trace and the tensiotrace of the LUT comes to equilibrium (Figure 5-2 (b)). The tensiotrace data of the LUT is then also stored in memory (second reference trace). For the remaining description of the overall measuring procedure consider Figure 5-3.

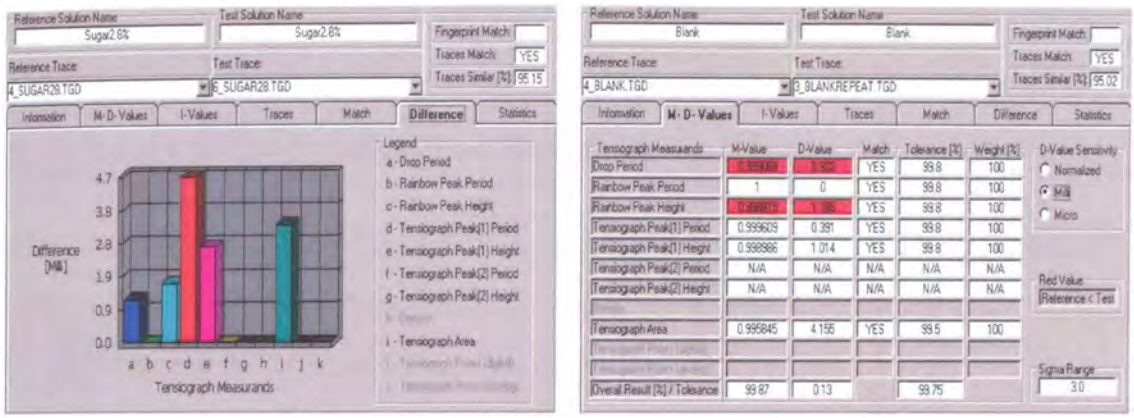

(a) (b)

Figure 5-3. (a) Comparison of two sugar solution tensiotraces measured with the same drophead and (b) comparison of two water tensiotraces after the cleaning procedure of the drophead.

Subsequent to the preparatory steps of the measuring procedure, as outlined above, the analysis of the LUT can begin, which involves the comparison of the LUT with the second reference trace that was recorded earlier in the process (here a sugar solution, see Figure 5-2 (b)). One example would be the QC of sugar solutions from different batches as shown in Figure 5-3 (a). The remaining step is to clean the drophead with pure water again, until the comparison of the test trace and the first (water) reference trace show acceptably small differences as shown in Figure 5-3 (b). The last step in the measurement procedure ensures that the drophead does not remain permanently contaminated, which otherwise would require cleaning of the drophead with an appropriate cleaning solution as mentioned above in this section. It also provides the information whether the overall measurement was satisfactory (Match-indicators in Figure 5-3 (b) show only YES according to the preset match criteria) or that there was a problem during the measuring procedure and the measurement should be repeated (one or more Match-indicators in Figure 5-3 (b) show NO according to the preset match criteria). Note that at this point of the discussion Match-indicators serve as a gauge as to how many cleaning or priming cycles are required to clean the drophead properly. Any cleaning or priming processes that are necessary during a measuring procedure, as described above, require typically about twenty to fifty pump cycles (see Chapter 6), which can be initiated from the data acquisition software package Acquire (Picture 4-8).

5.2 Cylindrical Flat Stainless Steel Drophead

Various weaknesses of the cylindrical concave PEEK drophead design, as discussed in the previous section, encouraged McMillan and the author to come up with a proposal for a new drophead design that would hopefully overcome the limitations of a concave drophead. It was suggested to exploit a cylindrical flat stainless steel core, which can be easily extended with a stainless steel knife-edge ring used as a variable height adjustment of the optical fibers. Figure 5-4 shows the arrangement and dimensions of the cylindrical flat drophead that includes the following features:

- Drophead shape is similar to approved cylindrical concave drophead.
- Fibers can be polished after the insertion into the drophead.
- Easy fiber adjustment with additional knife-edge ring.
- Stainless steel is resistant against almost all chemicals and organic solvents.

The cylindrical concave drophead has served as a model for the design of a flat stainless steel drophead, in this way the good characteristics of the concave drophead design can be copied and any weaknesses may possibly be eliminated. One of the weaknesses of the concave shaped drophead is the inability to polish the fibers after mounting them in the drophead, but it is possible to polish the optical fibers when they are inserted in the flat drophead. This has the advantage that the end-face of the fibers and the liquid drop-supporting surface of the flat drophead form a smooth surface, which is easy to clean and also provides a basis for excellent reproducibility of tensiotraces of the same liquid. Subsequent to a combined polishing process of the optical fibers and the liquid drop-supporting surface, the height of the fibers (here $1mm$, see Figure 5-4) can be adjusted by heat-shrinking a knife-edge ring onto the flat stainless steel core of the drophead. The envisaged use of the tensiograph in the water quality monitoring industry, and also in the pharmaceutical, dairy, food, brewery, beverage, and bioprocessing industries, requires a drophead with excellent impact resistance. Stainless steel is a suitable material, which is resistant against almost all chemicals and organic solvents that are used in these applications [5-2].

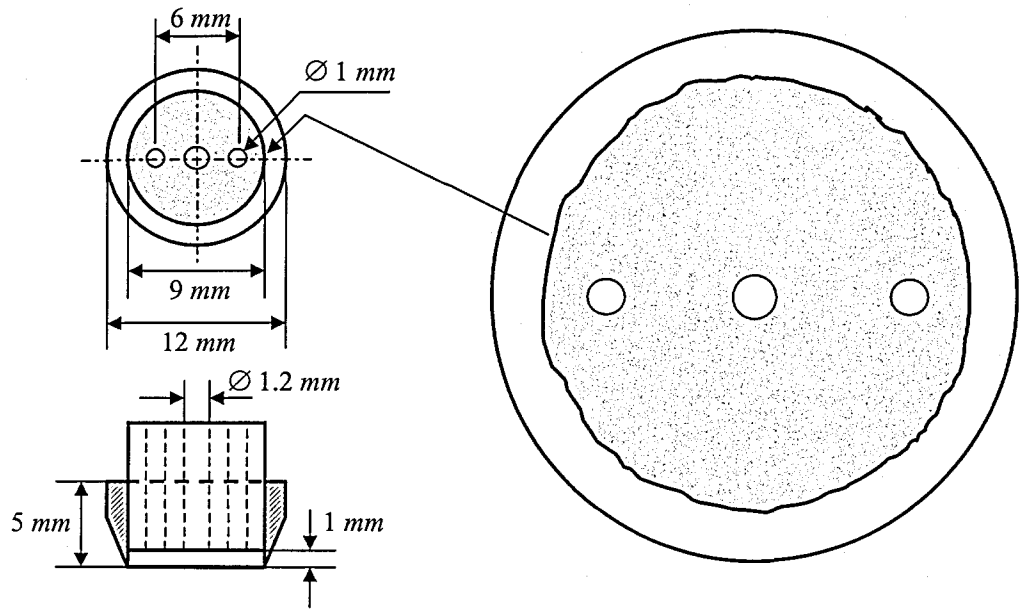

Figure 5-4. Dimensions of a cylindrical flat drophead and the magnification of the drop supporting knife-edge.

However, this design bears various problems that are briefly described below in this section. The following list provides an overview of these problems:

- Optical silica fibers crack when glued into stainless steel drophead.
- Protection of PMMA fibers against aggressive liquids is still required.
- Micro gap between stainless steel core and the knife-edge ring can aggravate contamination problems.
- Knife-edge is very sensitive to mechanical damage.

Fixing optical silica fibers in a stainless steel drophead, using special glue that holds the fibers in position and also seals the interface between silica and stainless steel, usually cracks the fibers due to the shrinkage of the glue during curing time. The brittleness of optical silica fibers is one of their major disadvantages and this is the reason why optical PMMA fibers are more suitable in conjunction with a stainless steel drophead. Conversely this diminishes the optical performance of a tensiographic instrument (see Figure 5-5) and also requires an additional coating of the end-faces of the fibers with a special resin that prevents chemical attack from aggressive liquids. Figure 5-5 (a) indicates that there is very little attenuation of a light signal in silica fibers in the wavelength range between 320*nm* and 1200*nm* [5-3], which is the optical range a tensiograph works in. The transmission spectrum of a PMMA fiber in Figure 5-5 (b) shows clearly that the range of low attenuation is smaller compared to that of silica fibers, which affects the optical performance of a tensiograph in the UV and IR regions.

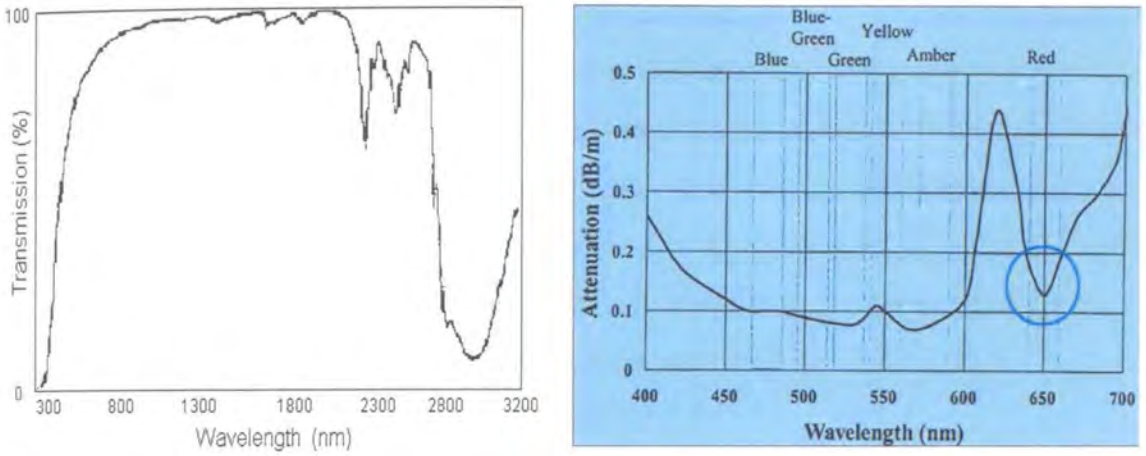

(a) **(b)**

Figure 5-5. (a) Transmissibility of silica within the range UV-A to IR-B and (b) attenuation of an PMMA fiber in the VIS range.

Another problem with the stainless steel flat drophead design arises from the fact that there exists a gap between the core of the drophead and the knife-edge ring after the assembly of these parts and consequently a relatively high probability that small particles in the LUT contaminate this cavity. The knife-edge of the drophead also lacks mechanical strength and hence can easily be damaged as illustrated in the magnification of Figure 5-4. Obviously, there were various problems introduced by the stainless steel flat drophead design, which were not present in the PMMA concave drophead design and therefore further drophead studies had to be carried out by co-workers of the tensiographic project and the author.

5.3 Plexiglas Spacer Disc Drophead

The study of a Plexiglas spacer disc (PSD) drophead was conducted in order to eliminate any problems with previous drophead designs and to discuss the theory and the practical use of a dimensionally invariant representation of tensiotraces.

5.3.1 Plexiglas Spacer Disc Studies

Several attempts have been made so far to produce an ideal drophead that generates reproducible tensiotraces of liquid samples. From the commercial point of view these attempts have generally met with failure, since there is a persistent problem of drophead contamination. It is obvious that the most appropriate shape of a drophead that reduces

the contamination issue to a minimum is a flat smooth surface without any gaps and bumps, which is used to support a pendant liquid drop. Figure 5-6 shows in principle how such a drophead could be realised. For research purposes only, PSDs with different diameter *d* and thickness *s* were produced in order to find the ideal dimensions of a PSD for a variety of liquids. A stainless steel liquid delivery tube is moulded into a centre-hole of the PSD and the fiber separation *f* can be varied, whereas the space between the fiber end-faces and the liquid supporting drophead surface is given by *s*.

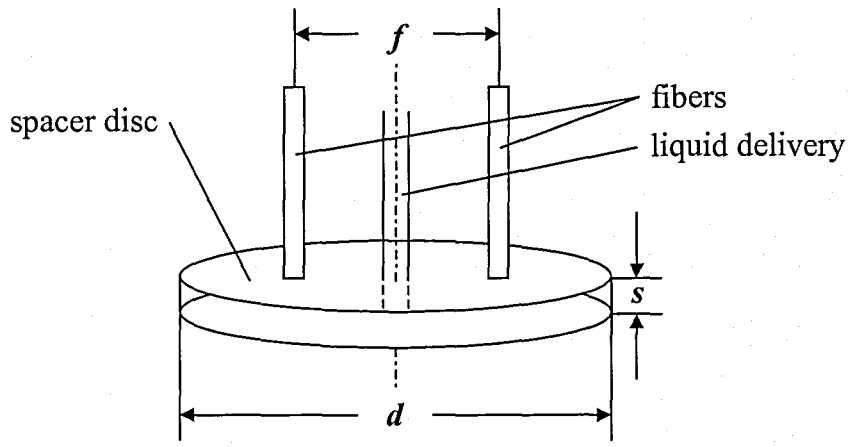

Figure 5-6. PSD with fiber position relative to PSD.

This drophead design has the major advantage of generating the desired space *s* and at the same time it provides excellent protection of the fiber end-faces. It also offers the simplest imaginable geometrical shape, which is very easy to produce accurately and presents a flat smooth drop-supporting surface without cavities.

Remember that the shape of a drophead and the position of the fibers are responsible for the distinct profile of tensiotraces that include a rainbow peak and tensiograph peak(s). Figure 5-7 shows various water tensiotraces that were obtained with different dropheads and fiber separations as outlined in Table 5-1.

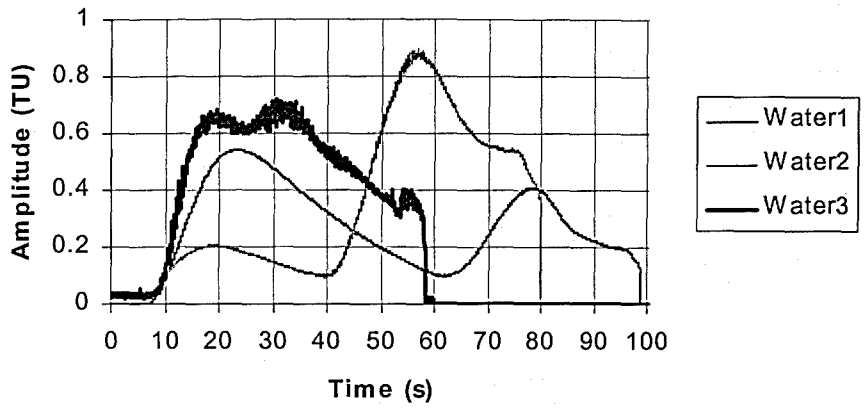

Figure 5-7. Water tensiotraces taken with differently sized PSDs and stainless steel drophead.

Tensiotrace	*d* PSD diameter [*mm*]	*f* Fiber separation [*mm*]	*s* PSD thickness [*mm*]	Pump speed [*s/stroke*]
Water1	SS drophead	SS drophead	SS drophead	200
Water2	8	6	2	200
Water3	6	4	1	200
Ethanol1	SS drophead	SS drophead	SS drophead	200
Ethanol2	6	6	3	200
Ethanol3	8	4	2	200
Ethanol4	6	4	3	429

Table 5-1. PSD dimensions for various measurements of different liquids.

A flat stainless steel knife-edge drophead, as described in the previous section, was used to generate the tensiotrace Water1. The aim of the PSD studies was to prove that there exists a drophead dimension with its associated fiber separation that would give a similar result as that created with a stainless steel drophead. Although the experiments have not been carried out exhaustively, it can clearly be seen from the tensiotraces in Figure 5-7 that this goal can be achieved by varying the PSD dimensions *d*, *s*, and the fiber separation *f*. The characteristic features seen for the tensiotrace Water2 in Figure 5-7 are undoubtedly evidence, since well-defined rainbow and tensiograph peaks exist. The level of noise seen is a result of the unoptimised working conditions and is not anticipated to be a problem. The studies of a PSD drophead have centred on the use of ethanol to simulate tensiotraces given by liquids with low surface tension. Figure 5-8

shows ethanol tensiotraces obtained with different dropheads and fiber separations. Also see Table 5-1 for more information.

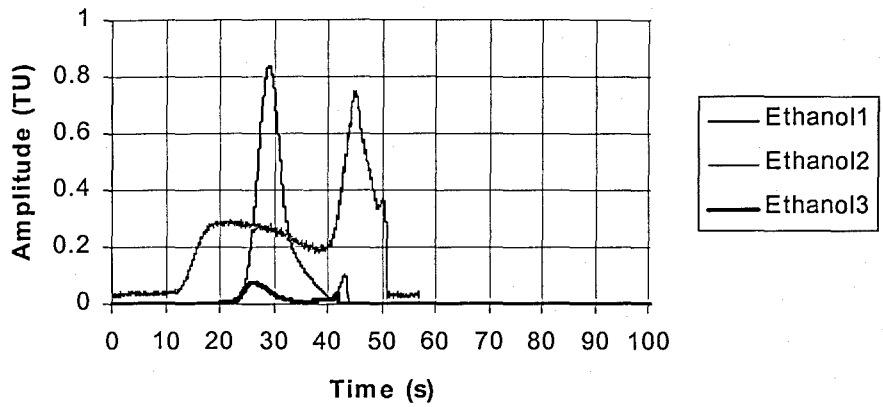

Figure 5-8. Ethanol tensiotraces taken with differently sized PSDs and stainless steel drophead.

Comparing the tensiotrace Ethanol1, which was obtained with a flat stainless steel knife-edge drophead as discussed in the previous section, with the tensiotrace Ethanol2 clarifies the advantage of a PSD design approach. The information content and profile of the trace Ethanol2 are very different to the trace Ethanol1, for which the tensiograph peak is not well defined and the principal features of the trace are all contained in the second half of the trace. This disadvantage, which has its nature in the fact of using the same drophead (optimised for water in these studies) for a vast variety of liquid samples, had to be looked into in more detail and led to the development work of a dimensionally invariant representation of tensiotraces, which is briefly discussed below in this section. Water and ethanol provide two liquids with a relatively high surface tension and a relatively low surface tension respectively and were chosen to simulate the two boundaries for a range of surface tensions of different liquids. The experiments of the PSD concentrated on the physical feasibility of such a drophead design and did not consider any chemical resistance studies of the drophead material and hence the use of water and ethanol was justified. Later in this chapter various reasons for using a material other than Plexiglas will be discussed and a final drophead design is given.

5.3.2 *Dimensionally Invariant Representation of Tensiotraces*

The observation that the tensiotrace profiles for water on a drophead (d=8mm) with fiber separation f=6mm and PSD thickness s=2mm and that of ethanol on a drophead (d=6mm) with fiber separation f=4mm and PSD thickness s=3mm are similar, strongly

suggested the utility of a dimensionally invariant representation of tensiotraces. The variation in pump speed for the ethanol tensiotrace (see Table 5-1) lengthens the drop period to that seen for liquids of higher surface tension. Figure 5-9 shows these two tensiotrace profiles of water and ethanol that have been obtained with dissimilar dropheads and different pump speeds.

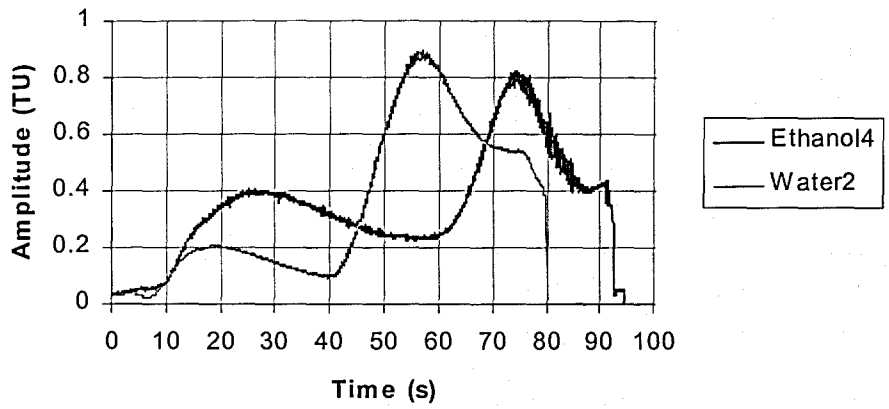

Figure 5-9. Tensiotrace comparison of different liquids taken with differently sized PSDs.

These tensiotraces are the result of a non-rigorous experimental procedure, but strong evidence suggests [5-4], using an approach via the Laplace equation (2-18) and the principal radii of a liquid drop as shown in Figure 2-8, that a continuously varying set of parameters, including the nature of the LUT, can give rise to an identical tensiotrace. The practical importance of this phenomenon is the utilisation of application specific dropheads, which can be optimised for the representation of extensive information content or the measurement of particular physical and chemical properties for example.

5.4 Flat Quartz Drophead

Previous sections of this chapter described several drophead designs and their related pros and cons, which finally led to a new flat quartz drophead design that is discussed in this section. The material of a PSD, as mentioned in Section 5.3, is obviously neither robust nor chemically inert enough to be considered for anything other than development work, and therefore quartz was chosen to replace the Plexiglas disc. Quartz meets the specific characteristics required by a robust and reproducible drophead that is easy to clean, withstands any chemical attacks from aggressive liquids [5-5], and protects the optical fibers with minimum optical constraints (see Figure 5-5 (a)). The flat quartz drophead consists of two parts as illustrated in Figure 5-10.

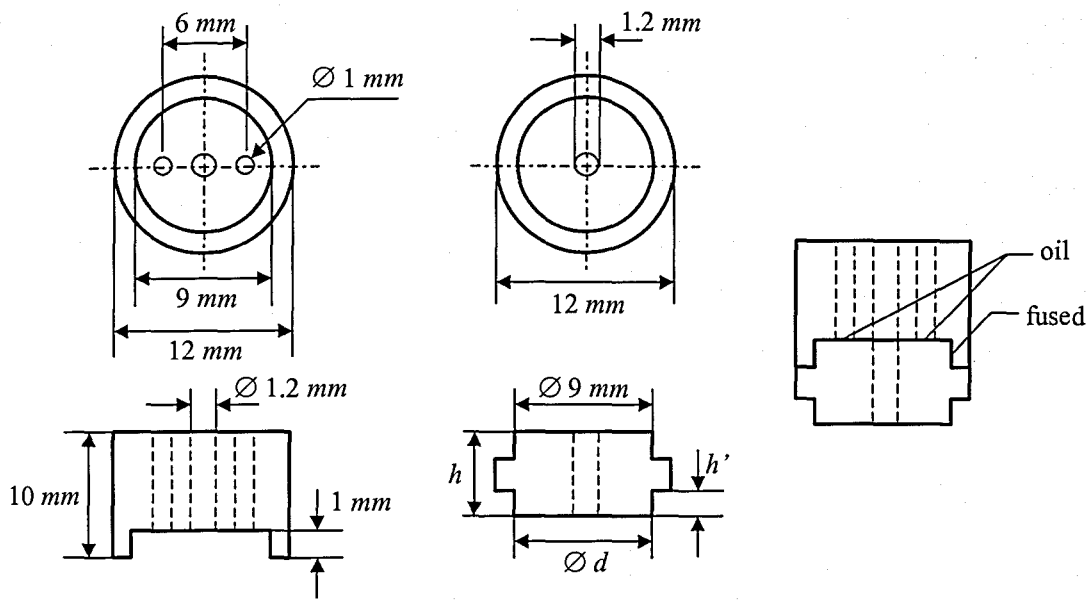

Figure 5-10. Dimensions of a cylindrical flat quartz drophead and the assembly of the two quartz drophead parts.

The optical silica fibers pass through precision-drilled holes of the upper quartz section of the drophead, but do not enter the lower quartz spacer disc. This guarantees that the fibers accurately retain their desired position and separation distance. Subsequent to fiber insertion, a quartz spacer disc is fused [5-6] into the gap of the upper part of the drophead as shown in Figure 5-10. Prior to the fusing process, refractive index matching oil is applied to the surface of the spacer disc in order to avoid Fresnel losses as described in Chapter 2. The numerical aperture (Eq. 2-9) and position of light injection into a pendant droplet are precisely defined by the optical properties of the quartz spacer disc, whilst h (see Figure 5-10) maintains the optical fibers the requisite distance from the lower surface of the drophead to produce optimal tensiotraces. Application specific dropheads can be manufactured by adjusting the dimensions h' and d of the quartz spacer disc (see Figure 5-10). A stainless steel liquid delivery tube is moulded into the centre-hole of the quartz spacer disc and fitted through a precision-drilled hole of the upper drophead section.

Concluding it can be said that most of the weaknesses considered in previous drophead designs have been eliminated. Cavities that resulted from interfaces between fibers and boreholes or between the knife-edge and the end-face of the drophead do not exist anymore. Fibers are not exposed to the LUT and yet the light intensity injected into a liquid drop barely attenuates passing through the thin quartz disc at the end-face of the drophead. Manufacturing thin quartz discs to high precision is easy compared to complex systems such as concave or knife-edge dropheads. The positioning of fibers is

only depending on the dimensions of the thin quartz disc and does not require precision-drilled and accurately distanced boreholes. The end-face of a flat quartz drophead is now resistant against almost all chemicals and organic solvents and can easily be cleaned. The only remaining disadvantage, compared to previous drophead designs, is its slightly worse first-time wetting capability, but this can be solved with an external jet of LUT that moisturises the end-face of the drophead just before the use of the tensiograph.

CHAPTER 6

SYSTEM ENGINEERING DEVELOPMENT

In this chapter various aspects that have been described in previous chapters from a single component point of view will now be discussed in a more apparatus embedded manner. The vibration damping system in Section 6.1 examines briefly the purpose of anti-vibration devices and covers then the vibration damping issue with regard to a tensiographic system. Section 6.2 begins with an introduction to Peltier elements, which is followed by a discussion of an integrated thermally controlled Peltier based module and its role as a temperature-keeping device in a tensiograph. Liquid delivery systems such as a stepper motor driven pump and constant head delivery form the basis of the discussion in Section 6.3, in which the emphasis is put on the pros and cons of using these devices in a liquid drop forming system. Section 6.4 illustrates the effects that stray light and evaporation of a liquid drop can have on the recording of a data set over the time of the life cycle of a drop. McMillan and the author of this thesis came up with the new idea of evaluating the performance of a complete system, with multiple noise and error sources (mechanical, optical, electrical), by using the information content and error budget approach. Section 6.5 describes how this approach is applied to a tensiographic apparatus. The system integration of a tensiograph is finally discussed in Section 6.6 of this chapter.

6.1 Vibration Damping System

Section 1.4.6 mentioned briefly the cause for disturbing vibration effects and Section 2.1.3.2 discussed mechanical vibration issues theoretically that usually diminish the overall performance of sensitive measuring equipment. These disturbing vibrations are in most cases twofold from an instrumentation point of view, i.e. external building vibrations and internal vibrations generated by cooling fans, electromagnetic switches, stepper motors, etc. Without proper contemplation of these vibration issues, a design of a sensitive measuring device will most likely be unsuccessful in terms of delivering the

expected high quality results. Therefore external as well as internal vibration sources have to be considered during the design process of an instrument. Figure 6-1 illustrates the principle of a vibration damping system as it is used in a tensiograph.

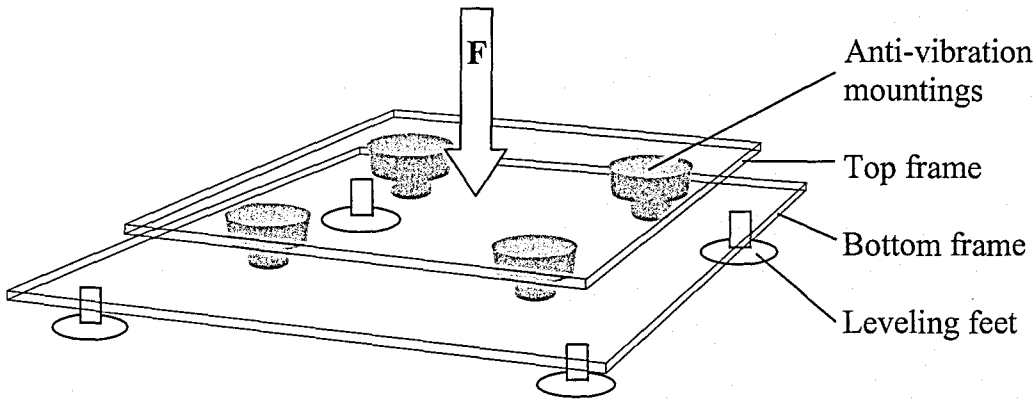

Figure 6-1. Vibration damping system of a tensiographic apparatus.

A bottom frame, resting on four levelling feet, forms the main supporting platform for all additional components that constitute a tensiograph. Later sections of this chapter describe these parts in more detail but in this section a more general approach has been chosen to describe an anti-vibration system. All vibrating devices, including a cooling fan, stepper motor pump, switch mode power supply, are placed onto this bottom frame. A top frame, which is separated from the bottom frame by anti-vibration mountings, supports the components of a tensiograph that are susceptible to external and internal vibrations. The anti-vibration feet need to be loaded with a certain mass m [kg] to operate properly (see Picture A2-6), which is here accomplished by mounting the thermal module (see Section 6.2) onto the top frame. The thermal module has to be located on the top frame in such a way that the resulting force

$$F = mg \qquad (g[ms^{-2}]\, gravitational\ acceleration)$$

acts on the centre point and perpendicular to the top frame as illustrated in Figure 6-1. By using the levelling feet of the anti-vibration system, it is always possible to vary the direction of the force vector F relative to the top frame. This fine tuning mechanism allows the user of a tensiograph to achieve both an equally distributed weight over the four existing anti-vibration mountings and the accurate levelling of the drophead incorporated in the temperature controlled environment, which will be further discussed in Section 6.2.

In order to test the performance of the anti-vibration system of a tensiograph, the following experiment was conducted. A flat stainless steel drophead, as discussed in

Chapter 5, was mounted vertically onto the surface of the top frame (see Figure 6-2) of an anti-vibration system as shown in Figure 6-1. A pendant drop of water ($50\mu l$) served as a vibration detector. An optical signal, injected into the drop through a source-fiber, was then transmitted via a collector-fiber to a light-to-electronic converter unit after its modulation that resulted from vibration and was subsequently recorded over time. Figure 6-3 shows the results that were recorded after a plastic ball ($1kg$) had been dropped from $1m$ above the surface of the workbench on which the experiment was carried out.

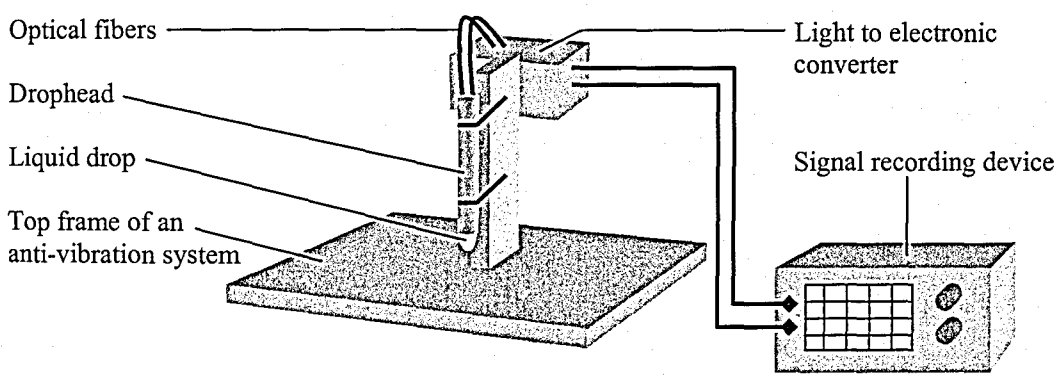

Figure 6-2. Experimental setup for anti-vibration system studies.

These results illustrate two vibrating instances caused by the impact of the plastic ball on the surface of the workbench, which initiated a number of responses from the anti-vibration system and the suspended liquid drop at the end-face of the drophead. In the first case (Figure 6-3 (a)), the top frame of the anti-vibration system was loaded with a mass of $8kg$, which shows clearly a quantitatively poorer performance than a system that had been loaded with a mass of $16kg$ as illustrated in Figure 6-3 (b). The amplitudes of the oscillating signal are generally greater and the decay of these amplitudes is slower in Figure 6-3 (a), which is due to the usage of the anti-vibration feet under unoptimised conditions (see Picture A2-6). It is also understood that the rather complex graphical representation of the vibrating signals include primarily two superimposed oscillations, namely the oscillations of the pendant liquid drop and the anti-vibration feet. It can be seen from Figure 6-3 (a) that the motion of the anti-vibration feet keeps the oscillating amplitude of the vibrating pendant drop for about $2s$ ($3s$ to $5s$) almost at a constant level, while Figure 6-3 (b) shows a more rapid decay of the oscillating amplitudes within this range due to a change of the overall weight resting on the anti-vibration feet. The experiment of generating an impact on the surface of a workbench falls into the category of external vibration isolation as outlined above, whereas the following discussion concentrates on internal vibration issues.

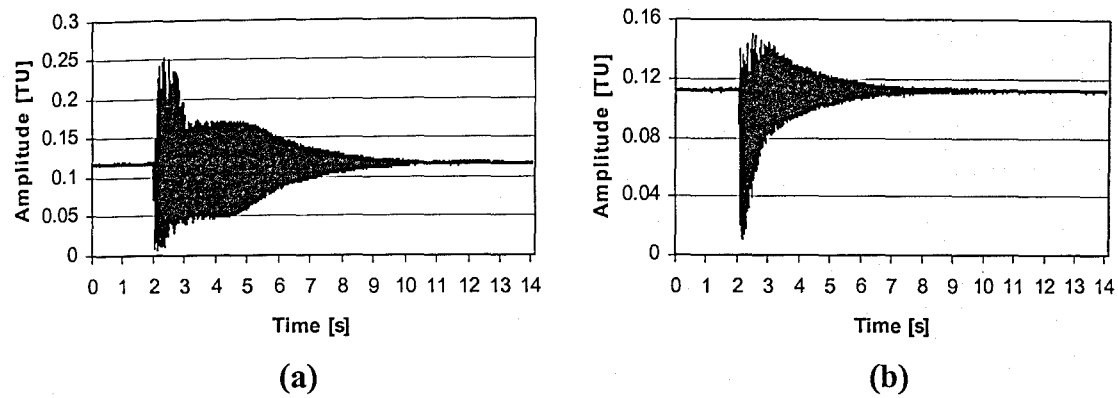

(a) (b)

Figure 6-3. Anti-vibration system test, (a) loaded with 8kg and (b) loaded with 16kg.

For the next experiment the anti-vibration feet were removed and the top frame, including the drophead assembly as shown in Figure 6-2, was placed directly onto the surface of the bottom frame of the mechanical structure shown in Figure 6-1. A tensiotrace, generated from the life cycle of a water drop, was then recorded and the top of the rainbow peak magnified as shown in Figure 6-4 (a). The same procedure was repeated but this time with the anti-vibration feed mounted back in place. Figure 6-4 (b) shows the result after recording it during the life cycle of a water drop. It has to be noted that there were several vibrating devices bolted to the bottom frame of the structure, which are not shown in the figures above. A stepper motor pump and a switch mode power supply (further discussed below) were respectively used to deliver the liquid to the drophead and supply the necessary power for the whole experimental arrangement. These devices generate vibration that has to be tackled and as can be seen from the magnified top of the rainbow peak, this is accomplished by using anti-vibration feet, which damp the vibration to a tolerable value (see Figure 6-4 (b)) compared to the noisy signal that had been generated without vibration precautions (see Figure 6-4 (a)).

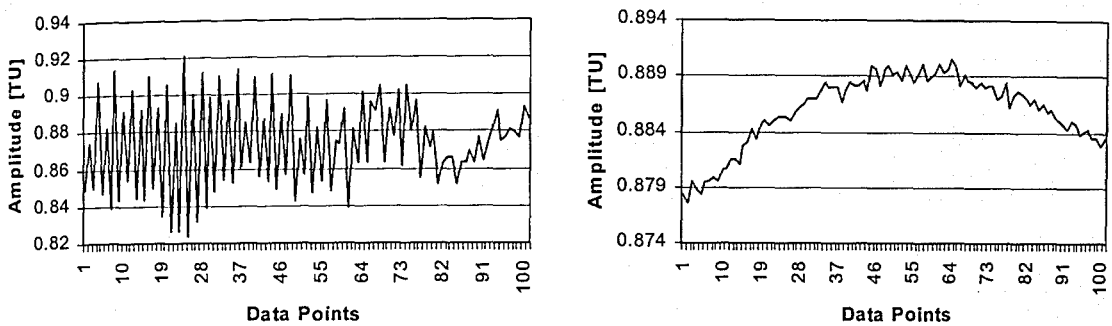

(a) (b)

Figure 6-4. Top of a tensiotrace rainbow peak, (a) without and (b) with vibration damping.

Concluding it can be said that it is important to consider internally and externally produced vibration. The exposure of the tensiograph to external vibration can usually be limited by setting up the instrument in an environment that generates very little or preferably no vibration, i.e. far away from machinery like motors, transformers, generators, etc., on a concrete stand instead of a swinging wooden floor, and isolation from traffic-induced vibration [6-1] are only a few examples to prevent excessively high external vibration amplitudes. However, the anti-vibration feet in a tensiograph will damp any building vibration that occurs and is greater than 3.6*Hz* (see Picture A2-6). Internal vibrations, generated by active components in a tensiograph, can be tackled more easily, because of their inherent nature of being greater than 10*Hz* with relatively small amplitudes, which will be efficiently damped (see Figures 2-11 and 6-4).

6.2 Thermal Module

Early 19th century scientists, Thomas Seebeck and Jean Peltier, first discovered the phenomena that are the basis for Peltier devices. Seebeck found that if one placed a temperature gradient across the junction of two dissimilar conductors, electrical current would flow [6-2]. Peltier, on the other hand, discovered that passing current through two dissimilar conductors caused heat to be either emitted or absorbed at the junction of the materials [6-3]. Employing this characteristic in a thermoelectric (TE) module is an effective technique that is utilised in solid-state heat pumps. The Peltier devices MELCOR CP 1.4-127-10L (see Picture A2-3) used for the TE module in a tensiograph consist of an array of Bismuth telluride semiconductor pellets [6-4], which have been 'doped' so that one type of charge carrier – either positive or negative – carries the

majority of current [6-5]. The pairs of P/N pellets are configured electrically in series, but thermally in parallel (see Figure 6-5).

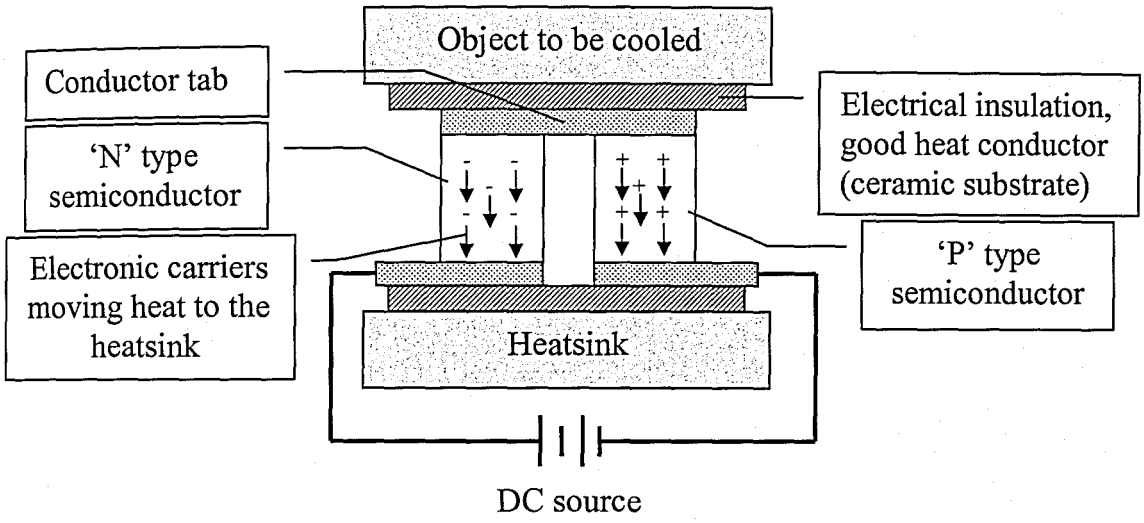

Figure 6-5. Solid-state heat pump assembly using a Peltier device.

Ceramic substrates provide the platform for the pellets and the small conductive tabs that connect them. When DC voltage is applied to the module, the positive and negative charge carriers in the pellet array absorb heat energy from one substrate surface and release it to the substrate at the opposite side. The surface where heat energy is absorbed becomes cold and the opposite surface where heat energy is released becomes hot. In other words, the circulating current carries heat from the thermal load to some type of heatsink, which can efficiently discharge the heat into the outside environment. The direction of heat pumping in a TE module is fully reversible. Changing the polarity of the DC power supply causes heat to be pumped in the opposite direction – a cooler can then become a heater.

Figure 6-6 illustrates the cross section of a thermal module as it is used in a tensiographic apparatus. This module incorporates a relatively large brass block to store the thermal energy Q that is needed to keep a pendant liquid drop, hanging from the drophead, at a constant temperature over the life cycle of the drop. The brass block was originally chosen to provide the necessary thermal properties as well as the appropriate weight for the spring mount anti-vibration feet shown in Picture A2-6. A later reassessment of the thermal module in conjunction with the existing anti-vibration system suggests that an aluminium block in comparison to a brass block would probably be more efficient (see Table A3-1). The weight that would be lost due to the use of an aluminium block could be added by mounting a heavier top frame (Figure 6-1).

However, the thermal module described in this thesis incorporates a brass block instead of an aluminium block.

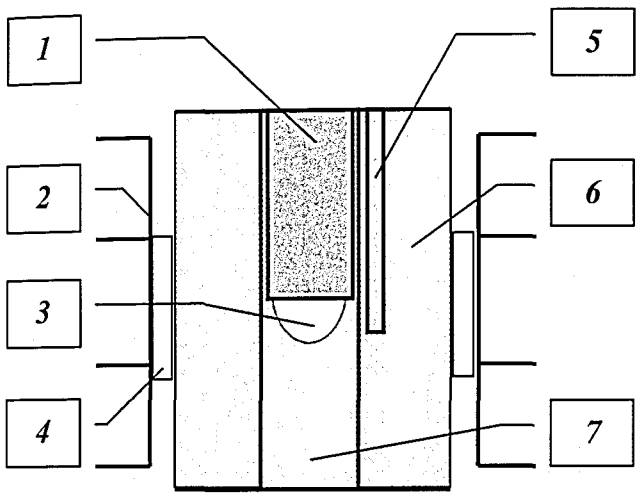

[1] Drophead support tube, stainless steel, ∅ x L: 12 x 150 mm, filled with stainless steel inserts
[2] Aluminium heatsink, 6 fins, H x W x D: 180 x 82 x 68 mm
[3] Liquid drop hanging from a stainless steel drophead, ∅ 9 mm
[4] Peltier H x W x D: 40 x 40 x 4.7 mm
[5] Temperature probe ∅ x L: 6 x 150 mm
[6] Brass block, H x W x D: 195 x 80 x 50 mm
[7] Through hole ∅ 12 mm

Figure 6-6. Cross-section of the Peltier based thermal module in a tensiograph.

One approach to describe the behaviour of a tensiographic thermal system, as shown in Figure 6-6, is finite element analysis (FEA) [6-6]. FEA consists of a computer model of a material or design that is analysed for specific results. Modifying an existing product is utilised to qualify the product for a new service condition. A modification of the tensiographic TE module was not anticipated during the time the author of this thesis was implicated with TE module issues and a more practical approach, described below in this section, had been chosen to analyse the brass-block TE module of a tensiograph. FEA could, however, be an important tool in relation to a redesign of the existing tensiographic TE module, involving an aluminium block in order to reduce the size of the module and also to increase efficiency.

The aim of the TE module (Picture A2-9) in a tensiograph is to keep the temperature of a pendant drop as constant as possible. An experimental setup as shown in Figure 6-7 was used to study the behaviour of a TE module consisting of two heatsinks **HS**, two Peltier devices **PD**, the drophead **DH**, and the brass block **BB**. A liquid sample **LS** can be drawn through the liquid delivery tube **LDT1** into the syringe of the pump **P** XP3000 (Picture A2-8) by moving the syringe plunger downwards. Subsequent to the filling procedure of the syringe the direction of the plunger movement changes and the liquid sample **LS** is pushed through the liquid delivery tube **LDT2** to the end-face of the drophead **DH**. Hence the temperature of a gradually growing liquid drop can then be measured with the thermometer **TM** Testo 925 (Picture A2-5) whose temperature probe is located in the borehole of the brass block **BB** and close to the end-face of the drophead **DH**. The temperature probe Pt100 (Picture A2-4) and the

electronic controller **EC** Cni3252-C24-DC (Picture A2-7) are part of a closed loop controlling unit (further discussed below in this section), which control the process temperature close to the end-face of the drophead **DH** according to the set point temperature of the TE module.

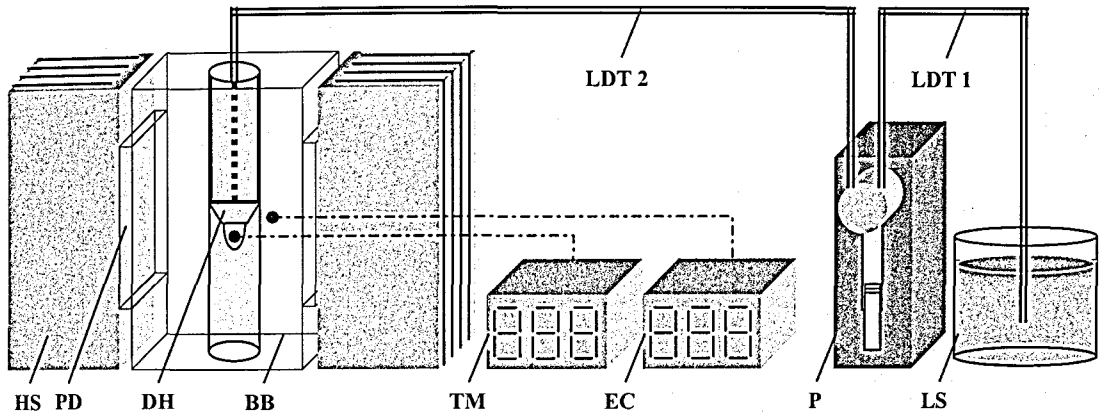

Figure 6-7. Experimental setup for thermal studies of a tensiographic apparatus.

For good thermal conductivity the stainless steel drophead **DH** (Picture A2-10) is filled with cylindrically shaped aluminium inserts with a centre hole to fit a stainless steel tube, which connects the end-face of the drophead **DH** and the liquid delivery tube **LDT2**. Apart from the possibility to measure the temperature of a liquid drop constantly with the thermometer **TM**, Figure 6-7 illustrates the TE module and liquid delivery system of an industrialized tensiograph used for realistic liquid analysis. The measurement of the temperature of a liquid drop with the thermometer **TM** as shown in Figure 6-7 would obviously diminish the concept of a gradually growing liquid drop under gravity and is therefore only part of this particular experimental setup, which concentrates on temperature studies only. To verify the effectiveness of the TE module as a temperature-keeping device, water samples with different temperatures were pumped via the liquid delivery tubes **LDT1** and **LDT2** to the end-face of the drophead **DH** using various plunger speeds of the pump **P**. The aim of this experiment was to prove that a gradually growing suspended liquid drop at the end-face of the drophead **DH** is continually kept at the set point temperature of the TE module over the life cycle of the drop. Figure 6-8 shows the results of this experiment.

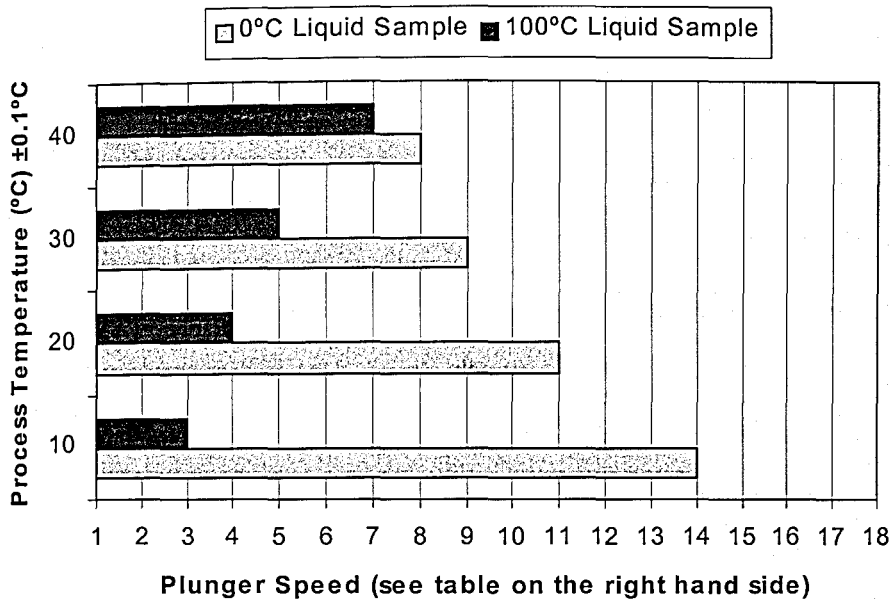

No	s/stroke
1	600
2	300
3	100
4	40
5	30
6	15
7	10
8	7.5
9	6.0
10	5.0
11	4.3
12	3.7
13	3.3
14	2.9
15	2.6
16	2.2
17	1.9
18	1.6

Figure 6-8. Heat conductivity performance of a tensiographic thermal module.

The length of the grey bars in Figure 6-8 illustrate the maximum speed the plunger of pump **P** can move upwards, forming a liquid drop at the end-face of the drophead **DH**, in order to adjust a 0°C water sample to certain process temperatures (±0.1°C) of the TE module, which had been selected before the measuring procedure. The process temperature of the liquid drop differed to the set point temperature of the TE module by more than ±0.1°C when the speed of the plunger of pump **P** was greater than the values represented by the maximum length of the grey bars (see Figure 6-8). Black bars in Figure 6-8 exemplify the same as grey bars with the exception that a water sample at 100°C was employed. There are several reasons for using water as the LUT in a heat conductivity experiment as described above, of which

- Availability
- High specific heat (see Table A3-1)
- Easy to set and hold at 0°C and 100°C without additional controlling devices

are the most important. Water is always available in laboratories or similar environments; consequently it can be obtained and used as a sample liquid without any problems. More important than the availability is the fact that the specific heat of water is very high and thus it absorbs, compared to other liquids, a relatively high amount of thermal energy Q of the brass block **BB** during the life cycle of a liquid drop. In this case it can simply be verified if the brass block **BB** is able to supply enough thermal energy Q to keep the temperature of a gradually growing suspended drop at a constant level. In order to cover a wide range of differences between the temperature of the

liquid sample **LS** and the brass block **BB** it is necessary to cool down or to heat up the liquid sample **LS** to a fixed and well-known temperature, which is easily done by using ice cubes in water (0°C) or by heating up a water sample to the boiling point (100°C). The thermal conductivity of water (see Table A3-1) compared to other liquids, like alcohol for example, is relatively high [6-7]. This fact diminishes the usefulness of water as the LUT for thermal conductivity studies slightly, but it does not have a significant effect on the results shown in Figure 6-7. The user of a tensiograph must only be aware of the possibility that in some cases it might be necessary to reduce a particular plunger speed by one unit if the LUT has got a lower thermal conductivity than water. The liquid sample **LS** is usually at room temperature before it is pumped to the end-face of the drophead **DH** and the speed of the plunger of pump **P** can then be adjusted between No 10 (5.0*s/stroke*) and No 13 (3.3*s/stroke*), or lower of course, for liquids with thermal conductivities ranging between $0.13 Wm^{-1}K^{-1}$ and $0.6 Wm^{-1}K^{-1}$ respectively, to work within the temperature range (10°C to 40°C) of the brass block **BB** without affecting the set point temperature of a pendant liquid drop.

The next experiment concentrates still on temperature studies, but this time from a different point of view. A test circuit, schematically shown in Figure 6-9, was used to examine the reliability of the controller driver circuit **CDC** (Schematic A2-1), the power booster circuit **PBC** (Schematic A2-2) and the full temperature range of the Brass Block **BB** related to the output voltage range of the electronic controller **EC** in Figure 6-7.

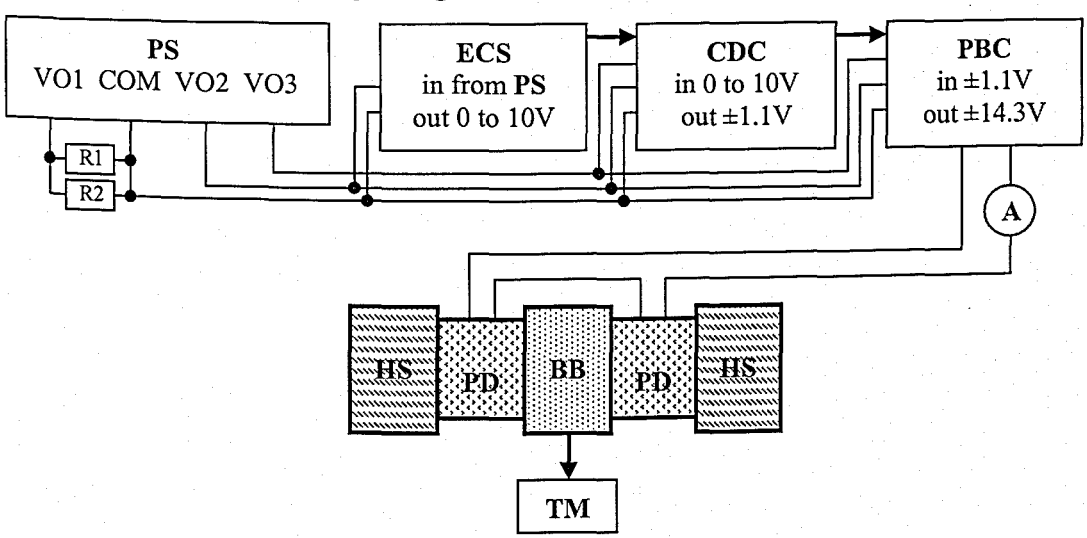

Figure 6-9. Schematic of a temperature test of a tensiographic TE module.

The output voltage of the electronic controller **EC** depends on its input and controlling parameters as described below in this section, which gave rise to a temporary replacement of the electronic controller **EC** with the electronic controller simulator

ECS (Figure 6-9) that can be adjusted manually from $0V$ to $10V$. The switch mode power supply **PS** (Picture A2-2) supplied the test circuit with DC power. To draw the minimum load current from the switch mode power supply **PS**, which is necessary for proper operation, resistors R1=R2=$10R/3W$ are connected across the output terminals VO1 and COM. At the beginning of the experiment (power off) the temperature of the brass block **BB**, close to the end-face of the drophead **DH** (Figure 6-7), and the room temperature of the laboratory in which the experiment took place, were measured (24.7°C) using the thermometer **TM** (Picture A2-5). The power supply **PS** was then switched on and the output voltage of the electronic controller simulator **ECS** was adjusted to $10V$. After 120 minutes the electric current ($1100mA$) through the Peltier devices **PD** and the temperature (60.3°C) of the brass block **BB**, close to the drophead **DH**, were measured with the ampere meter **A** and the thermometer **TM** respectively. Marker **[a]** of Figure 6-10 illustrates this stage of the experiment.

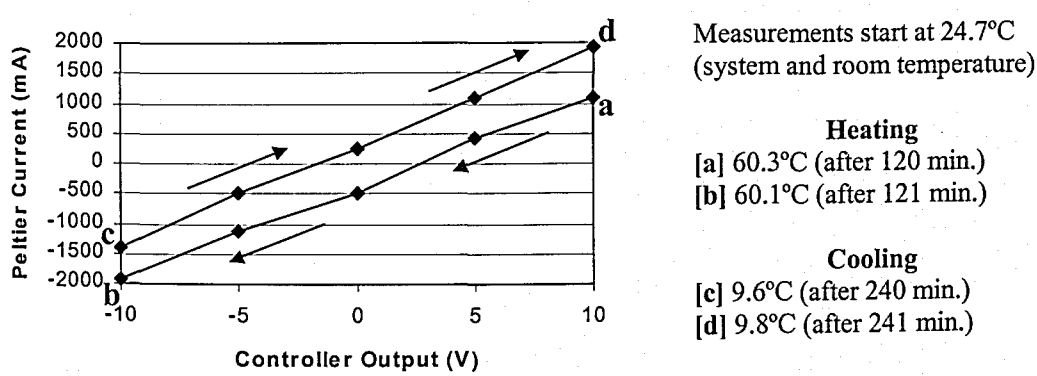

Figure 6-10. Hysteresis loop of a tensiographic thermal module during heating and cooling.

Note that the temperature of the brass block **BB** (60.3°C) was reached after 60 minutes, but 60 more minutes elapsed before the temperature was recorded to ensure that it was absolutely steady. In other words, 60.3°C is the maximum temperature of the brass block **BB** the TE module in Figure 6-9 can reach at room temperature 24.7°C. The measuring procedure continued as followed:

- Reduce output voltage of **ECS** to $5V$; measure current ($411mA$) using **A**.
- Reduce output voltage of **ECS** to $0V$; measure current ($-484mA$) using **A**.
- Reduce output voltage of **ECS** to $-5V$; measure current ($-1135mA$) using **A**.
- Reduce output voltage of **ECS** to $-10V$; measure current ($-1940mA$) using **A** and temperature (60.1°C) of **BB** close to **DH** using **TM**; between markers **[a]** and **[b]** of Figure 6-10 elapsed 1 minute.

- After 119 more minutes measure current (-1407*mA*) using **A** and temperature (9.6°*C*) of **BB** close to **DH** using **TM**; marker **[c]** of Figure 6-10 illustrates this stage of the experiment. Note that the temperature of **BB** was absolutely steady at this point, which means, that 9.6°*C* is the minimum temperature of the brass block **BB** the TE module in Figure 6-9 can reach at room temperature 24.7°*C*.
- Increase output voltage of **ECS** to -5*V*; measure current (-501*mA*) using **A**.
- Increase output voltage of **ECS** to 0*V*; measure current (258*mA*) using **A**.
- Increase output voltage of **ECS** to 5*V*; measure current (1103*mA*) using **A**.
- Increase output voltage of **ECS** to 10*V*; measure current (1938*mA*) using **A** and temperature (9.8°*C*) of **BB** close to **DH** using **TM**; between markers **[c]** and **[d]** of Figure 6-10 elapsed 1 minute.

The hysteresis of the electric current through the Peltier devices **PD**, that can be seen in Figure 6-10, is a result of the inherent Seeback effect of these devices, which generates a back EMF due to a temperature difference between the cold phase and the hot phase of the Peltier devices **PD**. Figure 6-10 also reflects the linear characteristic of Peltier devices in a TE module. Concluding it can be said that the TE module of a tensiograph operates perfectly over the entire temperature range (10 to 40°*C*) at room temperatures ranging from 15°*C* to 24°*C*, which is a requirement of McMillan and the author.

A closed loop circuit as schematically shown in Figure 6-11 is an ideal structure, which automatically controls the process temperature of the brass block **BB** by comparing this value with a set point temperature of the TE module.

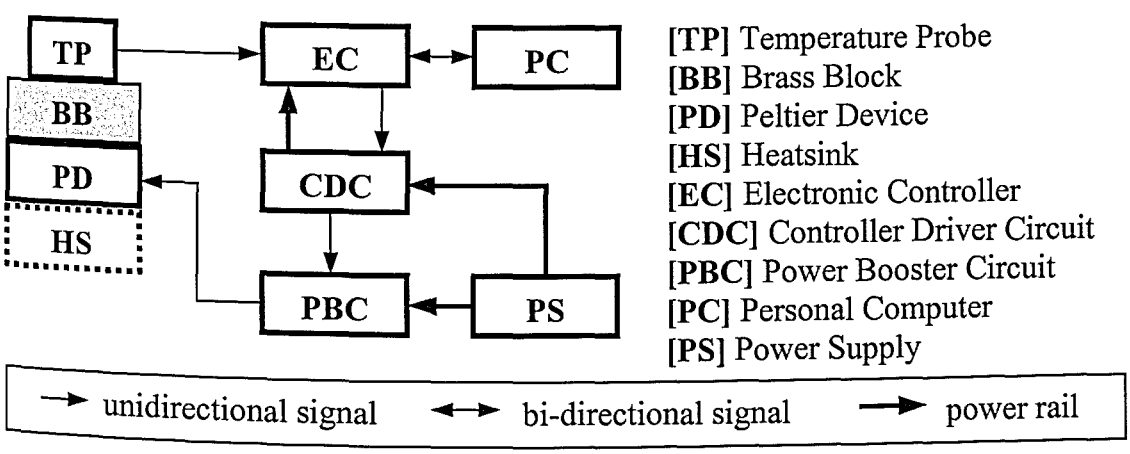

Figure 6-11. Structure of a tensiographic closed loop temperature controlled unit.

The electronic controller **EC** (Picture A2-7) is a proportional-integral-derivative (PID) type of feedback controller whose output is based on the difference between the user-defined set point and the measured process variable. Each element of the PID controller refers to a particular action taken on the difference [6-8]:

- **Proportional:** difference multiplied by a gain K_p. It is responsible for process stability. If K_p is too low then the process value can drift away; too high and the process value can oscillate.
- **Integral:** the integral of the difference multiplied by a gain K_i. It is responsible for driving the difference to zero, but setting K_i too high is to invite oscillation or instability.
- **Derivative:** the rate of change of the difference multiplied by a gain K_d. It is responsible for system response: K_d too low and the process value will oscillate; too high and the process value will respond slowly.

The electronic controller **EC** includes an auto-tune PID option, which involves the adjustment of K_p, K_i, and K_d to achieve an optimal system response. A resistive temperature detector (RTD) serves as the temperature probe **TP** (Picture A2-4) that detects the present temperature (process value) of the brass block **BB**. The resistance R of the temperature probe **TP** is a function of the temperature ϑ and within the temperature range (-50 ℃ to +250 ℃) the relationship R=f(ϑ) is almost linear, i.e. the temperature probe **TP** adjusts its resistance proportional to the temperature of the brass block **BB**. The resistance of the temperature probe **TP** is the input value of the electronic controller **EC** and represents the process variable, which is continuously compared with the set point variable. The difference between the set point and process variables determines in conjunction with the parameters K_p, K_i, and K_d the output voltage ($0V$ to $10V$) of the electronic controller **EC**. The output signal of the electronic controller **EC** is the input signal of the controller driver circuit **CDC** (Schematic A2-1) that converts the unipolar input signal to a bipolar DC voltage ($\pm 1.1V$), which is necessary to operate the TE module of a tensiograph in heating and cooling mode. The power booster circuit **PBC** (Schematic A2-2), connected to the output of the controller driver circuit **CDC**, is then able to drive an electric current in the range of $\pm 4A$ (see operational amplifier L465A in Table A2-1) through an electric load connected to its output. The Peltier devices **PD** in the TE module of a tensiograph draw an electric current to about $\pm 1940mA$ (see above) and consequently transfer heat from the brass block **BB** to the heatsinks **HS** where it is dissipated (cooling mode), or they transfer heat from the heatsinks **HS** to the brass block **BB** (heating mode). The switch mode power supply **PS** (Picture A2-2) provides the units **EC**, **CDC**, and **PBC** with power that is required to control the temperature of the TE module (**BB**, **PD**, **HS**) in Figure 6-11

efficiently within the range of 10 ℃ to 40 ℃. The electronic controller **EC** communicates via a serial communication port RS232 of the personal computer **PC** with the acquisition software Acquire (Picture 4-1), in which a set point variable can easily be chosen using the software interface of the electronic controller **EC** as shown in Figure 6-12. This software interface also displays the current process variable to ensure that the user of a tensiograph starts the examination of liquid drops only when a steady temperature of the TE module has been reached, i.e. the difference between the set point and process temperatures is zero (Figure 6-12).

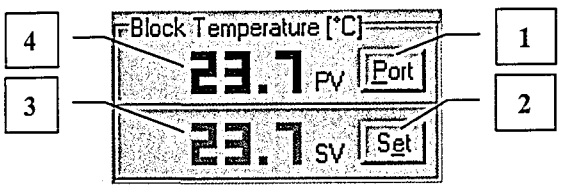

[1] Selection of the serial communication port (COM1 to COM4).
[2] Adjustment of the set point temperature (10 to 40°C).
[3] Display of the set point temperature.
[4] Display of the process temperature.

Figure 6-12. Software interface of the electronic controller of a tensiograph.

6.3 Liquid Delivery Systems

The two liquid delivery systems, namely constant head and stepper motor pump, are the subject of this section. First of all the behaviour of a constant head is explained followed by an analysis of tensiotraces that were generated using a stepper motor pump. Comparison of these liquid delivery systems emphasises the pros and cons of these devices and concludes this section.

6.3.1 Constant Head

The principle of a tensiographic constant head liquid delivery system, as it was utilised in an experimental setup, is shown in Figure 6-13. A glass beaker, termed constant head **CH**, is bolted to a solid metal rod that is adjustable in height and therefore labelled as height control **HC**. To produce a pendant drop at the end-face of the drophead **DH** pump **P** (which does not need to be exact or expensive) fills the constant head **CH** up to a level just above the outlet of the overflow **OF** with the sample liquid **SL**, followed by opening the valve **V** after the sample liquid **SL** in the constant head **CH** has reached the correct level. In order to reach the correct liquid level in the constant head **CH** pump **P**

must be deactivated and any excess liquid above the outlet of the overflow **OF** must have disappeared as illustrated in Figure 6-13.

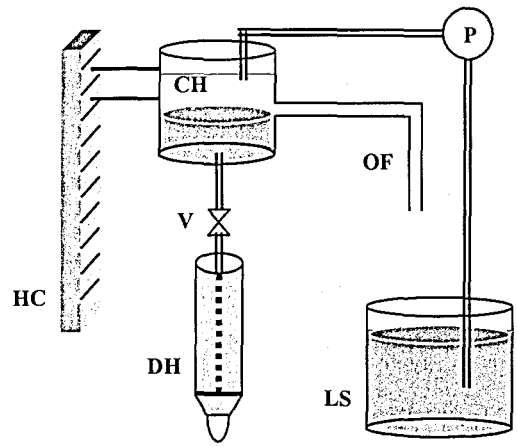

Figure 6-13. Principle of a tensiographic constant head liquid delivery system.

The liquid delivery tube between the constant head **CH** and the valve **V** is flexible allowing for height variations of the constant head **CH** without affecting the fixed height of the drophead **DH**. Varying the height of the constant head **CH** by shifting the height control **HC** up or down decreases or increases the drop period of a tensiotrace respectively. Without an automated height control **HC** it is extremely difficult to choose a particular drop period of a tensiotrace, as described below in conjunction with Figure 6-14.

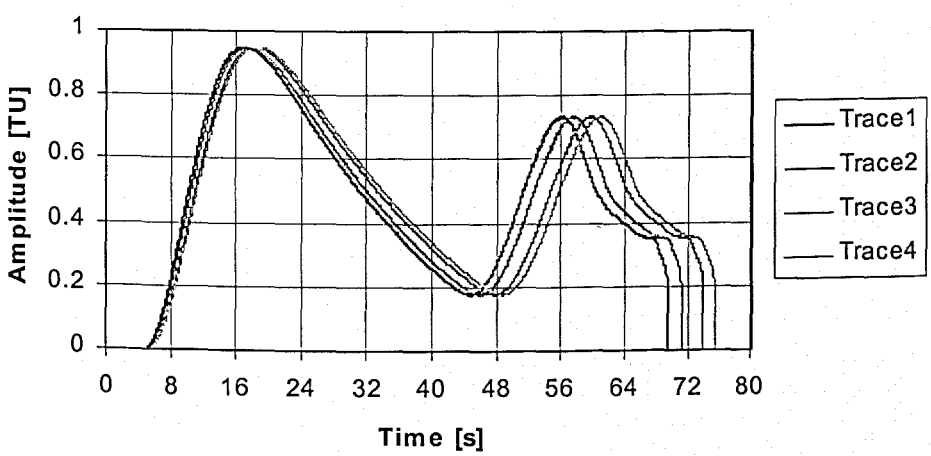

Figure 6-14. Data of Trace1 to Trace4 were acquired using a constant head liquid delivery system and water as sample liquid SL at room temperature (23.6°C) and atmospheric pressure (1018hPa). The variation in drop period is due to the changing level of the sample liquid SL in the constant head CH.

The volume ($V \approx 123 \mu l$) of a pure water drop hanging on the end-face of the drophead **DH** (Picture A2-10) – atmospheric pressure ($1018 hPa$), temperature (23.6 ℃) – is just about to fall off. This was verified by employing a stepper motor pump (Picture A2-8) and the pump-setting dialog (Picture 4-7) of the data acquisition package Acquire.

With

$$\Delta h = \frac{V}{\pi r^2}$$

follows

$$\Delta h = \frac{123 * 10^{-6}\, dm^3}{\pi * 0.15^2\, dm^2} = 0.00174 dm = 174 \mu m$$

where r is the inner radius of the constant head **CH** and Δh is the height difference of the liquid level after the consumption of the drop volume V from the reservoir of the constant head **CH**. Now it is obvious why manual exploitation of the height control **HC** is impractical considering the relatively high difference between the drop periods of tensiotraces (Figure 6-14) due to a quite small change of the liquid level ($174 \mu m$) in the constant head **CH**. Note the data of the tensiotraces shown in Figure 6-14 have been acquired successively – beginning with Trace1 – without refilling the constant head **CH** with the sample liquid **SL**. A constant head liquid delivery system is also rather susceptible to temperature and atmospheric pressure changes, thus it is difficult to run experiments in an uncontrolled environment over an extended period of time. But a constant head liquid delivery system has got advantages as well, which are discussed in Section 6.3.3.

6.3.2 Stepper Motor Pump

One of the most noticeable advantages of a stepper motor pump over a constant head liquid delivery system is the similarity in the drop period of tensiotraces acquired sequentially using the same liquid, plunger speed, drophead etc. Figure 6-15 shows the overplot of several tensiotraces that validates this statement. Precisely dispensed liquid to a drophead is in fact the reason to employ a fairly expensive stepper motor pump (Picture A2-8) contributing to the ability to fingerprint liquids of the same kind.

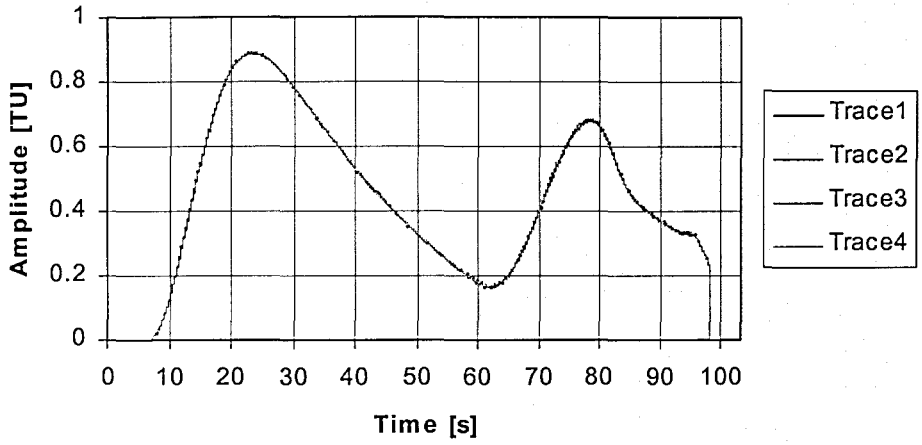

Figure 6-15. Data of Trace1 to Trace4 were acquired using a pump liquid delivery system and water as sample liquid SL at room temperature (23.3°C) and atmospheric pressure (1018hPa). The overplot of four similar data sets results in the visibility of only one trace.

Conversely, stepper motor pumps have a tendency to excite a pendant drop at the end-face of a drophead during drop formation causing increased signal noise amplitudes in the tensiotrace. Figure 6-16 shows the magnified sections for specific time periods in relation to their total drop periods shown in Figure 6-15.

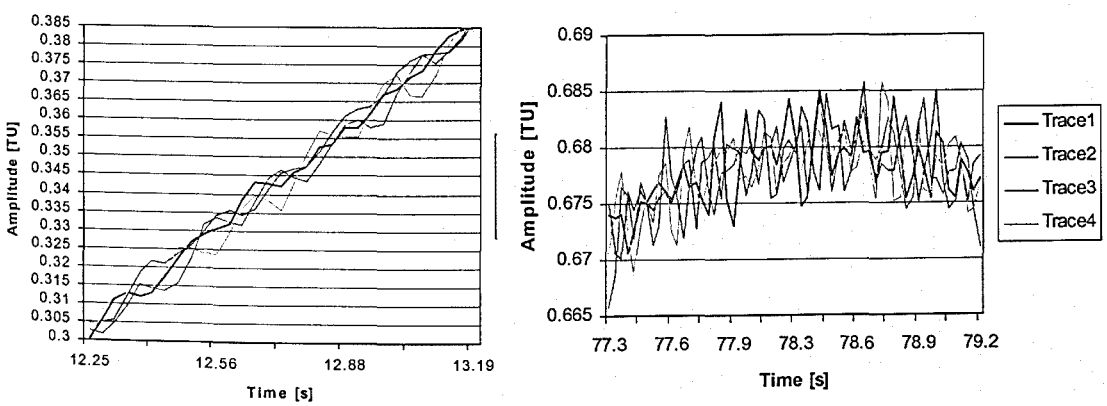

(a) (b)

Figure 6-16. Comparison of water tensiotraces Trace1 to Trace4 acquired at room temperature (23.3°C) and atmospheric pressure (1018hPa). (a) positive slope, (b) tensiograph peak. The maximum amplitude of the signal noise is less than 0.012 TU peak to peak.

It has to be noted that the maximum signal noise amplitude is very similar in sections that are moderately distant from each other, i.e. comparable noise patterns can be seen in the tensiotraces for relatively small or large drop volumes. One has to keep in mind that this particular effect is connected to the set of water tensiotraces in Figure 6-15 and diverges probably from the effect a stepper motor pump has on liquids with dissimilar properties, but the explanation for these noise patterns is the same. Consider also Figures 6-17 and 6-18 for the following description.

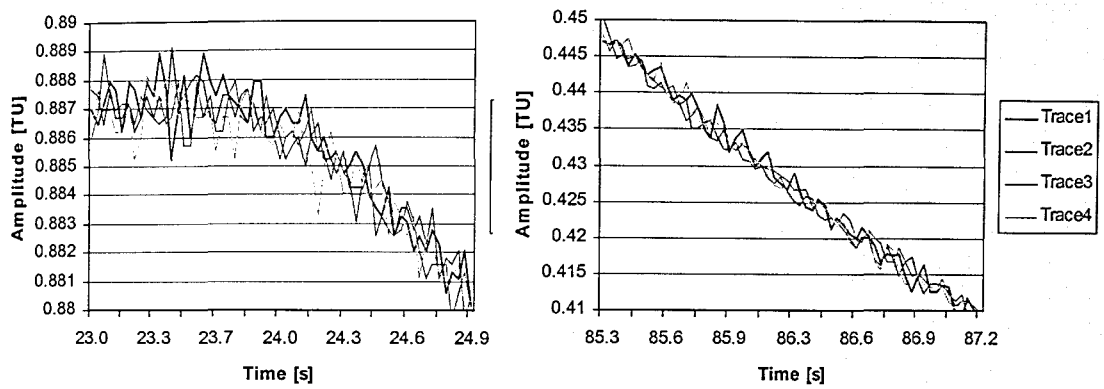

(a) (b)

Figure 6-17. Comparison of water tensiotraces Trace1 to Trace4 acquired at room temperature (23.3°C) and atmospheric pressure (1018hPa). (a) rainbow peak, (b) negative slope. The maximum amplitude of the signal noise is less than 0.005 TU peak to peak.

The theoretical coupling of light rays during the growth of a liquid drop (see Figure 2-6) may help to clarify the existence of different signal noise amplitudes in a tensiotrace. Each step of a stepper motor pump excites a pendant liquid drop causing the oscillation of the reflecting inner surface of the drop.

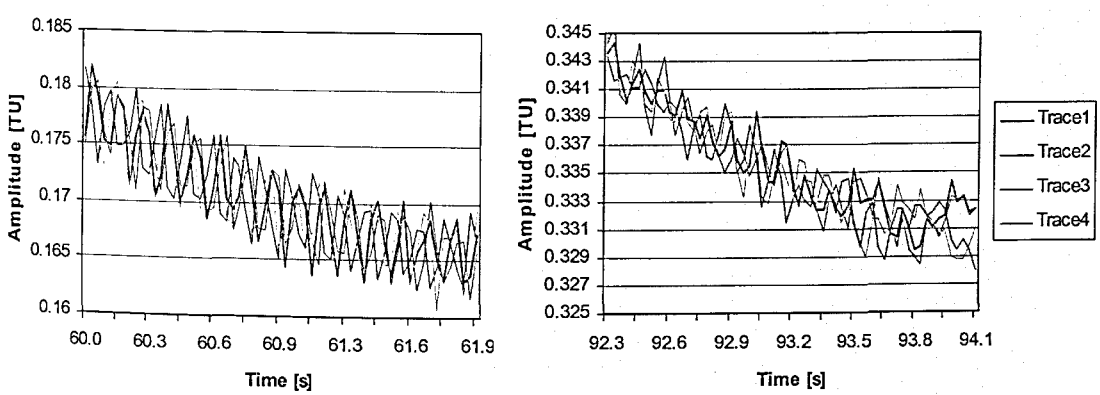

(a) (b)

Figure 6-18. Comparison of water tensiotraces Trace1 to Trace4 acquired at room temperature (23.3°C) and atmospheric pressure (1018hPa). (a) local minimum, (b) negative slope. The maximum amplitudes of the signal noise are respectively less than 0.01TU and 0.008TU peak to peak.

If V_1 is the drop volume (produced, for example, after the pump dispense time referring to the begin of the time section shown in Figure 6-16(a)) the oscillation of the reflecting inner surface of the drop (caused by single steps of the stepper motor pump) may have, depending on the curvature of the drop surface, great effect on the focal point **x** (see Figure 2-6(b), which in turn generates relatively large signal noise amplitudes. For the drop volume V_2, on the other hand, the conditions for ray coupling have changed and may therefore have only little effect on the focal point **y** (represented, for example, in Figure 6-17(a)). Consequently Figure 6-18(a) (maximum signal noise amplitudes,

compared to Figures 6-17(a) and 6-17(b), have increased) might represent the situation for the drop volume V_3 and the associated focal point **z** shown in Figure 2-6(b). There is obviously always a superimposed signal noise (varying in amplitude) in a tensiotrace caused by the micro-stepper pump (Picture A2-8). From the system engineering point of view the stepper motor pump of a tensiograph has to be optimised (decreasing the micro-step size) in order to reduce noise in a tensiotrace, but the micro-step size can only be reduced to a certain extend, hence tensiotrace-smoothing algorithms (discussed in Chapter 7) have to be applied to improve the quality of tensiotraces.

6.3.3 Comparison between Constant Head and Stepper Motor Pump

The previous two sections describe independently of each other the pros and cons of the constant head liquid delivery system and the stepper motor pump. The advantages of a constant head over a micro-stepper pump and vice versa are the subject of this section. Figure 6-19 shows the tensiotraces ConstHead and Pump acquired with a constant head liquid delivery system and a micro-stepper pump respectively.

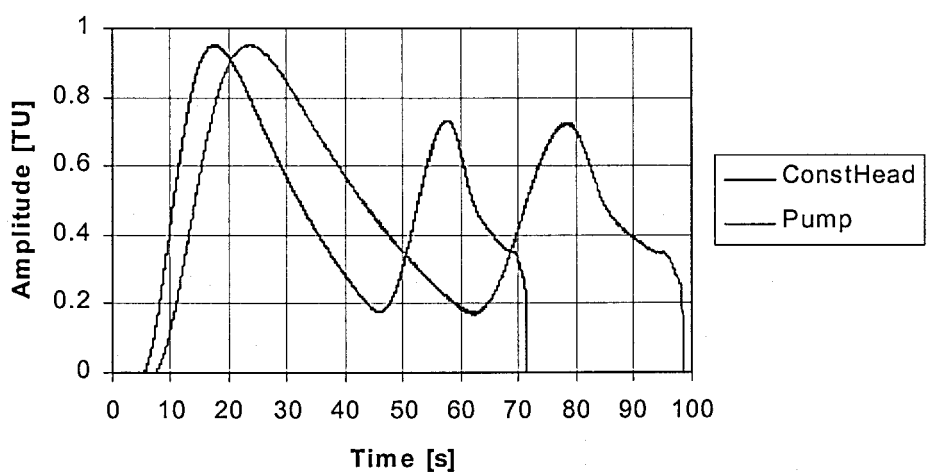

Figure 6-19. Data of tensiotraces ConstHead and Pump were acquired using water as sample liquid SL at room temperatures (23.6°C, 23.5°C respectively) and atmospheric pressure (1018hPa).

For experimental reasons the drop period of the tensiotrace ConstHead had to be less or equal the drop period of the tensiotrace Pump and was therefore adjusted to about 71*s* as illustrated in Figure 6-19. Remember it is extremely difficult to adjust the drop period of tensiotraces, acquired with a constant head liquid delivery system, manually using the height control **HC** in Figure 6-13.

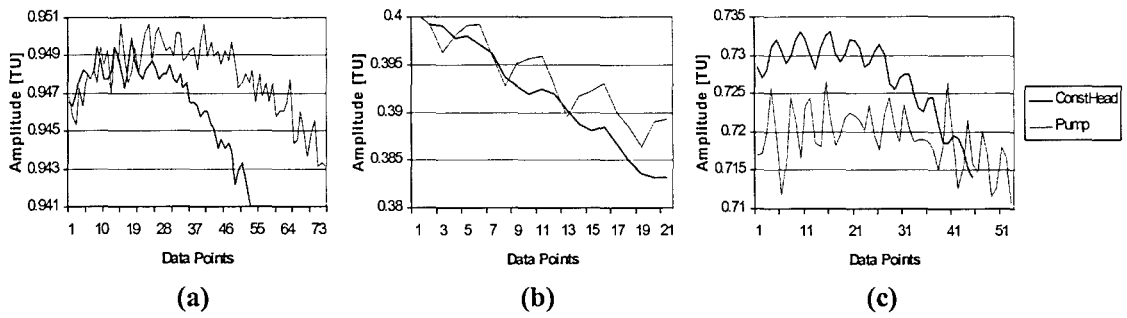

Figure 6-20. Comparison of water tensiotraces ConstHead and Pump acquired at room temperatures (23.6°C, 23.5°C respectively) and atmospheric pressure (1018hPa). (a) rainbow peak ConstHead (17.0s to 18.7s), Pump (22.6s to 24.9s); (b) negative slope ConstHead (35.4s to 36.0s), Pump (47.4s to 48.0s); (c) tensiograph peak ConstHead (57.3s to 58.6s), Pump (77.8s to 79.5s).

Figure 6-20 shows magnified sections of the tensiotraces ConstHead and Pump in order to compare the signal noise in both traces. It should be noted that the tensiotraces have dissimilar drop periods (see Figure 6-19), that is why the sections with similar amplitudes in Figures 6-20(a), 6-20(b), and 6-20(c) start at different positions on the time axis. Considering Figure 6-20 it can be said that a tensiotrace obtained with a constant head liquid delivery system is not as noisy as a tensiotrace obtained with a micro-stepper pump. This is due to a constant liquid flow in the constant head liquid delivery system whose magnitude of drop oscillation is less compared to micro-stepper pumps. This is a major advantage of a constant head liquid delivery system and this result was achieved although the flow rate of the liquid for the tensiotrace ConstHead was greater than the flow rate for the tensiotrace Pump, which usually increases the signal noise in a tensiotrace due to a more turbulent flow. That implies the signal noise in tensiotraces, acquired with a constant head liquid delivery system, decreases by lowering the flow rate of the liquid. Table 6-1 summarises the discussion about constant head versus pump.

	constant head		pump
liquid flow	CONSTANT		CHOPPED (due to micro-steps)
flow-rate adjustment	DIFFICULT (depending on height of constant head)		EASY
flow-rate stability	BAD (depending on liquid level in constant head)		GOOD
bubble build-up (in delivery tubes)	NO		YES (due to valve switchover)
cost	manual system	CHEAP	EXPENSIVE
	automated system	EXPENSIVE	

Table 6-1. constant head versus pump.

The question is which liquid delivery system is more suitable for a tensiographic apparatus? It depends on the application. If the flow rate adjustment or stability is not an issue the tensiograph could incorporate a manually operated constant head liquid delivery system that is inexpensive, generates relatively smooth tensiotraces, and avoids bubble build-up in liquid delivery tubes, which occur during switchover periods of the valves in a stepper motor pump. Though a stepper motor pump is expensive it is still the better liquid delivery system for a tensiograph. Weaknesses such as chopped liquid delivery and bubble build-up in liquid delivery tubes can be eliminated by tensiotrace-smoothing algorithms and frequent flushing of the liquid delivery tubes respectively.

6.4 Disturbing Effects

Any light penetrating the surface of a pendant drop from the outside and the evaporation of liquid during drop formation are disturbing effects for a tensiographic apparatus. This section describes the effect that stray light and evaporation have on tensiotraces.

6.4.1 Stray Light

Unwanted light, which travels through gaps (ventilation outlets etc) in the housing of a tensiograph from the outside to the inside, is recognised as stray light throughout this thesis. Stray light diverged by diffuse reflection at the relatively rough surface of the top frame (Figure 6-2) propagates towards the pendant drop incorporated in the brass block of the TE module (Figure 6-7). The stray light that is not totally reflected at the outer surface of the drop is refracted into the drop and subsequently injected into the

collector-fiber at the end-face of the drophead. To examine stray light disturbances at the end-face of a drophead the tensiotraces in Figure 6-21 were acquired with and without stray light protection.

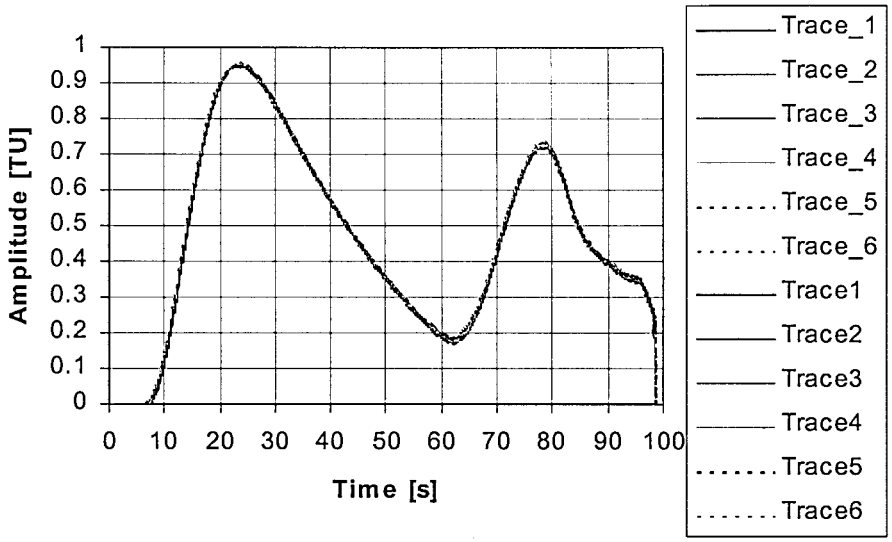

Figure 6-21. Data of Trace_1 to Trace_6 and Trace1 to Trace6 were acquired using a pump liquid delivery system and water as sample liquid SL at room temperatures (22.6°C, 22.4°C respectively) and atmospheric pressure (1016hPa). Trace_1 to Trace_6 were acquired without stray light protection whereas Trace1 to Trace6 were acquired with stray light protection in place. The overplot of twelve similar data sets results in the visibility of only one trace.

Several sections of the tensiotraces in Figure 6-21 have been chosen to compare the 'stray light contaminated traces' (labelled with an underscore in their name) versus 'stray light protected traces'. Figures 6-22, 6-23, and 6-24 show the results.

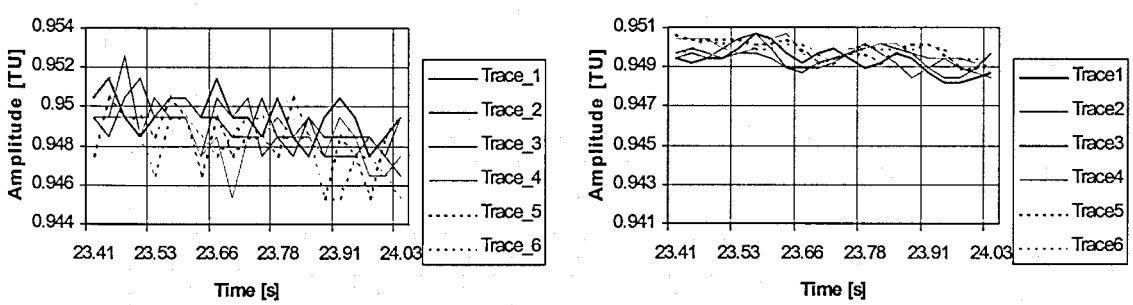

(a) (b)

Figure 6-22. Data of Trace_1 to Trace_6 and Trace1 to Trace6 were acquired using a pump liquid delivery system and water as sample liquid SL at room temperatures (22.6°C, 22.4°C respectively) and atmospheric pressure (1016hPa). (a) rainbow peak without stray light protection, (b) rainbow peak with stray light protection. The maximum amplitudes of the signal noise are respectively less than 0.007TU and 0.003TU peak to peak.

It should be noted that the visible 660*nm* LED (Table A2-1) was used to illuminate the inner drop and the photodiode (Table A2-1) with spectral response range 320 to 1100*nm* served as detector during the data acquisition for the tensiotraces shown in Figure 6-21.

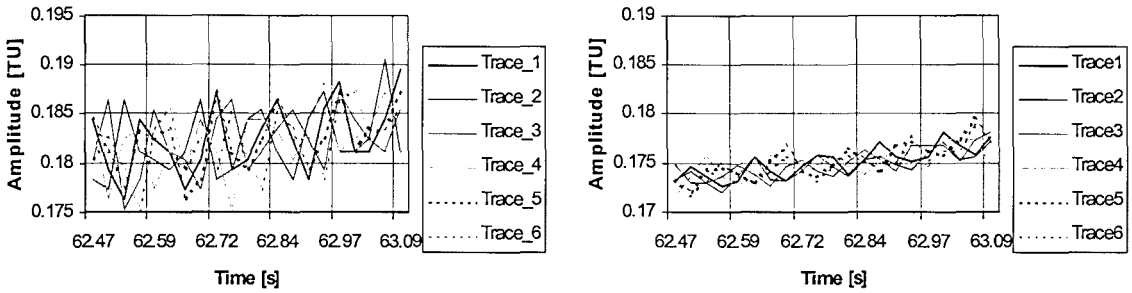

(a) (b)

Figure 6-23. Data of Trace_1 to Trace_6 and Trace1 to Trace6 were acquired using a pump liquid delivery system and water as sample liquid SL at room temperatures (22.6°C, 22.4°C respectively) and atmospheric pressure (1016hPa). (a) local minimum without stray light protection, (b) local minimum with stray light protection. The maximum amplitudes of the signal noise are respectively less than 0.013TU and 0.005TU peak to peak.

It can be seen from Figures 6-22(a), 6-23(a), and 6-24(a) that the signal noise amplitudes in tensiotraces with superimposed stray light noise are greater than the signal noise amplitudes of 'stray light protected tensiotraces' (Figures 6-22(b), 6-23(b), and 6-24(b)). Stray light (usually visible light in the range 380 to 780*nm*, Table A3-2) lies in the spectral range of the photodiode and therefore contributes with its complex signal (scattered refraction and reflection) to the light signal originating from the 660*nm* LED. Note that the pump effect (alternating maximum signal noise amplitudes), as described in Section 6.3.2, is also observable from these results.

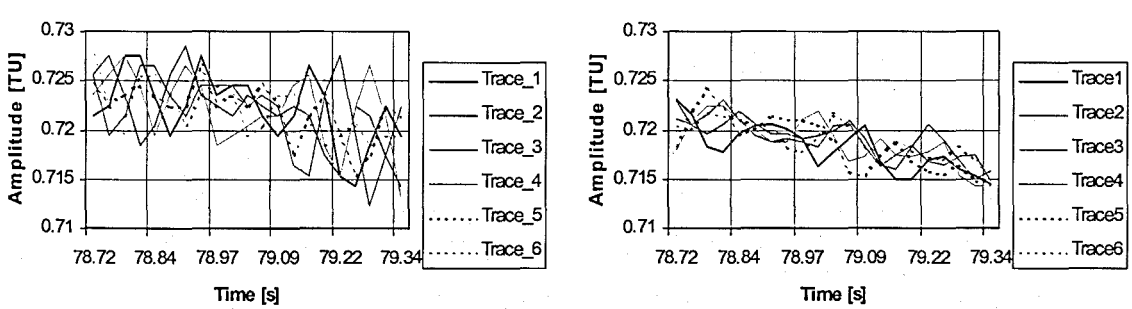

(a) (b)

Figure 6-24. Data of Trace_1 to Trace_6 and Trace1 to Trace6 were acquired using a pump liquid delivery system and water as sample liquid SL at room temperatures (22.6°C, 22.4°C respectively) and atmospheric pressure (1016hPa). (a) tensiograph peak without stray light protection, (b) tensiograph peak with stray light protection. The maximum amplitudes of the signal noise are respectively less than 0.014TU and 0.006TU peak to peak.

The assessment of this stray light experiment had an influence on the design for the housing of a tensiographic instrument. A 'light resistant' material is obviously the minimum requirement for such a housing, which is also equipped with light-baffling systems at gaps such as ventilation outlet, door hinges etc.

6.4.2 Evaporation

Evaporation of the pendant liquid drop during tensiographic data acquisition is a disturbing effect that deserves consideration. Figure 6-25 shows several tensiotraces for ethanol and water obtained at different temperatures. These tensiotraces are references for the following discussion.

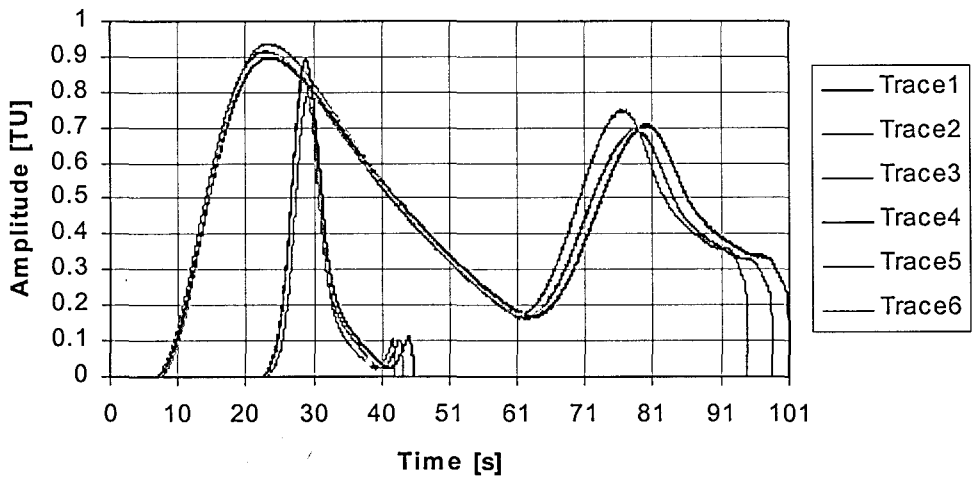

Figure 6-25. Water references Trace1 to Trace3 (drop period greater than 91s) and ethanol references Trace4 to Trace6 were acquired using a pump liquid delivery system at 12.0°C, 22.5°C, and 40.0°C respectively.

If the liquid delivery to the end-face of a drophead is cancelled after the time duration t_i (beginning with t_0=0), then evaporation of the liquid drop generates similar signal amplitudes (presents of noise) of the tensiotrace ($u(t_0)$ to $u(t_i)$) in reversed order, but usually on a different time scale beginning with $\tau_0=t_i$, i.e. $u(\tau_1)\approx u(t_{i-1})$, $u(\tau_2)\approx u(t_{i-2})$, ..., if the data acquisition process continues. An example may clarify this statement. From Figure 6-25 it can be seen $u(26s)$=0.2TU, $u(29s)$=0.8TU, and $u(32s)$=0.3TU are amplitudes of Trace6 at t_{i-2}, t_{i-1}, and t_i respectively. These are specific quantities of an ethanol tensiotrace obtained at 40.0 ℃. Now imagine one is acquiring the data for an ethanol sample under the same conditions as outlined above, but this time the liquid delivery is cancelled at t_i=32s and the data acquisition process of a gradually evaporating liquid drop continues at 40.0 ℃. The results after the evaporation process would then be as follows: $u(\tau_0)=u(32s)$, $u(\tau_1)\approx u(29s)$, and $u(\tau_2)\approx u(26s)$ where τ_0=32s, τ_1=120s, and τ_2=191s (see Section 6.4.3 for more information). Note that the time increments between τ_0, τ_1, and τ_2 are different. The use of the measuring procedure as

described in the example above delivered the tensiotraces in Figures 6-26 and 6-27 and the outcome is, evaporation has an insignificant affect on water samples during drop formation at 12.0 ℃ and 22.5 ℃, but the affect is significant at 40.0 ℃ (see Figure 6-26).

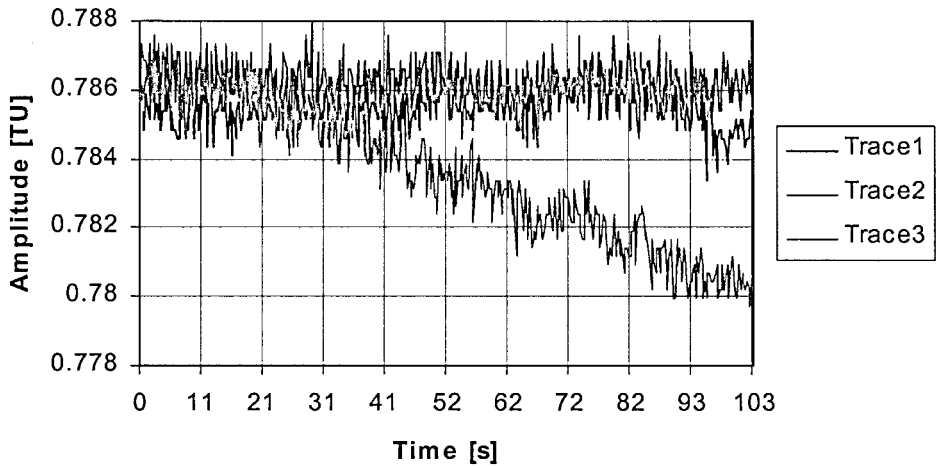

Figure 6-26. Trace1 to Trace3 are representations of evaporating pendant drops of water at 12.0°C, 22.5°C, and 40.0°C respectively. Liquid delivery to a drophead was cancelled respectively after 13.5s, 38.5s, and 18.5s (compared to the time axis of their associated reference tensiotraces) before the evaporation process was monitored. Traces are normalised to 0.786TU (maximum amplitude) in the series of traces.

Conversely, evaporation during the drop formation of ethanol samples is already a highly significant issue at 12.0 ℃ and 22.5 ℃ (see Figure 6-27). It should be noticed that the maximum signal noise amplitudes in the tensiotraces of these examples are less than 0.004TU peak to peak (no stray light protection!).

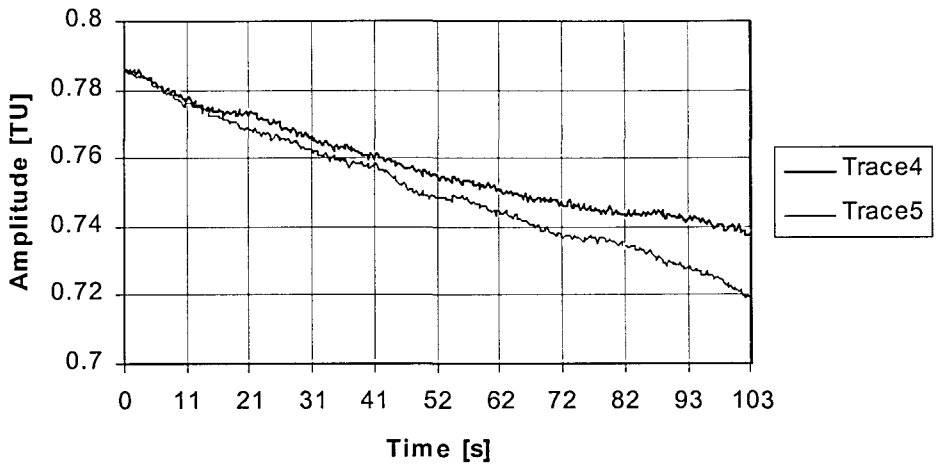

Figure 6-27. Trace4 and Trace5 are representations of evaporating pendant drops of ethanol at 12.0°C, and 22.5°C respectively. Liquid delivery to a drophead was cancelled after 27.5s (compared to the time axis of their associated reference tensiotraces) before the evaporation process was monitored. Traces are normalised to 0.786TU (maximum amplitude) in the series of traces.

Evaporation of liquid during drop formation on the drophead can be minimised by lowering the temperature of the TE module, but it can never be totally avoided and the user of a tensiograph must be aware of this fact.

6.4.3 Utilisation of Evaporation for Tensiotrace Data Acquisition

Although evaporation is regarded as a disturbing effect it can be utilised as an alternative to constant head liquid delivery. Figure 6-28 shows a tensiotrace generated during the evaporation process of an ethanol drop hanging on a drophead. Evaporation $Noise_{peakTOpeak}$<0.004TU compared to constant head $Noise_{peakTOpeak}$<0.005TU (see Figures 6-26 and 6-20(c) respectively) and at the same time the advantage of a stepper motor pump liquid delivery could be beneficial for some applications. Rather long drop periods, on the other hand, diminish the advantage of the evaporation method. However, this method might be interesting for applications using highly volatile liquids such as whiskey etc.

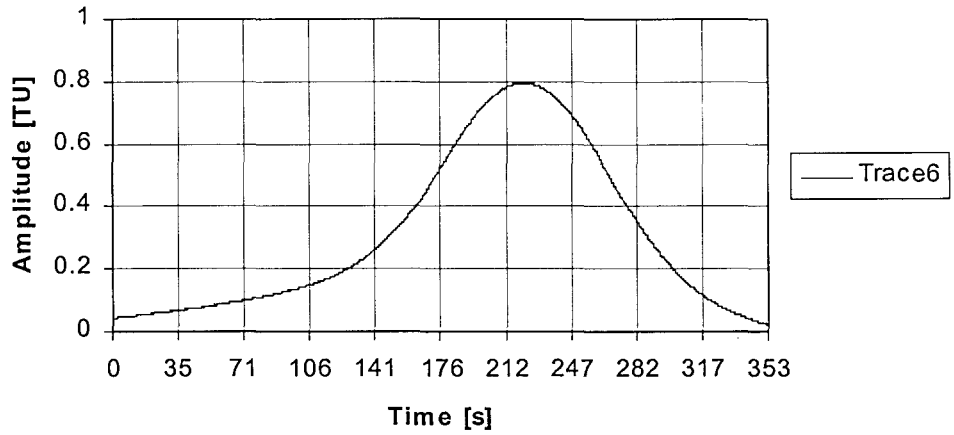

Figure 6-28. Trace6 is a representation of an evaporating pendant drop of ethanol at 40.0°C. Liquid delivery to a drophead was cancelled after 38.0s (compared to the time axis of the associated reference tensiotrace) before the evaporation process was monitored.

6.5 Error Budget and Information Content

Sometimes there is a tendency for someone involved in the design of a technical device to fall into the trap of thinking that a few strategically placed precision components will result in a device with precision performance. On rare occasions this will be true, but even an electronic circuit, for example, prepared with 0.01% resistors and expensive operational amplifiers will not perform to expectations if somewhere in the circuit there is an input offset current multiplied by a source resistance that gives a voltage error such as $10mV$. With almost any technical device, e.g. a tensiograph, there will be errors arising from many sources and it is essential to tally them, if for no other reason than to locate problem areas where better components or a design change might be needed. The error budget in this section results in rational design and eventually permits a careful performance estimate of the tensiographic apparatus culminating in a discussion about information content of a measurand in a tensiotrace, which is motivated by the remarkable theorems of Claude Shannon about data entropy [2-2, 2-3].

6.5.1 *Error Budget for a Tensiograph*

An optical signal injected into the source-fiber of the drophead in a tensiograph suffers from intensity losses at several places in the optical signal transfer system until it is picked up by the detector at the end of the light path. Figure 6-29 shows an experimental setup that was used to determine optical losses in each component of the optical signal transfer system, which comprises SMA connectors and PMMA fibers to couple and transfer an optical signal respectively.

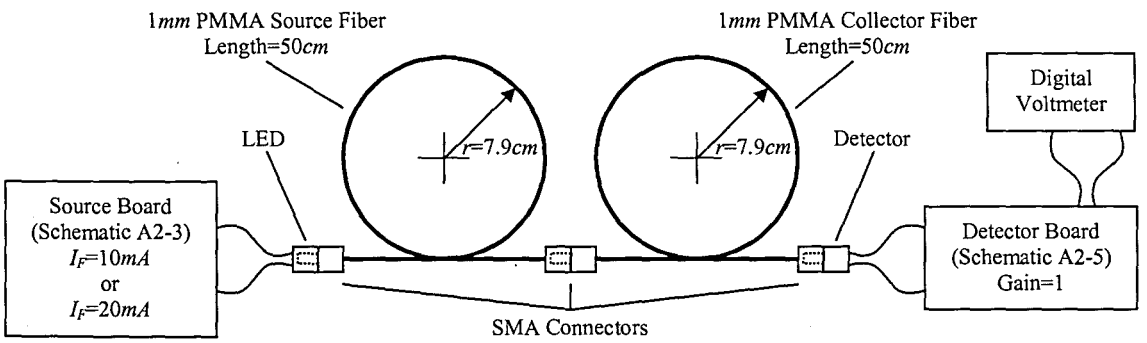

Figure 6-29. For the measurement of losses in the optical system of a tensiograph.

A constant current source (Schematic A2-3) drives a current consecutively through one of four LEDs (I_F=10mA for 470, 530nm LEDs; I_F=20mA for 660, 950nm LEDs) whose light is then coupled, using an SMA connector, into a bent (radius r=7.9cm) PMMA optical fiber (length=50cm, core diameter=1mm). Subsequently the light signal is either coupled directly into a second optical fiber or indirectly via a slowly growing drop of water. Note that both direct (SMA connector) and indirect (drop of water) coupling must be applied in order to obtain optical losses in the liquid quantitatively. The light coupled into the detector (photodiode S2386-18K) is then converted, using the circuit in Schematic A2-5 (gain=1), to a voltage V_{out} [V] measured with a digital voltmeter. Following this measurement the current I_{ph} [A] through the photodiode can be determined

$$I_{ph} = \frac{V_{out}}{R_1}$$

where R_1 [Ω] is the feedback resistor across pins 8 and 9 of U1C. Note that the input current of U1C is 100pA max and is therefore insignificant for the calculation of I_{ph} in this experimental setup. Further

$$\Phi_D = \frac{I_{ph}}{S(\lambda)}$$

is the optical power $[W]$ detected by the photodiode, where $S(\lambda)$ $[AW^{1}]$ is the photo sensitivity of the photodiode depending on the wavelengths λ $[nm]$ of the light sources. The optical power loss Φ_{LW} $[W]$ or Φ_{LdB} $[dB]$ in the light transfer system in Figure 6-29 is then

$$\Phi_{LW} = \Phi_{in} - \Phi_D, \quad or \quad \Phi_{LdB} = 10dB\log\left(\frac{\Phi_D}{\Phi_{in}}\right)$$

respectively, where Φ_{in} is the optical power coupled into the source fiber. Note that the absolute optical power Φ $[dBm]$ at a particular point in the optical system is determined

$$\Phi = 10dBm\log\left(\frac{\Phi_p}{1mW}\right)$$

where Φ_p $[mW]$ is the optical power at this point. Table 6-2 shows the error budget for the light transfer system of a tensiograph.

Error Budget for optical components of a tensiograph					
LED CHARACTERISTICS (see Table A2-1)					
Parameter	**Blue**	**Green**	**Red**	**IR**	**Unit**
Type	IF-E92B	IF-E93	IF-E97	IF-E91A	
λ Wavelength	470	530	660	950	*nm*
Φ_{in} Optical Power coupled into a 1*mm* PMMA Fiber	75 -11.2	75 -11.2	100 -10.0	100 -10.0	μW *dBm*
PHOTODIODE CHARACTERISTICS (see Table A2-1)					
Type	S2386-18K				
$S(\lambda)$ Photo Sensitivity	0.27	0.33	0.46	0.60	AW^{-1}
MEASURED AND CALCULATED VALUES (without water)					
V_{out1} Output Voltage	1.31	1.63	2.87	2.77	*V*
I_{ph1} Photo Current	13.1	16.3	28.7	27.7	μA
Φ_{D1} Optical Power Detected	48.5 -13.1	49.4 -13.1	62.4 -12.0	46.2 -13.4	μW *dBm*
Φ_{LW1} Optical Power Loss Φ_{LdB1}	26.5 1.9	25.6 1.8	37.6 2.0	53.8 3.4	μW *dB*
SOURCES OF OPTICAL POWER LOSS Φ_{LdB1}					
Fiber Connector Losses	1.7	1.6	1.7	1.7	*dB*
Fiber Bend Losses	0.1	0.1	0.1	0.1	*dB*
Fiber Length Losses	0.1	0.1	0.2	1.6	*dB*
WATER CHARACTERISTICS (see Figure 6-30)					
$a(\lambda)$ Absorption Coefficient	10^{-4}	$5*10^{-4}$	$5*10^{-3}$	10^{-1}	cm^{-1}
MEASURED AND CALCULATED VALUES (with water)					
V_{out2} Output Voltage	0.62	0.77	1.36	1.09	*V*
I_{ph2} Photo Current	6.2	7.7	13.6	10.9	μA
Φ_{D2} Optical Power Detected	23.0 -16.4	23.3 -16.3	29.6 -15.3	18.2 -17.4	μW *dBm*
Φ_{LW2} Optical Power Loss Φ_{LdB2}	52.0 5.1	51.7 5.1	70.4 5.3	81.8 7.4	μW *dB*
SOURCES OF OPTICAL POWER LOSS Φ_{LdB2}					
Refraction and reflection losses in a water drop and also significant absorption at 950*nm*.	3.2	3.3	3.3	4.0	*dB*

Table 6-2. Error budget for optical components of a tensiograph.

It should be noted that the results for V_{out1}, I_{ph1}, Φ_{D1}, Φ_{LW1}, and Φ_{LdB1} were obtained with the centre SMA connector (see Figure 6-29) in place, whereas V_{out2}, I_{ph2}, Φ_{D2}, Φ_{LW2}, and Φ_{LdB2} correspond to the optical signal through a pendant drop of water, which is detected at the end of the collector-fiber when the size of the water drop represents the rainbow peak (V_{out2} max) in a tensiotrace, i.e. the centre SMA connector was replaced with a flat stainless steel drophead and a stepper motor pump delivered water to the end-face of the drophead during the time the voltage V_{out2} was monitored. Knowing the optical losses in the SMA connectors and the PMMA fibers (see Picture A2-11 and Table A2-1 respectively) in Figure 6-29 the optical losses in the liquid (water in this case) can be determined. It can be seen from Figure 6-30 [6-9] (also see $a(\lambda)$ in Table 6-2) that optical losses due to absorption in water are negligible at

wavelengths 470, 530, and 660*nm*, but absorption at 950*nm* adds significantly to optical losses.

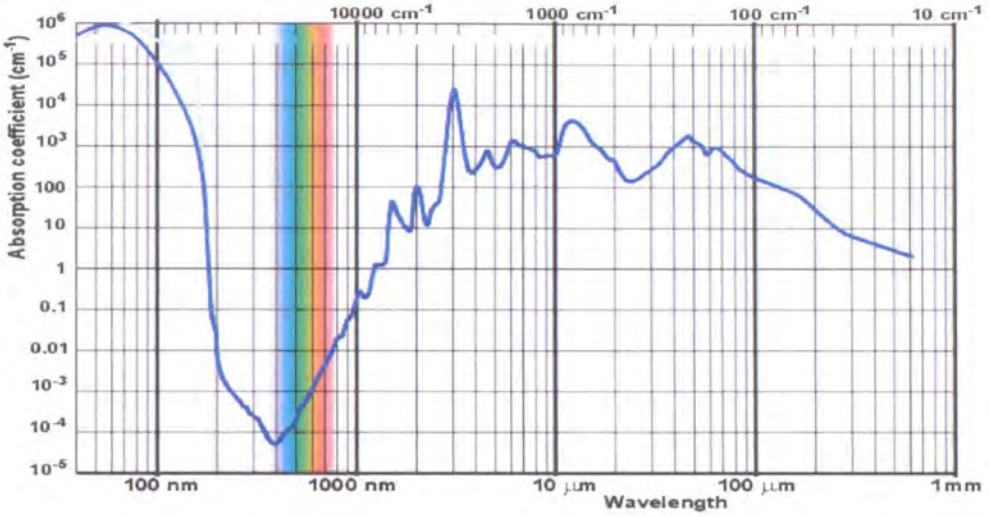

Figure 6-30. Absorption spectrum of water.

To this point the discussion about the error budget for a tensiographic instrument has only concentrated on the light transferring system in conjunction with a pendant drop of water used as the LUT. Liquids other than water will almost certainly have a dissimilar effect on the overall optical losses in the system, but the optical power detected by the photodiode at the end of the light path will always be less than the optical power in the directly coupled system as shown in Figure 6-29. It can be seen from Figure 6-31 that the optical power coupled into the light transferring system OPC is firstly attenuated by SMA connector and PMMA fiber losses (see OPD1) and secondly by liquid (water) losses (see OPD2).

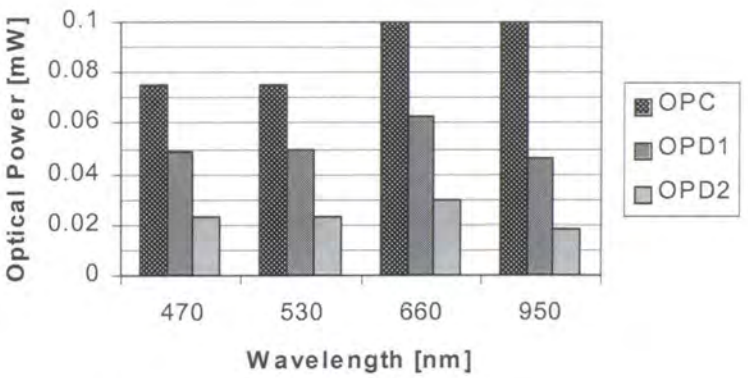

Figure 6-31. Power losses in the optical system of a tensiograph. (OPC) optical power coupled into a 1mm PMMA fiber. (OPD1) optical power detected in a bent two-fiber system. (OPD2) optical power detected through a pendant drop of water in a bent two-fiber system.

Nothing can be done in terms of 'liquid-improvement', because the liquid is the given quantity that has to be analysed, i.e. it must not be altered. Now assume that the light

sources in a tensiograph are fixed devices, thus the only way to increase the optical power detected by the photodiode is to improve the light transfer system (without liquid). It should be noted that the optical power losses in the light transfer system of a tensiograph depend on the wavelengths of the light sources. Figure 6-31 shows clearly the difference in optical power attenuation at the wavelengths 660 and 950*nm*.

Not only optical losses should be considered in the error budget for a tensiograph, but also the errors arising from vibration, stray light, etc that diminish the overall performance of the instrument. Most of these errors, described above in this chapter, are listed in Table 6-3 for easy reference.

Categorised Error Budget for a tensiograph				
		Error α_{pp} [*TU*]		
Category	**Test Conditions**	***min***	***max***	**Information**
External Vibration	load 8*kg* load 16*kg*		< 0.25 < 0.16	Figure 6-3(a) Figure 6-3(b)
Internal Vibration	no vib. damping with vib. damping		< 0.10 < 0.005	Figure 6-4(a) Figure 6-4(b)
Stepper Motor Pump	@ flow-rate (water) 1.249$\mu l/s$	< 0.005	 < 0.012	Figure 6-17 Figure 6-16
Constant Head	@ flow-rates (water) 1.618 to 1.783$\mu l/s$	< 0.003	 < 0.005	Figure 6-20(a, b) Figure 6-20(c)
Stray Light	without protection without protection with protection with protection	< 0.007 < 0.003	 < 0.014 < 0.006	Figure 6-22(a) Figure 6-24(a) Figure 6-22(b) Figure 6-24(b)
Evaporation	no stray light protection		< 0.004	Figure 6-26
Temperature Variations, EMI, Component Drift, Electronics, etc	@ room temperature (20 to 25 ℃)	< 0.001	< 0.003	Empirical observations
ADC	Incorporated in a PC		0.00049	Table A2-2

Table 6-3. Categorised error budget for a tensiograph.

From a system engineering point of view the noise amplitudes peak-to-peak (errors) α_{pp} in Table 6-3 can be interpreted as follows.

- A properly loaded anti-vibration system is the basis for the design of a noise-reduced AMFOS based instrument. Remember that the relatively large errors (α_{pp}<0.25*TU*, α_{pp}<0.16*TU*) arose from forced external vibration.
- Vibrating devices (stepper motor pump, switch mode power supply, etc) must not be bolted onto the top frame of the anti-vibration system (see Figure 6-1) in order to reduce the error (α_{pp}<0.10*TU*) resulting from undamped internal vibration. In addition, it does not make sense to consider tensiographic components, other than the vibration-damping system with regard to noise caused by internal vibration, as long as the error α_{pp} is not less than 0.005*TU*.

Any attempt to improve the SNR of a tensiotrace will fail if the anti-vibration system of a tensiograph performs insufficiently well.

- The noise generated by the stepper motor pump is rather complex because of relatively large amplitude variations (α_{pp}<0.005TU to α_{pp}<0.012TU) in the signal noise of the entire tensiotrace, which may be improved upon by varying the flow rate of the LUT, for example. However, it has been proven (see category constant head: α_{pp}<0.003TU to α_{pp}<0.005TU) that amplitude variations in the signal noise caused by liquid delivery are reducible. A stepper motor pump represents besides internal and external vibrations a considerable noise source.
- Disturbances due to stray light can easily be dealt with (housing, light baffling, etc).
- A relatively small and unvarying error (α_{pp}<0.004TU and probably less by employing stray light protection) in tensiotraces distinguishes the evaporation method from conventional liquid delivery techniques.
- At this development stage of a tensiograph it is unnecessary to consider errors arising from EMI, electronic components, and temperature drift. The observation of α_{pp}<0.003TU for the categories in Table 6-3 discussed so far firstly implies that this error also applies for the second last category, but it can be assumed that α_{pp} is even less than 0.001TU for this category because tensiotraces with SNR over 60dB have been recorded already (see Picture 4-5).
- After a rigorous assessment of the errors described above it is obvious that an ADC with a resolution greater than 12*bits* will not perform to expectations unless the overall error in the tensiographic instrument can be reduced to α_{pp}<0.00049TU.

An error budget is an excellent method to locate problem areas in a tensiograph where better components or a design change might be needed, but it provides only little information on the overall performance. Eq. (2-31) yields a single number that summarises the overall error. α_{ppMIN}<0.0041TU and α_{ppMAX}<0.0075TU are respectively the minimum and maximum overall errors calculated from the values in Table 6-3, which do not include the dynamic range of a tensiotrace. Note that forced external vibration and internal vibration without anti-vibration feet are not common in tensiographic experiments; hence they are excluded from calculations of the overall

error. Errors arising from internal vibrations with anti-vibration feet, evaporation, and the ADC are included in both α_{ppMIN} and α_{ppMAX}. It should also be noted that optical losses in Table 6-2 are not included in the overall errors α_{ppMIN} and α_{ppMAX}. The next section describes how to overcome these weaknesses so that the dynamic range of a tensiotrace, losses, and errors are treated equally for the estimate of the overall system performance.

6.5.2 Information Content with Regard to Tensiography

The previous section discussed system performance in terms of r.m.s-errors (Eq.(2-31)). A single number, not including the dynamic range of a tensiotrace, summarises the overall error in a system. This single number does not give information on signal quality, i.e. a tensiotrace of relatively low quality (α_{pp}=0.001TU, u_{max}=0.01TU, SNR=20dB) gives the impression to be qualitatively better than a tensiotrace of relatively high quality (α_{pp}=0.005TU, u_{max}=1.0TU, SNR=46dB), which is clearly the wrong perception. Furthermore, Eq.(2-31) is a disadvantageous choice for the summation of quantities when they are of different generic type, e.g. optical, mechanical, and electrical errors. The reassessment of these problems has led to a method that describes a two-sided differentiation of noise and losses that is illustrated in Figure 6-32 as the conceptual basis for the tensiographic information content (TIC) approach, where the dynamic range of a tensiotrace, losses, and errors are treated equally for the estimate of the overall system performance using Eq.(2-32).

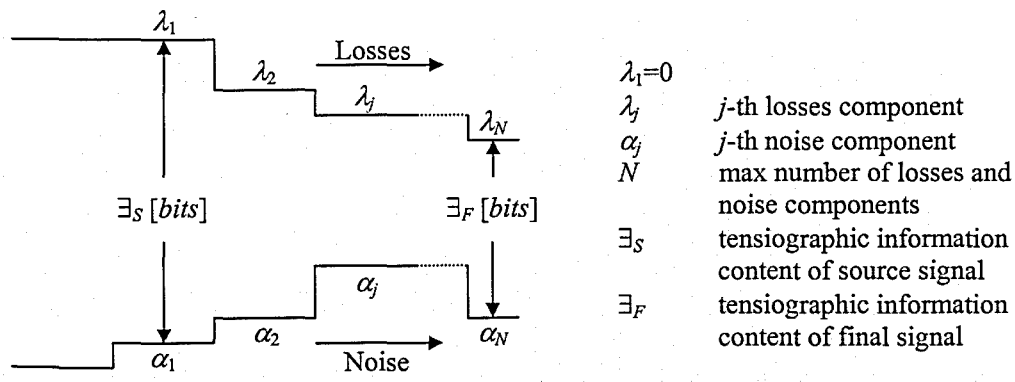

Figure 6-32. Conceptual basis for the tensiographic information content approach with two-sided differentiation of noise and losses.

A function relating to the energy change in a system has been termed the entropy-function by Rudolf Clausius [6-10], who chose the Greek word (τροπη =

change, conversion, transformation) and used the prefix "en" for "energy" to emphasise the energy change in a thermodynamic system. The value of the entropy-function for a particular state of a system is called the entropy. In general, it is impossible for irreversible processes in a macroscopic closed system for entropy to decrease. This is the principle of the increase in entropy and a statement of the second law of thermodynamics. The principle of entropy increase determines the direction of the process. For example, a falling stone that converts its energy into heat is a feasible process for which entropy increases during the fall and at the time of the impact on the ground. To cool down the stone so that it rises up is impossible. This would decrease in entropy as a consequence. Ludwig Boltzmann found that the entropy of a state is proportional to the natural logarithm of its thermodynamic probability, i.e. the principle of the increase in entropy is identical with the statement that naturally occurring processes alter a system in such way that it changes from less probable to more probable states. The analogy in signal processing is an entropy-function that describes the change in information of encoded signals transmitted over a noisy digital system [2-3]. The entropy is then the information content of the encoded signal at a particular point in the communications channel. The measurement of information is therefore the measurement of the uncertainty (error). That measurement is called entropy. If entropy is large, then a large amount of information is contained in the signal. If entropy is small, then only a small amount of information is contained in the signal. Noise in a communications channel is usually the principal cause of uncertainty. Motivated by these theorems McMillan and the author of this thesis introduced a metric that they have termed TIC (Eq.(2-32)), which describes the information content in a tensiographic signal by taking patterns from the entropy measurement of thermodynamic and communications systems. Note that the TIC includes both noise and losses. The TIC of the source $\exists_S$ does not depend on losses. The amount of information in a signal S is dependent on the error α ($\exists$ depends on α). A given signal S does not furnish the same information if the error is high or small. The amount of information $\exists$ is dependent on the correlation in the signal S. If S presents large features above the error α, it contains a lot of information. A non-amplified signal will always be subject to losses, i.e. the amplitude of the propagating signal S decreases gradually. Conversely, the amount of noise in the signal of interest might increase or decrease, depending on the characteristics of the system (CMRR of an electronic circuit, light baffling, noise filters,

etc), which could have the effect that the final signal S_F contains more information than the source signal S_S, ($\exists_F > \exists_S$). It should also be noted that the information content in a signal S is zero for $S<\alpha$ ($\exists<0$). A signal S_i, part of a tensiographic data set, with negative information content ($-\exists_i$) is useless, hence Eq.(2-32) has to be redefined which yields

$$\exists = \frac{\exists_N}{N}, \quad \exists_i = \exists_{i-1} + \log_2\left(\frac{S_i}{\alpha_i}\right), \quad \log_2\left(\frac{S_i}{\alpha_i}\right) \equiv 0 \; for \; \frac{S_i}{\alpha_i} < 1, \quad \begin{matrix} (\alpha_i > 0) \\ (1 \le i \le N) \\ (\exists_0 \equiv 0) \end{matrix} \tag{6-1}$$

where a signal S_i that falls into the region of the error threshold has no influence on the TIC $\exists_i$, which is rational because such a signal contains no useful information in tensiographic applications. Inspired by a theorem of C. Shannon [6-11] the average effective information content I_{SF} [*bits*] in a tensiotrace is determined

$$I_{SF} = \frac{\exists_S + \exists_F}{2}. \tag{6-2}$$

This quantity is also called the average mutual information, which gives a good estimate of the overall tensiographic system performance. The TIC is a special case of this mutual information since $I_{SS}=\exists_S$ and $I_{FF}=\exists_F$. The following example shows how to apply TIC in tensiography.

Assuming that the encapsulated linear power supply (Picture A2-1) generates the highest noise signal ($\alpha_{V\text{-}S}=1mV$) in the constant current sources of schematics A2-3, the relative voltage noise $\alpha_{V\text{-}LED}$ of the LED (only 660*nm* LED IF-E97 considered, see Table A2-1) would be approximately

$$\alpha_{V-LED} = \frac{\alpha_{V-S}}{V_F} = \frac{1mV}{1.7V} \approx 0.1\%$$

where V_F is the forward voltage across the LED. Note, the small signal gain of the transistor ZTX690B is $h_{fe}=1.0$ (see Table A2-1), which means that the relative current noise of the LED is $\alpha_{I\text{-}LED}\approx 0.1\%$. Note that the relative voltage noise $\alpha_{V\text{-}LED}$ is probably less than 0.1% due to the typical supply voltage rejection (SVR≈80*dB*) of the fixed voltage regulators (see Table A2-1) in the electronic circuit. However, employing the relative current noise $\alpha_{I\text{-}LED}=0.1\%$ in Figure 3-7 returns the relative intensity noise ($700*10^{-6}$) of the LED IF-E97 at 20*mA*, and the optical power error α_0 of the source (LED) is then

$$\alpha_0 = \Phi_{in} * 700 * 10^{-6} = 100\mu W * 700 * 10^{-6} = 70nW$$

where Φ_{in} is the optical power (LED source signal S_S) coupled into a $1mm$ PMMA fiber. Applying Eq.(6-1) with N=1, the TIC of the source signal is

$$\exists_S = \log_2\left(\frac{S_S}{\alpha_0}\right) = \log_2\left(\frac{100\mu W}{70nW}\right) = 10.48 bits.$$

With $\Phi_{D1}=S_{F\text{-}B}=62.4\mu W$ (see Table 6-2) the final TIC (Eq.(6-1), N=1) is

$$\exists_{F-B} = \log_2\left(\frac{S_{F-B}}{\alpha_0}\right) = \log_2\left(\frac{62.4\mu W}{70nW}\right) = 9.80 bits$$

where $S_{F\text{-}B}$ is the final blank (no water drop) signal at the detector after attenuation in the light transfer system of a tensiograph. It has been assumed that the signal noise in the light transfer system is constant. The losses of information due to the SMA connectors and PMMA fibers in the system are $0.68bits$. The tensiotrace in Figure 6-33 serves as reference for the calculation of the final TIC with respect to specific trace data.

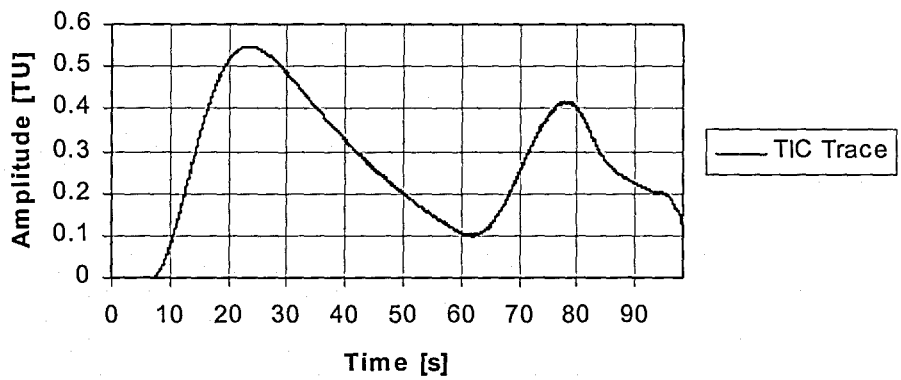

Figure 6-33. Tensiotrace of water for tensiographic information content calculations acquired at 22.7°C (660nm LED, RPH=0.548TU, SNR=52.5, data points=3152, α=0.0013TU).

The final TIC with respect to the maximum peak height in the tensiotrace (Eq.(6-1), N=1) is

$$\exists_{F-P} = \log_2\left(\frac{S_{F-P}}{\alpha}\right) = \log_2\left(\frac{0.548TU}{0.0013TU}\right) = 8.72 bits$$

where $S_{F\text{-}P}$ is the maximum peak height in the tensiotrace and α is the maximum error. The calculation of $\exists_{F\text{-}P}$ for tensiotraces is part of the analysis package Analyse (see Appendix 5). A more rigorous method to determine the final TIC of a tensiotrace is to use the entire data set of the trace. Applying Eq.(6-1) with N=3152 and α=0.0013TU (max data points and max error respectively, see Figure 6-33) the final TIC average is

$$\exists_{F-A} = 6.99\,bits$$

that includes additional information on the profile of the tensiotrace. The ethanol tensiotrace in Figure 6-34, for example, with the same maximum signal amplitude (S_F=0.548TU) compared to the tensiotrace in Figure 6-33 includes less information. The final TIC average is

$$\exists_{F-A-ethanol} = 2.97\,bits$$

assuming that the error (α=0.0013TU) is the same for both tensiotraces.

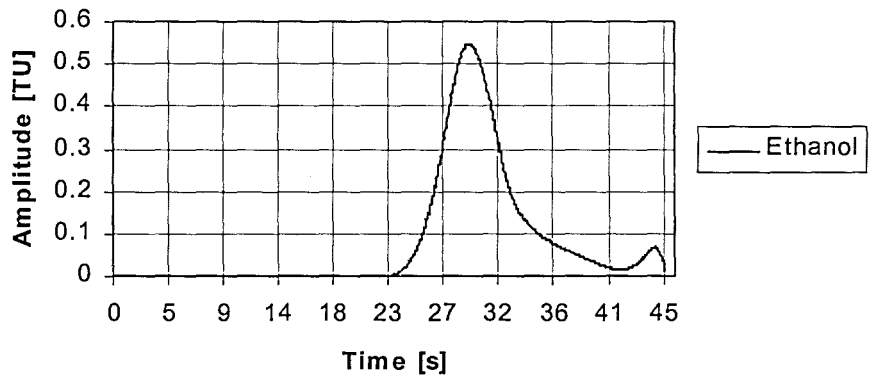

Figure 6-34. Tensiotrace for TIC calculations normalised to maximum RPH=0.548TU (LED 660nm).

The source and final TICs ($\exists_S$ and $\exists_F$ respectively) are related to each other but as single measurands they do not contain much information on the overall performance of a tensiograph. The average mutual information I_{SF} (Eq.(6-2), on the other hand, provides a good estimate of the overall performance, and

$$I_{SF-B} = \frac{\exists_S + \exists_{F-B}}{2} = \frac{10.48\,bits + 9.80\,bits}{2} = \underline{\underline{10.14\,bits}},$$
$$I_{SF-P} = \frac{\exists_S + \exists_{F-P}}{2} = \frac{10.48\,bits + 8.72\,bits}{2} = \underline{\underline{9.60\,bits}},$$
$$I_{SF-A} = \frac{\exists_S + \exists_{F-A}}{2} = \frac{10.48\,bits + 6.99\,bits}{2} = \underline{\underline{8.74\,bits}}$$

are respectively the average mutual information about the tensiographic system performance of a blank (no water drop) light path arrangement, light guidance through a water drop taking the max peak height of a tensiotrace, and light guidance through a water drop taking the TIC average of the entire tensiotrace. Note, the final signal (S_F) in a system contains no information if I_{SF} is half the TIC ($\exists_S$) of the source.

This section has shown that an error budget is inevitable for the proper design of a sensitive instrument such as the tensiograph that comprises a variety of error sources, which have to be dealt with in order to choose the most suitable components for the

system. A minimum overall error in a system is what needs to be achieved following an error budget and subsequent redesign of the system. The single number obtained from Eq.(2-31) considers mainly the quality of the components in a system and does not include the dynamic range of the signal. Hence TIC, which provides meaningful information on signal and system quality, has been introduced.

6.6 System Integration

The various parts that constitute a tensiographic instrument are shown in Figure 6-35. This figure is divided into five sections presenting the front view (top left), back view (top right), drophead (bottom left), side view (bottom right), and top view (centre) of the instrument. The TE module (top left, also Picture A2-9) is bolted to an aluminium frame using a solid nylon bracket with relatively low thermal conductivity (see Table A3-1), which consequently acts as a thermal insulator between the aluminium frame and the brass block. The Peltier devices (Picture A2-3) are sandwiched between the brass block and the heatsinks using a clamping mechanism. A heat sink compound, applied to the surfaces of the Peltier devices prior to the assembly of the TE module, improves the thermal conductivity.

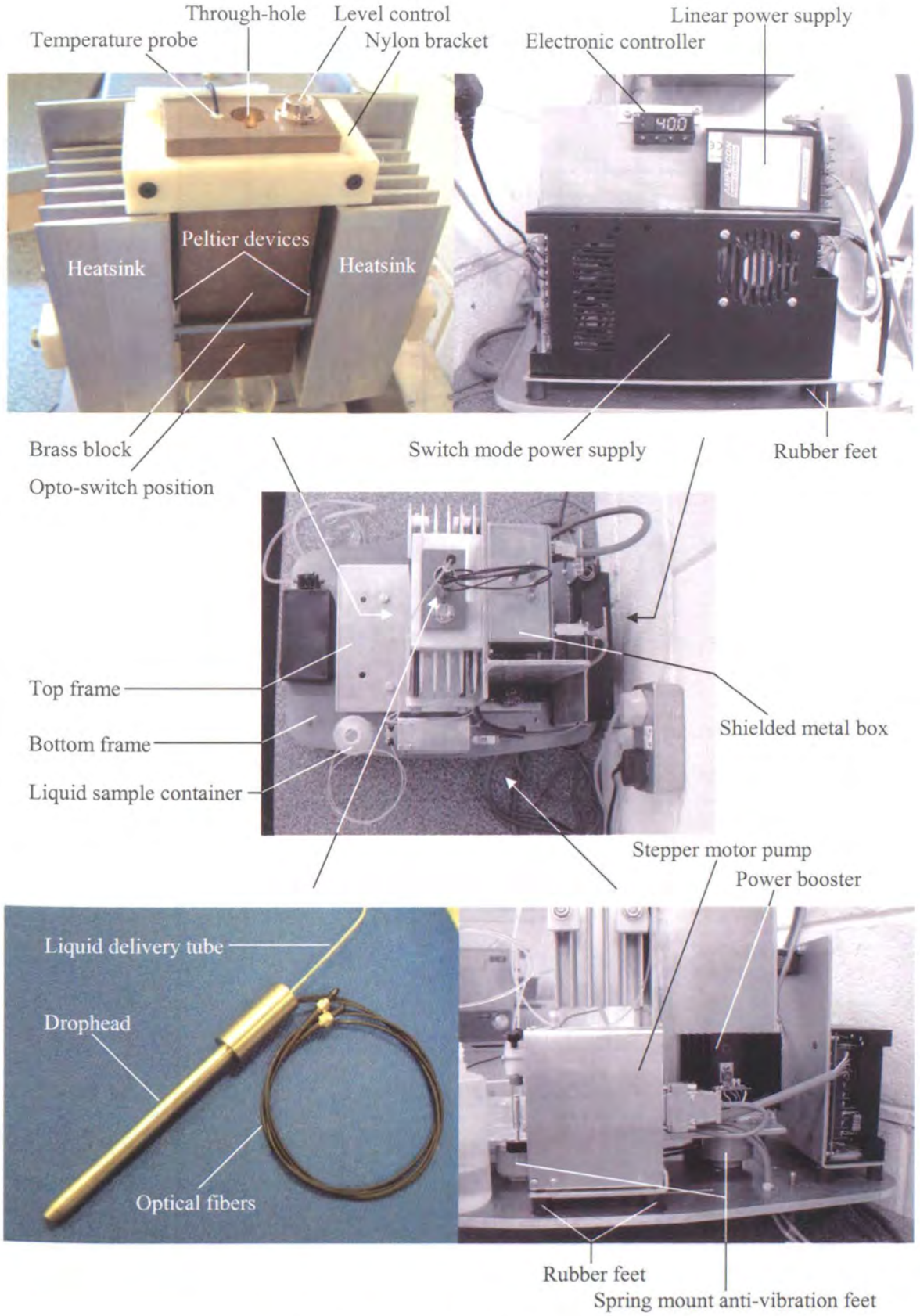

Figure 6-35. Integration of a tensiographic system.

A heat sink compound is squeezed into the $\varnothing 6mm$ borehole in the brass block before the temperature probe (Picture A2-4) is inserted. The length ($150mm$) of the temperature probe guarantees that the correct temperature close to the end-face of the drophead is

measured. The level control on top of the brass block can be used to adjust the angle of the through-hole in such a way that the drophead is exactly vertical when it is inserted into the brass block. The slotted through scan opto-switch (see Table A2-1) is located beneath the end-face of the drophead and in the centre of the through-hole in the brass block. A falling drop intercepts the optical barrier of the opto-switch (see Figure 3-8), which at the same time generates an electrical pulse that triggers the beginning or the end of a data acquisition process. The drophead (bottom left, also Picture A2-10) is inserted into the through-hole in the brass block and the optical fibers (source and detector) are connected to the shielded metal box (also see Figure 3-15) that encloses the electronic circuit boards (Schematics A2-3 and A2-5). The TE module, drophead, shielded metal box, and power booster (bottom right, also see Figure 3-14(b) and Schematic A2-2) form one unit that is bolted to the top frame of the instrument. Devices (top right in Figure 6-35) including the linear power supply (Picture A2-1), switch mode power supply (Picture A2-2), and electronic controller (Picture A2-7) with the associated controller driver board (see Schematic A2-1 and also Figure 3-14(a)) form another unit that is mounted on rubber feet, which rest on the bottom frame of a tensiograph. The rubber feet damp the vibration (low frequency) that arises from the fan incorporated in the switch mode power supply. The stepper motor pump (Picture A2-8), also bolted onto rubber feet that rest on the bottom frame, is connected to the sample container on one side and the liquid delivery tube of the drophead on the other side using PEEK tubing in order to pump the liquid from the sample container to the end-face of the drophead. The spring mount anti-vibration feet (Picture A2-6) combine the parts on the top frame with the parts on the bottom frame and provide at the same time vibration damping for a liquid drop hanging on the end-face of the drophead. A prototype of a tensiograph is shown in Figure 6-36. The apparatus is equipped with levelling feet that can be adjusted to obtain a precisely perpendicular drophead. The housing protects the inner parts against stray light and physical damage. The tensiograph is connected to a PC that can be used to acquire, store, and analyse tensiographic data. It is also used to control and monitor the light sources (LEDs), stepper motor pump, and temperature of the TE module.

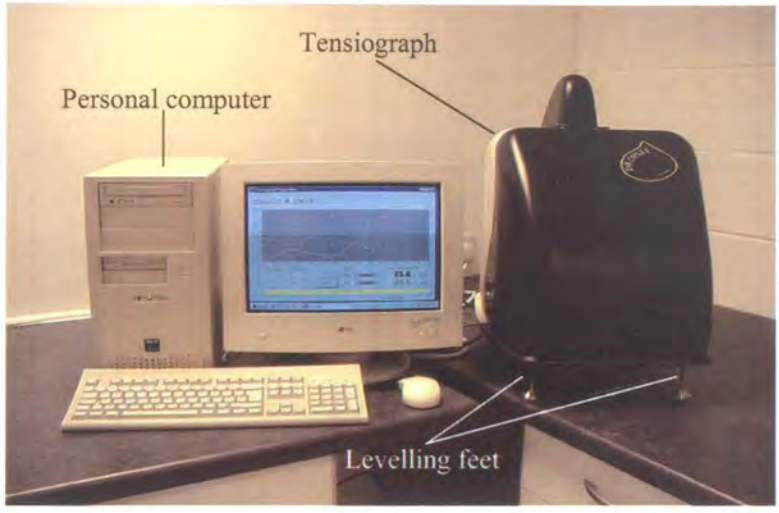

Figure 6-36. Prototype of a tensiograph.

This chapter described the system engineering development and highlighted the problems that occurred during this phase. The following chapter concentrates on tensiotrace analysis and smoothing algorithms for the de-noising process of tensiographic data sets.

CHAPTER 7

FINGERPRINT AND DATA ARCHIVING STUDIES

Previous chapters describe the tensiographic apparatus in general, but also concentrate on specific hardware and software issues of the tensiograph. The discussion in this chapter focuses on the data analysis of tensiotraces. A special method, which is outlined in Section 7.1, has been developed to improve the precise visualisation of the comparison of individual tensiotraces and the efficiency of tensiographic data archiving. For fingerprinting purposes it is important to de-noise tensiotraces before the analysis process. Two data-smoothing algorithms that have been used to de-noise tensiotraces are described in Section 7.2, which is also the last section of the thesis before the discussion of the conclusions and deliverables.

7.1 Data-Scatter and Data Archiving

This section refers to the introduction of the Hough transform inspired fingerprinting and archiving technique discussed in Chapter 2. Tensiotraces vary widely in their profile from liquid to liquid as can be seen in Figure 7-1, which shows the tensiotraces of water and ethanol. The feature space is based on dimensionless normalised units. This three-coordinate space is represented by (T,U,P), as shown in Figure 7-2. Remember that the coordinates (T_c,U_c) are computed by estimating the area between the T-axis and the tensiotrace and determining approximately the centroid of this area. It is essential to note that the (T,U)-plane in Figure 7-2(b) is basically used to represent the shape of tensiotraces as single dots.

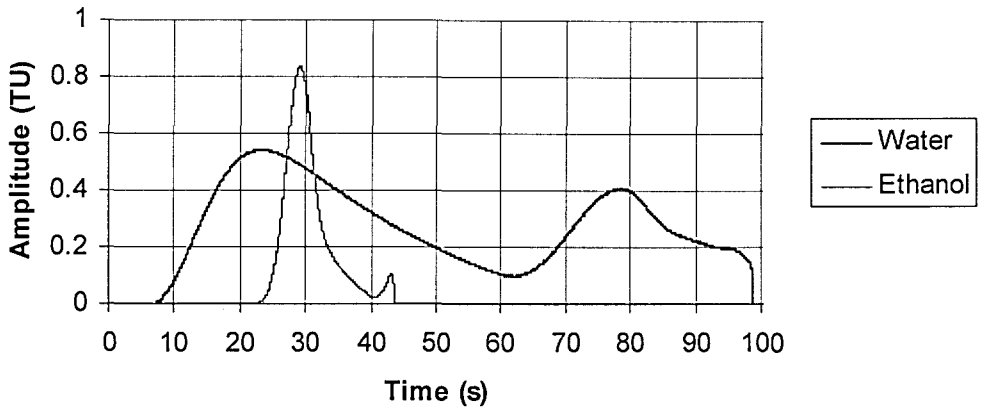

Figure 7-1. Two tensiotraces of different liquids acquired with a stainless steel knife-edge drophead @ 22.5°C and 660nm.

A shape analysis in most situations on its own should identify the nature of the LUT and give a taxiometric designation to this liquid. The height of the maximum peak of a tensiotrace is used to form a new axis, denoted as P, so that planes of (T,U,P) contain transformed points (T_c,U_c,P) from LUTs with different refractive index, colour and turbidity, i.e. lighter liquids with higher refractive index have usually a greater P-value than darker liquids with lower refractive index, depending on the wavelength of the selected LED.

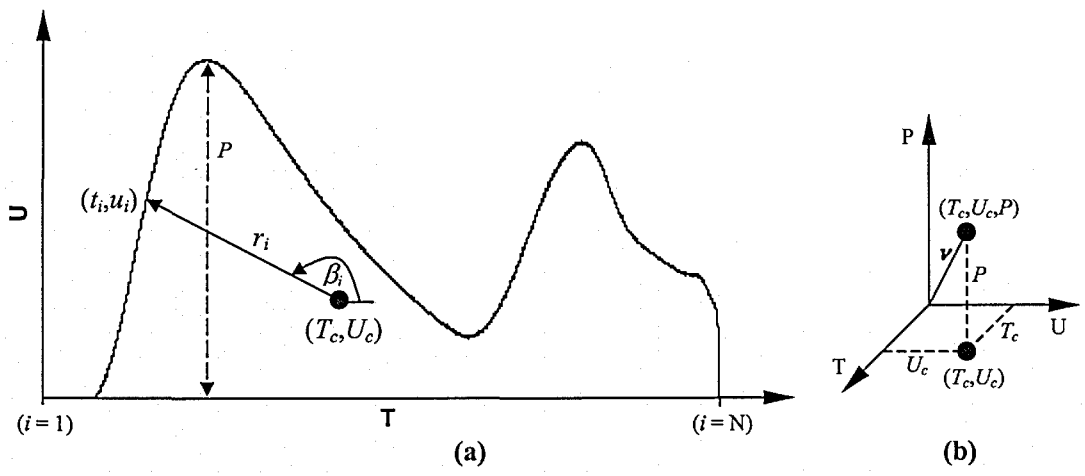

Figure 7-2. (a) Typical tensiotrace with centroid position (T_c,U_c), distance r_i and angle β_i of the i-th data point (t_i,u_i) in the (T,U)-plane, (b) feature-space (T,U,P) showing the transformed point (T_c,U_c,P) and feature-vector v.

Although the feature space (T,U,P) minimises the occurrence of *false-rejects* it still permits *false-accepts*. This can be seen by realising that it is possible for two different tensiotraces to have the same centroid (T_c,U_c) and maximum height P, and hence have equivalent feature vectors v. Therefore it is impossible to distinguish between the two traces from these two hypothetical liquids using the strategy above. To overcome this problem the GHT inspired technique for the rapid fingerprinting and conceptual

archiving of multianalyser tensiotraces has been developed. In its classical formulation in the field of image processing, the Hough transform [7-1] can only be used to detect curves, which can be defined by a closed form analytical equation. This was later extended to the formulation of the GHT, which employs a lookup table that can be used to detect arbitrary shapes in an image [7-2]. This lookup table is illustrated in Table 7-1 and each tensiotrace is conceptually linked with the, so called, (r,β)-table as demonstrated in Figure 7-2 (a), where r_i is the distance between the centroid (T_c,U_c) and the i-th data point of the tensiotrace, and β_i is the orientation that this data point has to the centroid.

Reference and Test trace	**(r,β)-table of the reference trace**		**(r,β)-table of the test trace**	
Data point	r_{ref}	β_{ref}	r_{tst}	β_{tst}
(t_1,u_1)	r_1	β_1	r_1	β_1
⋮	⋮	⋮	⋮	⋮
(t_i,u_i)	r_i	β_i	r_i	β_i
⋮	⋮	⋮	⋮	⋮
(t_N,u_N)	r_N	β_N	r_N	β_N

Table 7-1. (r,β)-tables of the reference and test traces used for the TT.

The comparison and fingerprinting technique, termed tensiotrace transform (TT), is a basic modification of the GHT. The initial step of the TT is to build up a representation of a reference trace, i.e. the trace of the known liquid. This is obtained by first choosing some arbitrary point inside the area between the trace and the T-axis. Tensiotraces vary radically in both their shape and length, hence the centroid (T_c,U_c) has been adopted as the best point with which to execute the TT. The centroid has the property of being a very stable point with respect to tensiotrace shape variations. Changes of the shape of a trace will move the centroid. The algorithm is based on an average of all the data points N of a trace and this makes it robust in that it produces small changes in the position of the centroid for small changes in the profile of a tensiotrace. It is noted that in certain cases the centroid may occur outside the trace boundary (in U-direction), but this does not affect the performance of the technique. In the implementation here, the centroid is computed from the area estimation algorithm

$$A = \sum_{i=1}^{N-1}\left(\frac{1}{2}(u_i + u_{i+1})(t_{i+1} - t_i)\right) \tag{7-1}$$

that leads to the estimated coordinates of the centroid (T_c,U_c)

$$T_c \equiv t_i \;\; for \; a_{i+1} > \frac{A}{2},\; a_{i+1} = a_i + \frac{1}{2}(u_i + u_{i+1})(t_{i+1} - t_i), \quad \begin{matrix}(0 \le i < N)\\ (a_0 \equiv 0)\end{matrix} \tag{7-2}$$

and

$$U_c \equiv j\,\Delta u \;\; for \; a_{j,i+1} > \frac{A}{2},\; a_{j,i+1} = a_{j,i} + \frac{1}{2}(u_i + u_{i+1})(t_{i+1} - t_i), \quad \begin{matrix}(0 \le i < N)\\ (0 \le j \le N_u)\\ (a_{j,0} \equiv 0)\end{matrix} \tag{7-3}$$

$$\begin{matrix} u_i \equiv (j+1)\Delta u \\ u_{i+1} \equiv (j+1)\Delta u \end{matrix} \; for \; \begin{matrix} u_i > (j+1)\Delta u \\ u_{i+1} > (j+1)\Delta u \end{matrix} \quad \Delta u = \left(\frac{k}{RES_{\max}}\right) \quad N_u = \mathrm{int}\left(\frac{p}{\Delta u}\right)$$

where Δu, with the step-width coefficient k (here 0.1) over the maximum resolution $RES_{\max}$ (here 4095, 12-bit) of the ADC, is the amplitude fraction that is successively summed in order to calculate the centroid coordinate U_c. N_u, with the maximum amplitude p of the tensiotrace over Δu, is the maximum number of steps (here int(p*40950)) in U-direction in order to reach the maximum peak height p, and A is the area between the T-axis and the tensiotrace. Note that decreasing the step-width coefficient k increases the precision of U_c, but also increases the time estimating U_c. Next, each data point along the trace is visited in turn where the orientation β and the distance from the centroid r are calculated. As each data point is visited the computed (r,β)-pair is stored in the columns r_{ref} and β_{ref} of the lookup table, indexed by i

$$r_i = \sqrt{(u_i - U_c)^2 + (t_i - T_c)^2} \qquad (1 \le i \le N) \tag{7-4}$$

and

$$\beta_i = \tan^{-1}\left(\frac{(u_i - U_c)}{(t_i - T_c)}\right) + x \quad \begin{matrix} (x = \pi) & \text{if} & ((t_i - T_c) < 0) & \text{else} & (x = 0) \\ (x = 2\pi) & & ((u_i - U_c) < 0 < (t_i - T_c)) & & \\ (\beta_i \equiv \pi/2) & & (t_i = T_c) \wedge (u_i > U_c) & & \\ (\beta_i \equiv 3\pi/2) & \text{for} & (t_i = T_c) \wedge (u_i \le U_c) & & (1 \le i \le N) \end{matrix} \tag{7-5}$$

Subsequently each data point along the test trace is visited computing the (r,β)-pairs by using the Eqs. (7-4) and (7-5). Again, as each data point is visited the computed (r,β)-pair is stored in the lookup table, this time in the columns reserved for the test trace r_{tst}

and β_{tst}, indexed by i. Note that the formulation of Eq. (7-5) generates only positive angles β_i in the range ($0 \leq \beta < 2\pi$) (mathematical convention: an angle in a (X,Y)-plane increases anti-clockwise beginning on the X-axis). At this point, the centroids $(T_c,U_c)_{ref}$ and $(T_c,U_c)_{tst}$ can be considered respectively as stacks of N_{ref} and N_{tst} exactly overlaying data points, where each point $(T_c,U_c)_i$ has been assigned a (r_i,β_i)-pair in the lookup table, i.e. reference and test trace are both represented as 'single points' in the (T,U)-plane. To compare the two tensiotraces an exchange operator Ξ has been defined that simply exchanges the two columns r_{ref} and r_{tst} in the lookup table

$$\Xi\{(r_{ref},\beta_{ref}),(r_{tst},\beta_{tst})\} \rightarrow \{(r_{tst},\beta_{ref}),(r_{ref},\beta_{tst})\} \tag{7-6}$$

When the steps above have been completed, it is possible to carry out the TT. This is done by once again visiting each data point $(t_i,u_i)_{ref}$ on the reference and $(t_i,u_i)_{tst}$ on the test trace and using the (r_i,β_i)-pair from the lookup table to compute $(t_c,u_c)_i$

$$(t_c,u_c)_i = ((t_i - r_i\cos(\beta_i)),(u_i - r_i\sin(\beta_i))) \qquad (1 \leq i \leq N) \tag{7-7}$$

The lowercase t_c and u_c indicate that the i-th value can be different to the (i-th + 1) value. If there is little difference between the reference and test traces, then each of the computed points $(t_c,u_c)_i$ for the reference trace will be close to the centroid $(T_c,U_c)_{ref}$, and each point $(t_c,u_c)_i$ for the test trace will be close to the centroid $(T_c,U_c)_{tst}$. If on the other hand the reference and test traces differ, the resulting TT will contain a high degree of scatter around the centroids. In the implementation of the TT the mean values as shown in Eqs. (7-8) and (7-9) are used to automate the measurement of the degree of scatter, where $\overline{T}$ and $\overline{U}$ represent the mean values that are calculated simply by summation over the entire number of data points N in the data set of either the reference trace or the test trace.

$$\overline{T} = \frac{1}{N}\sum_{i=1}^{N}\left\|r_i\cos(\beta_i)\right| - \left|T_c - t_i\right\| \qquad (N > 0) \tag{7-8}$$

and

$$\overline{U} = \frac{1}{N}\sum_{i=1}^{N}\left\|r_i\sin(\beta_i)\right| - \left|U_c - u_i\right\| \qquad (N > 0) \tag{7-9}$$

the deviations σ_T and σ_U of the mean values $\overline{T}$ and $\overline{U}$ are

$$\sigma_T = \sqrt{\frac{1}{N-1}\sum_{i=1}^{N}\left(\left|r_i\cos(\beta_i)\right| - \left|T_c - t_i\right| - \overline{T}\right)^2} \qquad (N>1) \tag{7-10}$$

and

$$\sigma_U = \sqrt{\frac{1}{N-1}\sum_{i=1}^{N}\left(\left|r_i\sin(\beta_i)\right| - \left|U_c - u_i\right| - \overline{U}\right)^2} \qquad (N>1) \tag{7-11}$$

Note that $|r_i\cos(\beta_i)|=|T_c-t_i|$ and $|r_i\sin(\beta_i)|=|U_c-u_i|$ before the exchange operator Eq. (7-6) is applied, i.e. the mean values Eqs. (7-8), (7-9) and the standard deviations Eqs. (7-10), (7-11) are zero. Pythagorean measures are the most obvious method of defining the 'Distance' δ between the reference and test trace data points and their associated centroids.

$$\delta = \sqrt{\overline{T}^2 + \overline{U}^2} \tag{7-12}$$

The overall 'Difference' Δ for the two dimensional projection of the data points in the (T, U)-plane is then given by

$$\Delta = \delta_{ref} + \delta_{tst} \tag{7-13}$$

where δ_{ref} is the averaged 'Distance' between the centroid $(T_c,U_c)_{ref}$ and the scattered data points of the reference trace and δ_{tst} is the averaged 'Distance' between the centroid $(T_c,U_c)_{tst}$ and the scattered data points of the test trace. The 'Closeness' ς of the two centroids of different liquids in the three-dimensional feature space (T,U,P) gives a measure of the distance between these particular points

$$\varsigma = \sqrt{\left(T_{c-ref} - T_{c-tst}\right)^2 + \left(U_{c-ref} - U_{c-tst}\right)^2 + \left(P_{ref} - P_{tst}\right)^2} \tag{7-14}$$

where T_{c-ref}, U_{c-ref} and P_{ref} are respectively the centroid coordinates and the highest peak of the reference trace, and T_{c-tst}, U_{c-tst} and P_{tst} are respectively the centroid coordinates and the highest peak of the test trace. It is important here to notice that the TT technique can be generally applied to any application that produces data sets in text format, which represent the data as two-dimensional arrays. The next section visualises the relatively theoretical discussion outlined above and describes briefly patterns that can be seen in the scatter diagrams after the TT was applied.

7.1.1 Diagnosing the Error

From the equations of the previous section it is usually quite difficult to fully understand the principle of the TT. Hence, the author of the thesis has generated six cases of the TT with different properties and limited data sets in order to show reoccurring patterns in the scatter diagrams. For the following discussion examine Figure 7-3 to Figure 7-8. The classification of the six cases is as follows:

A is associated with the reference trace, where **Ac, A1 to A5, r-A and β-A** denote the centroid, the data points, the distance between data points and centroid and the orientation that the data points have to the centroid respectively. **B** is associated with the test trace (the attributes are the same as for **A**).

Cases:

1. Amplitudes **A1** to **A5** are greater than **B1** to **B5** (different Δu); traces are not shifted (Figure 7-3).
2. Amplitudes **A1**, **A2** are greater than **B1**, **B2** and **A3** = **B3** and **A4**, **A5** are less than **B4**, **B5** (different Δu); traces are not shifted (Figure 7-4).
3. Amplitudes **A1** to **A5** are greater than **B1** to **B5** (same Δu); traces are not shifted (Figure 7-5).
4. Amplitudes **A1** to **A5** are equal **B1** to **B5**; test trace shifted to the right of the reference trace (same Δt) (Figure 7-6).
5. Amplitudes **A1**, **A2** are greater than **B1**, **B2** and **A3** = **B3** and **A4**, **A5** are less than **B4**, **B5** (different Δu); test trace is shifted to the right of the reference trace (same Δt) (Figure 7-7).
6. Amplitudes **A1** to **A5** are greater than **B1** to **B5** (same Δu); test trace is shifted to the right of the reference trace (same Δt) (Figure 7-8).

Results:

- Figure 7-3 and Figure 7-4 suggest the most basic patterns of the TT: Data point pairs **A1**, **B1** to **A5**, **B5** are horizontally further away from their centroids **Ac** and **Bc** the greater the difference between these data point pairs. If the data points **Ai** are greater than **Bi** (reference trace is above test trace) reference data points **Ai** are in the upper half of the scatter diagram while data points **Bi** are in the lower half. In contrast, if the data points **Ai** are less than **Bi** (reference trace

is below test trace) reference data points **Ai** are in the lower half of the scatter diagram while data points **Bi** are in the upper half. If the data points **Ai** are equal **Bi** these data points end up at the same position as their adversary centroids, i.e., **Ai** = **Bc** and **Bi** = **Ac**. These patterns occur after the comparison of similar tensiotraces that contain random signal noise. This means, tensiotraces of this kind are usually obtained with a properly working tensiograph.

- Figure 7-5 and Figure 7-6 show very special patterns of the TT: Data point pairs **A1**, **B1** to **A5**, **B5** are on opposite horizontal lines in the scatter diagram if the reference and test traces are horizontally shifted apart by the same distance Δu (no shift on the time axis $\Delta t = 0$). In contrast, if the tensiotraces are vertically shifted apart by the same distance Δt, but not shifted horizontally ($\Delta u = 0$), the data points **A1** to **A5** and **B1** to **B5** end up at the same position as their associated centroids **Ac** and **Bc**. These patterns usually occur in the scatter diagrams of the TT if the tensiographic instrument acquires tensiotraces with a systematic error (Figure 7-5: drophead tilted, electronic offset, etc.) following the data acquisition of a reference tensiotrace. The pattern in the scatter diagram of Figure 7-6 suggests that the data of the reference trace **A1** to **A5** was obtained with a greater remnant drop size than the data of the test trace **B1** to **B5**, which could happen when the temperatures are different between measurements.
- Figure 7-7 and Figure 7-8 show combinations of patterns in scatter diagrams that are discussed above in this section.

It can be concluded that the TT is not only an excellent method to analyse tensiotraces, but also a rather useful technique to set up a tensiographic apparatus properly. The next section describes common signal de-noising algorithms, which are an outstanding enhancement to the fingerprinting capability of tensiotraces with the TT.

	A (reference trace)				B (test trace)			
Data Point	u [TU]	t [ms]	r [1]	β [rad]	u [TU]	t [ms]	r [1]	β [rad]
1	0.215	0.223	0.142	4.70924110	0.180	0.223	0.168	4.70972827
2	0.720	0.446	0.363	1.57141341	0.677	0.446	0.329	1.57147718
3	0.913	0.670	0.556	1.57079633	0.893	0.670	0.545	1.57079633
4	0.749	0.893	0.392	1.57022745	0.735	0.893	0.387	1.57022010
5	0.450	1.116	0.093	1.56600066	0.442	1.116	0.094	1.56605168
Centroid	0.357	0.670	0	4.71238898	0.348	0.670	0	4.71238898
	A – B				A-Scatter		B-Scatter	
Data Point	Δu [TU]	Δt [ms]	Δr [1]	Δβ [rad]	u [TU]	t [ms]	u [TU]	t [ms]
1	0.035	0	-0.026	-0.00048717	0.383	0.752	0.322	0.601
2	0.043	0	0.034	-0.00006377	0.391	0.649	0.314	0.693
3	0.020	0	0.011	0	0.368	0.670	0.337	0.670
4	0.014	0	0.005	0.00000735	0.362	0.673	0.343	0.667
5	0.008	0	-0.001	-0.00005102	0.356	0.665	0.349	0.675
Centroid	0.009	0	0	0	0.357	0.670	0.348	0.670

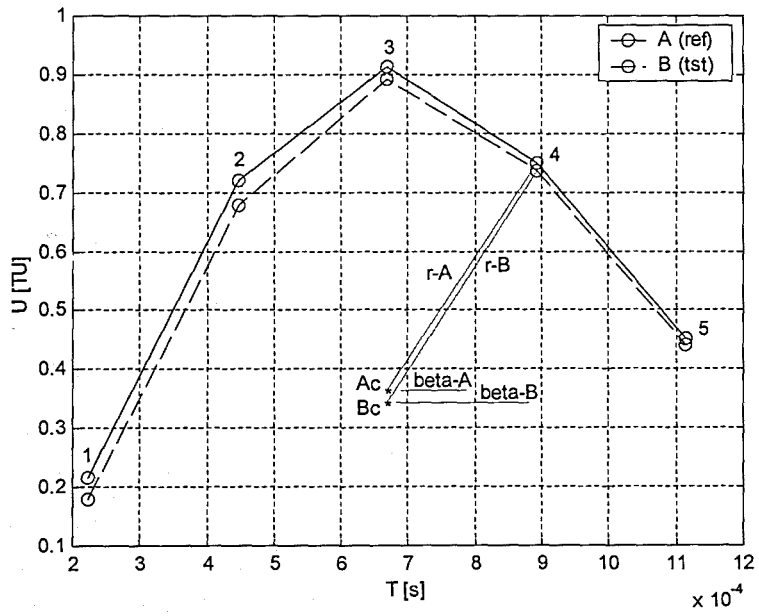

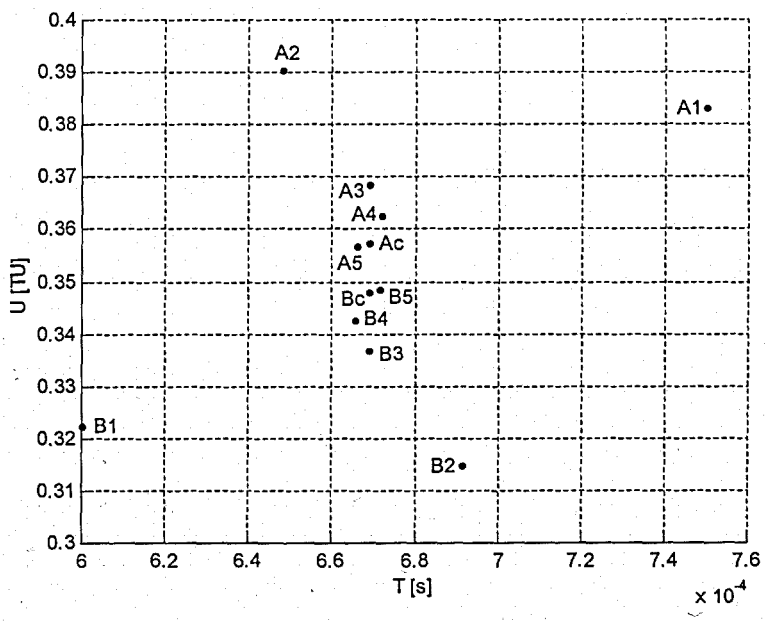

Figure 7-3. Showing a table with tensiographic values and the associated trace-diagram as well as the scatter-diagram (A: reference trace, B: test trace). Properties: $u_{1,2,3,4,5ref} > u_{1,2,3,4,5tst}$; $u_{cref} > u_{ctst}$; $t_{1,2,3,4,5ref} = t_{1,2,3,4,5tst}$.

	A (reference trace)				B (test trace)			
Data Point	u [TU]	t [ms]	r [1]	β [rad]	u [TU]	t [ms]	r [1]	β [rad]
1	0.215	0.223	0.142	4.70924110	0.180	0.223	0.180	4.70990565
2	0.720	0.446	0.363	1.57141341	0.677	0.446	0.317	1.57150295
3	0.913	0.670	0.556	1.57079633	0.913	0.670	0.553	1.57079633
4	0.749	0.893	0.392	1.57022745	0.781	0.893	0.421	1.57026664
5	0.450	1.116	0.093	1.56600066	0.476	1.116	0.116	1.56695152
Centroid	0.357	0.670	0	4.71238898	0.360	0.670	0	4.71238898
	A – B				A-Scatter		B-Scatter	
Data Point	Δu [TU]	Δt [ms]	Δr [1]	Δβ [rad]	u [TU]	t [ms]	u [TU]	t [ms]
1	0.035	0	-0.038	-0.00066455	0.395	0.790	0.322	0.576
2	0.043	0	0.046	-0.00008954	0.403	0.642	0.314	0.703
3	0	0	0.003	0	0.360	0.670	0.357	0.670
4	-0.032	0	-0.029	-0.00003919	0.328	0.654	0.389	0.685
5	-0.026	0	-0.023	-0.00095086	0.334	0.560	0.383	0.758
Centroid	-0.003	0	0	0	0.357	0.670	0.360	0.670

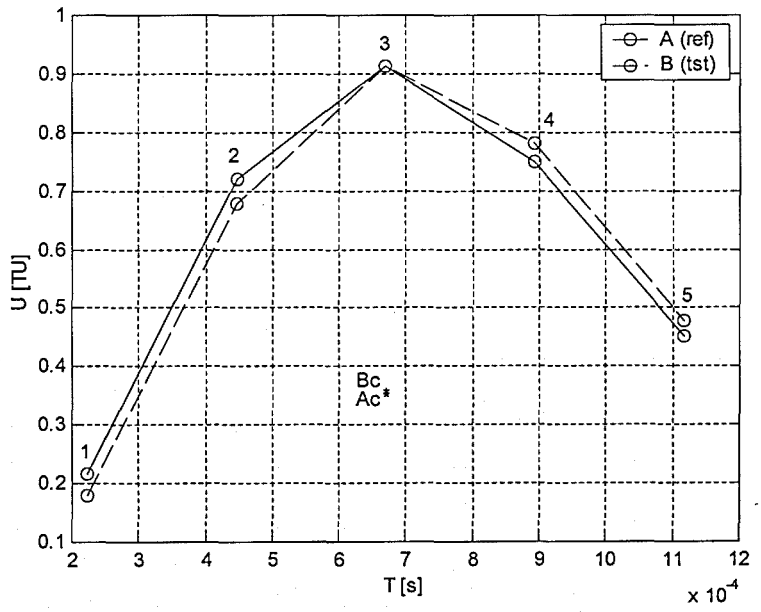

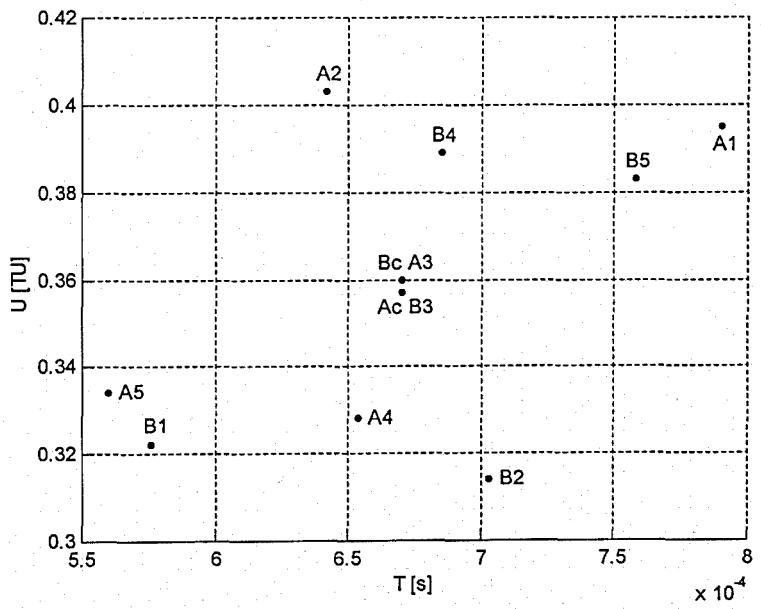

Figure 7-4. Showing a table with tensiographic values and the associated trace-diagram as well as the scatter-diagram (A: reference trace, B: test trace). Properties: $u_{1,2ref} > u_{1,2tst}$; $u_{3ref} = u_{3tst}$; $u_{4,5ref} < u_{4,5tst}$; $u_{cref} < u_{ctst}$; $t_{1,2,3,4,5ref} = t_{1,2,3,4,5tst}$.

Data Point	A (reference trace) u [TU]	t [ms]	r [1]	β [rad]	B (test trace) u [TU]	t [ms]	r [1]	β [rad]
1	0.215	0.223	0.142	4.70924110	0.180	0.223	0.162	4.70962973
2	0.720	0.446	0.363	1.57141341	0.685	0.446	0.343	1.57144939
3	0.913	0.670	0.556	1.57079633	0.878	0.670	0.536	1.57079633
4	0.749	0.893	0.392	1.57022745	0.714	0.893	0.372	1.57019686
5	0.450	1.116	0.093	1.56600066	0.415	1.116	0.073	1.56468681
Centroid	0.357	0.670	0	4.71238898	0.342	0.670	0	4.71238898

Data Point	A – B Δu [TU]	Δt [ms]	Δr [1]	Δβ [rad]	A-Scatter u [TU]	t [ms]	B-Scatter u [TU]	t [ms]
1	0.035	0	-0.020	-0.00038863	0.377	0.733	0.322	0.615
2	0.035	0	0.020	-0.00003598	0.377	0.658	0.322	0.683
3	0.035	0	0.020	0	0.377	0.670	0.322	0.670
4	0.035	0	0.020	0.00003059	0.377	0.681	0.322	0.658
5	0.035	0	0.020	0.00131385	0.377	0.766	0.322	0.548
Centroid	0.015	0	0	0	0.357	0.670	0.342	0.670

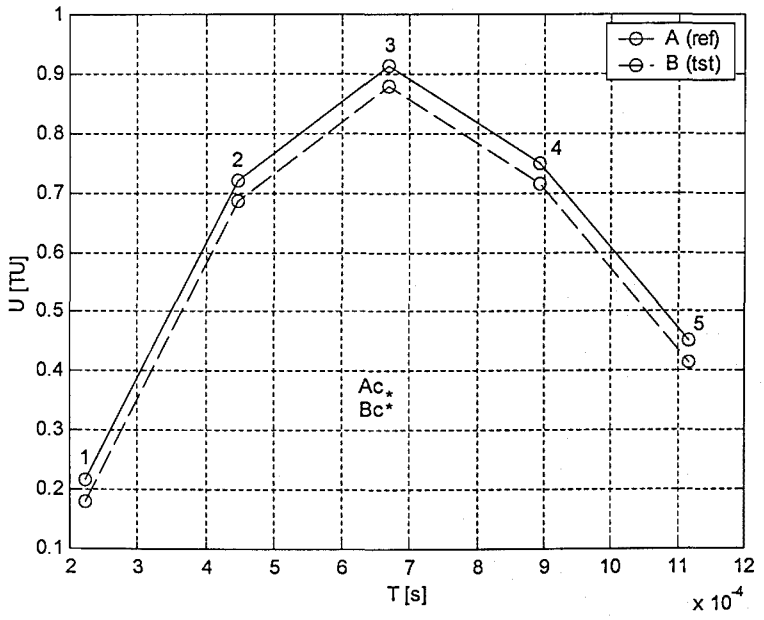

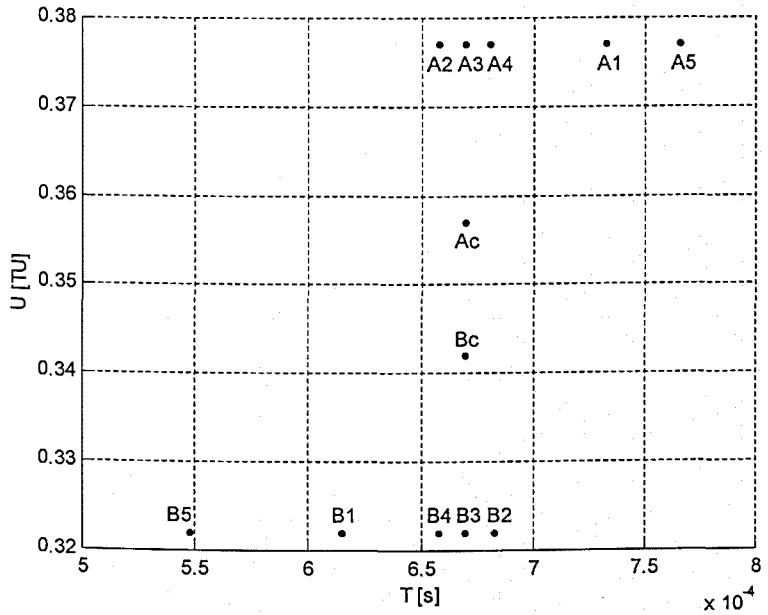

Figure 7-5. Showing a table with tensiographic values and the associated trace-diagram as well as the scatter-diagram (A: reference trace, B: test trace). Properties: $u_{1,2,3,4,5ref} > u_{1,2,3,4,5tst}$ (same difference); $u_{cref} > u_{ctst}$; $t_{1,2,3,4,5ref} = t_{1,2,3,4,5tst}$.

Data Point	A (reference trace) u [TU]	t [ms]	r [1]	β [rad]	B (test trace) u [TU]	t [ms]	r [1]	β [rad]
1	0.215	0.223	0.142	4.70924110	0.215	0.446	0.142	4.70924110
2	0.720	0.446	0.363	1.57141341	0.720	0.670	0.363	1.57141065
3	0.913	0.670	0.556	1.57079633	0.913	0.893	0.556	1.57079633
4	0.749	0.893	0.392	1.57022745	0.749	1.116	0.392	1.57022745
5	0.450	1.116	0.093	1.56600066	0.450	1.339	0.093	1.56600066
Centroid	0.357	0.670	0	4.71238898	0.357	0.893	0	4.71238898

Data Point	A – B Δu [TU]	Δt [ms]	Δr [1]	Δβ [rad]	A-Scatter u [TU]	t [ms]	B-Scatter u [TU]	t [ms]
1	0	-0.223	0	0	0.357	0.670	0.357	0.893
2	0	-0.224	0	0.00000276	0.357	0.670	0.357	0.893
3	0	-0.223	0	0	0.357	0.670	0.357	0.893
4	0	-0.223	0	0	0.357	0.670	0.357	0.893
5	0	-0.223	0	0	0.357	0.670	0.357	0.893
Centroid	0	-0.223	0	0	0.357	0.670	0.357	0.893

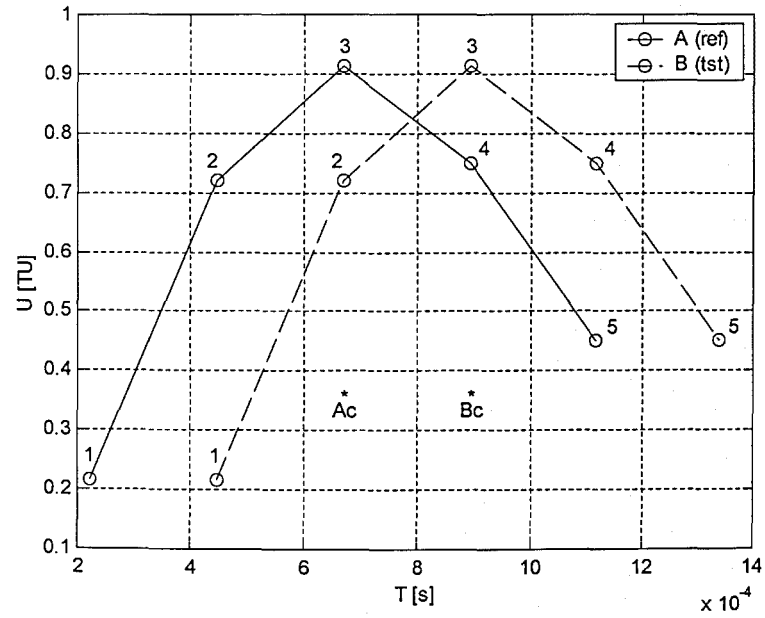

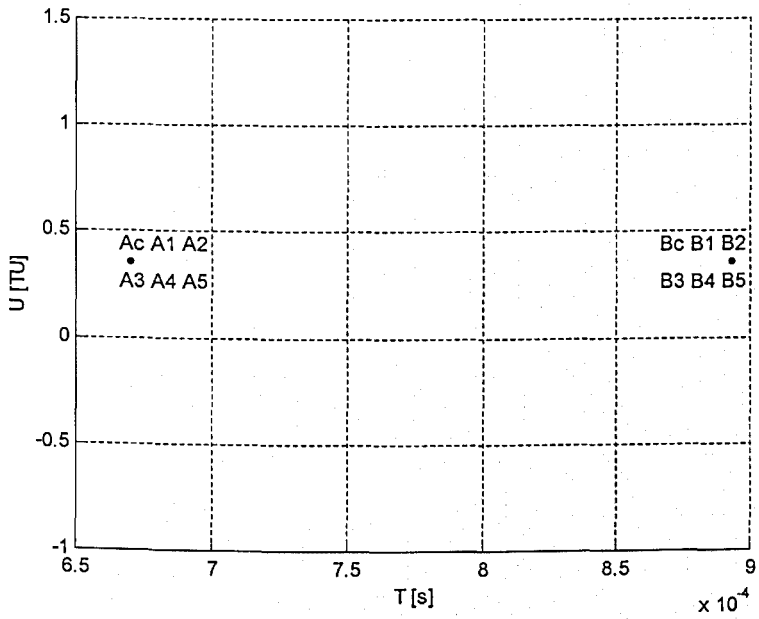

Figure 7-6. Showing a table with tensiographic values and the associated trace-diagram as well as the scatter-diagram (A: reference trace, B: test trace). Properties: $u_{1,2,3,4,5ref} = u_{1,2,3,4,5tst}$; $u_{cref} = u_{ctst}$; $t_{1,2,3,4,5ref} < t_{1,2,3,4,5tst}$.

Data Point	A (reference trace) u [TU]	t [ms]	r [1]	β [rad]	B (test trace) u [TU]	t [ms]	r [1]	β [rad]
1	0.215	0.223	0.142	4.70924110	0.180	0.446	0.180	4.70990565
2	0.720	0.446	0.363	1.57141341	0.677	0.670	0.317	1.57149980
3	0.913	0.670	0.556	1.57079633	0.913	0.893	0.553	1.57079633
4	0.749	0.893	0.392	1.57022745	0.781	1.116	0.421	1.57026664
5	0.450	1.116	0.093	1.56600066	0.476	1.339	0.116	1.56695152
Centroid	0.357	0.670	0	4.71238898	0.360	0.893	0	4.71238898
Data Point	**A – B** Δu [TU]	Δt [ms]	Δr [1]	Δβ [rad]	**A-Scatter** u [TU]	t [ms]	**B-Scatter** u [TU]	t [ms]
1	0.035	-0.223	-0.038	-0.00066455	0.395	0.790	0.322	0.799
2	0.043	-0.224	0.046	-0.00008639	0.403	0.642	0.314	0.925
3	0	-0.223	0.003	0	0.360	0.670	0.357	0.893
4	-0.032	-0.223	-0.029	-0.00003919	0.328	0.654	0.389	0.908
5	-0.026	-0.223	-0.023	-0.00095086	0.334	0.560	0.383	0.981
Centroid	-0.003	-0.223	0	0	0.357	0.670	0.360	0.893

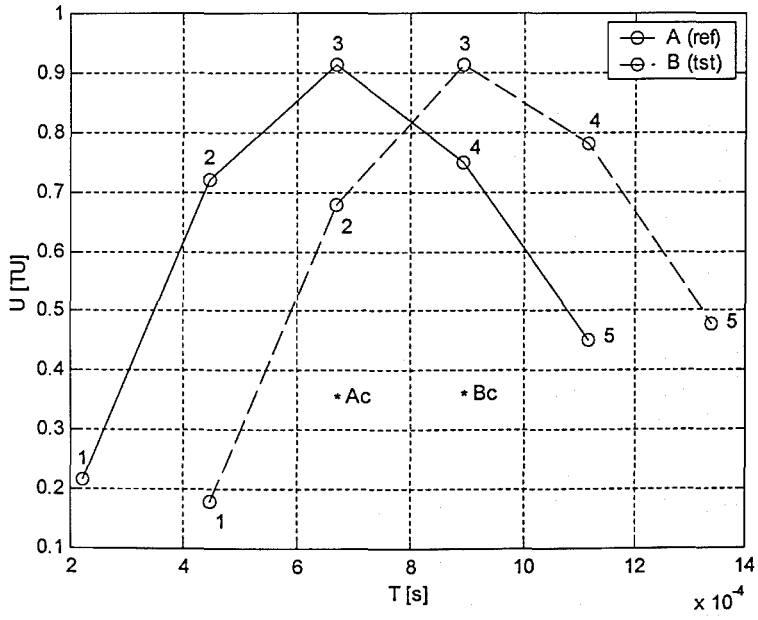

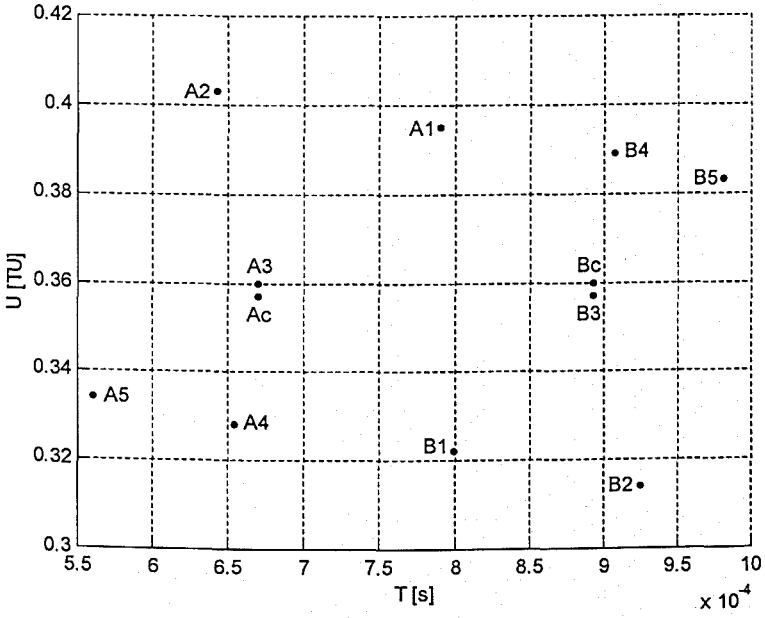

Figure 7-7. Showing a table with tensiographic values and the associated trace-diagram as well as the scatter-diagram (A: reference trace, B: test trace). Properties: $u_{1,2ref} > u_{1,2tst}$; $u_{3ref} = u_{3tst}$; $u_{4,5ref} < u_{4,5tst}$; $u_{cref} < u_{ctst}$; $t_{1,2,3,4,5ref} < t_{1,2,3,4,5tst}$.

Data Point	A (reference trace) u [TU]	t [ms]	r [1]	β [rad]	B (test trace) u [TU]	t [ms]	r [1]	β [rad]
1	0.215	0.223	0.142	4.70924110	0.180	0.446	0.162	4.70962973
2	0.720	0.446	0.363	1.57141341	0.685	0.670	0.343	1.57144647
3	0.913	0.670	0.556	1.57079633	0.878	0.893	0.536	1.57079633
4	0.749	0.893	0.392	1.57022745	0.714	1.116	0.372	1.57019686
5	0.450	1.116	0.093	1.56600066	0.415	1.339	0.073	1.56468681
Centroid	0.357	0.670	0	4.71238898	0.342	0.893	0	4.71238898
	A – B				A-Scatter		B-Scatter	
Data Point	Δu [TU]	Δt [ms]	Δr [1]	Δβ [rad]	u [TU]	t [ms]	u [TU]	t [ms]
1	0.035	-0.223	-0.020	-0.00038863	0.377	0.733	0.322	0.838
2	0.035	-0.224	0.020	-0.00003306	0.377	0.658	0.322	0.906
3	0.035	-0.223	0.020	0	0.377	0.670	0.322	0.893
4	0.035	-0.223	0.020	0.00003059	0.377	0.681	0.322	0.881
5	0.035	-0.223	0.020	0.00131385	0.377	0.766	0.322	0.771
Centroid	0.015	-0.223	0	0	0.357	0.670	0.342	0.893

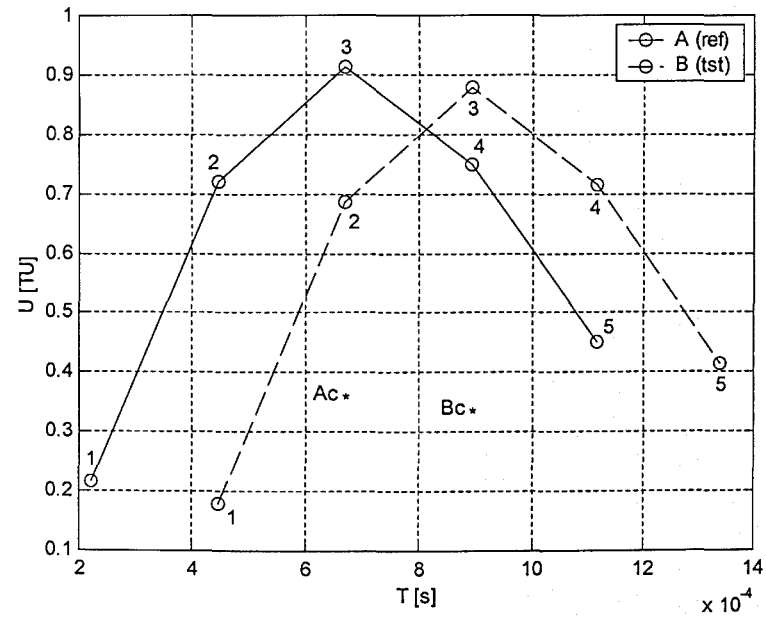

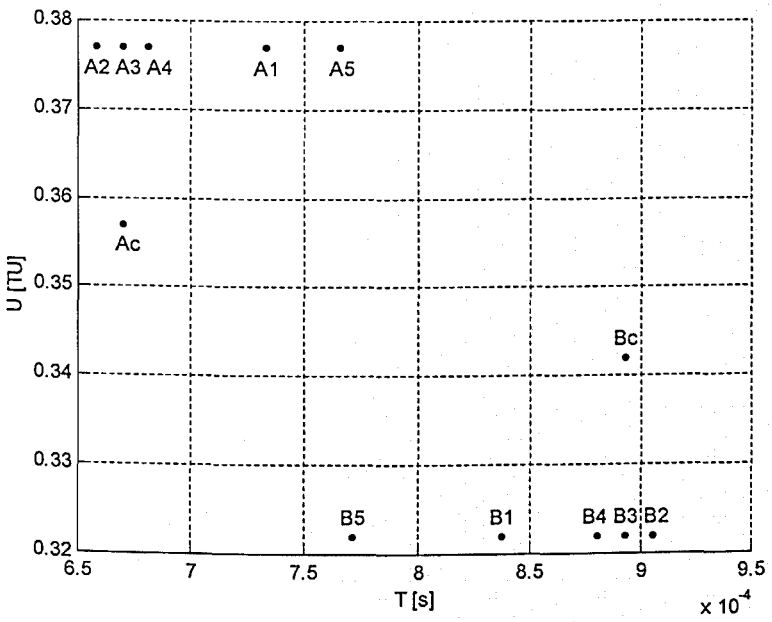

Figure 7-8. Showing a table with tensiographic values and the associated trace-diagram as well as the scatter-diagram (A: reference trace, B: test trace). Properties: $u_{1,2,3,4,5ref} > u_{1,2,3,4,5tst}$ (same difference); $u_{cref} > u_{ctst}$; $t_{1,2,3,4,5ref} < t_{1,2,3,4,5tst}$.

7.2 Data Smoothing

Previous chapters examine precautionary techniques utilized in tensiography, which contribute to the improvement of the SNR. These techniques, including vibration damping, ambient light baffling, precise temperature control, etc., have been proven extremely useful in order to obtain tensiotraces of high quality. However, some tensiographic data sets require signal de-noising prior fingerprinting procedures. Signal de-noising is one of the most serious problems in digital signal processing [7-3]. Any practical signal, apart from useful information, contains traces of irrelevant influence (interference or noise). The model of such a signal can be described as

$$u(t) = f(t) + \sigma\alpha(t) \tag{7-15}$$

where $f(t)$ is the useful signal, $\alpha(t)$ is the noise, σ is the noise level and $u(t)$ is the signal under consideration. In most cases it can be suggested that the function $\alpha(t)$ is described by the white (Gaussian) noise model [7-4], and information about the noise is contained in the high frequency spectral region of the signal, while the useful information is contained in the low frequency one. The aim of signal de-noising is to minimise the term $\sigma\alpha(t)$ in Eq. (7-15) as much as possible without causing severe distortion in the useful signal $f(t)$. Sections 2.1 and 2.2 of Chapter 2 briefly discuss the theory of noise contributions, whereas the next two sections describe different methods of de-noising tensiotraces in a more practical way.

7.2.1 Averaging Algorithm

The first data-smoothing (or signal de-noising) method described here is an averaging algorithm that has been especially adapted for the use of the de-noising procedure of tensiotraces. The equation

$$ADS = \left\{ \frac{u_1 + \ldots + u_n}{n}, \frac{u_2 + \ldots + u_{n+1}}{n}, \ldots, \frac{u_{N-n+1} + \ldots + u_N}{n}, c \right\} \quad \begin{matrix} N, n \in \aleph \\ N > 2n > 2 \end{matrix} \tag{7-16}$$

$$c = \begin{cases} 0 & \begin{matrix} n = 2 \\ n > 2 \end{matrix} \\ (0k, \ldots, 0k)_{k=N-n+2}^{N} & \end{cases} \quad if$$

returns the averaged data set (*ADS*) of a tensiotrace, where u_i is the amplitude of a single data point in a tensiographic data set, N is the maximum number of data points in this data set and n is the number of data points used for each averaging calculation in *ADS*. Figure 7-9 shows a plot of the reference tensiotrace *RT*, which is used as the bases for the explanation of de-noising processes. In order to analyse a de-noised data set of *RT* in more detail the signals under test have been magnified in the zoom-region *Z* as shown below in this section.

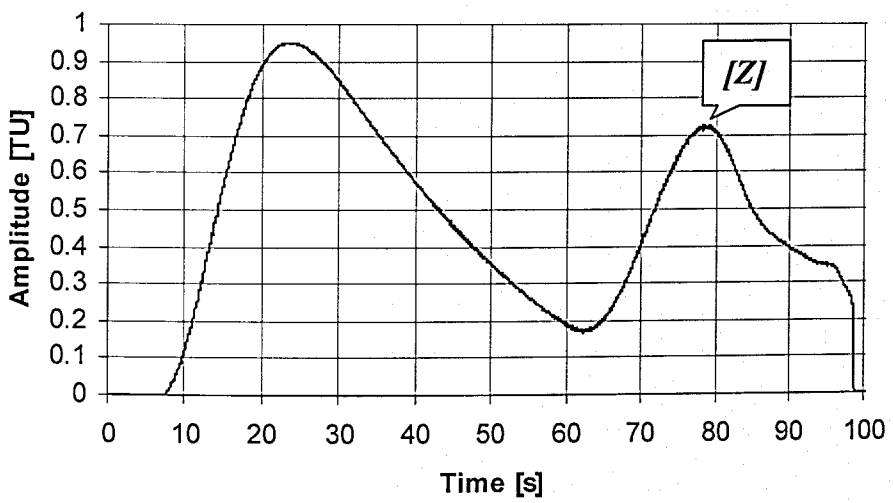

Figure 7-9. Reference tensiotrace *[RT]* of water obtained at 23.5°C using a micro-stepper pump and a 660nm LED. The data of this tensiotrace provides the bases for the explanation of de-noising processes. *[Z]* is the zoom-region for detailed analysis.

Figure 7-10 shows the magnified region *Z* of *RT* before the employment of Eq. (7-16). *RT* was acquired using a tensiograph equipped with 'noise-reducing' devices, namely, anti-vibration feet, high-resolution stepper motor pump, ambient light baffling, etc., but the quality of the SNR of *RT* is relatively low. This could be a result of a temporarily noisy environment at the location of the tensiograph during the data acquisition process.

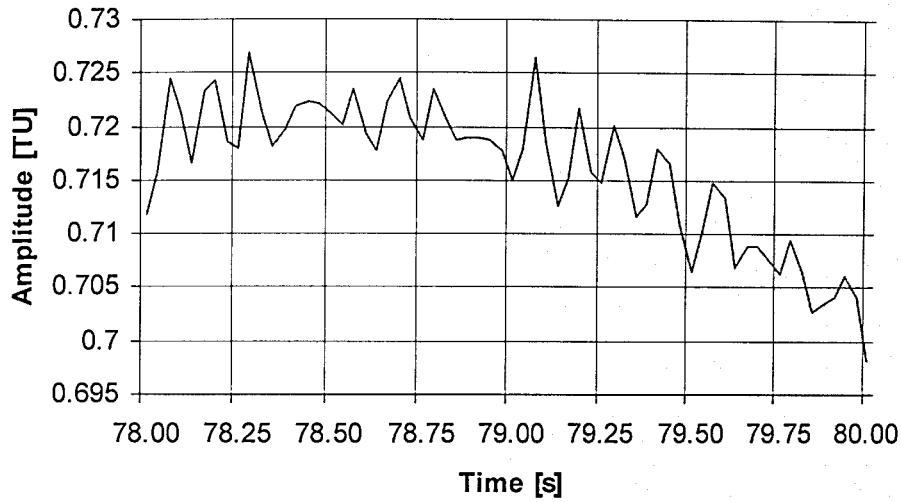

Figure 7-10. A signal-fraction in the zoom-region *[Z]* of the reference tensiotrace *[RT]*.

However, for fingerprinting purposes a tensiographic data set, as represented by *RT*, should be de-noised prior additional data analysis procedures. Figure 7-11 shows the signals before and after Eq. (7-16) was applied to *RT* with $n = 3$ and $n = 12$.

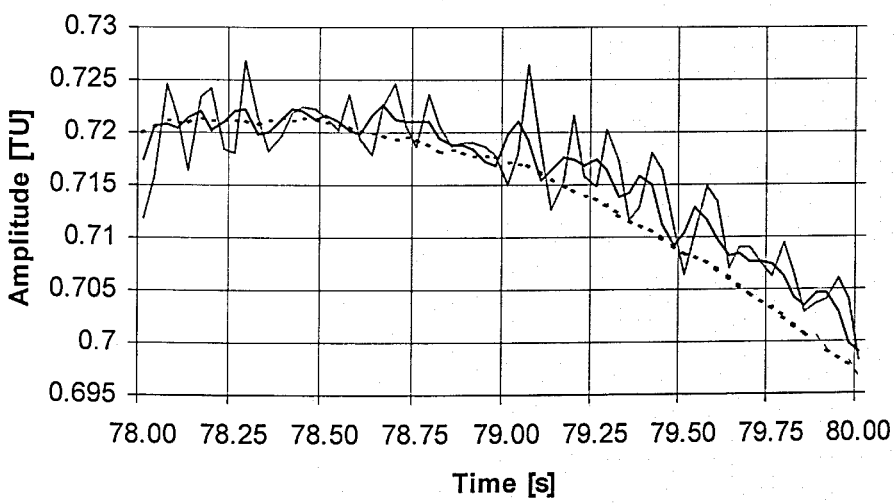

Figure 7-11. The signal-fractions in the zoom-region *[Z]* of the reference tensiotrace *[RT]*. The grey signal is showing the raw data of *[RT]*. The solid black signal and the dotted signal are showing the 3-point and 12-point averaged smoothed data set of *[RT]* respectively.

There is obviously a severe distortion of the signals the greater n is. Hence Eq. (7-16) should only be applied to tensiographic data sets with relatively low noise content, in order to obtain qualitatively good smoothed signals with a reasonably small averaging parameter n. The advantage of the averaging algorithm described above is that it can be quickly implemented and used. The next section describes a more complex method of de-noising signals.

7.2.2 Wavelet Transform

Wavelet analysis is presently one of the most promising data analysis technologies and signal de-noising is just one application in a wide range of intellectual activities [7-5]. Wavelets are a special class of functions (or sequences) that are widely used for analysing time series, i.e., a sequence of observations recorded over time such as a data set of a tensiotrace. Just as Fourier analysis is based upon the notion of representing (or re-expressing) a time series as a linear combination of sinusoids, the idea underlying wavelet analysis is to represent a series as a linear combination of wavelets. In Fourier analysis, each sinusoid is associated with a particular frequency f, so is can be deduced what frequencies are important in a particular time series by studying the magnitudes of the coefficients of the various sinusoids in the linear combination [7-6]. In contrast, each wavelet is associated with two independent variables, namely, time t and scale τ, because each wavelet is essentially nonzero only inside a particular interval of times, namely, $[t - \tau, t + \tau]$. Within that interval the wavelet spends roughly an equal amount of time above and below zero, so it appears to be a 'small wave' centred at time t and having a width of 2τ. Thus it can be learned how a time series varies on particular scales across time if it is re-expressed using wavelets [7-7]. Although this thesis concentrates entirely on data sampled over time, in fact wavelets are used extensively with data sampled over other independent variables, including two dimensional grids, parametric curves within a two dimensional surface and three dimensional objects [7-8]. Because this thesis is concerned about signal de-noising and not about wavelets as such, it would be useful for a reader who wants to delve more into wavelet analysis to consider the references [7-9, 7-10, 7-11].

The following discussion concentrates on signal de-noising using the wavelet transform tool in MATLAB [7-12]. The reference tensiotrace in Figure 7-9 served as the data set under test in this signal de-noising study and will be hereafter referred to as *RT*. The MATLAB function

$$[DDS,...] = WDENCMP(...,RT,'db',\sigma,...)$$

returns a de-noised data set (*DDS*) of the input signal *RT*, where '*db*' is a wavelet function of the Daubechies wavelet family [7-13] and wavelet decomposition is performed at level σ. Note that there exist a variety of wavelet families in order to suit

different applications and dimensions of data sets as mentioned above. Figure 7-12 shows the *DDS* of *RT* as a result of the '*db*' wavelet transform performed at 2nd level.

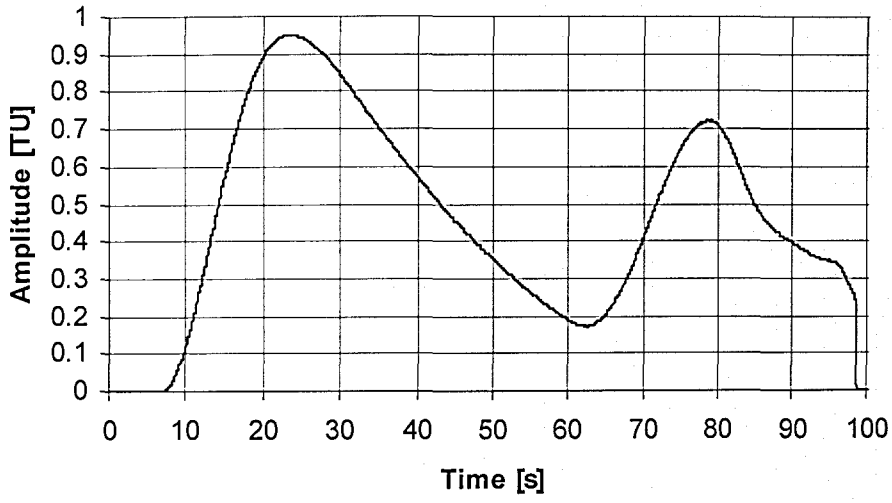

Figure 7-12. Showing the reference tensiotrace *[RT]* past de-noising procedures with a 2nd level wavelet transform.

The Comparison of the tensiotraces in Figure 7-9 and Figure 7-12 does not clearly reveal the improvement of the SNR following the 2nd level wavelet de-noising procedure. For a more methodical analysis of these two tensiotraces it is very convenient to zoom into a fraction of the data sets and Figure 7-13 shows the region *Z*, as illustrated in Figure 7-9, of *RT* before and after the 1st and 2nd level wavelet de-noising process.

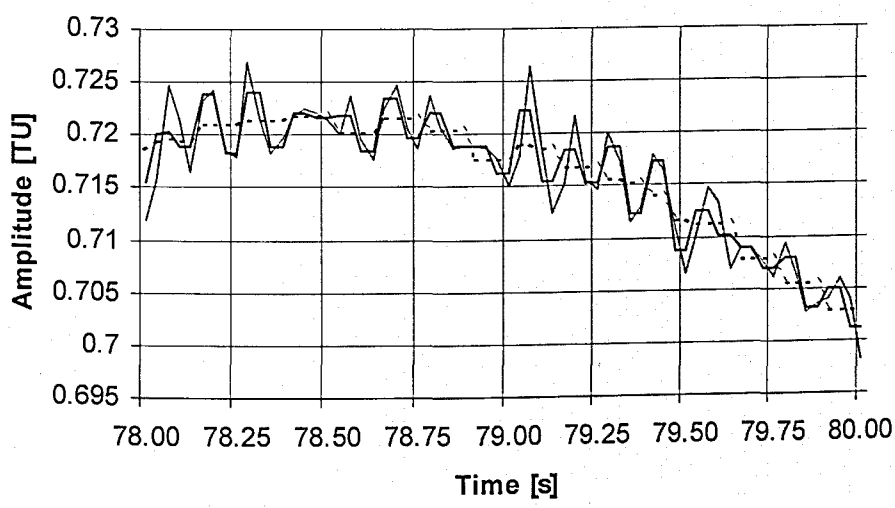

Figure 7-13. The signal-fractions in the zoom-region *[Z]* of the reference tensiotrace *[RT]*. The grey signal is showing the raw data of *[RT]*. The solid black signal and the dotted signal are showing the wavelet transform of the 1st and 2nd level de-noised data set of *[RT]* respectively.

It can be clearly seen from Figure 7-13 that the trend of the raw tensiotrace *RT* is preserved in the 1st and 2nd level wavelet de-noised tensiotraces. To observe the de-

noised data sets of the 1st and 2nd level wavelet transform in more detail the magnified regions *Z* are shown in Figure 7-14 and Figure 7-15 respectively.

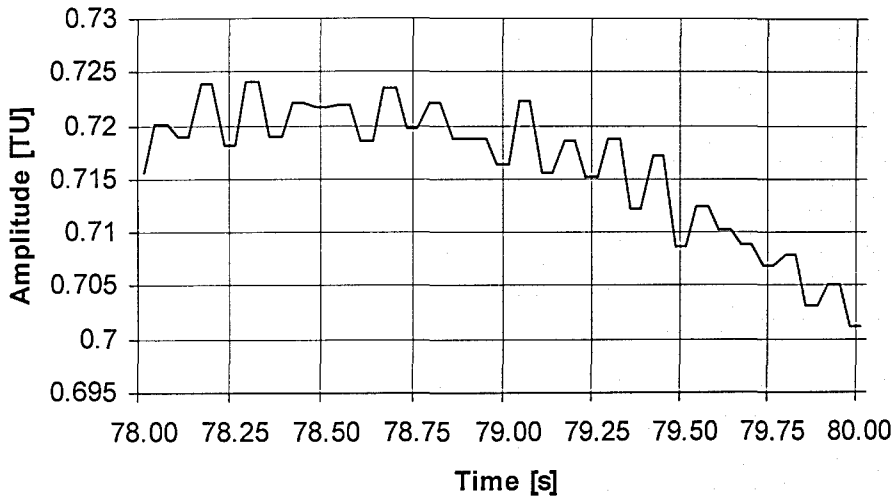

Figure 7-14. The signal-fraction in the zoom-region *[Z]* of the reference tensiotrace *[RT]* showing the wavelet transform of the 1st level de-noised data set of *[RT]*.

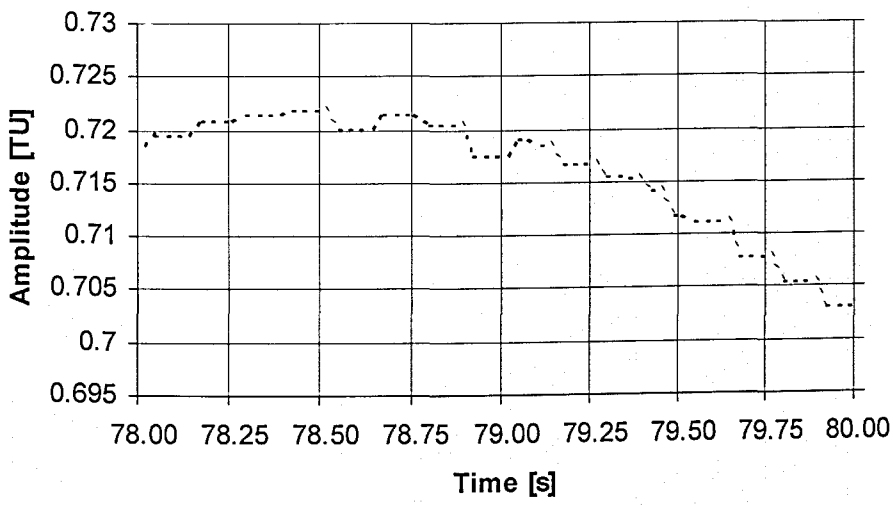

Figure 7-15. The signal-fraction in the zoom-region *[Z]* of the reference tensiotrace *[RT]* showing the wavelet transform of the 2nd level de-noised data set of *[RT]*.

The SNR has been increased by 5.6% (MATLAB analysis) following the 2nd level wavelet de-noising process of *RT* (compare Figures7-9, 7-12 and Figures 7-10, 7-15). It is also important to notice that the smoothed data sets here are less distorted than the *ADS* samples of Section 7.2.1. This is a major advantage of the wavelet transform. There are many combinations (wavelet family, noise level, signal frequency, etc.), which have to be considered carefully in order to choose a suitable wavelet function and noise level for a particular signal that has to be de-noised using wavelet transform. Inappropriate wavelet parameters will cause more damage than good. For that reason an

analyst, specialised in wavelet transform, is usually required to obtain the proper parameters through pre-analysing data sets with an appropriate tool, for example, MATLAB. This is a disadvantage of the de-noising method described here, which generally requires more time and theoretical knowledge compared to the simple de-noising method in Section 7.2.1. In this thesis the author has only dealt with a very small part of wavelet transform limited to just one wavelet family, two noise levels and one particular tensiotrace. It would have been far beyond the scope of this thesis to describe a rigorous data analysis using wavelet transforms, but the brief discussion about de-noising in this section has shown that there is a lot of potential in this technology that will be extremely useful for tensiographic applications in the future. Next, the reader of this thesis will find the Conclusions and Deliverables.

CONCLUSIONS AND DELIVERABLES

The thesis reports the work over an extended period, which has produced a physical reality of a working, easy to operate and reliable instrument. All aspects of this instrument have been engineered and the first important conclusion is that the present work has fundamentally advanced the instrumental basis of tensiography. The instrument now is at the point where application studies of some value can be undertaken. Indeed, many such application studies have been made; not least of which was the successful 5th Framework European Union (EU) project AQUA-STEW undertaken with two major water companies IRH, Nancy and ADASA, Barcelona [c-1].

The second major conclusion is that this work has introduced a new system design technique based on information for opto-electronic systems engineering. The work described here is broad and gives a fully developed example of the successful use of the new method. The starting point for this study was that an upgrade of the tensiographic system was necessary. However, no established engineering principles really could cope with the engineering problems requiring the integrated engineering of optical, electronic, thermal, mechanical and software systems so as to minimise noise and maximise signal quality. Information approaches to complex systems, such as described here, have previously been developed only for telescope engineering, which are coincidently systems with many types of noise contributions. This system engineering development has extended these approaches to optical monitoring equipment and as such constitutes an important and original contribution. The utility of these techniques have then been fully demonstrated through practice. Well-defined and proscribed steps to the engineering of the tensiographic system have been followed in this current development resulting in an instrument of high precision. Quite simply, the proof of the approach demonstrated in practice.

While the work described here has been in most places rapidly superseded by new commercial technological developments, it is the belief of the author that this thesis represents a landmark study in tensiography as a new scientific-industrial technology for both laboratory and process control applications. The thesis is very unusual in that it describes the work done by the author while in the employ of Carl Stuart Ltd., Tallaght, Dublin and for a shorter period Kelman Ltd., Lisburn, N. Ireland. Subsequently, work

was done in collaboration with two major water companies in a €1,200,000 EU project. Such industrial involvement is very important for any engineering project, as it has raised the stage of engineering to professional levels in every area. The new and universal systems engineering method devised by the author may have some important contributions in future projects in which multi-energy systems are being designed. The claim here is that the work is for the most part of a very high quality and probably as such is not typical of PhD studies, which rarely one suspects deliver commercial quality products. It is worth pointing out that the work described is the launch pad for the current commercial developments of this technology in Carl Stuart Ltd.

Importantly, the various solutions to the many engineering problems proposed here for the instrument arrived through the author working with a diverse team of engineers and applications people. Eventually a system was devised that answered all the demands of this diverse and demanding group, which is a notable achievement in itself. The recent and remarkable application results from Morrin [c-2], Bertho [c-3] and Dunne [c-4] are testament to the value of the instrument developed by the author. The instrument has, in addition to good instrumental sensitivity, accuracy and precision, many other attributes, which are worthy of mention and were devised by the author to answer the needs of these applications researchers. The most important are firstly the design of a thermal Peltier module, which can be varied in a relatively wide temperature range (10°C to 40°C). This requirement arose from the huge variety of solutions that had to be analysed in order to verify the quality of the instrument by testing the applicability for different important applications. These vital measurements had been conducted in a harsh laboratory environment with people causing mechanical disturbances, doors opening and closing, operating machinery and ambient light interference. Precise measurements were only made possible by protecting the instrument using sophisticated anti-vibration and light baffling systems. However, the key elements of a tensiograph are the drophead and the liquid delivery system and continuous development of these central devices has been of enormous benefit to all researchers involved in the tensiographic project.

It is clear that tensiography and micro-volume spectroscopy is developing internationally (Singapore, China, Texas EPA). This impressive growth can be seen as being in part led by the work of the author as an important member in the Carl Stuart team, but also working closely with Augousti in Kingston University. It must be concluded that the work described here is of some very real value, in the first instance to

Carl Stuart Ltd., but ripples of disturbance from these engineering developments have gone out to encourage the wider development of the new technology. From 1999 with the appearance of the Nanodrop spectrometer a whole international development has opened up in micro-volume spectral analysis largely led by the need to do Deoxyribonucleic Acid (DNA), Ribonucleic Acid (RNA) and other UV bio-assays. The work of McMillan on drop analysis was quoted in the Nanodrop patents, but in reality the micro-volume UV and fluorescence spectrometer are not really drop analysers as they pull the liquid sample up into a capillaries for the analysis. This method causes problems of cleaning and very short OPL, but the commercial development has been very successful and this is not the top selling instrument in the world. McMillan, O'Neill and Smith undertook recent studies of micro-volume measurements, based on the idea of actually using the drop as a cuvette. These techniques are in fact drop spectrometers and new analytical equations will be devised to provide a sound theoretical basis for drop spectroscopy, which is recognisable as a modified Beer's law. Drop spectrometers have a higher sensitivity than traditional instruments. The actual reasons for this are rather complex and not of concern to this thesis, but here it is important to point out that the work reported has contributed to these new and exciting developments.

The commercial plans of Carl Stuart Ltd. are now in place and a commercialisation project, funded by the Scientific Research & Development Institute RTI, commenced in 2007. The objectives of this project were successfully achieved in the detection and fingerprinting of PP in real waters [c-5]. This study was however one of a number of important application studies done under the supervision of McMillan for wine [c-6] and water [c-7] quality assurance. It is concluded that these objectives for a new major project have come directly from not just the engineering advances of the author, but from his research collaboration with McMillan. The author is cited on many papers as outlined in the List of Publications of Appendix 0.

REFERENCES

References are listed in the form *[x-y] reference*, where x and y represent the chapter number and the index of the reference within this chapter respectively.

[1-1] T. Tait, Phil. Mag. 27, (1864), p. 176.

[1-2] Rayleigh, Phil. Mag. 48, (1899), pp. 321 – 327.

[1-3] McMillan N.D., Measuring a property of a liquid, US Patent Serial No. 175859 and similar patents in 17 other countries.

[1-4] McMillan N.D., A liquid drop forming device, Belgian Patent No. 1001659A6, Application No. 8901247 with applications proceeding in 17 other countries.

[1-5] Tomihito Kambara and Tomoe Kiba, Stalagmometric titration, Talanta, Volume 19, Issue 4, April 1972, pp 399 – 406.

[1-6] J. Tyndall, On some phenomena connected with the motion of liquids, Proc. Roy. Inst. G.B., Jan. 27, 1854.

[1-7] J. Tyndall, On Rainbows, Proc. Roy. Inst. G.B., Jan. 18, 1884.

[1-8] N.D. McMillan, O. Finlayson, F. Fortune, M. Fingleton, D. Daly, D. Townsend, D.D.G. McMillan and M.J. Dalton, The fibre drop analyser: a new multianalyser analytical instrument with applications in sugar processing and for the analysis of pure liquids, Meas. Sci. Technol. 3, (1992), pp. 746 – 764.

[1-9] C. H. Wang, A. T. Augousti, J. Mason, N. D. McMillan, Capacitive drop tensiograph: a novel multianalysing technique for measuring the properties of liquids, Meas. Sci. Technol. 10 (1999), pp. 19 – 24.

[1-10] A. Augousti, J. Mason, H. Morgan, and N. D. McMillan, Ultrasonic tensiography measurements on liquid drops for liquid fingerprinting, Sensors and Their Applications XII, S. J. Prosser and E. Lewis (Eds), IOP Publishing 2003, pp. 297 – 302.

[1-11] A. Augousti, J. Mason, H. Morgan, and N. D. McMillan, Application of ultrasonic tensiography to analysis of red wine, accepted for presentation, Photon04, Glasgow, September 2004.

[1-12] J. Tyndall, The Rainbow and its Congeners, New Fragments, Longmans, London (1892), pp. 199 – 223.

[1-13] N.D. McMillan, F.J.M. Fortune et al, A fiber drop analyser: A new analytical instrument for the individual, sequential, or collective measurement of the physical and chemical properties of liquids, Rev. Sci. Instrum, 63 (6), June 1992, pp. 3431 – 3454.

[1-14] N.D. McMillan, V. Lawlor, M. Baker and S. Smith, From Stalagmometry to Multianalyser Tensiography: The Definition of the Instrumental, Software and Analytical Requirements for a New Departure in Drop Analysis, Studies in Interface Science, Drops and Bubbles in Interfacial Research, Elsevier Science B.V., (1998), pp. 593 – 705.

[1-15] N.D. McMillan, O. Finlayson, F. Fortune, M. Fingleton, D. Daly, D. Townsend, D.D.G. McMillan and M.J. Dalton, The fibre drop analyser: a new multianalyser analytical instrument with applications in sugar processing and for the analysis of pure liquids, Meas. Sci. Technol. 3, (1992), pp. 746 – 764.

[1-16] Norman D. McMillan, Eon O'Mongain, James Walsh, Liam Breen, Duncan G.E. McMillan, Michael J. Power, John P. O'Dea, Seamus M. Kinsella, Mairead P. Kelly, Conor Hammil, and Dermot Orr, Preliminary investigation into the analytical potential of a multi-wavelength fiber drop analyser with special reference to applications in medical diagnostics, Optical Engineering 33(12), (1994), pp. 3871 – 3890.

[1-17] N.D. McMillan, F.E. Feeney, M.J.P. Power, S.M. Kinsella, M.P. Kelly, C. Hammil, K.W. Thompson, J.P. O'Dea, A QUALITATIVE STUDY OF FIBRE DROP TRACES ON MECHANICALLY EXCITED DAMPED VIBRATIONS OF DROPS OF PURE LIQUIDS USING FFT ANALYSIS, Marcel Dekker, Inc., (1994).

[1-18] N.D. McMillan, P. Davern, V. Lawlor, M. Baker, K. Thompson, J. Hanrahan, M. Davis, J. Harkin, M. Bree, P. Goossens, S. Smith, D. Barratt, R. Corden, D.G.E. McMillan, D. Lane, The instrumental engineering of a polymer fiber drop analyser for both quantitative and qualitative analysis with special reference to fingerprinting liquids, Colloids and Surfaces, A: Physicochemical and Engineering Aspects, 114 (1996), pp. 75 – 97.

[1-19] R. Miller, A. Hofmann, R. Hartmann, K. Schano, and A. Halbig, Adv. Mater. 4(5) (1992), pp. 370 – 374.

[1-20] N.D. McMillan, R. Jordan, D. Phillips, M. O'Neill, M. Reddin, J. Nolan, R. Harnedy, J. Harkin, V. Lawlor, L.R.L. McMillan, Wai Yip Lo, Wayne Mitchell, A New Approach to the Information Processing of Multivariate Data from the Tensiograph Multianalyser Traces Obtained on Commercial Beers and their Constituents, Institute of Technology Carlow, Kilkenny Road, Ireland, (1998).

[1-21] N.D. McMillan, D. Dowling, M. O'Neill, T. Yeomans, R. Miller, A New Tensiograph Approach to Concentration Measurements of Pure Protein Solutions using Tensiotrace Area D-Values Introduced through a Comparative Study of Sensitivity against a Standard UV-visible Analysis for Bovine Serum Albumen, OESI-IMVIP '98, Optical Engineering Society of Ireland & Irish Machine Vision and Image Processing Joint Conference.

[2-1] M. O'Neill, New tensiograph signal processing and multivariate methods with confirmatory measurement programmes in brewing, bioengineering and pure liquids applications, Institute of Technology Carlow, Kilkenny Road, Ireland, Thesis submitted to the National Council for Educational Awards for the degree of Doctor of Philosophy, December 2000, pp. 218 – 225.

[2-2] E.S.F Electronic, Goettingen, Germany, (2001), anti-vibration systems specialists.

[2-3] Shannon C. E., "Communications in the Presents of Noise", Proc. IRE, 37, 1949.

[2-4] Shannon C. E., "A Mathematical Theory of Communications", BSTJ, 27, 1948.

[2-5] D. H. Ballard, Generalising the Hough transform to detect arbitrary shapes, Pattern Recognition, 13 (1981), pp. 111 – 122.

[2-6] J. R. Taylor, AN INTRODUCTION TO Error Analysis, 2nd ed., (1997), pp. 215-218.

[2-7] R. Johnson, G. Bhattacharyya, Statistics – Principles and Methods, 2nd ed., (1992), pp. 577-603.

[3-1] E. Schruefer, Elektrische Messtechnik: Messung elektrischer und nichtelektrischer Groessen, 5. durchgesehene Auflage, Muenchen; Wien: Hanser, 1992, ISBN 3-446-17128-2.

[3-2] R. F. Shea, Transistor Circuit Engineering, Sixth Printing April 1963, John Wiley & Son Inc., Library of Congress Catalogue Card Number: 57-8896, pp 62-67.

[3-3] U. Tietze, C. Schenk, Halbleiter-Schaltungstechnik, 10. Auglage Berlin; Springer, 1993, ISBN 3-540-56184-6, pp. 423-424.

[3-4] D. Carbery, S. Riedel, N. McMillan, An Experimental Investigation Into the Engineering Basis for a New Fiber Optic Small Volume Drop Surface Analyser, Sensors and their Applications XI/ISMCR 2001, pp. 209-214.

[3-5] I. N. Bronstein, K. A. Semendjajew, Taschenbuch der Mathematik, 25. Aufl, B. G. Teubner Verlagsgesellschaft, Stuttgart, 1991, ISBN 3-8154-2000-8, p. 114.

[3-6] U. Tietze, C. Schenk, Halbleiter-Schaltungstechnik, 10. Auglage Berlin; Springer, 1993, ISBN 3-540-56184-6, p. 855.

[4-1] B. Stroustrup, The C++ Programming Language, 2nd ed., Addison-Wesley, (1991), ISBN 0-201-53864-4.

[4-2] Visual Basic Books Online (Creating ActiveX Components), Microsoft Visual Basic Professional Edition, Version 5.0, © 1987-1997 Microsoft Corp.

[4-3] D. E. Comer, Computer Networks and Internets, 1st ed., Prentice-Hall Inc., (1997), ISBN 0-13-239070-1.

[5-1] M. O'Neill, New tensiograph signal processing and multivariate methods with confirmatory measurement programmes in brewing, bioengineering and pure liquids applications, Institute of Technology Carlow, Kilkenny Road, Ireland, Thesis submitted to the National Council for Educational Awards for the degree of Doctor of Philosophy, December 2000, pp. 157 – 161.

[5-2] Eldon James Corp., Loveland Co 80538, Properties of Materials, pages 3, 4, and 11.

[5-3] Lawrence Berkeley National Laboratory, Berkeley campus of the University of California, http://eande.lbl.gov/ECS/aerogels/saoptc.htm, April 2004.

[5-4] N. D. McMillan et al, New approaches to dimensionally invariant tensiograph theory and progress towards direct-uncorrected drop volume measurements of surface tension, Institute of Technology Carlow, Kilkenny Road, Ireland, (2001).

[5-5] Sunergia Group Inc., 11703 Bowman Green Drive, Reston VA 20190, USA, Sunergia Medical, Biotechnology Instrumentation Distribution, Sunergia Info-Flash, Volume 1, Issue 1, page 2.

[5-6] Optiglas Ltd., 52/54 Fowler Road, Hainault, Essex, IG6 3UT, England, Optical Components, Cuvettes and Reference Materials.

[6-1] Protection of a monumental building against traffic-induced vibrations, Soil Dynamics and Earthquake Engineering, Volume 17, Issue 5, July 1998, Page 289-296, Paolo Clemente and Dario Rinaldis.

[6-2] Laser induced voltage in CMR thin films and its device application, Physica C: Superconductivity, Volumes 364-365, November 2001, Pages 656-658, P. X. Zhang, J. B. Wang, G. Y. Zhang, H. –U. Habermeier and W. K. Lee.

[6-3] Numerical modelling and a design of a thermoelectric dehumidifier, Applied Thermal Engineering, Volume 22, Issue 4, March 2002, Pages 407-422, J. G. Vián, D. Astrain and M. Domínguez.

[6-4] Richardson ML, Gangolli S, eds. B157 Bismuth telluride. In: The dictionary of substances and their effects. Cambridge, UK: Royal Society of Chemistry, 1992: 684 (Vol 1).

[6-5] Beliles RB. Bismuth, Bi. In: Clayton GD, Clayton FE, eds. Toxicology. 4th ed. New York, USA: J. Wiley & Sons, 1994: 1948-54 (Patty's industrial hygiene and toxicology; Vol II Pt C).

[6-6] T. D. Hien and M. Kleiber, Stochastic finite element modelling in linear transient heat transfer, Comput. Methods Appl. Mech. Eng. 144 (1997), pp. 111 – 124.

[6-7] K. + R. Gieck, Technische Formelsammlung, 29. deutsche Auflage, (1989), Gieck Verlag, D-8034 Germering, ISBN 3-920379-17-9, p. Z5.

[6-8] B. Dietmar, Basiswissen Elektronik, Bd.9 Regelungstechnik, vde-verlag gmbh, (1988), D-1000 Berlin 12, ISBN 3-8007-1292-X, pp. 27-49.

[6-9] M. Chaplin, Water structure and behaviour (Molecular Vibration and Absorption), Water and Aqueous Systems Research, London South Bank University, Borough Road, London SE1 0AA, UK, http://www.lsbu.ac.uk/water/, (18/07/2005).

[6-10] Bergmann, Schaefer, Mechanik Akustik Wärme, Lehrbuch der Experimentalphysik, Band 1, 10. Auflage, Walter de Gruyter, ISBN 3 11 012391 6, (1990), pp. 722-735.

[6-11] N. J. A. Sloane & Aaron D. Wyner, "Claude E. Shannon Collected Papers", IEEE Press, 1993, pp. 5-83.

[7-1] P. V. C. Hough, Methods and means of recognising complex patterns, U.S. Patent 3069654, (1962).

[7-2] R. O. Duda and P. E. Hart, Use of the Hough transform to detect lines and curves in pictures, Communications of the ACM, 15 (1972), pp. 11 – 15.

[7-3] Donoho, D.L. De-Noising by soft-threshholding, IEEE Trans. On Inf. Theory, vol. 41, 3, 1995, pp. 613-627.

[7-4] G. Corn, T. Corn, Mathematics reference book for scientists and engineers, Moscow, Nauka Publishers, 1977.

[7-5] I. Daubechies, Ten Lectures on Wavelets, CBMS, SIAM, 61, 1994, 75.

[7-6] Whittaker E. T. and Robinson G., Practical Fourier Analysis, Ch. 10 in The Calculus of Observations: A Treatise on Numerical Mathematics, 4th ed., New York: Dover, pp. 260-284, 1967.

[7-7] Mallat S. G., A Wavelet Tour of Signal Processing, Second Edition, Academic Press, San Diego, 1999.

[7-8] Stollnitz E. J., DeRose T. D. and Salesin D. H., Wavelets for Computer Graphics: Theory and Applications, Morgan Kaufmann, San Francisco, 1996.

[7-9] Bruce A. G. and Gao H. Y., Applied Wavelet Analysis with S-PLUS, Springer, New York, 1996.

[7-10] Ogden R. T., Essential Wavelets for Statistical Applications and Data Analysis, Birkhaeuser, Boston, 1997.

[7-11] Percival D. B. and Walden A. T., Wavelet Methods for Time Series Analysis, Cambridge University Press, Cambridge, UK, 2000.

[7-12] MathWorks, Inc., MATLAB (The Language of Technical Computing), Version 5.3.1.29215a (R11.1), September 28, 1999.

[7-13] Y. Meyer, Wavelets: Algorithms and Applications, Society for Industrial and Applied Mathematics, Philadelphia, 1993, pp. 13-31, 101-105.

[c-1] Water Quality Surveillance Techniques for Early Warning by Interface Sensors, EVK1-2000-00736 Area Code: 1.1.4.-1.5.1 AQUA-STEW, http://www.fwr.org/fp5.pdf, Co-ordinator: Georges Pottecher email: rech@irh.fr, Direction Des Etudes Et De La Recherche Irh Genie De L' Environnement FR, Partners: Institut de Recherches Hydrologiques IRH – Ggenie de l' Environnement SA Vandoeuvre-les-Nancy FR, Carl Stuart Ltd. Dublin IE, Institute of Technology Carlow IE, National University of Ireland, Dublin – University College Dublin IE, Kingston University Kingston upon Thames GB, Liverpool John Moores University Liverpool GB, Kelman Ltd. Lisburn GB, Queen's University of Belfast GB, ADASA Sistemas S.A. Barcelona ES.

[c-2] Tensiographic drop volume methods for characterisation of alcohols and bi-functional liquids, D. Morrin, N.D. McMillan, K. Beverley, M. O'Neill, B. O'Rourke, G. Dunne, A. Augousti, J. Mason, F. Murtagh and M. Kokuer, Proc. SPIE Vol. 5826, 2005, pp. 670-678.

[c-3] Optical studies into the SPLITS effect: New insights into controlling sampling errors in turbid solutions for analytical instruments, A.C. Bertho, D.D.G. McMillan, N.D. McMillan, S.R.P. Smith and B O'Rourke, Proc. SPIE Vol 5826, pp. 99-109.

[c-4] Optical monitoring of proteins at solid surfaces, G. Dunne, L. McConnell, R. Miller, N.D. McMillan, B. O'Rourke and C.I. Mitchell, Proc. of SPIE, Vol. 5824, 2005, pp. 199-204.

[c-5] A feasibility study into differential tensiography for water pollution studies with some important monitoring proposals, AC Bertho, DDG McMillan, ND McMillan, B O'Rourke, G Doyle, M O'Neill, Sensors and their Applications XII (IOPP, Bristol and Philadelphia, Sept 2003), pp. 291-296.

[c-6] Application of Characteristic Vector Analysis to multianalyser tensiography for the study of aqueous-ethanol solutions and French wine solutions, M. O'Neill, N.D. McMillan, G. Doyle, P. Pringuet and E. O'Mongain, Proc. of SPIE Vol. 5827, 2005, pp. 244-254.

[c-7] Ecological tensiography: initial application study of watercolour from an Irish bog, unpolluted river and rivers receiving mine effluent, D.D.G. McMillan, A.C. Bertho, B. O'Rourke, D. Phillips, M. O'Neill and D. Morrin, Sensors and their Applications XII (IOPP, Boston and Philadelphia, 2003), pp. 591-598.

APPENDIX 0

LIST OF PUBLICATIONS

N. D. McMillan, S. Riedel, J. McDonald, M. O'Neill, N. Whyte, A. Augousti and J. Mason, A Hough Transform Inspired Technique for the Rapid Fingerprinting and Conceptual Archiving of Multianalyser Tensiotraces, Dublin City University, Irish Machine Vision and Image Processing Conference Proceedings, ISBN 1 872 327 22 2, (1999), pp. 330-346.

N. D. McMillan, S. M. Riedel, A. T. Augousti and J. Mason, The development of a commercial multivariate laboratory and process control measurement system with industrial and medical applications, Institute of Physics, Sensors and their Applications XI Proceedings, ISBN 0-7503-0821-4, (2001), pp. 191-196.

D. Carbery, S. Riedel, and N. McMillan, An experimental investigation into the engineering basis for a new fiber optic small drop surface analyser, Institute of Physics, Sensors and their Applications XI Proceedings, ISBN 0-7503-0821-4, (2001), pp. 209-214.

D. Carbery, N. D. McMillan, M. O'Neill, S. R. P. Smith, S. Riedel, B. O'Rourke, A. Augousti and J. Mason, Drop shape sensor modelling and imaging: new measurement approaches for refractive index monitoring, Institute of Physics, Sensors and their Applications XII Proceedings, ISBN 0-7503-0978-4, (2003), pp. 585-590.

D. Morrin, N. D. McMillan, K. Beverley, M. O'Neill, B. O'Rourke, G. Dunne, S. Riedel, A. Augousti, J. Mason, F. Murtagh and M. Kökü̈er, Possible new tensiograph drop volume method for surface tension measurement without correction factors: further studies on tensiotrace relationships, Institute of Physics, Sensors and their Applications XII Proceedings, ISBN 0-7503-0978-4, (2003), pp. 599-605.

Kevin Tiernan, Sven Riedel, Norman D. McMillan, David Kennedy, Andreas T. Augousti, Julian Mason, and G. Doyle, Design from chaos: applying data entropy methods for complex system design, Proc. SPIE Int. Soc. Opt. Eng. 4876, 1357 (2003), 17 pages.

N. D. McMillan, B. O'Rourke, S. M. Riedel, M. O'Neill, A. E. O'Neill, A. C. Bertho, G. Doyle, K. Beverley, J. Hammond, A. Augousti, J. Mason, D. O. Skelly, A. T. O'Neill, D. Boller, S. J. Cave, A new democratic phase coherent data-scatter technique for calibration, measurement, fingerprinting and rapid archival identification of ultraviolet-visible multi-component food spectra, Analytica Chimica Acta 511, (2004), pp. 119-135.

G. Doyle, N. D. McMillan, F. Murtagh, M. O'Neill, S. Riedel, T. S. Perova, S. Unnikrishnan, and R. A. Moore, Phase coherence theory for data-mining and analysis: application studies in spectroscopy, Proc. SPIE Int. Soc. Opt. Eng. 5823, 70 (2005), 12 pages.

G. Doyle, N. D. McMillan, F. Murtagh, M. O'Neill, and S. Riedel, An introduction to the generalised theory of data scatter, Proc. SPIE Int. Soc. Opt. Eng. 5823, 258 (2005), 11 pages.

N. D. McMillan, J. Egan, D. Denieffe, S. Riedel, K. Tiernan, G. McGowan, and G. Farrell, Applying new data-entropy and data-scatter methods for optical digital signal analysis, Proc. SPIE Int. Soc. Opt. Eng. 5825, 437 (2005), 11 pages.

N. D. McMillan, J. Egan, D. Denieffe, S. Riedel, K. Tiernan, D. G. E. McMillan, G. Farrell, David Kennedy, Greg Doyle, G. McGowan, A. Augousti, and J. Mason, A new data diffraction method for digital signal analysis and optoelectronic-fiber system-digital design, Proc. SPIE Int. Soc. Opt. Eng. 5825, 550 (2005), 12 pages.

R. A. Moore, S. Unnikrishnan, T. S. Perova, N. D. McMillan, S. Riedel, M. O'Neill, and G. Doyle, Investigation of correlation between characteristics of Raman spectra and parameters of data-scattering obtained from phase coherence theory, Proc. SPIE Int. Soc. Opt. Eng. 5826, 379 (2005), 8 pages.

D. Morrin, N. D. McMillan, K. Beverley, M. O'Neill, B. O'Rourke, G. Dunne, S. Riedel, A. Augousti, J. Mason, F. Murtagh, and M. Köküer, Tensiograph drop volume method for characterisation of alcohols and bifunctional liquids, Proc. SPIE Int. Soc. Opt. Eng. 5826, 670 (2005), 9 pages.

APPENDIX 1

GLOSSARY OF ABBREVIATIONS

Acronyms are listed in alphabetical order, with the expansion of an acronym given in parenthesis. For example, the acronym *PC* is followed by the expansion, (*Personal Computer*)[1]. A superscript number is used to point out the chapter in which the acronym appeared for the first time. Note that the superscript numbers 0 and 8 are used for the Abstract and Conclusions and Deliverables respectively. The list in this appendix includes terminology found in literature as well as self-defined abbreviations used throughout this thesis.

A/D (Analogue to Digital)[4]
ADC (Analogue to Digital Converter)[1]
ADS (Averaged Data Set)[7]
AMFOS (Amplitude Modulated Fiber Optic Sensor)[1]
API (Application-Programming Interface)[4]
BRI (Brewing Research International)[1]
CCD (Charge Coupled Device)[1]
CMRR (Common Mode Rejection Ratio)[3]
CPU (Central Processing Unit)[4]
D/A (Digital to Analogue)[4]
DAC (Digital to Analogue Converter)[3]
dB (decibel)[1]
DC (Direct Current)[1]
DDS (De-noised Data Set)[7]
DIO (Digital Input-Output)[4]
DMA (Direct Memory Access)[3]
DNA (Deoxyribonucleic Acid)[8]
DOS (Disk Operating System)[4]
DP (Drop Period)[1]

EDP (Event Driven Programming)[4]

EMF (Electro Magnetic Field)[3]

EMI (Electromagnetic Interference)[3]

EU (European Union)[8]

FDA (Fiber Drop Analyser)[1]

FDT (Fiber Drop Trace)[1]

FEA (Finite Element Analysis)[6]

FED (Flow-Event-Diagram)[4]

FFT (Fast Fourier Transform)[1]

GHT (Generalised Hough Transform)[2]

GUI (Graphical User Interface)[4]

HPLC (High-Pressure Liquid Chromatography)[1]

IC (Integrated Circuit)[3]

IDE (Integrated Development Environment)[4]

IR (Infrared)[1]

LED (Light Emitting Diode)[1]

LSB (Least-Significant-Bit)[4]

LUT (Liquid Under Test)[1]

NA (Numerical Aperture)[2]

OOP (Object-Oriented Programming)[4]

OPL (Optical Path Length)[2]

PID (Proportional-Integral-Derivative)[6]

PC (Personal Computer)[1]

PCB (Printed Circuit Board)[3]

PEEK (Poly-Ether-Ether-Ketone)[1]

PMMA (polymethylmethacrylate)[1]

PME (Properties Methods Events)[4]

PMS (Portable Multi-channel Spectrometer)[1]

PP (Priority Pollutants)[0]

PSD (Plexiglas Spacer Disc)[5]

QC (Quality Control)[1]

r.m.s. (root mean squared)[2]

RNA (Ribonucleic Acid)[8]

RPH (Rainbow Peak Height)[1]

RPP (Rainbow Peak Period)[1]

RS-232 (defines serial, asynchronous communication)[4]

RTD (Resistive Temperature Detector)[6]

SDK (Software Development Kit)[4]

silica (silicon dioxide SiO_2 used in optical glass fibers)[1]

SNR (Signal-to-Noise Ratio)[1]

sr (steradian, the unit of a solid angle)[2]

TE (Thermoelectric)[6]

TIC (Tensiographic Information Content)[2]

TIR (Total Internal Reflection)[1]

TPH (Tensiograph Peak Height)[1]

TPP (Tensiograph Peak Period)[1]

TT (Tensiotrace Transform)[2]

TU (Tensiograph Units)[1]

UV (ultraviolet)[1]

UV-vis (Ultra-Violet-Visible)[1]

APPENDIX 2

TENSIOGRAPH COMPONENTS SPECIFICATIONS

The specifications of the components are brief – they include neither detailed explanations nor examples. Instead, the specifications are meant to serve as supplementary information. For a more comprehensive version of a particular specification links to manufactures, distributors, source of data sheets etc. have been added.

Encapsulated AC/DC Linear Power Module				
Distributor	***Location***	***Road***	***Town***	***County/Postcode***
Amplicon Liveline Limited	Centenary Industrial Estate	Hollingdean Road	Brighton	East Sussex BN2 4AW
Additional Details				
Model	***Ripple Noise***	***Voltage accuracy***	***Temp. coeff.***	
365D	1.0mV rms	±1.0%	±0.02%/°C	
Output Specification				
	Output +V	***Output -V***		
Vnom	+15V	-15V		
Imax	+200mA	-200mA		

Picture A2-1. Encapsulated linear power module.

Universal Input Switch Mode Power Supply				
Distributor	***Location***	***Road***	***Town***	***County/Postcode***
Amplicon Liveline Limited	Centenary Industrial Estate	Hollingdean Road	Brighton	East Sussex BN2 4AW
Additional Details				
Model	***Ripple and Noise***	***Output Power***	***Temp. coeff.***	***Line regulation***
PU200-41	2% peak-to-peak	200W	±0.04%/°C	±0.5% max.
Output Specification				
	Output 1	***Output 2***	***Output 3***	***Output 4***
Vnom	+5V	+15V	-15V	+24V
Imin	3A	0A	0A	0A
Imax	30A	6A	4A	4A
Tolerance	2%	4%	4%	4%

Picture A2-2. Switch mode power supply.

Peltier Device				
Manufacturer	***Distributor***	***Road***	***Town***	***County/Postcode***
Melcor	Thermo Electric Devices	High Street	Moreton-in-Marsh	Gloucestershire GL56 0AF
Additional Details				
Model	***Dimensions***	***P/N Pellets***		
CP 1.4-127-10L	40 x 40 x 4.7 mm	127		
Ratings				
Imax	***Qmax***	***Vmax***	***ΔTmax***	
3.9A	33.4W	15.4V	70°C	

Picture A2-3. Peltier device.

Temperature Sensor				
Manufacturer	***Distributor***	***Road***	***Town***	***County/Postcode***
LAB FACILITY	RS Components Ltd.	Birchington Road	Corby	Northants NN17 9RS
Additional Details				
Model	***Dimensions***	***Sensing Length***	***Accuracy***	***Temp. Range***
Pt100, 4-wire sensor in stainless steel probe	∅ 6mm length 150mm	25mm	±0.06°C at 0°C	-50 to +250°C

Picture A2-4. Temperature sensor (100Ω @ 0°C).

Thermometer				
Manufacturer	***Distributor***	***Road***	***Town***	***County/Postcode***
TESTO	RS Components Ltd.	Birchington Road	Corby	Northants NN17 9RS
Additional Details				
Model	***Accuracy***	***Temp. Range***	***Temp. Probe***	
Testo 925	+1 digit	-50 to +1000°C	Type K input [±1°C, +0.5%] (-40 to +900°C)	

Picture A2-5. Thermometer.

Spring Mount Anti-Vibration Mountings				
Manufacturer	***Road***	***Town***	***County/Postcode***	***Web-Page***
Farrat Isolevel Ltd.	Balmoral Road	Altrincham	Cheshire WA15 8HJ	www.farrat.com
Additional Details				
Model	***Dimensions [mm]***	***Minimum Load***	***Optimum Load***	***Maximum Load***
CR11	D 53, L 77, W39, CRS 55, d 7.5, H 59	3 kg $\omega_n = 4.5$ Hz	4 kg $\omega_n = 3.6$ Hz	5 kg $\omega_n = 3.2$ Hz

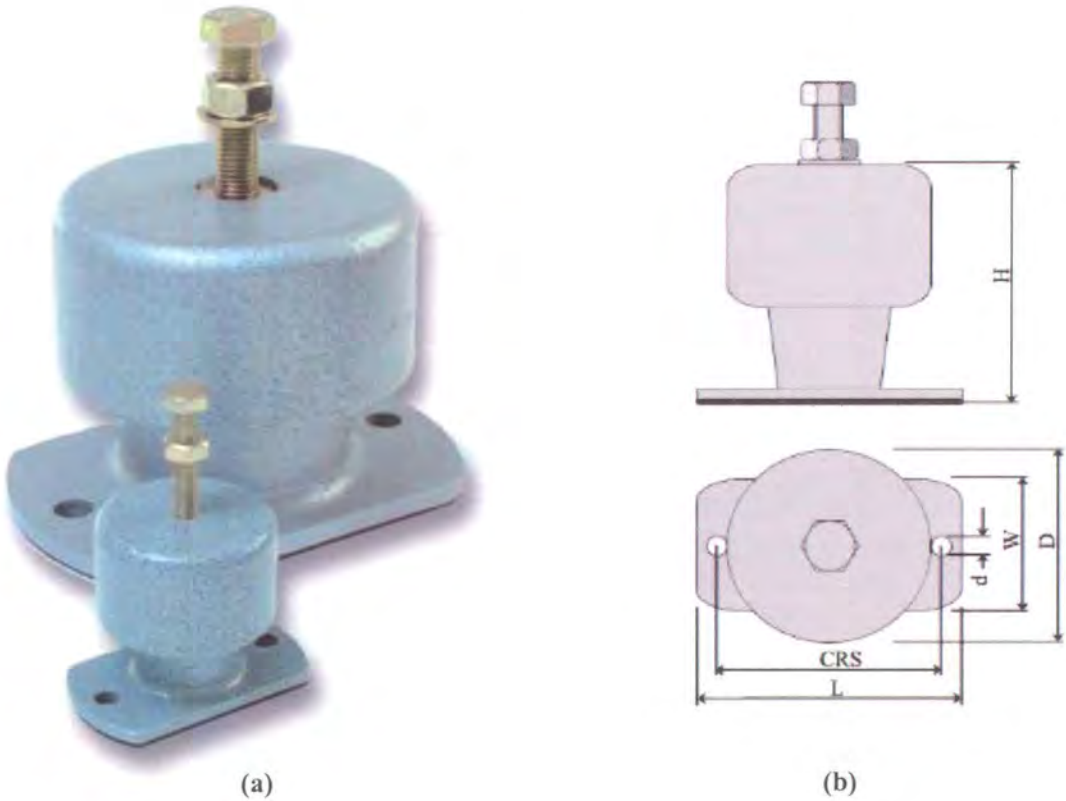

Picture A2-6. Spring mount anti-vibration mounting.

Temperature Controller iSeries (Cni3252-C24-DC)				
Manufacturer	***Location***	***Road***	***Town***	***County/Postcode***
OMEGA	One Omega Drive River Bend Technology Centre	Northbank	Irlam	Manchester M44 5EX UK

Specifications	
Accuracy	± 0.5°C temp; 0.03% reading process
Resolution	1°/0.1°; 10μV process
Temperature Stability	1) RTD: 0.04°C/°C 2) TC @ 25°C (77°F): 0.05°C/°C (Cold Junction Compensation) 3) Process: 50 ppm/°C
NMRR, CMRR	60dB, 120dB
A/D Conversion	Dual slope
Reading Rate	3 samples per second
Digital Filter	Programmable
Display	Single 4-digit 9-segment LED
Warm up to Rated Accuracy	30min
RTD Input	100/500/1000Ω Pt sensor, 2-, 3- or 4-wire
Voltage Input	0 to 100mV, 0 to 1V, 0 to 10Vdc
Input Impedance	10MΩ for 100mV, 1MΩ for 10Vdc
Current Input	0 to 20mA (5 ohm load)
Step Response	0.7sec for 99.9%
Setpoint Adjustment	-1999 to 9999 counts
Span Adjustment	0.001 to 9999 counts
Offset Adjustment	-9999 to +9999 counts
Modes	Time and Amplitude Proportional Control Modes; selectable Manual or Auto PID, Proportional, Proportional with Integral, Proportional with Derivative with Anti-reset Windup and ON/OFF
Auto Tune	Operator initiated from front panel
Analogue Output	Non-Isolated, Proportional 0 to 10Vdc
Communications (RS232)	300 to 19.2k baud
Environmental Conditions	0 to 55°C, 90% RH non-condensing
Power Supply	12 – 36Vdc, 5W

Picture A2-7. Programmable Temperature Controller.

Digital Stepper Motor Pump XP3000			
Manufacturer	***Road***	***Town***	***County/Postcode***
CAVRO Scientific Instruments, Inc.	242 Humboldt Court	Sunnyvale	CA 94086

Specifications		
Resolution		24000 steps
Plunger Drive:	***Principle***	Rack and pinion drive with quadrature encoder and home flag
	Travel	30mm
	Plunger Speed	Variable from 1.2secs/stroke to 20min/stroke
Syringes:	***Sizes***	50µl, 100µl, 250µl, 500µl, 1.0ml, 2.5ml, 5.0ml
	Barrel Material	Borosillicate Glass
	Plunger Material	Stainless Steel
	Seal Material	Virgin Teflon (PTFE, TFE)
	Precision	< 0.05% CV at full stroke (250µl syringe and above) < 0.1% CV at full stroke (50µl and 100µl syringe)
	Accuracy	< 1% at full stroke
Valve Drive:	***Turn time***	Circa 250ms between adjacent ports (3-port valve)
	Drive	Stepper motor with optical encoder for positioning feedback
Valves:	***Plug Material***	Virgin Teflon
	Body Material	Kel-F
	Fittings	¼ - 28" tubing and syringe, M6 or ¼ - 28" syringe fittings
Environmental:	***Operating Temp.***	59°F (15°C) to 104°F (40°C)
	Operating Hum.	20-95% RH at 104°F (40°C)
	Storage Temp.	-4°F (20°C) to 149°F (65°C)
Power Supply:	***Voltage***	24Vdc ± 10%
	Current	1.5A (peak)
Interface:	***Type***	RS-232, RS-485 or CAN
	Baud Rate	9600 or 38400 (RS-232 and RS-485 only)
	Format	Data Bits: 8, Parity: No, Stop Bit: 1, Half Duplex
Communications		Data terminal and OEM protocol (with error recognition)

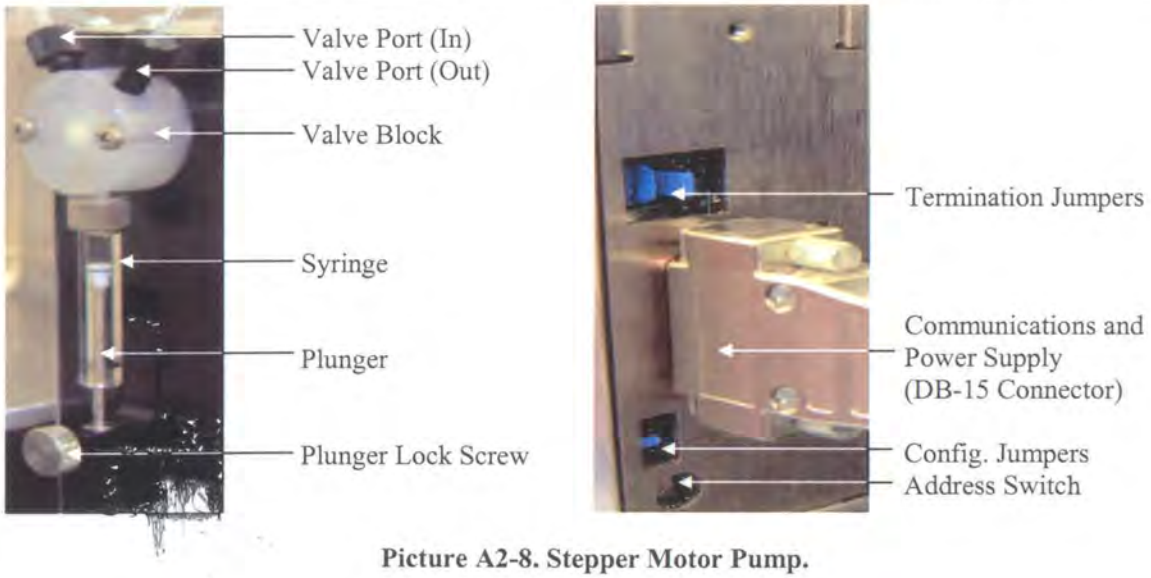

Picture A2-8. Stepper Motor Pump.

Thermoelectric module				
Manufacturer		***Road***	***Town***	***County/Postcode***
Thermo Electric Devices		High Street	Moreton-in-Marsh	Gloucestershire GL56 0AF
Additional Details				
Type	***H [mm]***	***W [mm]***	***D [mm]***	***Comment***
Brass Block	195	80	50	Boreholes for drophead (∅ 12*mm*) and temperature probe (∅ 6*mm*, H=150*mm*).
Heatsink	180	82	68	Aluminium, 6 fins.
Peltier Device	40	4.7	40	Also see Picture A2-3
Temperature Probe	150	-	-	Also see Picture A2-4

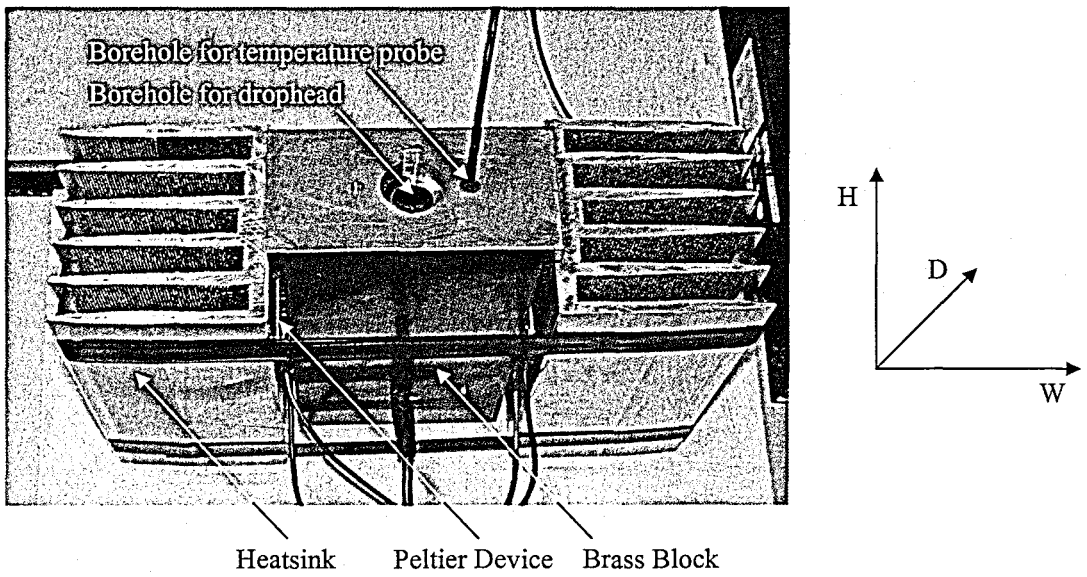

Picture A2-9. Thermoelectric module.

Flat Drophead					
L	Stainless steel Liquid delivery tube	Stainless steel End-face	Stainless steel Knife-edge	Stainless steel Outer sleeve	Optical fibers
150.0mm	inner ∅ 1.0mm	∅ 9.0mm	∅ 9.0mm	inner ∅ 9.0mm	core ∅ 1.0mm
	outer ∅ 1.2mm			outer ∅ 12.0mm	
Additional Information					
The drophead is filled with cylindrically shaped aluminium inserts with a centre hole to provide an optimised thermal interface between the liquid delivery tube and the outer sleeve of the drophead.					

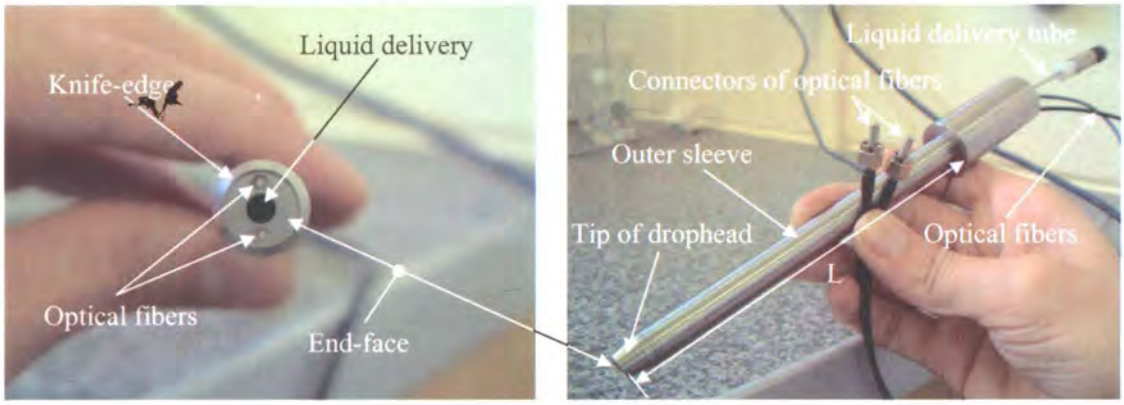

Picture A2-10. Flat stainless steel drophead.

SMA connector and housing for optical sources and detector			
Distributor	***Road***	***Town***	***County/Postcode***
RS Components Ltd.	Birchington Road	Corby	Northants NN17 9RS
Additional Details			
Information	***Inner Diameter***	***Typical Loss***	***Material***
Designed specifically for the installer who demands fast and easy assembly. The design of the rear of the connector crimps directly on the optical fiber (eliminating pull-away from the connector) or incorporates an optical source or detector. Mates with male SMA connector.	2.4*mm*	0.5*dB*	Stainless Steel

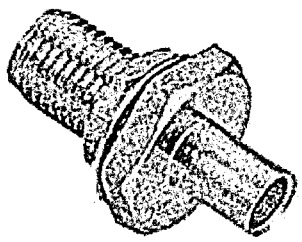

Picture A2-11. SMA connector.

Controller Driver Circuit			
Design	***Version***	***Input***	***Output***
Sven Riedel et al	01	0 to 10V from electronic controller	±1.1V

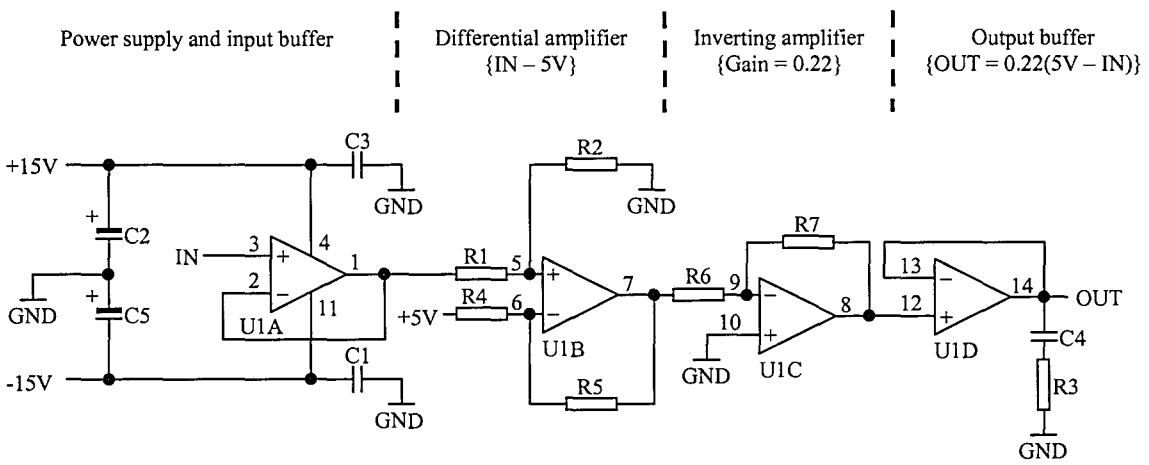

+15V, -15V, GND	From Switch Mode Power Supply
R1, R2, R4, R5, R6	10k, 0.25W, 1%
R3	4R7, 0.25W, 1%
R7	2k2, 0.25W, 1%
C1, C3, C4, C6	0.1µF, 50V, Ceramic
C2, C5, C7	10µF, 25V, Tantalum
U1	LF347N (Operational Amplifier)
U2	LM2931AZ-5 (Voltage Regulator)

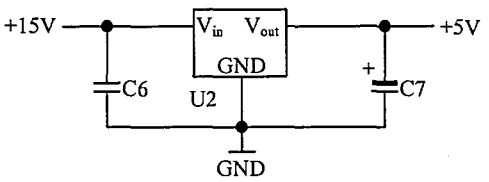

Schematic A2-1. Controller Driver.

Power Booster Circuit			
Design	***Version***	***Input***	***Output***
Sven Riedel	01	±1.1V from controller driver	±14.3V

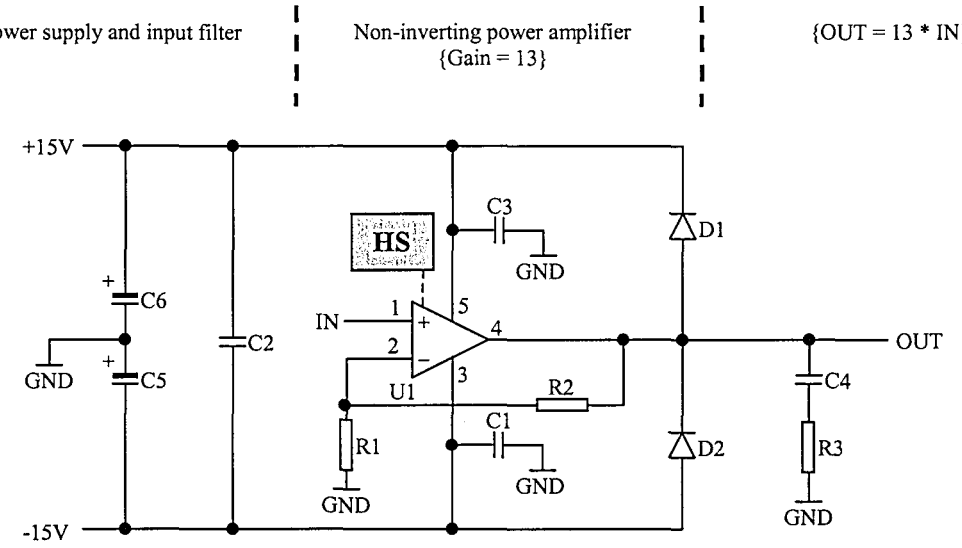

+15V, -15V, GND	From Switch Mode Power Supply
R1	10k, 0.25W, 1%
R2	120k, 0.25W, 1%
R3	4R7, 0.25W, 1%
C1, C3, C4	0.1μF, 50V, Ceramic
C2	0.01μF, 50V, Ceramic
C5, C6	10μF, 25V, Tantalum
D1, D2	1N4001 (Diode)
U1	L465A (Power Amplifier)
HS	2.0°C/W (Heatsink)

Schematic A2-2. Power Booster.

Source and Opto-Switch Circuits			
Design	***Version***	***Input***	***Output***
Sven Riedel	01	From digital outputs of the acquisition board	To analogue input of the acquisition board

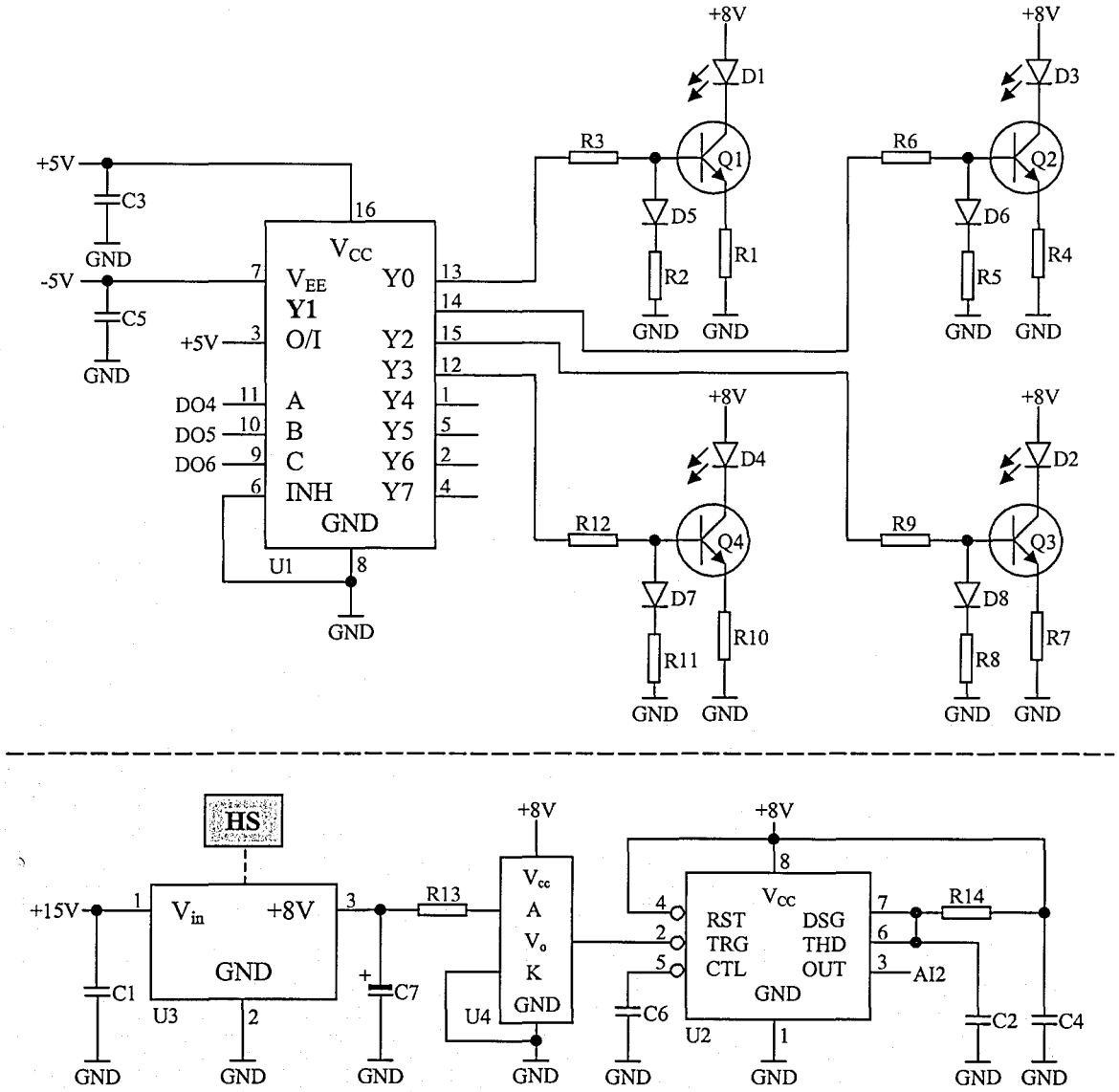

+15V, GND	From Encapsulated Linear Power Supply		
+5V, -5V	From Voltage Regulator (Detector Board)		
R1, R4	110R, 0.5W, α = ± 3ppm/°C		
R2, R5, R8, R11	200R, 0.6W, 1%	**U1**	MM74HC4051N (Analogue Multiplexer)
R3, R6, R9, R12	100R, 0.6W, 1%	**U2**	NE555N (Timer)
R7	91R, 0.5W, α = ± 3ppm/°C	**U3**	MC7808CT (Voltage Regulator +8V)
R10	75R, 0.5W, α = ± 3ppm/°C	**U4**	Slotted Opto Switch with Logic
R13	300R, 0.6W, 1%	**HS**	Clip-on Heatsink
R14	200k, 0.6W, 1%	**D1 – D4**	LEDs (respectively blue, red, green, infrared)
C1, C2, C3, C4, C5	0.1μF, 50V, Ceramic	**Q1 – Q4**	ZTX690B (NPN-Medium Power Transistor)
C6	0.01μF, 50V, Ceramic	**DO4, DO5, DO6**	From Digital Outputs (Acquisition Board)
C7	10μF, 25V, Tantalum	**AI2**	To Analogue Input (Acquisition Board)
D5 – D8	1N4001 (Diodes)		

Schematics A2-3. Optical sources and opto-switch.

Detector-Board Circuit			
Design	***Version***	***Input***	***Output***
Sven Riedel et al	01	From digital outputs of the acquisition board	To analogue input of the acquisition board

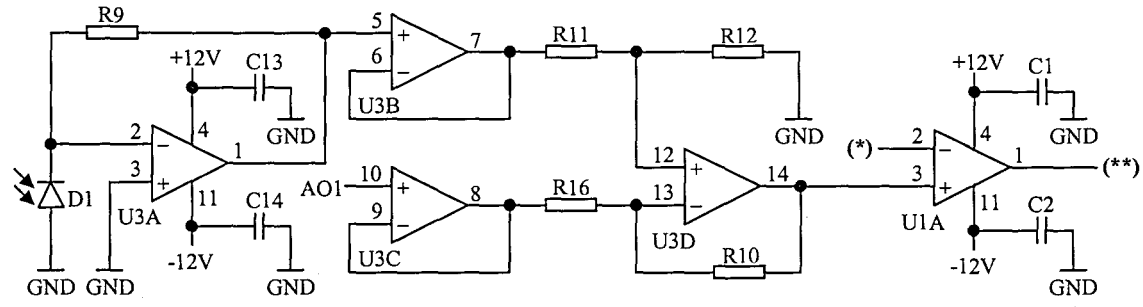

(a) (b) (c_1)

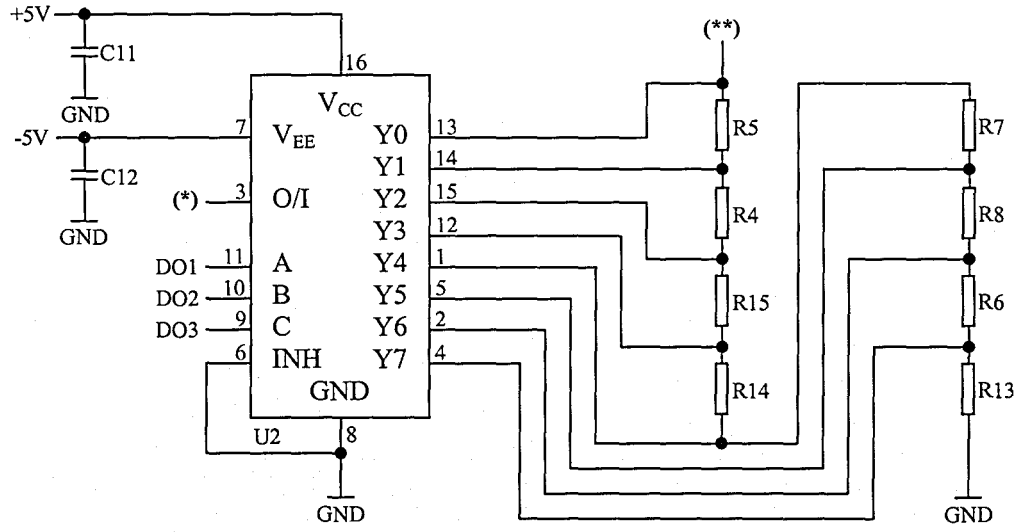

(c_2)

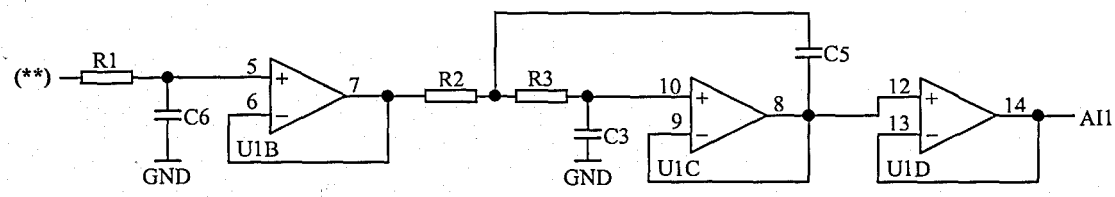

(d)

Detector-Board Circuit (continued)			
Design	***Version***	***Input***	***Output***
Sven Riedel et al	01	From digital outputs of the acquisition board	To analogue input of the acquisition board

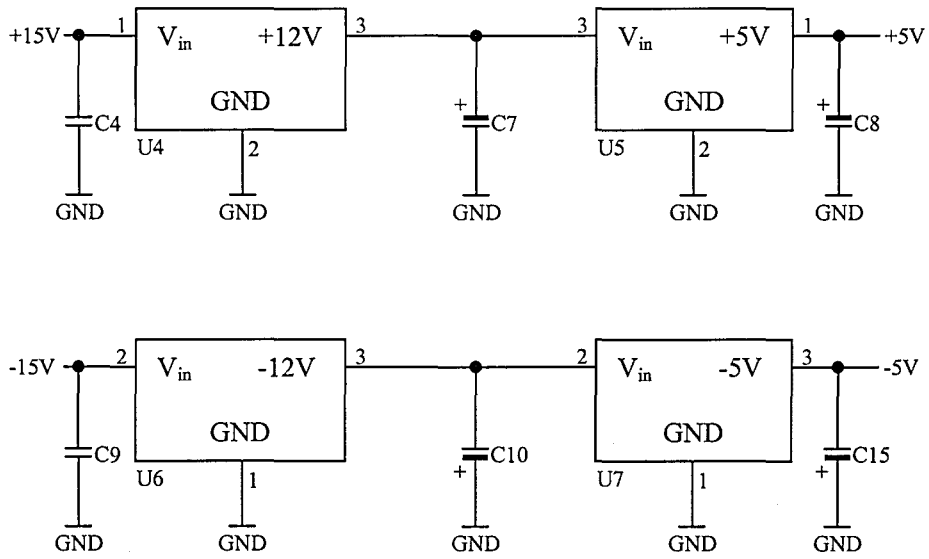

(e)

+15V, -15V, GND	From Encapsulated Linear Power Supply		
R1	39k, 0.6W, 1%		
R2	36k, 0.6W, 1%	**U1, U3**	OP497FP (Operational Amplifier)
R3	68k, 0.6W, 1%	**U2**	MM74HC4051N (Analogue Multiplexer)
R4	18k, 0.6W, 1%	**U4**	KA7812ATU (Voltage Regulator +12V)
R5	51k, 0.6W, 1%	**U5**	LM2931AZ-5 (Voltage Regulator +5V)
R6	1k6, 0.6W, 1%	**U6**	LM7912CT (Voltage Regulator –12V)
R7	3k, 0.6W, 1%	**U7**	LM79L05ACZ (Voltage Regulator –5V)
R8	2k4, 0.6W, 1%	**DO1, DO2, DO3**	From Digital Outputs (Acquisition Board)
R9	100k, 0.6W, 1%	**AI1**	To Analogue Input (Acquisition Board)
R10, R12	6k2, 0.6W, 1%	**AO1**	From Analogue Output (Acquisition Board)
R11, R16	20k, 0.6W, 1%	**D1**	FDR850IR (Si PiN Photodiode)
R13	11k, 0.6W, 1%		
R14	5k1, 0.6W, 1%		
R15	7k5, 0.6W, 1%		
C1, C2, C4, C5, C6			
C9, C11, C12, C13			
C14	0.1μF, 50V, Ceramic		
C3	0.047μF, 50V, Ceramic		
C7, C8, C10, C15	10μF, 25V, Tantalum		

Schematics A2-4. Detector-Board (a) photocurrent to voltage converter, (b) high input-impedance subtraction, (c_1, c_2) switchable gain amplifier, (d) 3rd order Bessel low-pass filter, (e) constant voltage supply.

Detector-Board Circuit			
Design	***Version***	***Input***	***Output***
Sven Riedel	02	From digital outputs of the acquisition board	To analogue input of the acquisition board

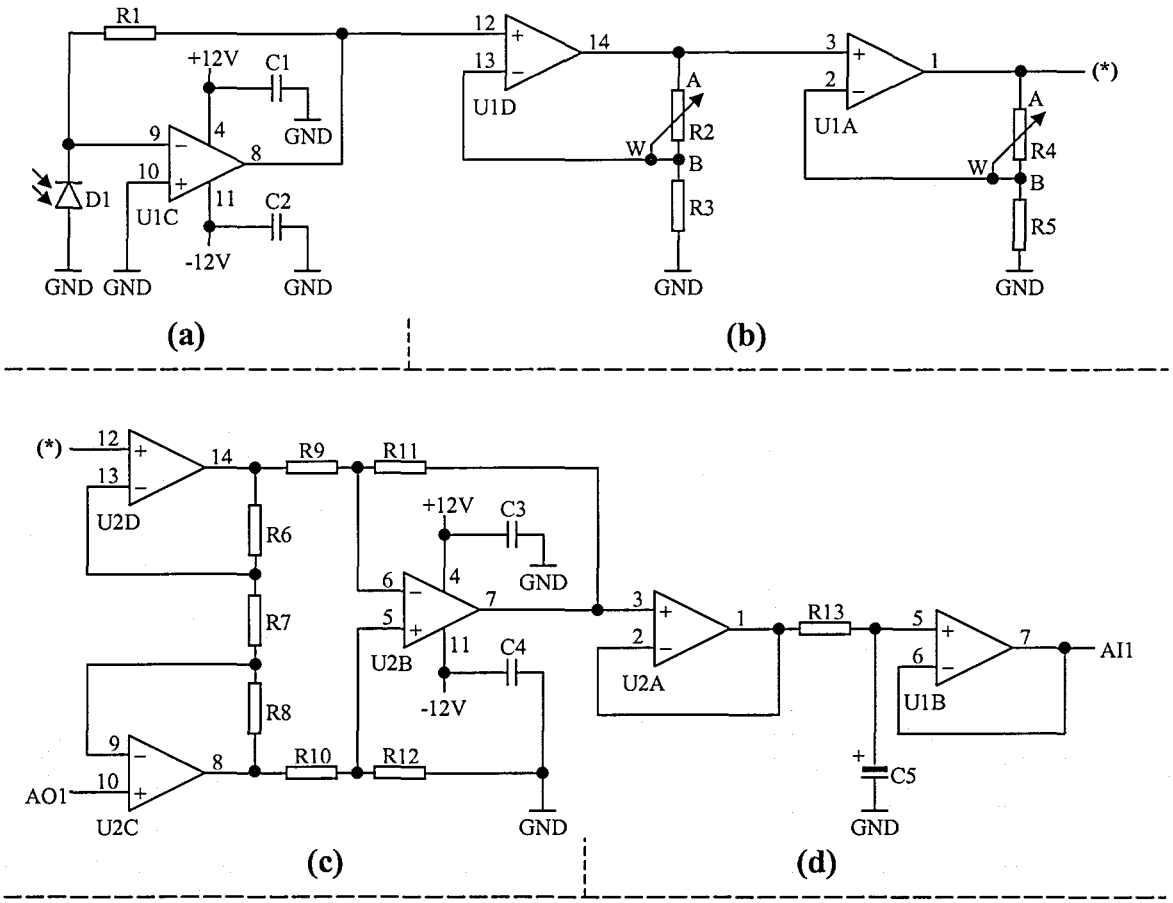

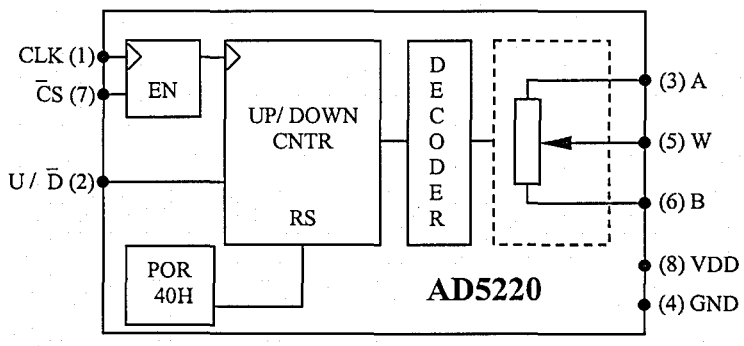

(e)

Detector-Board Circuit (continued)			
Design	***Version***	***Input***	***Output***
Sven Riedel	02	From digital outputs of the acquisition board	To analogue input of the acquisition board

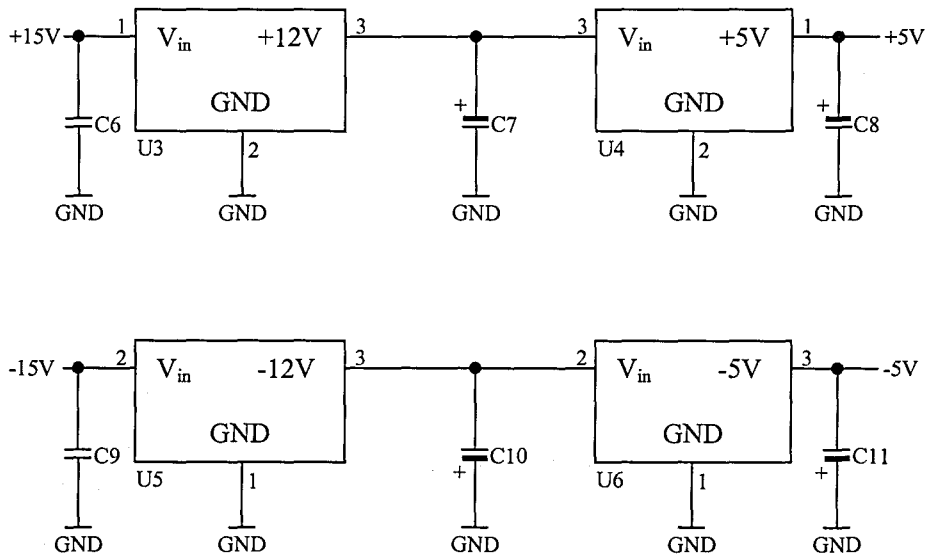

(f)

+15V, -15V, GND	From Encapsulated Linear Power Supply		
R1	100k, 0.1%		
R2, R4	AD5220 (Variable R, 100k)	**U1, U2**	OP497FP (Operational Amplifier)
R3, R5, R6, R8,		**U3**	KA7812ATU (Voltage Regulator +12V)
R9, R10, R11, R12	10k, 0.1%	**U4**	LM2931AZ-5 (Voltage Regulator +5V)
R7, R13	2k87, 0.1%	**U5**	LM7912CT (Voltage Regulator –12V)
C1, C2, C3, C4,		**U6**	LM79L05ACZ (Voltage Regulator –5V)
C6, C9	0.1μF, 50V, Ceramic	**AO1**	From Analogue Output (Acquisition Board)
C5	2.2μF, 25V, Tantalum	**AI1**	To Analogue Input (Acquisition Board)
C7, C8, C10, C11	10μF, 25V, Tantalum	**D1**	S2386-18K (Si Photodiode)
U/D (AD5220)	Digital I/O-Port 0 (Acquisition Board)		
CLK (AD5220)	Digital I/O-Port 2 (Acquisition Board)		
CS (AD5220)	Connected to GND		
VDD (AD5220)	Connected to +5V		

Schematics A2-5. Detector-Board (a) photocurrent to voltage converter, (b) variable gain amplifier (c) instrumentation amplifier, (d) low-pass filter, (e) digitally controlled variable resistor device, (f) constant voltage supply.

DC to 10Hz Noise Test Circuit for the LTC1051 Operational Amplifier			
Design	***Supply Voltage***	***Operating Temperature Range***	***Gain***
Linear Technology	V_s=±5V	T_A=25 ℃	G=10000

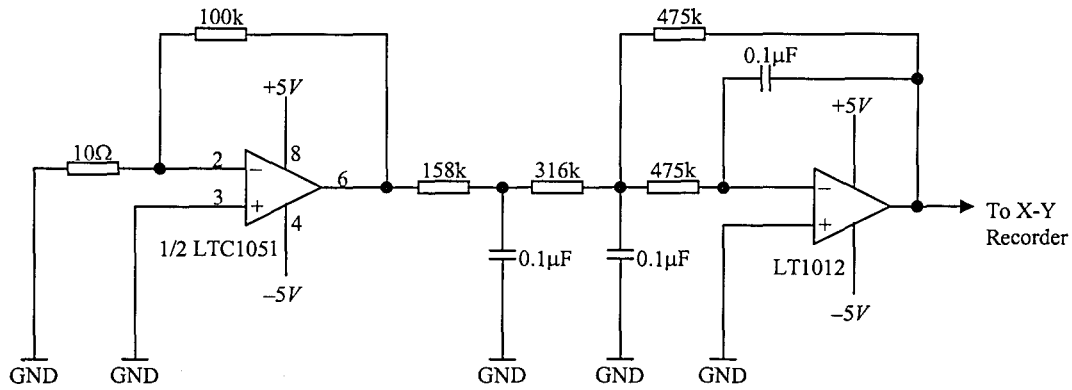

Schematic A2-6. Noise test circuit for operational amplifier.

Hardware specifications of components used in a tensiograph			
High efficiency power operational amplifier L465A (SGS)			
Distributor	**Road**	**Town**	**County/Postcode**
RS Components Ltd.	Birchington Road	Corby	Northants NN17 9RS

Electrical characteristics (V_s=±15V, T_{amb}=25°C unless otherwise specified)

Parameter		Test conditions		Min.	Typ.	Max.	Unit
V_s	Supply voltage			±3		±20	V
V_i	Input voltage					±20	V
V_{di}	Differential input voltage					±15	V
I_o	Peak output current					4	A
P_{tot}	Power dissipation (T_{case}=90°C)					20	W
T_j	Junction temperature			-40		150	°C
$R_{th\ j\text{-}case}$	Thermal resistance junction-case					3	°C/W
T_{sd}	Thermal shutdown junction temp.				145		°C
I_d	Quiescent drain current	V_s=±18V			45		mA
I_b	Input bias current				0.3	1	µA
V_{os}	Input offset voltage				±2	±20	mV
I_{os}	Input offset current					±200	nA
SR	Slew-Rate				14		V/µs
V_o	Output voltage swing	f=1kHz	I_p=0.5A	26	27		V_{pp}
			I_p=4A		25		V_{pp}
		f=10kHz	I_p=0.5A		27		V_{pp}
			I_p=4A		24		V_{pp}
B_w	Power bandwidth	P_o=1W	R_L=4Ω		100		kHz
R_i	Input resistance (pin 1)	f=1kHz		100	500		kΩ
G_v	Voltage gain (open loop)				80		dB
e_N	Input noise voltage	B=10 to 10000			2	6	µV
i_N	Input noise current				100		pA
CMR	Common mode rejection	R_g≤10kΩ	G_v=30dB		70		dB
SVR	Supply voltage rejection	R_g=22kΩ	G_v=10		60		dB
		V_{ripple}=0.5V_{rms}	G_v=100		40		dB
		f_{ripple}=100Hz					
η	Efficiency	f=1kHz R_L=4Ω	I_p=3A		66		%

Si Photodiode S2386-18K (HAMAMATSU)			
Distributor	**Post Box**	**Town**	**Postcode**
LasIRvis Optoelectronic Components Ltd.	PO Box 428	Bedford	MK42 8BF

Characteristics (T_{amb}=25°C unless otherwise specified)

Parameter		Test conditions	Min.	Typ.	Max.	Unit
λ	Spectral Response Range		320		1100	nm
λ_p	Peak Sensitivity Wavelength			960		nm
S	Photo Sensitivity	@470nm @530nm @660nm @950nm		0.27 0.33 0.46 0.60		A/W
I_d	Dark Current	V_R=10mV		2.0		pA

Hardware specifications of components used in a tensiograph (continued)

Plastic Fiber Optic Blue LED IF-E92B (Industrial Fiber Optics, Inc.)

Distributor	Post Box	Town	Postcode
LasIRvis Optoelectronic Components Ltd.	PO Box 428	Bedford	MK42 8BF

Characteristics (T_{amb}=25°C unless otherwise specified)

	Parameter	Test conditions	Min.	Typ.	Max.	Unit
λ_{peak}	Peak Wavelength			470		nm
$\Delta\lambda$	Spectral Bandwidth	(50% of λ_{peak})		25		nm
Φ_{in}	Output Power	Coupled into polished Plastic Fiber (core ∅1mm, length 10cm) I_F=10mA		75 -11		µW dBm
I_F	Forward Current	DC			35	mA
V_F	Forward Voltage	I_F = 20mA			4.0	V

Plastic Fiber Optic Green LED IF-E93 (Industrial Fiber Optics, Inc.)

Distributor	Post Box	Town	Postcode
LasIRvis Optoelectronic Components Ltd.	PO Box 428	Bedford	MK42 8BF

Characteristics (T_{amb}=25°C unless otherwise specified)

	Parameter	Test conditions	Min.	Typ.	Max.	Unit
λ_{peak}	Peak Wavelength			530		nm
$\Delta\lambda$	Spectral Bandwidth	(50% of λ_{peak})		50		nm
Φ_{in}	Output Power	Coupled into polished Plastic Fiber (core ∅1mm, length 10cm) I_F=10mA		75 -11		µW dBm
I_F	Forward Current	DC			35	mA
V_F	Forward Voltage	I_F = 20mA			4.0	V

Plastic Fiber Optic Super-Bright Red LED IF-E97 (Industrial Fiber Optics, Inc.)

Distributor	Post Box	Town	Postcode
LasIRvis Optoelectronic Components Ltd.	PO Box 428	Bedford	MK42 8BF

Characteristics (T_{amb}=25°C unless otherwise specified)

	Parameter	Test conditions	Min.	Typ.	Max.	Unit
λ_{peak}	Peak Wavelength			660		nm
$\Delta\lambda$	Spectral Bandwidth	(50% of λ_{peak})		40		nm
Φ_{in}	Output Power	Coupled into polished Plastic Fiber (core ∅1mm, length 10cm) I_F=20mA		100 -10		µW dBm
I_F	Forward Current	DC			40	mA
V_F	Forward Voltage	I_F = 40mA			1.7	V

Plastic Fiber Optic IR LED IF-E91A (Industrial Fiber Optics, Inc.)

Distributor	Post Box	Town	Postcode
LasIRvis Optoelectronic Components Ltd.	PO Box 428	Bedford	MK42 8BF

Characteristics (T_{amb}=25°C unless otherwise specified)

	Parameter	Test conditions	Min.	Typ.	Max.	Unit
λ_{peak}	Peak Wavelength			950		nm
$\Delta\lambda$	Spectral Bandwidth	(50% of λ_{peak})		40		nm
Φ_{in}	Output Power	Coupled into polished Plastic Fiber (core ∅1mm, length 10cm) I_F=20mA		100 -10		µW dBm
I_F	Forward Current	DC			50	mA
V_F	Forward Voltage	I_F = 50mA			1.5	V

Hardware specifications of components used in a tensiograph (continued)

Optical PMMA Fiber (Industrial Fiber Optics, Inc.)

Distributor	Post Box	Town	Postcode
LasIRvis Optoelectronic Components Ltd.	PO Box 428	Bedford	MK42 8BF

Characteristics (T_{amb}=25°C unless otherwise specified)

Parameter		Test conditions	Min.	Typ.	Max.	Unit
d_c	Core Diameter			1.0		mm
d_j	Jacket Diameter		2.13	2.20	2.27	mm
Φ_A	Attenuation	@470nm @530nm @660nm @950nm		0.1 <0.1 0.2 1.6		dB/m
NA	Numerical Aperture			0.51		
ϑ_o	Oper. Temperature		-55		+70	°C

NPN small signal Transistor ZTX690B (Zetex)

Distributor	Road	Town	County/Postcode
RS Components Ltd.	Birchington Road	Corby	Northants NN17 9RS

Electrical characteristics (T_{amb}=25°C unless otherwise specified)

Parameter		Test conditions	Min.	Typ.	Max.	Unit
I_C	Collector current				2.0	A
I_{CC}	Continues collector current			100		mA
P_D	Power dissipation				1.0	W
V_{CE}	Collector-Emitter voltage				45.0	V
h_{FE}	DC current gain	(I_C=100mA, V_{CE}=1.0V)	500			
h_{fe}	Small Signal current gain	(I_C=100mA, V_{CE}=1.0V, f=1.0MHz)	1.0			

General use operational amplifier LF347N (National Semiconductor)

Distributor	Road	Town	County/Postcode
RS Components Ltd.	Birchington Road	Corby	Northants NN17 9RS

Electrical characteristics (@V_{cc}=±15V, T_{amb}=25°C unless otherwise specified)

Parameter		Test conditions	Min.	Typ.	Max.	Unit
V_{cc}	Supply Voltage				±18	V
GBP	Gain Bandwidth Product			4.0		MHz
SR	Slew Rate			13.0		V/µs
V_{os}	Input Offset Voltage			10.0		mV
I_B	Input Bias Current			200		pA
ϑ_o	Operating Temperature		0		+70	°C

Precision Picoampere Input Current Operational Amplifier OP-497 (Analog Devices)

Distributor	Road	Town	County/Postcode
RS Components Ltd.	Birchington Road	Corby	Northants NN17 9RS

Electrical characteristics (@V_{cc}=±15V, T_{amb}=25°C unless otherwise specified)

Parameter		Test conditions	Min.	Typ.	Max.	Unit
V_{os}	Input Offset Voltage	-40°C ≤ T_{amb} ≤ +85°C		20	50	µV
TCV_{os}	Input Offset Voltage drift			0.2	0.5	µV/°C
I_B	Input Bias Current			30	100	pA
TCI_B	Input Bias Current drift			0.5		pA/°C
I_{os}	Input Offset Current			15	100	pA
TCI_{os}	Input Offset Current drift			0.2		pA/°C
CMR	Common-Mode Rejection	V_{CM} = ±13V	120	140		dB
V_o	Output Voltage Swing	R_L = 10kΩ	±13	±14		V
V_s	Supply Voltage Range	-40°C ≤ T_{amb} ≤ +85°C	±2.5		±20	V
SR	Slew Rate		0.05	0.15		V/µs
GBW	Gain Bandwidth Product			500		kHz
e_n p-p	Voltage Noise	0.1Hz to 10Hz		0.3		µVp-p

Hardware specifications of components used in a tensiograph (continued)						
8-Channel Analog Multiplexer MM74HC4051 (National Semiconductor)						
Distributor	**Road**	**Town**	**County/Postcode**			
RS Components Ltd.	Birchington Road	Corby	Northants NN17 9RS			
Electrical characteristics (T_{amb}=25°C unless otherwise specified)						
Parameter		**Test conditions**	**Min.**	**Typ.**	**Max.**	**Unit**
V_{CC}	Supply Voltage		2		6	V
V_{EE}	Supply Voltage		0		-6	V
V_{in}	DC Input Voltage		0		V_{CC}	V
V_{out}	DC Output Voltage		0		V_{CC}	V
ϑ_o	Operating Temperature		-40		+85	°C
P_D	Power Dissipation				600	mW
R_{on}	"ON" Resistance	V_{EE}=-4.5V, V_{CC}=4.5V		20	90	Ω
High Precision Timer NE555N (Phillips Semiconductors)						
Distributor	**Road**	**Town**	**County/Postcode**			
RS Components Ltd.	Birchington Road	Corby	Northants NN17 9RS			
Electrical characteristics (@V_{CC}=+5V to +15V, T_{amb}=25°C unless otherwise specified)						
Parameter		**Test conditions**	**Min.**	**Typ.**	**Max.**	**Unit**
V_{CC}	Supply Voltage		4.5		16	V
I_{CC}	Supply Current	V_{CC} = 15V, $R_L = \propto$		10	15	mA
P_D	Power Dissipation				600	mW
ϑ_o	Operating Temperature		0		+70	°C
	Timing error (monostable)	R_A = 2kΩ to 100kΩ				
t_M	Initial accuracy	C = 0.1μF		1.0	3.0	%
$\Delta t_M/\Delta T$	Drift with temperature			50	150	ppm/°C
$\Delta t_M/\Delta V$	Drift with supply voltage			0.1	0.5	%/V
	Timing error (astable)	R_A, R_B= 1kΩ to 100kΩ				
t_A	Initial accuracy	C = 0.1μF		5	13	%
$\Delta t_A/\Delta T$	Drift with temperature	V_{CC} = 15V			500	ppm/°C
$\Delta t_A/\Delta V$	Drift with supply voltage			0.3	1	%/V
V_{OL}	Output Voltage (low)	V_{CC}=15V, I_{sink}=100mA		2.0	2.5	V
V_{OH}	Output Voltage (high)	V_{CC}=15V, I_{source}=100mA	12.8	13.3		V
t_{OFF}	Turn-off time	$V_{RESET} = V_{CC}$		0.5	2.0	μs
t_R	Rise time of output			100	300	ns
t_F	Fall time of output			100	300	ns
Increment/Decrement Digital Potentiometer AD5220 (Analog Devices)						
Distributor	**Road**	**Town**	**County/Postcode**			
RS Components Ltd.	Birchington Road	Corby	Northants NN17 9RS			
Electrical characteristics (V_{DD}=5V, T_{amb}=25°C unless otherwise specified)						
Parameter		**Test conditions**	**Min.**	**Typ.**	**Max.**	**Unit**
V_{DD}	Supply Voltage		2.7		5.5	V
I_{DD}	Supply Current			15	40	μA
P_{DISS}	Power Dissipation			75	200	μW
PSS	Power Supply Sensitivity			0.004	0.015	%/%
N	Resolution		7			Bits
INL	Integral Nonlinearity	R_{AB} = 10kΩ	-1	±0.5	+1	LSB
		R_{AB} = 50kΩ, 100kΩ	-0.5	±0.2	+0.5	LSB
$\Delta V_W/\Delta T$	Voltage Divider Temp. Coeff.	Code = 40_H		20		ppm/°C
V_{WFSE}	Full-Scale Error	Code = $7F_H$	-2	-0.5	0	LSB
V_{WZSE}	Zero-Scale Error	Code = 00_H	0	+0.5	+1	LSB
V_{IH}	Input Logic High		2.4			V
V_{IL}	Input Logic Low				0.8	V
I_{IL}	Input Current	V_{IN} = 0V or 5V			±1	μA

Hardware specifications of components used in a tensiograph (continued)			
Slotted, Through Scan Opto Switch with Logic			
Distributor	**Road**	**Town**	**County/Postcode**
RS Components Ltd.	Birchington Road	Corby	Northants NN17 9RS

Electrical characteristics (T_{amb}=25°C unless otherwise specified)

	Parameter	Test conditions	Min.	Typ.	Max.	Unit
	Diode					
V_F	Forward Voltage	@I_F = 29mA			1.5	V
V_R	Reverse Voltage				3	V
I_F	Continues Forward Current				50	mA
	Photodetector					
V_{CC}	Supply Voltage range		+4.5		+16	V
I_{sink}	Output sink current				15	mA
I_o	Operating Current				15	mA
P_D	Power dissipation				250	mW
	Coupled					
t_{PD}	Propagation Delay Time (high to low, or low to high)			5		µs
t_{OR}	Output rise time			150	180	ns
t_{OF}	Output fall time			23	50	ns
ϑ_o	Operating Temperature		-40		+100	°C

Low dropout fixed voltage regulator LM2931AZ-5			
Distributor	**Road**	**Town**	**County/Postcode**
RS Components Ltd.	Birchington Road	Corby	Northants NN17 9RS

Electrical characteristics (V_{IN}=14.4V, I_o=10mA, T_{amb}=25°C unless otherwise specified)

	Parameter	Test conditions	Min.	Typ.	Max.	Unit
V_o	Output Voltage	6V≤V_{IN}≤26V, I_o≤100mA -40°C≤T_j≤+125°C	4.75	5	5.25	V
V_F	Forward Input Voltage				26	V
e_N	Output Noise Voltage	10Hz to 100kHz		500		µVrms
SVR	Supply Voltage Rejection	f_o=120Hz		80		dB
ΔV_o	Line Regulation	9V≤V_{IN}≤16V 6V≤V_{IN}≤26V		2 4	10 30	mV mV
ΔV_o	Load Regulation	5mA≤I_o≤100mA		14	50	mV
$R_{thj\text{-}case}$	Thermal Resistance junction-case				55	°C/W
ϑ_o	Operating Temperature		-40		+85	°C
ϑ_j	Junction Temperature				+125	°C

Table A2-1. Hardware specifications of components used in a tensiograph.

Acquisition Board PC30G				
Distributor	***Location***	***Road***	***Town***	***County/Postcode***
Amplicon Liveline Limited	Centenary Industrial Estate	Hollingdean Road	Brighton	East Sussex BN2 4AW

Analogue Inputs	
Number of Channels	16 single-ended or 8 differential (software selectable)
Resolution	12-bits (1 in 4096)
Total System Accuracy (absolute accuracy)	
Linearity: ***Integral***	± 0.05% FS
Differential	± ¾ LSB max.
A/D Input Voltage-Ranges	± 5V, ± 10V, 0 to 10V
Data Acquisition Rate	100kHz
Input Impedance: ***On Channel***	10M/20pF
Off Channel	10M/100pF
Offset Voltage	± 5 LSB adjustable to 0
Input Bias Current	± 100pA/°C
Input Bias Offset Drift	± 30ppm/°C
Input Gains:	
Ranges	1, 10, 100, 1000 (software selectable)
Gain Error	Adjustable to 0
Gain Accuracy	0.25% max, 0.05% typical for gains < 1000
CMRR for various gains	1% max, 0.1% for gain = 1000
Monotonicity	0 to 70°C
Temperature Drift:	
Full Scale Error Drift	6ppm/°C
Bipolar Zero Drift	1ppm/°C
Gain	± 30ppm/°C
Input Over Voltage Protection	± 12V
A/D FIFO Buffer Size	16 samples
General Gain/Queue Length	31
A/D Clock:	
Internal Clock	2MHz or 8MHz (software selectable)
Clock frequency tolerance	0.01%
Clock Drift	10ppm/°C
Internal Clock Divider	2 x 16 bit stages
External Clock	TTL compatible
External Trigger	TTL compatible
Channel List Length	31
Block Scan Mode	Up to 256 channels per block; all channels converted at max. throughput on each clock pulse
Noise Levels (p-p)	G = 1: ± 1 bit; G = 10: ± 1 bit; G = 100: ± 2 bits Noise levels will vary according to environmental conditions
Data Acquisition Modes	Polled I/O, Interrupts, Single and Dual Channel DMA

Acquisition Board PC30G (continued)	
Analogue Outputs	
Number of Channels	4
Resolution	Two 12-bit, two 8-bit
Accuracy	± 1 LSB (12-bit), 0 LSB (8-bit)
Differential Nonlinearity	± 1 LSB max.
Output Ranges	± 5V, ± 10V, 0 to 10V (software selectable)
Offset Error	Unipolar: ¼ LSB typical, 1 LSB max. (12 bit) Bipolar: ½ LSB typical, 2 LSB max. (12 bit)
Gain: *Ranges* *Error*	x1, x2 2 LSB typical, 5 LSB (12 bit)
Settling Time to ½ LSB	10μs max. in a Load of 500pF, 2kΩ
Throughput Rate	500kHz (depending on computer)
Temperature Drift	100ppm/°C of full scale
Max. Current Output Source	5mA maximum
Monotonicity	0 to 70°C
Digital I/O	
Number of I/O Lines	24 in 3 ports (8255 PPI)
Voltage Compatibility	TTL
Interface Selection	Programmable for simple I/O, strobed I/O, or handshake I/O
Max. Input Voltage	5.5V
Max. Current Source/Sink	± 1mA
Timer/Counter Specifications	
Resolution	16 bits
Voltage Compatibility	TTL
Number of Counters	3 (2 used for A/D timing)
Environmental Specifications	
Operating Temperature	0 to 70°C
Storage Temperature	-55 to 150°C
Relative Humidity	5% to 95% noncondensing
Power Requirements	
+ 5V	500mA typ.
+12V	100mA typ.
-12V	100mA typ.
Software Support	
Supported by EDR Software Development Kit	
DOS language support	
Windows 3.1 language support (DLL)	
Windows 95 language support	

Table A2-2. Hardware Specifications of the acquisition board PC30G.

APPENDIX 3

TABLES OF PHYSICAL AND CHEMICAL PROPERTIES

Material @ 20°C	Thermal Conductivity [W $m^{-1}K^{-1}$]	Specific Heat[a] [Ws $kg^{-1}K^{-1}$]	Specific Weight [kg m^{-3}]
Aluminium Al	237	890	2700
Brass 70Cu, 30Zn	109	388	8500
Stainless Steel (18-8) 74Fe, 18Cr, 8Ni	15	460	7800
Nylon	0.25	-	1150
Water H_2O	0.6	4182	998

Table A3-1. Thermal and mechanical properties of various materials. (Source: Kaye & Laby, Table of Physical and Chemical Constants, Fifteenth Edition, Longman Group Limited 1986, ISBN 0582463548.

Radiation Type	Abbreviation	Wavelength [nm]	Frequency [THz]	Photons [eV]
Vacuum-UV	VUV (UV-C)	100 – 200	3000 – 1500	12.4 – 6.2
Far-UV	FUV (UV-C)	200 – 280	1500 – 1070	6.2 – 4.4
Medium-UV	UV-B	280 – 315	1070 – 950	4.4 – 3.9
Near-UV	UV-A	315 – 380	950 – 790	3.9 – 3.3
Light	VIS	380 – 780	790 – 385	3.3 – 1.6
Near-IR	NIR (IR-A)	780 – 1400	385 – 215	1.6 – 0.9
Near-IR	NIR (IR-B)	1400 – 3000	215 – 100	0.9 – 0.4
Medium-IR	MIR (IR-C)	3000 – $5*10^4$	100 – 6	0.4 – 0.025
Far-IR	FIR (IR-C)	$5*10^4$ – 10^6	6 – 0.3	0.025 – 10^{-3}

Table A3-2. The spectral range of the optical radiation in vacuum. (Source: Bergmann • Schaefer, Lehrbuch der Experimentalphysik, Band III Optik, 8. Auflage, Walter de Gruyter 1987, ISBN 3110108828, p. 639.

Physical/Chemical Constant	Symbol	Value	Unit	Comment
Elementary Charge	e	$1.6021892 * 10^{-19}$	As	
Bolzmann-Constant	k	$1.380662 * 10^{-23}$	JK^{-1}	$k = R/N_A$
Universal (molar) Gas-Constant	R	8.31441	$Jmol^{-1}K^{-1}$	
Avogadro-Constant	N_A	$6.0221358 * 10^{23}$	mol^{-1}	

Table A3-3. Physical and Chemical constants. (Source: Bergmann • Schaefer, Lehrbuch der Experimentalphysik, Band III Optik, 8. Auflage, Walter de Gruyter 1987, ISBN 3110108828, p. 1098.

[a] Energy Units in specific heat constants: 1J(joule) = 1Ws = 0.2388cal

APPENDIX 4

STATISTICS TABLES

z	.09	.08	.07	.06	.05	.04	.03	.02	.01	.00
3.5	0.99984	0.999835	0.99983	0.99982	0.99981	0.9998	0.99979	0.99978	0.99977	0.99976
3.4	0.99975	0.99974	0.99973	0.99972	0.99971	0.9997	0.99969	0.99968	0.99967	0.99966
3.3	0.99965	0.99964	0.99963	0.99961	0.99959	0.99957	0.99955	0.99954	0.99952	0.9995
3.2	0.99948	0.99947	0.99945	0.99943	0.99941	0.99939	0.99937	0.99935	0.99933	0.9993
3.1	0.99928	0.99925	0.99922	0.9992	0.99918	0.99916	0.99913	0.99908	0.99905	0.99901
3.0	0.99898	0.99895	0.99889	0.99887	0.99885	0.9988	0.99875	0.99871	0.99868	0.99865
2.9	0.9986	0.99855	0.9985	0.99845	0.9984	0.99835	0.99828	0.9982	0.99815	0.9981
2.8	0.99805	0.9980	0.99794	0.9979	0.99784	0.99773	0.9977	0.9976	0.9975	0.9974
2.7	0.99735	0.9973	0.9972	0.9971	0.9970	0.9969	0.9968	0.9967	0.9966	0.9965
2.6	0.9964	0.9963	0.9962	0.9961	0.9960	0.9959	0.9957	0.9956	0.9955	0.9953
2.5	0.9952	0.9951	0.9949	0.9948	0.9946	0.9945	0.9943	0.9941	0.9940	0.9938
2.4	0.9936	0.9934	0.9932	0.9931	0.9929	0.9927	0.9925	0.9922	0.9920	0.9918
2.3	0.9916	0.9913	0.9911	0.9909	0.9906	0.9904	0.9901	0.9898	0.9896	0.9893
2.2	0.9890	0.9887	0.9884	0.9881	0.9878	0.9875	0.9871	0.9868	0.9864	0.9861
2.1	0.9857	0.9854	0.9850	0.9846	0.9842	0.9838	0.9834	0.9830	0.9826	0.9821
2.0	0.9817	0.9812	0.9808	0.9803	0.9798	0.9793	0.9788	0.9783	0.9778	0.9772
1.9	0.9767	0.9761	0.9756	0.9750	0.9744	0.9738	0.9732	0.9726	0.9719	0.9713
1.8	0.9706	0.9699	0.9693	0.9686	0.9678	0.9671	0.9664	0.9656	0.9649	0.9641
1.7	0.9633	0.9625	0.9616	0.9608	0.9599	0.9591	0.9582	0.9573	0.9564	0.9554
1.6	0.9545	0.9535	0.9525	0.9515	0.9505	0.9495	0.9484	0.9474	0.9463	0.9452
1.5	0.9441	0.9429	0.9418	0.9406	0.9394	0.9382	0.9370	0.9357	0.9345	0.9332
1.4	0.9319	0.9306	0.9292	0.9279	0.9265	0.9251	0.9236	0.9222	0.9207	0.9192
1.3	0.9177	0.9162	0.9147	0.9131	0.9115	0.9099	0.9082	0.9066	0.9049	0.9032
1.2	0.9015	0.8997	0.8980	0.8962	0.8944	0.8925	0.8907	0.8888	0.8869	0.8849
1.1	0.8830	0.8810	0.8790	0.8770	0.8749	0.8729	0.8708	0.8686	0.8665	0.8643
1.0	0.8621	0.8599	0.8577	0.8554	0.8531	0.8508	0.8485	0.8461	0.8438	0.8413
0.9	0.8389	0.8365	0.8340	0.8315	0.8289	0.8264	0.8238	0.8212	0.8186	0.8159
0.8	0.8133	0.8106	0.8078	0.8051	0.8023	0.7995	0.7967	0.7939	0.7910	0.7881
0.7	0.7852	0.7823	0.7794	0.7764	0.7734	0.7703	0.7673	0.7642	0.7611	0.7580
0.6	0.7549	0.7517	0.7486	0.7454	0.7422	0.7389	0.7357	0.7324	0.7291	0.7257
0.5	0.7224	0.7190	0.7157	0.7123	0.7088	0.7054	0.7019	0.6985	0.6950	0.6915
0.4	0.6879	0.6844	0.6808	0.6772	0.6736	0.6700	0.6664	0.6628	0.6591	0.6554
0.3	0.6517	0.6480	0.6443	0.6406	0.6368	0.6331	0.6293	0.6255	0.6217	0.6179
0.2	0.6141	0.6103	0.6064	0.6026	0.5987	0.5948	0.5910	0.5871	0.5832	0.5793
0.1	0.5753	0.5714	0.5675	0.5636	0.5596	0.5557	0.5517	0.5478	0.5438	0.5398
0.0	0.5359	0.5319	0.5279	0.5239	0.5199	0.5160	0.5120	0.5080	0.5040	0.5000

Table A4-1. Standard normal probabilities P(z), [P(-z) = 1 – P(z)], source: (R. Johnson, G. Bhattacharyya, Statistics - Principles and Methods, 2nd ed., 1992, pp. 630-631).

The values in Table A4-1 were calculated from the integral:

$$P(z) = \frac{1}{\sqrt{2\pi}} \int_0^z e^{-\frac{1}{2}t^2}\, dt$$

N	0	.05	.10	.15	.20	.25	.30	.35	.40	.45	•••	1.0
50	100	73	49	30	16	8.0	3.4	1.3	0.4	0.1		
60	100	70	45	25	13	5.4	2.0	0.6	0.2			
70	100	68	41	22	9.7	3.7	1.2	0.3	0.1			
80	100	66	38	18	7.5	2.5	0.7	0.1				
90	100	64	35	16	5.9	1.7	0.4	0.1				
100	100	62	32	14	4.6	1.2	0.2					

Table A4-2. The percentage probability $Prob_N(|r| \geq |r_o|)$ that N measurements of two uncorrelated variables give a correlation coefficient with $|r| \geq |r_o|$, as a function of N and r_o. (Blanks indicate probabilities less than 0.05%), source: (J. R. Taylor, AN INTRODUCTION TO Error Analysis, 2nd ed., 1997, pp. 290-291).

The values in Table A4-2 were calculated from the integral:

$$\Pr ob_N\left(|r| \geq |r_o|\right) = \frac{2\Gamma\left[\frac{N-1}{2}\right]}{\sqrt{\pi}\Gamma\left[\frac{N-2}{2}\right]} \int_{|r_o|}^{1} \left(1-r^2\right)^{\frac{N-4}{2}} dr$$

Euler's definition of the Gamma-function Γ(x):

$$\Gamma(x) \equiv \int_0^{\infty} e^{-t} t^{x-1} dt$$